Free Surface Waves on Swirling Flows

by

Emanuele Zuccoli

Thesis

Submitted to the University of Warwick

for the degree of

Doctor of Philosophy

Mathematics Institute

September 2023

THE UNIVERSITY OF
WARWICK

Contents

Chapter 6   Conclusions and future research   136

Appendix A The Convective Wave Equation for a general two-dimensional flow in polar coordinates   141

Appendix B An analytical dipole solution of the unsteady Oseen equations   151

Appendix C Attempts to formally justify the closure boundary condition for the 2D deep-water waves model   156

Acknowledgments

I would like to thank my supervisors Dwight Barkley and Ed Brambley for their support and guidance during my PhD. Their knowledge has always been a source of motivation for me to implement new ideas.

My deepest thanks go to my family for their continuous support throughout this journey.

I would also like to thank the University of Warwick for having funded this work.

Declarations

This thesis is submitted to the University of Warwick in support of my application for the degree of Doctor of Philosophy. It has been composed by myself and has not been submitted in any previous application for any degree.

The work presented (including data generated and data analysis) was carried out by the author. The material in Chapter 4 forms part of a manuscript submitted to the Journal of Fluid Mechanics with authors E. Zuccoli, E. J. Brambley, D. Barkley—Zuccoli *et al.* (2023).

Abstract

Motivated by the observation of surface waves rotating around the cores of vortices generated in a swimming pool, in this work we have studied the response of various free-surface swirling flows to small perturbations. While a variety of linear waves can arise in these problems—e.g. surface gravity waves, inertial waves and Rossby waves—we primarily focus here on the surface gravity waves like those observed in the swimming pool. The behaviour of the aforementioned waves depends on the both the swirling flow considered and the geometry of the problem. Different configurations have been analysed, with an increase in the complexity of the corresponding mathematical problems. In particular, we started with the study of waves in simple rotating systems, such as a rigid-walled cylinder rotating at a uniform angular velocity. We then moved to the study of non-dispersive shallow-water waves convected by either a vortex or a dipole flow in a laterally unbounded domain. Finally, we generalized the previous model and include dispersion effects coming from considering either finite-depth and deep-water waves. For the latter, we derived a reduced two-dimensional set of equations by introducing a closure boundary condition valid along the free surface. For each of these problems we neglected the effects associated to nonlinearities, viscosity, surface tension and compressibility, thus considering only the competition between gravity and convection. In order to simulate waves in a laterally unbounded region we imposed a non-reflecting boundary condition. For most of the problem studied, however, an analytical form to impose such a boundary condition is not accessible, thus we applied absorbing layer methods. In particular, for shallow-water waves we derived a Perfectly Matched Layer (PML) formulation with inclusion of advection effects; for non-shallow-water waves, on the other hand, we proposed a simple, but novel damping layer formulation with no need to introduce the additional unknowns of the PML formulation.

Chapter 1

Introduction

Rotating flows are very common. Examples range from practical and engineering applications such as swirling flows in turbines and combustion chambers (Sauer *et al.* 2018), contrails and vortex breakdown due to tip vortices on airplane wings (Mager 1972, Scorer and Davenport 1970), to naturally occurring phenomena involving geophysical and astrophysical flows such as Jupiter's Great Red Spot and accretion disks (Makhmalbaf *et al.* 2017, Mamatsashvili and Rice 2009, Ziampras *et al.* 2023). Vortices are a special and important class of rotating flows. These flows can be intuitively thought to have a strong azimuthal velocity component with respect to the other two components and this inspired researchers to find possible analytical vortex solutions and validate them experimentally. The interested reader should refer to the following books for more theoretical details on vortex dynamics: Drazin and Riley (2006), Saffman (1992), Wu *et al.* (2006).

A major source of interest in the study of vortical flows is given by their interaction with waves. This is true not only because of the beauty of the phenomena involved, but also for the variety of applications and implications these might have. Relevant examples can be found in acoustics (Fetter 1964, Kopiev and Belyaev 2010, Nazarenko *et al.* 1995), geophysical fluid dynamics (Bühler and McIntyre 2005), hydrodynamic stability theory (Acheson 1976, Bach *et al.* 2014, Jansson *et al.* 2006, Tophoj *et al.* 2013), and wave generation by turbulence (Cerda and Lund 1993, Lund and Rojas 1989).

In this work we focus on the interaction between vortices and surface waves propagating on the upper free surface of a fluid. A more detailed introduction on the related topics and models used is given in the following paragraphs.

1.1 Experimental generation of vortices

In a laboratory, vortices can be generated in a number of different ways. Here we mention two techniques often employed. The first one is named "Gravitational Collapse". It consists in filling a rotating tank with fluid, while a
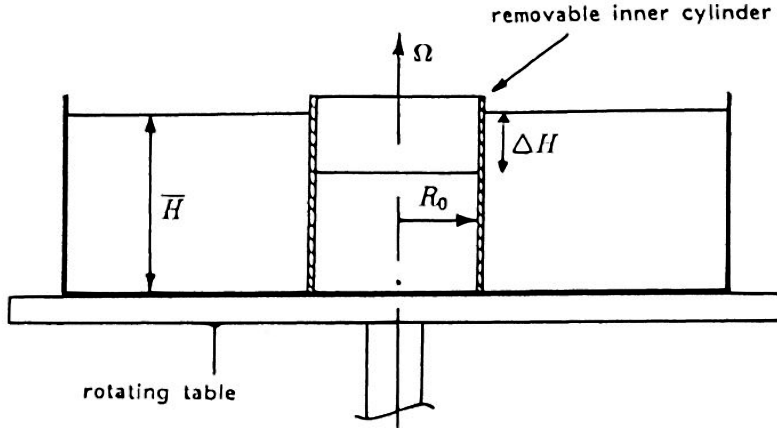
Figure 1.1: Experimental setup to use the Gravitational Collapse for generating vortices in a laboratory. The tank rotates at angular velocity Ω and contains fluid at height $\bar{H}$. ΔH is the fluid height difference between the inner and the outer fluid, whereas R_0 is the radius of the inner cylinder. Image has been taken from Flòr (2010).

bottomless cylinder with internal radius—say R_0—is placed concentrically in the tank with the fluid inside the inner cylinder at a level differing from that outside it–see figure 1.1. After the inner cylinder is withdrawn vertically, a gravity driven flow arises in radial direction. This radial motion is deflected by the Coriolis force, and after a time of typically π/Ω an equilibrium state is reached where the flow is close to being purely azimuthal. Following Kloosterziel and Heijst (1992), a possible analytical representation of the resulting flow is given by

$$u_\theta(r) = \frac{\Omega r}{2} e^{-\frac{r^2}{R_0^2}}, \tag{1.1}$$

where u_θ is the azimuthal velocity component and r the radial coordinate. We will refer to this flow as Gaussian Vortex.

The second suitable technique for creating vortices is achieved by continuously withdrawing fluid from a sink located at the centre of a rotating tank. This was well studied by Andersen *et al.* (2006) who conducted both an experimental and analytical study to analyse and control the resulting free surface swirling flow, which is called Bathtub Vortex. As depicted in figure 1.2, close to the bottom boundary of the tank the flow is not entirely azimuthal due to the development of an Ekman layer (Cushman-Roisin and Beckers 2011, Ch. 8); however, sufficiently far away from the bottom, the flow becomes purely azimuthal and a possible analytical representation for that can be given by:

$$u_\theta(r) = \sqrt{\frac{\Omega}{\nu}} \frac{F}{\pi r} \left(1 - e^{-\frac{r^2}{R_0^2}}\right), \tag{1.2}$$

where F is the flow rate at which the fluid leaves the drain-hole, R_0 is the radius of the drain-hole, Ω is the angular velocity of the tank and ν the kinematic
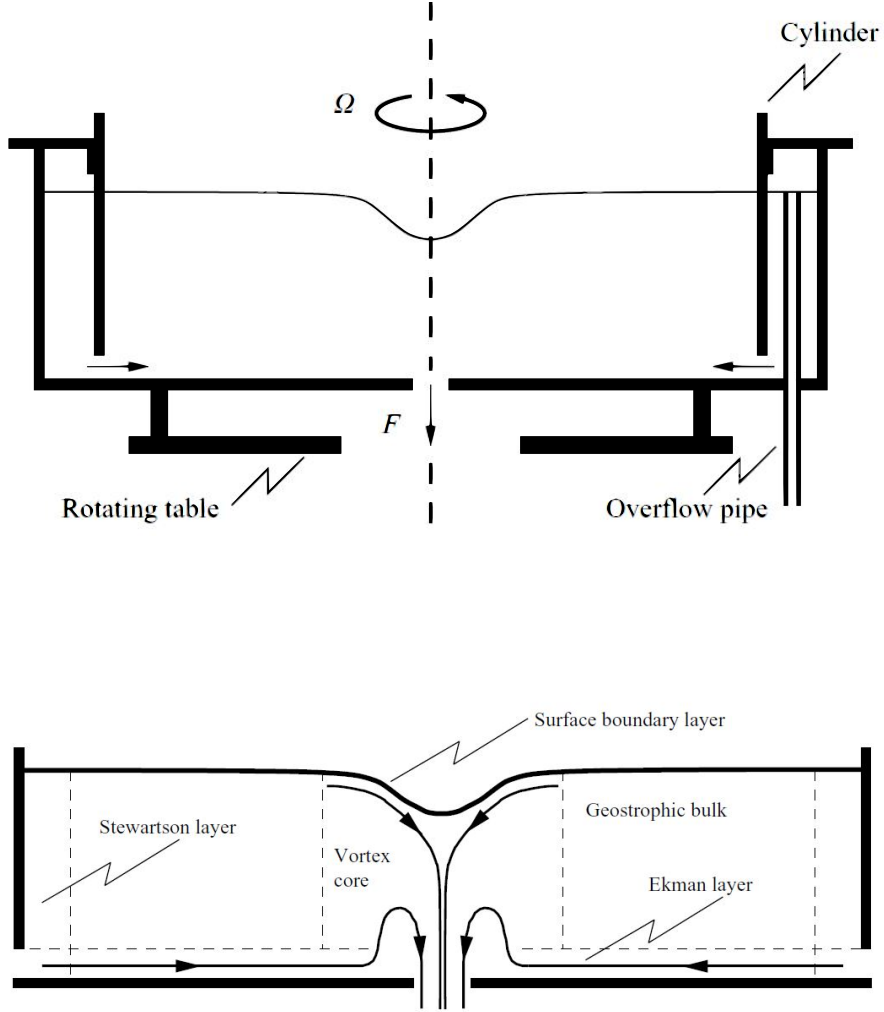
Figure 1.2: Experimental set up to generate a bathtub vortex (above). Characteristic regions of the flow in a bathtub vortex (below). The rotating table spins with angular velocity Ω. The fluid drains from the hole at a rate F. Images have been taken from Andersen *et al.* (2006).

viscosity of the fluid.

The form of the azimuthal velocity (1.2) is equivalent to an instantaneous snapshot of a Lamb-Oseen flow, which we are going to use extensively throughout the thesis. The Lamb-Oseen flow is an exact solution of the time-dependent Navier-Stokes equations (see Drazin and Riley (2006) for more details), and this fact, together with the experimental results just mentioned, make this flow a realistic vortex model to work with. Its form is given by

$$u_\theta(r,t) = \frac{\Gamma_0}{2\pi r}\left(1 - e^{-\frac{r^2}{4\nu t}}\right), \tag{1.3}$$

with Γ_0 denoting the initial circulation of the vortex. Near the centre it behaves as a solid-body rotational flow, while far away from the centre it is equivalent to a potential vortex. For this reason it overcomes other simplified vortex models, e.g. the Rankine vortex, which does not take into account
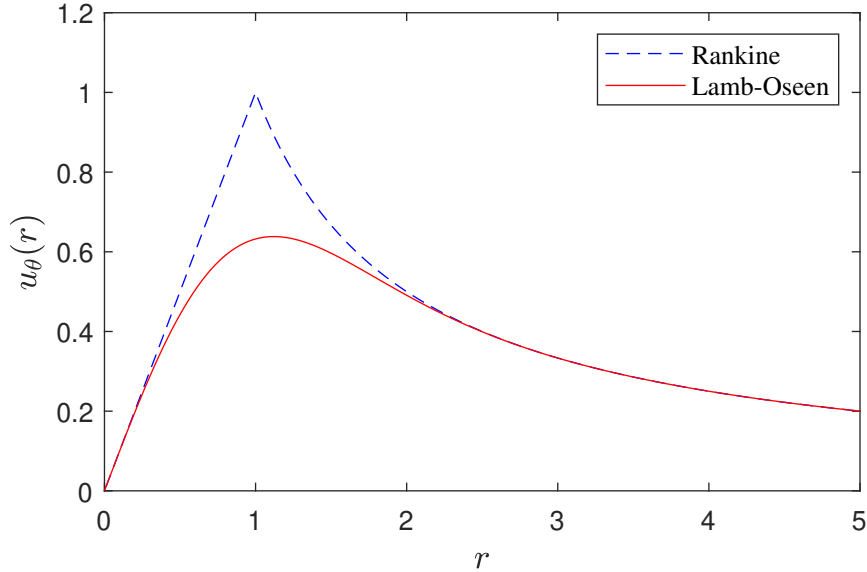
Figure 1.3: Comparison between a Rankine vortex and a steady Lamb-Oseen vortex ($4\nu t = 1$) as function of the radial coordinate.

the viscous dissipation mechanism resulting in the spreading of the vorticity initially concentrated within the core. Figure 1.3 shows a comparison between the Lamb-Oseen vortex and the Rankine vortex, highlighting particularly the overlapping of the two functions both in the core and in the outer potential region.

1.2 Vortex-waves interaction in rotating free surface flows

Rotating flows are known to support the propagation of many different type of waves. These are often viewed as small perturbations to an equilibrium state, also known as a base flow, and the behaviour of such waves depends both on the particular velocity field of the base flow and on the geometry of the problem under consideration. One important class of such waves are interfacial surface waves. These are waves forming at the interface between two fluids with different physical properties, and they often are strongly localized close to the interface. In fact, the initial motivation of this PhD work was out of curiosity concerning vortices and waves interacting in a swimming pool. An "experiment" (Skipp 2020) created pairs of vortices by drawing a dinner plate through the water. The initial waves generated by this disturbance disperse rapidly, leaving remarkably long-lived vortices with surface waves that appear trapped in the vortex, but which propagate around the vortex in the opposite direction to the vortex flow. Changes in the surface height can be easily visualized by light and dark patterns on the swimming pool floor. A photograph of the phenomena, together with a schematic representation, is
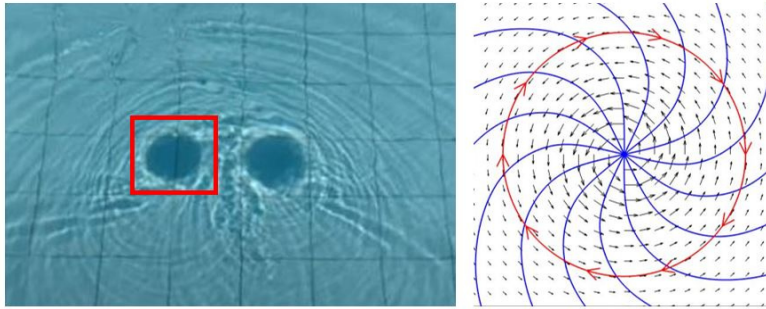
Figure 1.4: The physical scenario motivating this work. Surface waves are trapped within a rotating vortex flow, but propagate in the direction opposite the direction of rotation. Left: Photograph of two vortices in a swimming pool (a still taken from the video of Skipp 2020). Right: schematic of the flow and surface waves on the left-hand vortex. Black arrows show the base velocity field. Blue lines show the wave crests. Red arrows show the direction of propagation of the waves.

shown in figure 1.4; interested readers are encouraged to follow the reference for a video. The main objective of the present work is indeed to study the vortex-surface waves interaction appearing in free surface swirling flows.

Based on the example of the waves travelling in the pool, we can make the following assumptions that will help in highlighting the main physical ingredients hence simplifying the mathematics involved in our problems. We assume the pair of vortices travel with uniform velocity U_∞ and have a horizontal reference length scale comparable to the size of the core of one of the two vortices. We call this length a. Moreover, there exist two other length scales in the picture: the mean height of the pool h_∞ and a length l_κ responsible for viscous dissipation. We take the latter to be the Kolmogorov length scale. Thus, we can define four time scales of interest associated to different physical phenomena: $t_\nu = \frac{l_\kappa^2}{\nu}$ the viscous time scale, $t_g = \sqrt{\frac{h_\infty}{g}}$ the time scale associated to gravity acceleration, $t_{U_\infty} = \frac{a}{U_\infty}$ the inertial time scale due to the convection of the vortices and $t_\gamma = \sqrt{\rho \frac{a^3}{\gamma}}$ the one associated with surface tension γ. Using typical values of $\nu = 10^{-6}[m^2/s]$, $\rho = 10^3[Kg/m^3]$ and $\gamma = 0.073[m^3/s^2]$ for water and estimating $a = 10[cm]$, $U_\infty = 0.2[m/s]$ and $l_\kappa = 0.01[m]$, the four time scales are about

$$t_\nu = 10^2[s], \qquad t_g = 0.3[s] \qquad t_{U_\infty} = 0.5[s] \qquad t_\gamma = 3.7[s]. \qquad (1.4)$$

Clearly there is a separation of scales between the viscous time scale and the other three. So, we can easily neglect viscous contributions in the governing equations. Also, there is a separation between the time scale associated to surface tension and those involving the mean flow and gravity. Moreover, it is known that for water-air interface, capillary waves dominate the dynamics for waves whose wavelength is lower than $1.73[cm]$—see Whitham (1974)—

that is the capillary length. Even though we acknowledge that from figure 1.4 the wavelength of the waves looks comparable to the capillary length, due to the previous separation of time scales and owing to the mathematical complexities that surface tension would bring to the waves dynamics, we still neglect surface tension in our problems. Finally, assuming the perturbations to have a small amplitude with respect to the base swirling flow, we can also neglect the nonlinear advective term in the perturbations dynamics. A more detailed derivation and analysis on the general governing equations will be carried out in the next chapter.

In the next paragraphs we will recall what has been done in the literature about three main aspects concerning waves and free surface swirling flows that are yet not very well explored and that explore in this work. The first one deals with the presence of a background vortex flow on which waves can propagate. Indeed, many wave phenomena have been investigated only in the absence of a base vortex flow—see Johnson (1997) for a review on the subject. The second major point concerns the treatment of non-reflecting boundaries. More specifically, in principle we are going to simulate waves over horizontally unbounded domains; when truncation is needed for numerical purposes waves must exit the boundary without being reflected backwards. The third and last difficulty comes from the character of the waves, i.e. whether they are supposed to be non-dispersive or dispersive— see Whitham (1974) for further details.

1.3   Waves in simple rotating systems

Waves on a swirling flow have been studied numerically in Mougel *et al.* (2014, 2015, 2017) for three sufficiently simple rotating fluid systems: solid-body rotation, potential vortex and Rankine vortex. These have been studied supposing the fluid is confined inside a rigid cylindrical container. Their studies reveal the presence of four main types of waves as long as the flow does not form a dry region at the bottom boundary. Such waves are surface gravity waves, inertial waves, Rossby waves, and centrifugal waves (figure 1.5). The first three waves are observed for solid-body rotation, while centrifugal waves and gravity waves arise in the potential vortex problem. Depending on the context, each of these waves can be easily recognized and distinguished by its spatial structure and the associated frequency of oscillation.

An interesting feature of the potential vortex flow is the occurrence of an instability due to an interaction between centrifugal and gravity waves. This instability is termed "Polygon Instability" due to the polygonal shapes appearing on the free surface when the interaction occurs. The problem was initially studied by Tophoj *et al.* (2013) and subsequently by Mougel *et al.* (2017) where they showed that the interaction involves these two types of
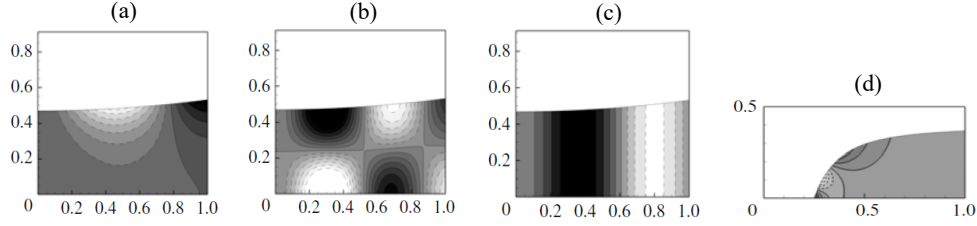
Figure 1.5: Example of surface gravity wave (a), inertial wave (b), Rossby wave (c) and centrifugal wave (d). The quantity plotted here is the real part of the pressure in the $r-z$ plane for the first three type of waves, and the real part of the velocity potential in the $r-z$ plane for the fourth type of wave. These four type of waves can be distinguished by their spatial structure: surface gravity waves are oscillatory in the radial direction, but evanescent in the axial direction. Inertial waves are oscillatory in both directions. Rossby waves are independent of the axial direction; they oscillate only along r. Centrifugal waves are oscillatory in the radial direction, but very localized where the free surface is steep. The first three figures (a–c) have been taken from (Mougel *et al.* 2015). Figure (d) has been taken from (Mougel *et al.* 2017).

wave modes, one of which is dependent on the outer boundary. The resonance mechanism can be easily understood by looking at the diagram in figure 1.6 showing the intersection of the gravity waves branches with those belonging to the centrifugal waves. At those intersection points modes with a small positive imaginary part in the corresponding eigenvalues appear, leading to the aforementioned instability.

Instabilities of vortices in horizontally unbounded domains have been found to occur within the shallow-water limit, as studied by Ford (1994). However, it is worth noting that the study of shallow-water rotating flows is rather different to the study of finite-depth rotating flows on two counts: firstly, shallow-water rotating flows can only rotate very slowly before the deformation in the free surface at the centre of the vortex touches the bottom boundary and a dry inner region is formed; and secondly, shallow-water waves are nondispersive and have a fixed wave speed, while finite-depth water waves are dispersive such that any wave speed is available to the system, and for example a wave can exist whose speed matches the flow speed at a given location.

Surface waves have also been studied by Hunt *et al.* (2015) by considering the effects of an electric field on both linear and nonlinear inviscid, irrotational waves. Moreover, two-dimensional surface waves in electrohydrodynamics and magneohydrodynamics have been studied by Hunt (2019), Hunt and Dutykh (2021), Hunt and Vanden-Broeck (2015), although in the present work we do not consider any electric or magnetic field. Finally, for interested readers, additional material involving inertial and Rossby waves can be found in Johnson (1997), Greenspan (1969) and McWilliams (2006).
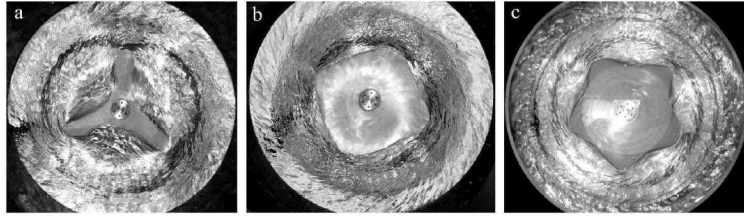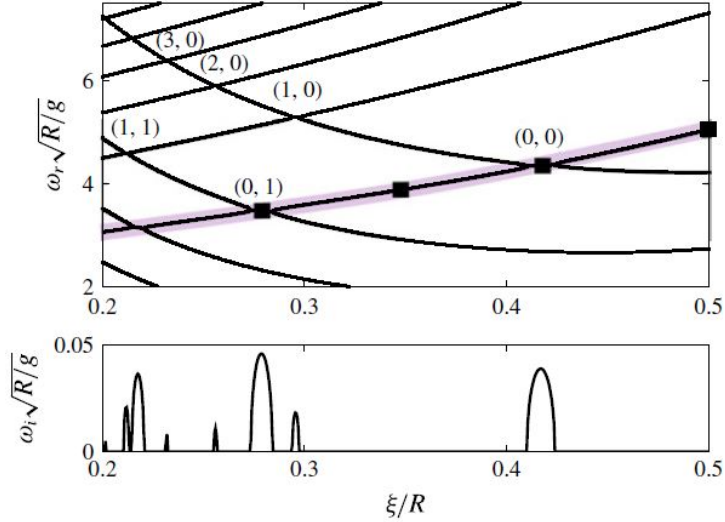
Figure 1.6: Top image: interaction mechanism between gravity and centrifugal waves in the potential free surface vortex problem studied by Mougel *et al.* (2017). The picture has been taken from the same paper. $\omega_r \sqrt{R/g}$ represents the scaled real part of the eigenvalues (oscillation frequencies) as function of the scaled size of the dry area ξ/R. On the other hand, $\omega_i \sqrt{R/g}$ represents the scaled imaginary part of the eigenvalues (the growth rate if positive). The branches going up are those of gravity waves; the branches going down are those of centrifugal waves. Bottom image: the polygonal patterns formed due to the instability. The picture has been taken by Jansson *et al.* (2006)

1.4 Non-reflecting boundary conditions

Usually vortices like those appearing in the swimming pool propagate naturally in laterally unbounded domains, so that the resulting wave propagation problems also have to be studied in the same unlimited region. This introduces one of the main points that we have covered throughout this thesis, which is the imposition of non-reflecting boundary conditions (NRBC). The basic idea is that at infinity there are no sources of waves, therefore any source of waves coming in from infinity should be avoided. Finding new formulas and methods to impose such a desired behaviour of waves at infinity is by itself a research field and a literature review is discussed below. However, before going through that, let us explain the main idea using the simplest 1D wave equation. The physical scenario is displayed in figure 1.7, with a right-going wave leaving the domain without any reflection. We want to describe this mathematically. Let
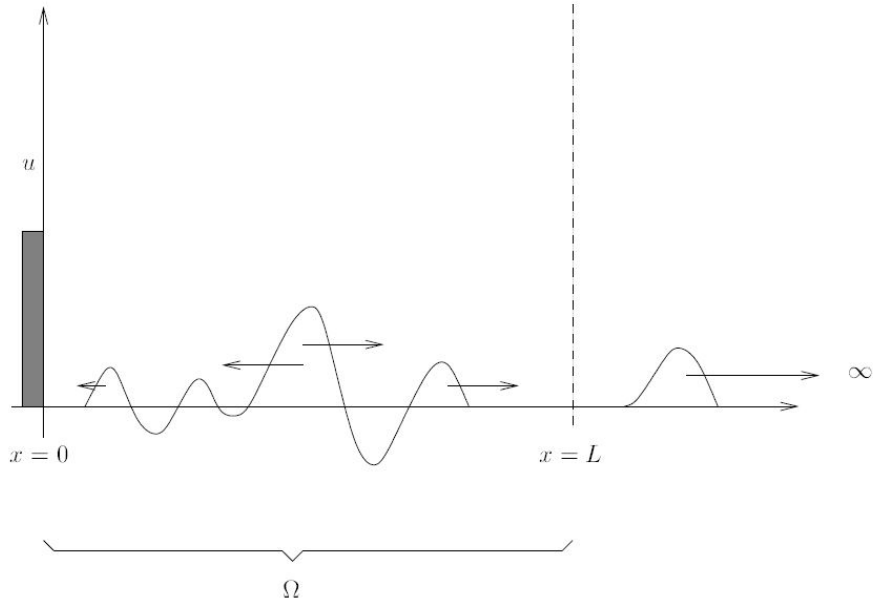
Figure 1.7: Example of a wave leaving the domain Ω without begin reflected backward. This is the result of applying a NRBC. Picture has been taken by Sim (2010).

us consider the 1D wave equation:

$$\frac{\partial^2 u}{\partial t^2} - c^2 \frac{\partial^2 u}{\partial x^2} = 0, \quad x \in \Omega \equiv [0, L], \tag{1.5}$$

with suitable boundary conditions and where $c = const.$ represents the constant phase speed of the waves. Defining $v = \partial_t u + c\partial_x u$ and $w = \partial_t u - c\partial_x u$, equation above can be re-written as a first order system of PDEs of the form

$$\begin{aligned}
\frac{\partial v}{\partial t} - c\frac{\partial v}{\partial x} &= 0, \\
\frac{\partial w}{\partial t} + c\frac{\partial w}{\partial x} &= 0.
\end{aligned} \tag{1.6}$$

Its solution is given by $v(x,t) = \phi(x+ct)$ and $w(x,t) = \psi(x-ct)$, being ϕ and ψ two arbitrary functions representing an incoming wave (moving to the left) and an outgoing wave (moving to the right), respectively. Now, if we want our waves to exit the boundary $x = L$ without coming back, then we need to impose the Non-Reflecting Boundary Condition:

$$v(L,t) = 0 \Rightarrow \frac{\partial u(L,t)}{\partial t} + c\frac{\partial u(L,t)}{\partial x} = 0. \tag{1.7}$$

Equation (1.7) for u is the exact NRBC obtained by formally using the Method of Characteristics. This method is widely used in Applied Mathematics in order to study hyperbolic problems and hence it is the simplest way to derive a Non-Reflecting Boundary Condition. A classical reference on the topic can be found in Fritz (1978).

We give a review of the main works done to deal with different formulation of non-reflecting boundary conditions for wave propagation problems. The first part is devoted to finding exact boundary conditions based on the characteristics analysis; the second part instead deals with Perfectly Matched Layers that are novel methods to impose the non-reflecting behaviour.

The pioneering work on NRBC was performed by Engquist and Majda (1977) for plane waves. They first obtained the exact NRBC in terms of a pseudo-differential operator computed by Laplace-Fourier transforming the wave equation in time and space respectively. Then, they localized the pseudo-differential operator by expanding it in Taylor series around a small wave speed, hence obtaining a hierarchy of local NRBCs. The first and second approximations are still widely used. Higdon (1986, 1987, 1994) generalized the results of Engquist and Majda by deriving a high-order NRBC capable of absorbing exactly waves travelling at a given wave speed and incident with a known angle at the transparent artificial boundary. The boundary conditions derived by Engquist, Majda and Higdon, however, could contain operators whose spatial and temporal derivatives might be higher than two. To limit this increasing in the order of the derivatives, Givoli and Neta (2003) reformulated the boundary condition introduced by Higdon without spatial derivatives higher than two. This goal is achieved by introducing J auxiliary variables in the formulation representing waves travelling at the know constant velocity c_j. Later on Hagstrom and Hariharan (1998) extended the formulation of Givoli and Neta to non-dispersive waves in both polar and spherical coordinates. It was Lindquist *et al.* (2012) who generalized that to dispersive waves in polar coordinates. Regarding spherical waves, Bayliss and Turkel (1980), inspired by the high-order NRBCs introduced by Higdon, derived a sequence of local operators by increasingly annihilating terms coming from the far-field expansion of an outgoing spherical wave solution. Exact boundary conditions for spherical waves, however, were derived later in a very elegant way by Grote and Keller for the non-dispersive wave equation (Grote and Keller 1995, 1996, 2000) and then extended to electromagnetic and elastic waves too (Grote 2000a,b, 2006, Grote and Sim 2009).

As far as Perfectly Matched Layers (PMLs) formulation are concerned, the initial work was done by Berenger (1994) to deal with Maxwell equations. The initial formulations in his work were based on splitting the electromagnetic fields into two parts, the first containing the tangential derivatives and the second containing the normal derivatives. Damping is then enforced only upon the normal direction. Later, Zhao and Cangellaris (1996) proposed a formulation without splitting the electromagnetic field. Similar approaches were then applied to wave phenomena in elasticity (Basu and Chopra (2007), Chew and Liu (1996)) and fluid dynamics (Söderstrom *et al.* (2010)). The main disadvantage in the PML formulations lies in the high number of additional

unknowns that have to be defined in order to close the system of equations. A more recent and novel formulation that tries to reduce such an issue was proposed by Sim (2010) for the non-dispersive (with possibly varying velocity) wave equation. As discussed, this offers a big advantage in terms of new variable definitions, especially in 2D spatial problems.

1.5 Modelling the convection in shallow-water waves

When waves are driven by a background vortex flow in an unbounded region their behaviour can be complicated and rich. A prototype model for this will be derived in chapter 3 and consists in studying a Convective Wave Equation (CWE) of the form

$$D_t^2 \phi - c^2 \nabla^2 \phi = 0, \tag{1.8}$$

where $D_t = \partial_t + \boldsymbol{U_0} \cdot \nabla$ represents the convective derivative due to the background vortex flow $\boldsymbol{U_0}$, $c = \sqrt{gH}$ the wave speed in the Shallow-Water limit and ϕ the velocity potential associated to the perturbation. Due to the convective derivative operator, this model is the first attempt to describe the advection effect that a prescribed background flow has on the dynamics of the surface gravity waves. The CWE has been widely studied only recently as an analogue to the behaviour of rotating black holes. The pioneering work on the topic was done by Unruh (1981) who showed that the dynamics of rotating black holes is exactly equivalent to the dynamics of surface gravity waves on vortices. A more recent and complete work is contained in the PhD thesis by Patrick (2019). Within these studies, there are two main features that we are going to focus on throughout this work because of their relevance in the Fluid Dynamics field: the first one is called rotational superradiance–see Patrick and Weinfurtner (2020), Richartz *et al.* (2015), Torres (2019), Torres *et al.* (2017)–and represents the amplification of an incident wave into the vortex, whereas the second one is called ergoregion instability (Oliveira *et al.* 2014)— or even superradiance instability as it is directly related to the superradiance amplification mechanism (Cardoso *et al.* 2004)—and represents the possibility of exciting unstable normal modes having an exponential growth rate in time. The instability can be also seen as a resonance condition between the surface gravity waves and the vortex, as shown in (Dolan *et al.* 2012, Patrick *et al.* 2018, Torres *et al.* 2018). Even though these two effects are linked one another, here we give more emphasis on the latter as we are interested in investigating the possible unstable modes interacting with a base vortex flow. The paper inspiring the material developed in chapter 3, in fact, is that by Oliveira *et al.* (2014), who showed that a potential vortex in an "unbounded" fluid can give rise to unstable normal modes beyond a certain rotation rate of the vortex.

1.6 Dispersive models for waves on swirling flows

As explained in the previous section, the Convective Wave Equation holds only under the Shallow-Water approximation. Such limit though ceases to be valid in many contexts. It is therefore important to derive new models capable of dealing with the dispersive character of non-shallow-water waves, which comes from finite-depth effects. The pioneering effort in this direction was made by Boussinesq (1871). We briefly give the main ideas and the generalizations that leads to more recent models. The Boussinesq equation and subsequent models are all based on the potential flow assumption, as well as the approximation that the free surface remains flat and it is located at a level, say $z = H$. The flow is also bounded at the bottom $z = 0$ and neither viscosity nor surface tension is included. For simplicity, we just focus here on the linear problem. The strategy shown here to derive Boussinesq-type equations is based on depth-averaging the governing Laplace equation and then use integration by parts to link the average potential and the fluid elevation. By doing so, one can obtain a hierarchy of wave equations that approximate better and better the dispersive effects in a finite-depth configuration. The order of convergence of the approximate model is dictated by the truncation in the series of integrals computed. In particular, Boussinesq kept only the first three terms in the series, obtaining the following PDE:

$$\left(1 - \frac{H^2}{2}\nabla^2\right)\frac{\partial^2 \phi}{\partial t^2} - gH\left(1 - \frac{H^2}{6}\nabla^2\right)\nabla^2\phi = 0. \tag{1.9}$$

More accurate and recent models have been derived by keeping higher order terms in the series. This might ultimately lead to the following pseudo-differential equation

$$\frac{\partial^2 \phi}{\partial t^2} - ig\nabla\tanh(-iH\nabla)\phi = 0, \tag{1.10}$$

in the absence of a background flow, and to the following in case a base flow is present

$$D_t^2\phi - ig\nabla\tanh(-iH\nabla)\phi = 0. \tag{1.11}$$

Equation (1.11) has been studied analytically by means of the Ray-Tracing method (Bühler 2014) in the paper by Torres *et al.* (2018) in order to predict the oscillation frequencies of surface waves propagating over a potential vortex. A further generalization of that model was derived by Milewski and Keller (1996) including viscosity and surface tension too.

1.7 Contents of the chapters

In this thesis we overcome some of the drawbacks present in the literature or not yet fully investigated. The different problems studied in this work are explained by increasing complexity. More precisely, the contents are organized as follows:

- Chapter 2 is devoted to the derivation of the general stability equations for free surface swirling flows, highlighting the role of the boundary conditions. Then, simple configurations are analysed and studied in detail; analytical results are presented to give more insight into the problem as well as to validate the numerical codes built up.

- Chapter 3 is about the study of wave propagation problems in unbounded domains, using in particular the Convective Wave Equation. This model is deeply studied either when the convection is due to a monopolar vortex and when it is due to a dipole flow. Solutions are computed both in the frequency and in time domain. For the dipole case, a full PML formulation is derived and the problem is solved by time marching using the Method of Lines.

- Chapter 4 deals with the study of surface waves over a Lamb-Oseen vortex flow in a finite-depth configuration. Two main kind of modes are discovered and analysed. Furthermore, we conducted a parametric study involving different azimuthal mode numbers, Froude numbers and fluid heights so as to analyse the influence that each of these have on the dynamics of surface gravity modes.

- Chapter 5 is devoted to the derivation of a novel 2D model for studying the vortex-surface waves interaction in deep-water. We believe that such model overcomes the difficulties coming from the inclusion of higher dispersive terms presented earlier in equation (1.11). Moreover the model is valid for any nontrivial two-dimensional background flow, and able to take into account both the possible non-zero vorticity and the free surface deformation.

- Chapter 6 is a summary of the work done during this PhD and some possible future ideas to be implemented along the same research line.

Chapter 2

Waves on bounded free surface swirling flows

In this chapter we are going to derive the equations governing the linear propagation of waves in a specified free surface swirling flow. This is equivalent to study the linear stability of the free surface swirling flow. We assume here the base flow to be purely azimuthal and radially dependent only; moreover, the geometry is cylindrical with rigid walls both at a fixed radius $r = R$ and at the bottom $z = 0$. The physically relevant assumptions we make are those of neglecting viscous dissipation, surface tension effects and compressibility. Hence, the main equations will be the incompressible Euler equations. We will start our investigation of the mathematical problem by studying what happens if no vortex is present. Despite this is very well-known in the literature, it is instructive to do the calculations in order to highlight some of the features concerning surface gravity waves. We will then move to the so-called Newton's Bucket problem and solve it both numerically and analytically whenever possible. The study of these two rather simple problems lays the foundations for studying more complicated problems involving waves on laterally unbounded vortices, which will be addressed in subsequent chapters.

2.1 Euler equations linearised about a steady swirling flow

In this section we want to derive the equations describing the linear stability of a steady swirling flow, i.e. a purely azimuthal base flow, in a cylindrical reference system. Incompressible Euler equations read

$$\rho\frac{\partial \boldsymbol{u}}{\partial t} + \rho(\boldsymbol{u} \cdot \nabla)\boldsymbol{u} + \nabla P = 0,$$
$$\nabla \cdot \boldsymbol{u} = 0. \tag{2.1}$$

14

Dividing by ρ and calling $p = \frac{P}{\rho}$, equations (2.1) become

$$\frac{\partial \boldsymbol{u}}{\partial t} + (\boldsymbol{u} \cdot \nabla)\boldsymbol{u} + \nabla p = 0,$$
$$\nabla \cdot \boldsymbol{u} = 0. \tag{2.2}$$

In order to investigate the linear stability, we can express both the velocity field $\boldsymbol{u}$ and the pressure field p as the sum of two terms: the first one given by the equilibrium steady state $(\boldsymbol{U_0}, P_0)$ whereas the second given by a perturbation term, whose amplitude is controlled by a small parameter $\epsilon \ll 1$ as

$$\boldsymbol{u} = \boldsymbol{U_0} + \epsilon \boldsymbol{u}',$$
$$p = P_0 + \epsilon p'. \tag{2.3}$$

Substituting these expressions into (2.2), at the first order in ϵ we get the following equations in the unknowns $(\boldsymbol{u}', p')$

$$\frac{\partial \boldsymbol{u}'}{\partial t} + (\boldsymbol{u}' \cdot \nabla)\boldsymbol{U_0} + (\boldsymbol{U_0} \cdot \nabla)\boldsymbol{u}' + \nabla p' = 0,$$
$$\nabla \cdot \boldsymbol{u}' = 0. \tag{2.4}$$

In the present work, every time the base flow is a monopolar vortex, it will be always assumed that this is axisymmetric, that is $\boldsymbol{U_0} = U_0(r)\hat{\boldsymbol{\theta}}$. We define the angular velocity field as

$$\Omega_0(r) = \frac{U_0(r)}{r}, \tag{2.5}$$

and after having omitted the apex $'$ for notation convenience, the governing equations read

$$\frac{\partial u_r}{\partial t} + \Omega_0 \left(\frac{\partial u_r}{\partial \theta} - 2u_\theta \right) + \frac{\partial p}{\partial r} = 0,$$
$$\frac{\partial u_\theta}{\partial t} + \Omega_0 \left(\frac{\partial u_\theta}{\partial \theta} + u_r \right) + u_r \frac{d(r\Omega_0)}{dr} + \frac{1}{r}\frac{\partial p}{\partial \theta} = 0,$$
$$\frac{\partial u_z}{\partial t} + \Omega_0 \frac{\partial u_z}{\partial \theta} + \frac{\partial p}{\partial z} = 0,$$
$$\frac{1}{r}\frac{\partial}{\partial r}(ru_r) + \frac{1}{r}\frac{\partial u_\theta}{\partial \theta} + \frac{\partial u_z}{\partial z} = 0. \tag{2.6}$$

Looking for a solution in the form of rotating waves in the azimuthal direction θ

$$u_r = u(r,z)e^{-i\omega t + im\theta},$$
$$u_\theta = v(r,z)e^{-i\omega t + im\theta},$$
$$u_z = w(r,z)e^{-i\omega t + im\theta},$$
$$p = \phi(r,z)e^{-i\omega t + im\theta}, \tag{2.7}$$
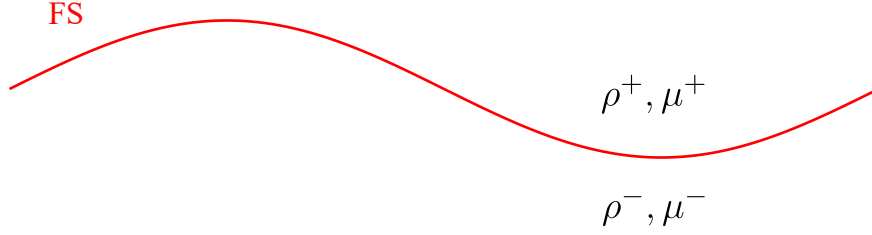
Figure 2.1: Free surface separating two fluids having different physical properties.

system (2.6) reduces to

$$
\begin{aligned}
&(-i\omega + im\Omega_0)\,u - 2\Omega_0 v + \frac{\partial \phi}{\partial r} = 0, \\
&(-i\omega + im\Omega_0)\,v + \left(\Omega_0 + \frac{d(r\Omega_0)}{dr}\right) u + \frac{im}{r}\phi = 0, \\
&(-i\omega + im\Omega_0)\,w + \frac{\partial \phi}{\partial z} = 0, \\
&\frac{1}{r}\frac{\partial}{\partial r}(ru) + \frac{im}{r}v + \frac{\partial w}{\partial z} = 0,
\end{aligned}
\tag{2.8}
$$

where now we have omitted the r-dependence of Ω_0 in order to use a lighter notation. Equations (2.8) are valid in the bulk; now we are going to deal with the boundary conditions so that our differential problem is well-posed.

2.2 Free surface problem

Let us consider two fluids divided by an interface surface as shown in figure 2.1. The free surface can be implicitly expressed as

$$
f(r, \theta, z, t) = 0.
\tag{2.9}
$$

In a cylindrical geometry, assuming the fluid height is a single-valued function, it can also be written as

$$
z = h(r, \theta, t).
\tag{2.10}
$$

The presence of a free surface adds a further unknown to the problem since the function $h(r, \theta, t)$ has to be determined. What makes the free surface shape an unknown is two boundary conditions that have to be imposed at the interface itself in order to close the differential problem. The two boundary conditions are a kinematic and a dynamic boundary conditions. In this work we will always assume the upper fluid to be dynamically passive, in particular at rest and having constant pressure. As a matter of fact, we are interested only in the dynamics of the fluid below the free surface. Let us now formally derive the two free surface boundary conditions just mentioned.
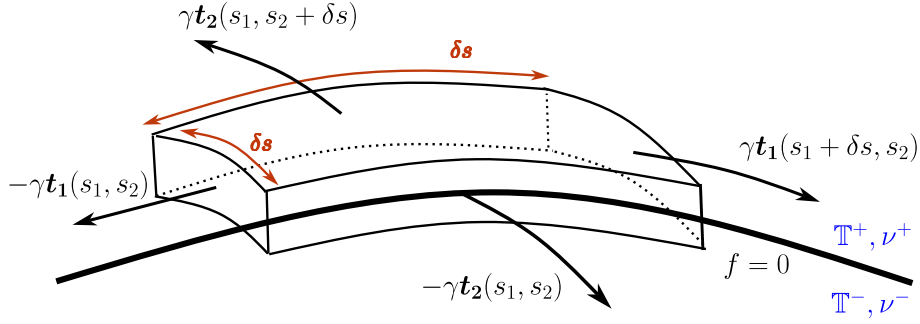
Figure 2.2: Stresses on an interface surface between two fluids

2.2.1 Kinematic boundary condition

The kinematic boundary condition expresses that along the free surface every particle follows the fluid motion. Consequently we have that the material derivative of the surface is zero, i.e.

$$\frac{Df}{Dt} = 0, \quad at \quad z = h. \tag{2.11}$$

Letting $f = z - h(r, \theta, t)$, by the previous relation we get

$$u_z - \frac{Dh}{Dt} = 0, \tag{2.12}$$

i.e.

$$u_z = \frac{\partial h}{\partial t} + u_r \frac{\partial h}{\partial r} + \frac{u_\theta}{r} \frac{\partial h}{\partial \theta}, \quad at \quad z = h. \tag{2.13}$$

2.2.2 Dynamic boundary condition

The dynamic boundary condition states that all forces acting on and within the interfacial surface must balance. Generally, this includes inertial forces, body forces, pressure and viscous stresses and the force due to the surface tension (γ), which we are going to assume to be constant.

Let us consider an infinitesimal volume of fluid accross the free surface, as depicted in figure 2.2. The element has area δs^2 and a height much smaller than δs. For this reason, in the force balance we can ignore both the inertial contribution and that coming from the body forces. The force balance on the infinitesimal element involves only the stresses that either the lower and upper fluid exert on the element and the force from inside the interface which is due to the surface tension. The equilibrium condition implies

$$\delta s^2 \mathbb{T}^+ \cdot \boldsymbol{n} + \delta s^2 \mathbb{T}^- \cdot (-\boldsymbol{n}) + \delta s \gamma \Big(\boldsymbol{t_1}(s_1 + \delta s, s_2) - \boldsymbol{t_1}(s_1, s_2) \Big)$$
$$+ \delta s \gamma \Big(\boldsymbol{t_2}(s_1, s_2 + \delta s) - \boldsymbol{t_2}(s_1, s_2) \Big) = 0, \quad at \quad z = h. \tag{2.14}$$

We recall that for a Newtonian, incompressible fluid, the stress tensor $\mathbb{T}$ (per

unit-density) is defined as

$$\mathbb{T} = -p\mathbb{I} + \nu\left(\nabla\boldsymbol{u} + \nabla\boldsymbol{u}^T\right). \tag{2.15}$$

Proceeding with the derivation of the dynamic boundary condition, if we divide by δs^2 equation (2.14) and take the limit $\delta s \to 0$, we get

$$\mathbb{T}^+ \cdot \boldsymbol{n} - \mathbb{T}^- \cdot \boldsymbol{n} = -\gamma\left(\frac{\partial \boldsymbol{t_1}}{\partial s_1} + \frac{\partial \boldsymbol{t_2}}{\partial s_2}\right) \equiv \gamma\kappa\boldsymbol{n}, \quad at \quad z = h, \tag{2.16}$$

where κ represents the curvature of the interface. Now, using the properties that $\boldsymbol{t_1} \cdot \boldsymbol{n} = 0$ and $\boldsymbol{t_2} \cdot \boldsymbol{n} = 0$, after differentiating them with respect to s_1 and s_2 respectively, we can write

$$\begin{aligned} \frac{\partial \boldsymbol{t_1}}{\partial s_1} \cdot \boldsymbol{n} + \boldsymbol{t_1} \cdot \frac{\partial \boldsymbol{n}}{\partial s_1} &= 0, \\ \frac{\partial \boldsymbol{t_2}}{\partial s_2} \cdot \boldsymbol{n} + \boldsymbol{t_2} \cdot \frac{\partial \boldsymbol{n}}{\partial s_2} &= 0, \end{aligned} \tag{2.17}$$

hence the curvature can be written as

$$\kappa = -\left(\frac{\partial \boldsymbol{t_1}}{\partial s_1} + \frac{\partial \boldsymbol{t_2}}{\partial s_2}\right) \cdot \boldsymbol{n} = \boldsymbol{t_1} \cdot \frac{\partial \boldsymbol{n}}{\partial s_1} + \boldsymbol{t_2} \cdot \frac{\partial \boldsymbol{n}}{\partial s_2} = \nabla_s \cdot \boldsymbol{n}, \tag{2.18}$$

where ∇_s is the surface gradient operator. This operator is the gradient operator taking effect on a surface, hence can be defined as

$$\nabla_s = \nabla - \boldsymbol{n}(\boldsymbol{n} \cdot \nabla). \tag{2.19}$$

It is indeed the standard gradient subtracted from its normal component. Through the differential relationship $\boldsymbol{n}(\boldsymbol{n} \cdot \nabla) = \nabla \times \boldsymbol{n} \times \boldsymbol{n}$, application of the surface gradient to the normal unit vector $\boldsymbol{n}$ yields

$$\kappa = \left(\nabla - \nabla \times \boldsymbol{n} \times \boldsymbol{n}\right) \cdot \boldsymbol{n} \equiv \nabla \cdot \boldsymbol{n}. \tag{2.20}$$

Therefore, the dynamic boundary condition takes the final form

$$\mathbb{T}^+ \cdot \boldsymbol{n} - \mathbb{T}^- \cdot \boldsymbol{n} = \gamma(\nabla \cdot \boldsymbol{n})\boldsymbol{n}, \quad at \quad z = h. \tag{2.21}$$

In case the effects of both surface tension and viscosity are negligible, the stress tensor reduces to $\mathbb{T} = -p\mathbb{I}$ and the dynamic boundary condition simply states a balance of the pressure across the interface

$$p^- = p^+, \quad at \quad z = h. \tag{2.22}$$

Equation (2.22) is the version of the dynamic boundary condition we are always going to use throughout the thesis.

2.2.3 Free surface shape for a generic axisymmetric swirling flow

As previously stated, in this section we consider a base steady velocity field of the form $\boldsymbol{U_0}(r, \theta, z) = U_0(r)\hat{\boldsymbol{\theta}}$. The associated equilibrium equations then read

$$
-\frac{U_0^2(r)}{r} + \frac{\partial P_0}{\partial r} = 0,
$$
$$
\frac{\partial P_0}{\partial z} = -g,
$$

(2.23)

where g is the gravity acceleration. By integrating the second equation we obtain

$$
P_0(r, z) = -gz + f(r),
$$

(2.24)

and inserting it into the first one we get

$$
f'(r) = \frac{U_0^2(r)}{r} \Rightarrow f(r) = \int \frac{U_0^2(r)}{r} dr + C,
$$

(2.25)

being C an arbitrary constant. Now, the shape of the base free surface $h_0(r)$ is obtained by using the dynamic boundary condition (2.22). Let $\bar{P}_0$ be the constant pressure on the free surface, we obtain

$$
P_0(r, h_0(r)) = \bar{P}_0,
$$

(2.26)

that is

$$
-gh_0(r) + \int \frac{U_0^2(r)}{r} dr + C = \bar{P}_0.
$$

(2.27)

We can always set $C = \bar{P}_0$ so that

$$
h_0(r) = \frac{1}{g} \int \frac{U_0^2(r)}{r} dr.
$$

(2.28)

2.2.4 Linearisation of the boundary conditions at the free surface for inviscid flows and with no surface tension

Through the kinematic and dynamic boundary conditions, the free surface enters the problem as a new unknown. Consequently, we can express it as the sum of a steady free surface (derived in the previous paragraph) and a small perturbation

$$
h(r, \theta, t) = h_0(r) + \epsilon h'(r, \theta, t), \quad \epsilon \ll 1.
$$

(2.29)

Now, recalling the perturbation velocity, we expand expressions (2.13) and (2.22) in Taylor series around the steady free surface $h_0(r)$. Starting with the kinematic boundary condition, its linearised version reads

$$
u_z' = \frac{\partial h'}{\partial t} + \frac{U_0(r)}{r} \frac{\partial h'}{\partial \theta} + u_r' \frac{dh_0(r)}{dr}, \quad at \quad z = h_0(r).
$$

(2.30)

Following the hypothesis for the pressure to be constant on the free surface and neglecting surface tension, after linearisation, the dynamic boundary condition (2.22) reads

$$h' = \frac{1}{g}p', \qquad at \quad z = h_0(r).\tag{2.31}$$

We can combine the two conditions obtaining a unique one that links the pressure and the velocity components at the free surface

$$u'_z = \frac{1}{g}\left(\frac{\partial p'}{\partial t} + \frac{U_0(r)}{r}\frac{\partial p'}{\partial \theta}\right) + \frac{dh_0(r)}{dr}u'_r, \qquad at \quad z = h_0(r).\tag{2.32}$$

Following the notation previously used for the rotating waves as in equations (2.8), we finally write the linearised boundary condition at the free surface as

$$w = \frac{1}{g}\left(-\mathrm{i}\omega + \mathrm{i}m\Omega_0(r)\right)\phi + \frac{dh_0(r)}{dr}u, \qquad at \quad z = h_0(r).\tag{2.33}$$

2.2.5 Stability problem in a confined cylindrical geometry

We want to study the linear stability problem of a steady axisymmetric swirling flow whose upper boundary is given by its steady free surface and has finite radius and finite depth. Since, as shown in the previous section the unknowns of the equations are supposed to be travelling waves in the azimuthal direction, we can consider the domain of the problem as the cross section of a cylinder delimited by the free surface at the top. The physical domain is shown in figure 2.3. The differential problem governing the phenomenon is described

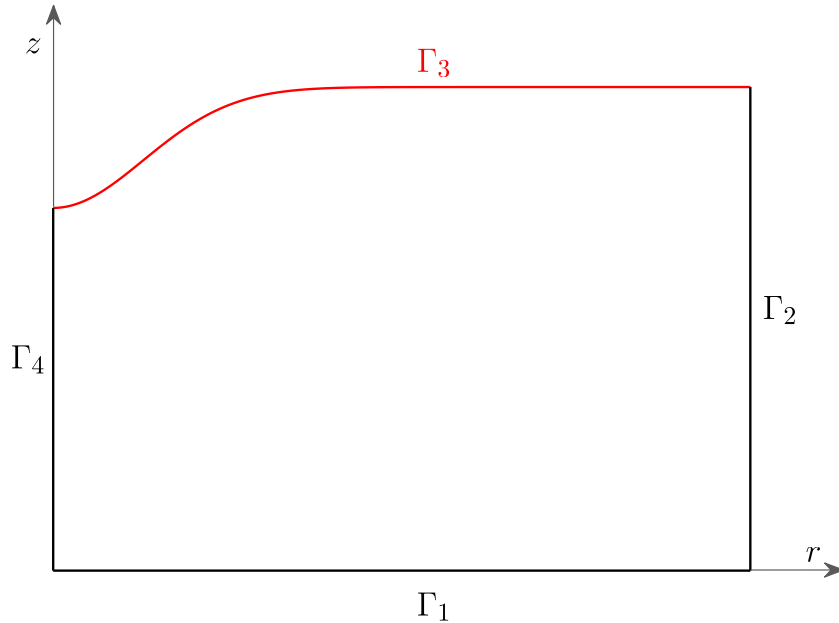
Figure 2.3: Physical domain of the problem in the $r-z$ plane. The free surface $h_0(r)$ is drawn in red and represented by the boundary Γ_3. Also, Γ_1 represents the bottom wall of the cylinder $z = 0$; Γ_2 the lateral boundary $r = R$ and Γ_4 the axis of the cylinder $r = 0$.

by the following set of equations and boundary conditions

$$
\begin{aligned}
&(-\mathrm{i}\omega + \mathrm{i}m\Omega_0)\, u - 2\Omega_0 v + \frac{\partial \phi}{\partial r} = 0,\\
&(-\mathrm{i}\omega + \mathrm{i}m\Omega_0)\, v + \left(\Omega_0 + \frac{d(r\Omega_0)}{dr}\right) u + \frac{\mathrm{i}m}{r}\phi = 0,\\
&(-\mathrm{i}\omega + \mathrm{i}m\Omega_0)\, w + \frac{\partial \phi}{\partial z} = 0,\\
&\frac{1}{r}\frac{\partial}{\partial r}(ru) + \frac{\mathrm{i}m}{r}v + \frac{\partial w}{\partial z} = 0,\\
&w = \frac{1}{g}\left(-\mathrm{i}\omega + \mathrm{i}m\Omega_0\right)\phi + u\frac{dh_0}{dr},\quad on \quad \Gamma_3,\\
&w = 0,\quad on \quad \Gamma_1,\\
&u = 0,\quad on \quad \Gamma_2,\\
&(\boldsymbol{u}, \phi) = (u, v, w, \phi) < \infty,\quad on \quad \Gamma_4.
\end{aligned}
\tag{2.34}
$$

We start now to study simpler mathematical problems with respect to equations (2.34), given by few simplifications in the form of the base velocity field and/or the type of perturbation considered (axisymmetric or not).

2.3 Stability of a flow at rest and surface gravity waves

Let us consider a fluid initially at rest filling a cylinder of radius R and whose free surface is initially constant as shown in figure 2.4:

$$
\boldsymbol{U_0}(r) = \boldsymbol{0} \Rightarrow h_0(r) = H.
\tag{2.35}
$$

The equations governing the perturbation dynamics are given by

$$
\begin{aligned}
&\frac{\partial u_r'}{\partial t} + \frac{\partial p'}{\partial r} = 0,\\
&\frac{\partial u_\theta'}{\partial t} + \frac{1}{r}\frac{\partial p'}{\partial \theta} = 0,\\
&\frac{\partial u_z'}{\partial t} + \frac{\partial p'}{\partial z} = 0,\\
&\frac{1}{r}\frac{\partial}{\partial r}\left(ru_r'\right) + \frac{1}{r}\frac{\partial u_\theta'}{\partial \theta} + \frac{\partial u_z'}{\partial z} = 0,
\end{aligned}
\tag{2.36}
$$

whereas the boundary conditions read

$$
\begin{aligned}
&u_r' = 0,\quad at \quad r = R,\\
&(\boldsymbol{u}, p') < \infty,\quad at \quad r = 0,\\
&u_z' = 0,\quad at \quad z = 0,\\
&u_z' = \frac{1}{g}\frac{\partial p'}{\partial t},\quad at \quad z = H.
\end{aligned}
\tag{2.37}
$$

21
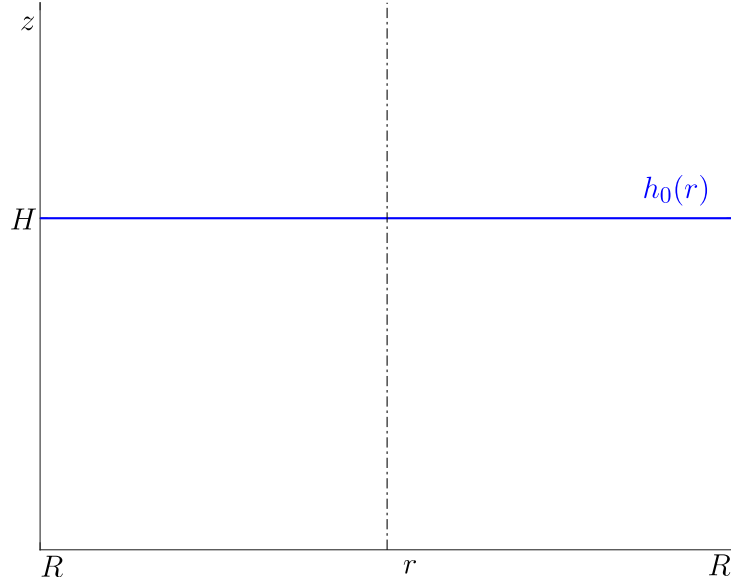
Figure 2.4: Geometry of the problem in the case of no swirl.

We can easily reduce the system (2.36) to a single PDE in the pressure by taking the divergence of the momentum equation and re-arranging the boundary conditions accordingly. By doing so, the resulting differential problem reads

$$
\begin{aligned}
&\Delta p' = 0, \\
&\frac{\partial p'}{\partial r} = 0, \quad at \quad r = R, \\
&\frac{\partial p'}{\partial z} = 0, \quad at \quad z = 0, \\
&\frac{\partial p'}{\partial z} = -\frac{1}{g}\frac{\partial^2 p'}{\partial t^2}, \quad at \quad z = H,
\end{aligned}
\tag{2.38}
$$

where $\Delta = \frac{\partial^2}{\partial r^2} + \frac{1}{r}\frac{\partial}{\partial r} + \frac{1}{r^2}\frac{\partial^2}{\partial \theta^2} + \frac{\partial^2}{\partial z^2}$ is the Laplacian in cylindrical coordinates. As usual, looking for a solution in terms of temporal normal modes—$p'(r, \theta, z, t) = \phi(r, z)e^{-i\omega t + im\theta}$—the previous system reduces to

$$
\begin{aligned}
&\frac{\partial^2 \phi}{\partial r^2} + \frac{1}{r}\frac{\partial \phi}{\partial r} - \frac{m^2}{r^2}\phi + \frac{\partial^2 \phi}{\partial z^2} = 0, \\
&\frac{\partial \phi}{\partial r} = 0, \quad at \quad r = R, \\
&\frac{\partial \phi}{\partial z} = 0, \quad at \quad z = 0, \\
&\frac{\partial \phi}{\partial z} = \frac{\omega^2}{g}\phi, \quad at \quad z = H,
\end{aligned}
\tag{2.39}
$$

System (2.39) can now be solved in closed form by means of separation of variables. We set $\phi(r, z) = a(r)b(z)$, obtaining the following two ODEs re-

22

spectively:

$$a''(r) + \frac{1}{r}a'(r) - \frac{m^2}{r^2}a(r) + k^2 a(r) = 0, \tag{2.40}$$
$$b''(z) = k^2 b(z).$$

The first of the two equations above is a Bessel equation. In particular, in order to reduce it to the standard form, we make a change of variable setting $x = kr$. This yields

$$a''(x) + \frac{1}{x}a'(x) - \frac{m^2}{x^2}a(x) + a(x) = 0, \tag{2.41}$$

whose general solution is

$$a(x) = A J_m(x) + B Y_m(x), \tag{2.42}$$

being J_m and Y_m the m-th Bessel functions of first and second kind respectively. Coming back to the original coordinate r, the solution is written as

$$a(r) = A J_m(\lambda r) + B Y_m(\lambda r). \tag{2.43}$$

We impose now the boundary conditions along the radial coordinate:

$$a(0) < \infty \Rightarrow B = 0,$$
$$a'(R) = 0 \Rightarrow J_m'(kR) = 0 \Rightarrow kR = \alpha_{m,n} \Rightarrow k_{m,n} = \frac{1}{R}\alpha_{m,n}, \tag{2.44}$$

begin $\alpha_{m,n}$ the zeros of the m-th Bessel function derivative. As far as the z-dependence is concerned, we have to solve the following equation

$$b'' - k^2 b = 0, \tag{2.45}$$

which, for any (m, n) mode becomes

$$b''_{m,n} - k^2_{m,n} b_{m,n} = 0. \tag{2.46}$$

The general solution of (2.46) is

$$b_{m,n}(z) = C_{m,n} e^{-k_{m,n}z} + D_{m,n} e^{k_{m,n}z}. \tag{2.47}$$

Imposition of the last two boundary conditions in (2.39) yields $D_{m,n} = C_{m,n}$ and the dispersion relation

$$\omega^2_{m,n} = g k_{m,n} \tanh(k_{m,n}H) \Rightarrow \omega_{m,n} = \pm\sqrt{g k_{m,n} \tanh(k_{m,n}H)}. \tag{2.48}$$

Therefore, the general solution for each mode can be expressed as

$$\phi_{m,n} = \mathcal{A}_{m,n} J_m(k_{m,n} r) \cosh k_{m,n} z,$$
$$\omega_{m,n} = \pm \sqrt{g k_{m,n} \tanh(k_{m,n} H)}.$$
(2.49)

Examples of the exact eigenmodes with their relative frequencies is shown in figure 2.5 for azimuthal wavenumbers $m = 0, 1, 2$, $R = 1$ and $H = 1$.
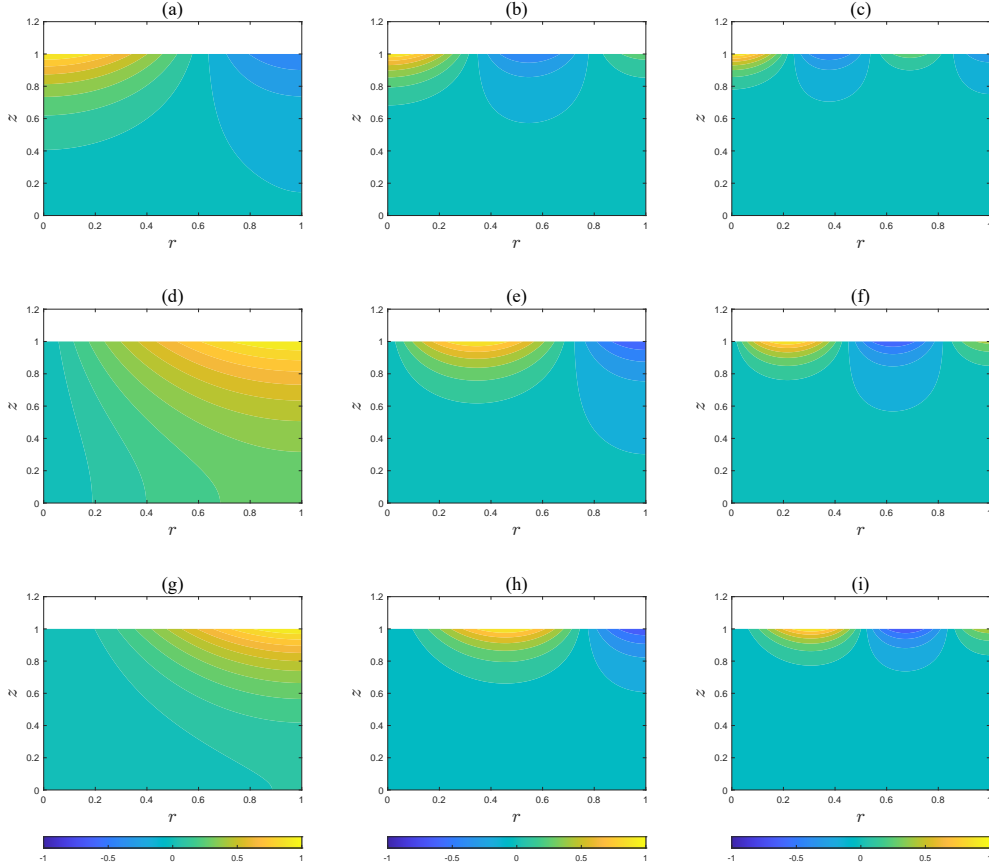
Figure 2.5: Exact eigensolutions of surface gravity waves given by equations (2.49) for $m = 0$ (first row), $m = 1$ (second row) and $m = 2$ (third row). The real part of the pressure eigenmodes is shown here. The corresponding eigenvalues are the following: (a): $\omega_{0,1} = 6.128$. (b): $\omega_{0,2} = 8.296$. (c): $\omega_{0,3} = 9.990$. (d): $\omega_{1,1} = 4.144$. (e): $\omega_{1,2} = 7.231$. (f): $\omega_{1,3} = 9.151$. (g): $\omega_{2,1} = 5.461$. (h): $\omega_{2,2} = 8.110$. (i): $\omega_{2,3} = 9.889$.

2.3.1 Infinitely axially extended cylinder

In the particular case the system has infinite depth, the acceptable solution of equation (2.46) is given by

$$b_{m,k}(z) = C_{m,k} e^{\lambda_{m,k} z}.$$
(2.50)

By imposing the boundary condition at the free surface, the dispersion relation now modifies into

$$\omega_{m,n} = \pm\sqrt{gk_{m,k}}. \tag{2.51}$$

This is the well-known dispersion relation for deep-water surface gravity waves and can be further seen as the asymptotic solution of (2.48) as $H \to \infty$. A representation of the effects of a finite depth both in a shallow and deep water limit is is given in figure 2.6 for axisymmetric modes ($m = 0$). Even for depths of unit magnitude (figure 2.6 Right), it is clear how quickly with depth the dispersion relation (2.48) becomes indistinguishable to the one for the deep-water regime (2.51). This is because the $\tanh(\cdot)$ function becomes one very quickly. For instance, the first radial wavenumber $k_{0,1} \simeq 3$, and hence $\tanh(k_{0,1}) \simeq 1$ already. More significant variations in the spectrum between the finite and infinite depth cases are expected to occur for values of H much smaller than one.
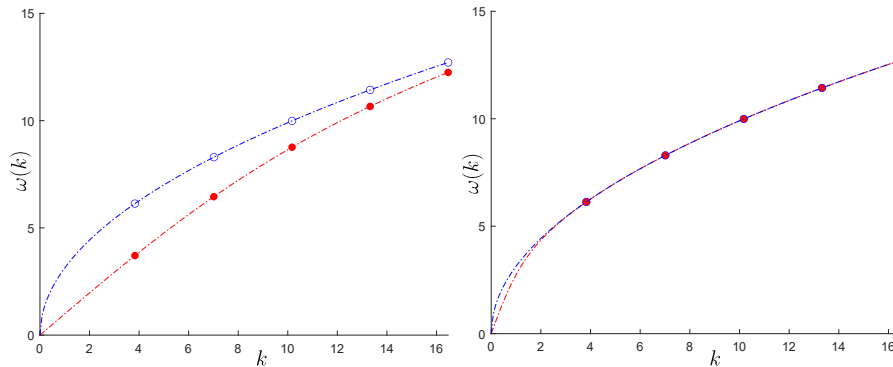
Figure 2.6: Dispersion of deep-water surface gravity waves (blue diagram), and finite-depth surface gravity waves (red diagram) for $m = 0$, $R = 1$ and two different fluid depths. Left: $H = 0.1$. Right: $H = 1$.

2.4   Free surface Newton's bucket problem

In this section, instead of considering a fluid at rest, we assume that it rotates with a constant angular velocity. The system is bounded again by the plane $z = 0$ at the bottom and by the free surface at the top–figure 2.7. The importance of studying this kind of free surface problem lies not only in its historical significance (Newton was the first who tried to deal with it) and the real applications where this problem is relevant, but also because it can be used as an elegant and simpler problem to understand some of the main features on the stability of more complicated swirling flows, such as the Lamb-Oseen vortex that we are going to study later in this work. The Newton's bucket problem was extensively studied in Mougel *et al.* (2015), but we also study the same problem for two main reasons: the first one is to validate our numerical spectral code which we are going to adapt and use in the next
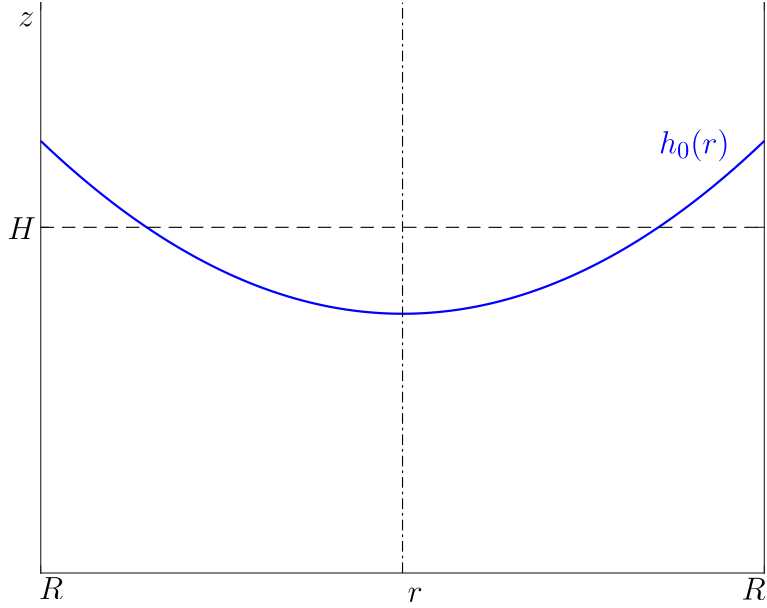
Figure 2.7: Geometry of the Newton's bucket problem.

chapters for different problems. Secondly, we will add to the work of Mougel *et al.* (2015) a more analytical part consisting of finding the eigenmodes in closed form when the domain is unbounded below the free surface. We start the analysis by introducing the parameters appearing in the problem and the corresponding base quantities. We assume the flow to be confined in a cylinder of radius R, initially occupying a volume $\pi R^2 H$. The fluid is put into rotation with a constant angular velocity Ω and is subject to centrifugal and gravity acceleration. We express both the velocity and pressure fields as the sum of a steady equilibrium flow and a small amplitude perturbation. For the specific problem we have:

$$
\begin{aligned}
\boldsymbol{U}(r,\theta,z,t) &= \Omega r \hat{\boldsymbol{\theta}} + \boldsymbol{u}(r,\theta,z,t), \\
P(r,\theta,z,t) &= \bar{P} + g\Big[H + \frac{\Omega^2}{2g}\Big(r^2 - \frac{R^2}{2}\Big) - z\Big] + p(r,\theta,z,t),
\end{aligned}
\tag{2.52}
$$

where $\bar{P}$ is the ambient constant pressure above the free surface and $h_0(r) = H + \frac{\Omega^2}{2g}\Big(r^2 - \frac{R^2}{2}\Big)$ is the base free surface obtained using the dynamic boundary condition on the pressure. After linearising about the equilibrium solution, the following equations and boundary conditions for the perturbations are

26

obtained

$$\frac{\partial \boldsymbol{u}}{\partial t} + \Omega \frac{\partial \boldsymbol{u}}{\partial \theta} + 2\Omega(\hat{\boldsymbol{z}} \times \boldsymbol{u}) + \nabla p = 0,$$

$$\nabla \cdot \boldsymbol{u} = 0,$$

$$u_r = 0, \quad at \quad r = R,$$

$$u_z = 0, \quad at \quad z = 0, \tag{2.53}$$

$$u_z = \frac{\partial h}{\partial t} + \Omega \frac{\partial h}{\partial \theta} + h_0'(r)u_r, \quad on \quad z = h_0(r),$$

$$p = gh, \quad on \quad z = h_0(r),$$

where $h_0'(r)$ is the derivative of $h_0(r)$ with respect to r.

We can non-dimensionalize the system above by means of the following transformations:

$$(r, \theta, z) \to (Rr, \theta, Rz), \qquad t \to \frac{t}{\Omega},$$

$$\boldsymbol{u} \to (\Omega R)\boldsymbol{u}, \qquad p \to (\Omega R)^2 p, \tag{2.54}$$

so that, after combining the two boundary conditions on the free surface $z = h_0(r)$, the dimensionless differential problem reads

$$\frac{\partial \boldsymbol{u}}{\partial t} + \frac{\partial \boldsymbol{u}}{\partial \theta} + 2\hat{\boldsymbol{z}} \times \boldsymbol{u} + \nabla p = 0,$$

$$\nabla \cdot \boldsymbol{u} = 0,$$

$$u_r = 0, \quad at \quad r = 1, \tag{2.55}$$

$$u_z = 0, \quad at \quad z = 0,$$

$$u_z = aF^2 \left(\frac{\partial p}{\partial t} + \frac{\partial p}{\partial \theta} \right) + h_0'(r)u_r, \quad on \quad z = h_0(r),$$

where now $h_0(r) = a\left[1 + F^2\left(\frac{r^2}{2} - \frac{1}{4}\right)\right]$, $h_0'(r) = aF^2 r$, $a = \frac{H}{R}$ is the aspect ratio, giving the ratio between the fluid height and the radius of the cylinder. Finally, $F = \frac{\Omega R}{\sqrt{gH}}$ the Froude number measuring the competition between inertial and gravity effects; alternatively, how fast the fluid rotates. Although the governing equations in (2.55) are equivalent to those written in a rotating reference frame due to the term $2\hat{\boldsymbol{z}} \times \boldsymbol{u}$ (as it is typically the case for geophysical flows), here these equations are valid in a non-rotating reference frame, as they govern the perturbations over a solid-body rotational flow.

The differential problem above can be re-arranged in terms of the pressure only. In order to do so, let us take the divergence of the momentum equation. We have:

$$2\nabla \cdot \left(\hat{\boldsymbol{z}} \times \boldsymbol{u}\right) + \Delta p = 0. \tag{2.56}$$

We introduce the axial vorticity $\xi_z = \frac{1}{r}\frac{\partial}{\partial r}\left(ru_\theta\right) - \frac{1}{r}\frac{\partial u_r}{\partial \theta}$. Then, $\nabla \cdot (2\hat{\boldsymbol{z}} \times \boldsymbol{u}) = -2\xi_z$, obtaining

$$\Delta p - 2\xi_z = 0. \tag{2.57}$$

On the other hand, if we take the curl of the momentum equation and project

it onto the z-axis, we get an evolution equation for ξ_z:

$$\frac{\partial \xi_z}{\partial t} + \frac{\partial \xi_z}{\partial \theta} = 2\frac{\partial u_z}{\partial z}. \tag{2.58}$$

Applying the convective operator $\partial_t + \partial_\theta$ to equation (2.58) and using the momentum equation along the axial direction, we can write

$$\left(\frac{\partial}{\partial t} + \frac{\partial}{\partial \theta}\right)^2 \xi_z = -2\frac{\partial^2 p}{\partial z^2}. \tag{2.59}$$

Finally, application of the convective operator squared to equation (2.57), yields

$$\left(\frac{\partial}{\partial t} + \frac{\partial}{\partial \theta}\right)^2 \Delta p + 4\frac{\partial^2 p}{\partial z^2} = 0. \tag{2.60}$$

Regarding the boundary conditions in equation (2.55), these can be re-written in terms of the pressure only as

$$D_t\frac{\partial p}{\partial r} + \frac{2}{r}\frac{\partial p}{\partial \theta} = 0, \quad at \quad r = 1, \tag{2.61a}$$

$$\frac{\partial p}{\partial z} = 0, \quad at \quad z = 0, \tag{2.61b}$$

$$aF^2 D_t^2(D_t^2 + 4)p + (D_t^2 + 4)\frac{\partial p}{\partial z} - 2aF^2 D_t\frac{\partial p}{\partial \theta} = aF^2 D_t^2 r\frac{\partial p}{\partial r}, \quad on \quad z = h_0(r), \tag{2.61c}$$

where for notation convenience $D_t = \partial_t + \partial_\theta$ is the convective operator introduced before.

Equation (2.60) is the so-called Poincaré equation. It has a different character depending on the rotation rate of the flow and will therefore give rise to different kind of waves (Greenspan 1969). Indeed, by taking the usual normal modes decomposition $p = \phi(r,z)e^{-i\omega + im\theta}$ and calling $\lambda = \omega - m$, the Poincaré equation becomes

$$\frac{\partial^2 \phi}{\partial r^2} + \frac{1}{r}\frac{\partial \phi}{\partial r} - \frac{m^2}{r^2}\phi + \left(\frac{\lambda^2 - 4}{\lambda^2}\right)\frac{\partial^2 \phi}{\partial z^2} = 0. \tag{2.62}$$

If $|\lambda| > 2$ equation above is elliptic and admit regular eigenmode solutions represented by surface gravity waves. On the contrary if $|\lambda| < 2$, with $\lambda \neq 0$, the equation is hyperbolic and its solution are represented by singular inertial waves. Finally, if $\lambda \to 0$, the equation becomes degenerate and its solutions are given by Rossby Waves which do not depend on the axial coordinate z. These three categories of waves are those arising as long as the system remains wet, i.e. does not form a dry region on the bottom boundary. As studied in Mougel *et al.* (2015), when the Froude number exceeds $F = 2$, a dry region forms and also another type of waves arise, the Edge Waves. However, in this work we will always stick within the wet case.

2.4.1 Weak formulation and numerical solution of Newton's bucket problem

In this section we are going to derive the weak formulation of the Newton's bucket problem defined in terms of the physical variables (2.55) and then use this to develop a numerical scheme. We first decompose both the velocity and the pressure in normal modes of the form

$$\boldsymbol{u} = [u, v, w](r, z)e^{-\mathrm{i}\omega t + \mathrm{i}m\theta}, \qquad p = \phi(r, z)e^{-\mathrm{i}\omega t + \mathrm{i}m\theta}. \tag{2.63}$$

Defining $\lambda = \omega - m$, equations (2.55) become

$$-2v + \frac{\partial\phi}{\partial r} = \mathrm{i}\lambda u, \tag{2.64a}$$

$$2u + \frac{\mathrm{i}m}{r}\phi = \mathrm{i}\lambda v, \tag{2.64b}$$

$$\frac{\partial\phi}{\partial z} = \mathrm{i}\lambda w, \tag{2.64c}$$

$$\frac{1}{r}\frac{\partial}{\partial r}\left(ru\right) + \frac{\mathrm{i}m}{r}v + \frac{\partial w}{\partial z} = 0, \tag{2.64d}$$

$$u = 0, \quad on \quad r = 1, \tag{2.64e}$$

$$w = -\mathrm{i}\lambda\phi + h_0'(r)u, \quad on \quad z = h_0(r), \tag{2.64f}$$

$$w = 0, \quad on \quad z = 0, \tag{2.64g}$$

where again $h_0(r) = a\left[1 + \frac{F^2}{2}\left(r^2 - \frac{1}{2}\right)\right]$ is the dimensionless base free surface and $h_0'(r)$ its derivative with respect to r. Since our domain is curvilinear, we first make a change of coordinates to map from the physical domain to a square $S \in [-1, 1]^2$:

$$x = 2r - 1,$$
$$y = \frac{2}{h_0(r)}z - 1. \tag{2.65}$$
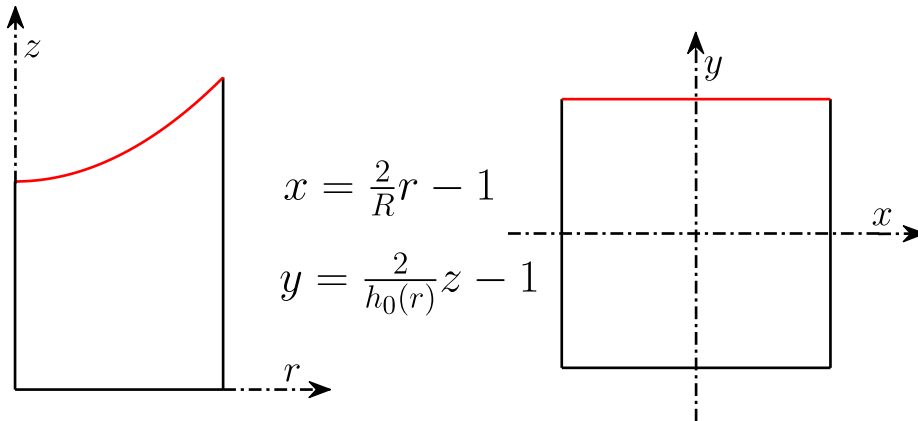
The transformation is shown in figure 2.8.

Figure 2.8: Transformation from the original physical domain to the square $S = [-1, 1] \times [-1, 1]$.

The derivatives transform according to

$$\frac{\partial}{\partial r} = 2\left[\frac{\partial}{\partial x} - \frac{h_0'(x)}{h_0(x)}(y+1)\frac{\partial}{\partial y}\right],$$
$$\frac{\partial}{\partial z} = \frac{2}{h_0(x)}\frac{\partial}{\partial y}.$$

(2.66)

At this point, we add an artificial viscous term in the momentum equation along the radial coordinate. This is useful to ensure the inertial modes to be sufficiently smooth and well-resolved in their spatial structure. Indeed, inertial modes have an oscillatory structure in both the radial and the axial direction, thus an artificial viscous term would prevent those modes to resemble numerically spurious modes due to a poor resolution in the discretization. However, as we will show later the effects of such an artificial viscosity does not influence the surface gravity modes that are going to be the most important and discussed modes in this work. The aforementioned dissipative term is defined as $\mathcal{D}^2 = \frac{\partial^2}{\partial x^2}$. This is sufficient in our weak formulation to ensure diffusion without the need to introduce a full Laplacian operator, which would cause unnecessary difficulties during the re-mapping of the domain. In this way, the final differential problem written in the new coordinate system reads

$$-2v + 2\left[\frac{\partial\phi}{\partial x} - \frac{h_0'(x)}{h_0(x)}(y+1)\frac{\partial\phi}{\partial y}\right] - \nu\frac{\partial^2 u}{\partial x^2} = \mathrm{i}\lambda u,$$

(2.67a)

$$2u + \frac{2im}{(x+1)}\phi = \mathrm{i}\lambda v,$$

(2.67b)

$$\frac{2}{h_0(x)}\frac{\partial\phi}{\partial y} = \mathrm{i}\lambda w,$$

(2.67c)

$$\frac{1}{(x+1)}\left[\frac{\partial}{\partial x}((x+1)u) - \frac{h_0'(x)}{h_0(x)}(y+1)(x+1)\frac{\partial u}{\partial y}\right] + \frac{im}{(x+1)}v + \frac{1}{h_0(x)}\frac{\partial w}{\partial y} = 0,$$

(2.67d)

$$u(y,1) = 0,$$

(2.67e)

$$w(-1,x) = 0,$$

(2.67f)

$$w(x,1) = -\mathrm{i}\lambda\phi(x,1) + 2h_0'(x)u(x,1)$$

(2.67g)

In equations (2.67) we have emphasised that h_0 and its derivative are already given as functions of the scaled radial coordinate x.

We are going to obtain the weak formulation of problem (2.67) and then the corresponding approximate discrete algebraic version. We look for the unknowns in different spaces depending on the boundary conditions. As opposed to what done in Shen (1997), in order not to define vector spaces dependent on the azimuthal wavenumber m, we first multiply the θ-momentum equation and the continuity equation by $\frac{1}{2}(x+1)$. We can now define vector spaces which do not depend on the azimuthal wavenumber; in particular, based

on the boundary conditions for u and w, we define

$$
\begin{aligned}
X_u &:= \{u \in H^1(S) : u(1, y) = 0\}, \\
X_v &:= H^1(S), \\
X_w &:= \{w \in H^1(S) : w(x, -1) = 0\}, \\
Q &:= H^1(S),
\end{aligned}
\tag{2.68}
$$

so that we can look for the unknowns in the corresponding spaces above, i.e. $u \in X_u$, $v \in X_v$, $w \in X_w$ and $\phi \in Q$. In order to get the weak formulation of the problem, we chose a vector test function $\boldsymbol{v} = (v_x, v_\theta, v_y) \in X_u \times X_v \times X_w$, a scalar test function $q \in Q$, we multiply the governing equations by these test functions and integrate over the square S. After having integrated and exploited the boundary conditions, the following weak formulation reads: find $(u, v, w, \phi) \in X_u \times X_v \times X_w \times Q$ such that for any $(v_x, v_\theta, v_y, q) \in X_u \times X_v \times X_w \times Q$ we have

$$
\int_S -2v_x v + 2v_x \left(\frac{\partial \phi}{\partial x} - \frac{h_0'(x)}{h_0(x)}(y+1)\frac{\partial \phi}{\partial y} \right) + \nu \frac{\partial v_x}{\partial x}\frac{\partial u}{\partial x} = i\lambda \int_S v_x u, \tag{2.69a}
$$

$$
\int_S v_\theta(x+1)u + imv_\theta \phi = i\lambda \int_S \frac{x+1}{2} v_\theta v, \tag{2.69b}
$$

$$
\int_S v_y \frac{2}{h_0(x)}\frac{\partial \phi}{\partial y} = i\lambda \int_S v_y w, \tag{2.69c}
$$

$$
\int_S -(x+1)\frac{\partial q}{\partial x}\frac{\partial u}{\partial x} - q\frac{h_0'(x)}{h_0(x)}(y+1)(x+1)\frac{\partial u}{\partial y} + imqv - \frac{\partial q}{\partial y}\frac{(x+1)}{h_0(x)}w
$$
$$
\tag{2.69d}
$$

$$
+ \int_{-1}^1 \frac{2h_0'(x)(x+1)}{h_0(x)}q(x,1)u(x,1) = i\lambda \int_{-1}^1 \frac{(x+1)}{h_0(x)}q(x,1)\phi(x,1). \tag{2.69e}
$$

 Problem (2.69) defines a generalised eigenvalue problem whose eigenvalues are λ. Indeed, after having defined the space $W = X_u \times X_v \times X_w \times Q$, it can be written more elegantly and compactly as:

find $(\boldsymbol{u}, \phi) \in W$ such that

$$
\mathcal{A}((\boldsymbol{u}, \phi); (\boldsymbol{v}, q)) = \lambda \mathcal{B}((\boldsymbol{u}, \phi); (\boldsymbol{v}, q)), \quad \forall (\boldsymbol{v}, q) \in W. \tag{2.70}
$$

What we are going to do in the following paragraph is to approximate its solution by constructing the corresponding algebraic problem by means of a Galerkin Spectral Method.

Algebraic reduction of the differential problem

In order to obtain a numerical solution of problem (2.70) we first have to approximate the velocity and pressure spaces. We will use a Galerkin Spectral approximation since we are dealing with a weak differential problem. Let us

denote with $\mathbb{Q}_N(S)$ the space of polynomials given by

$$\mathbb{Q}_N(S) := \{v(x,y) = \sum_{i,j=0}^{N} a_{ij} x^i y^j, \quad a_{ij} \in \mathbb{R}\}. \tag{2.71}$$

Because all the velocity components and the pressure belong to different vector spaces, we are going to define proper basis functions for each of them. This will be done through Legendre polynomials and their combination so that the boundary conditions for any velocity components are satisfied. In an analogous way to what has been done for the continuous case, the approximate vector spaces are

$$
\begin{aligned}
X_{u_N} &= \{u_N(x,y) \in \mathbb{Q}_N : u_N(1,y) = 0\}, \\
X_{v_N} &= \{v_N(x,y) \in \mathbb{Q}_N\}, \\
X_{w_N} &= \{w_N(x,y) \in \mathbb{Q}_N : w_N(x,-1) = 0\}, \\
X_{\phi_N} &= \{\phi_N(x,y) \in \mathbb{Q}_N\}.
\end{aligned}
\tag{2.72}
$$

We then expand the unknowns in terms of Legendre polynomials both in the x and y coordinate according to

$$
\begin{aligned}
u_N(x,y) &= \sum_{i=0}^{N-1} \sum_{j=0}^{N} u_{i,j} L_i^\star(x) L_j(y), \\
v_N(x,y) &= \sum_{i=0}^{N} \sum_{j=0}^{N} v_{i,j} L_i(x) L_j(y), \\
w_N(x,y) &= \sum_{i=0}^{N} \sum_{j=0}^{N-1} w_{i,j} L_i(x) L_j^\diamond(y), \\
\phi_N(x,y) &= \sum_{i=0}^{N} \sum_{j=0}^{N} \phi_{i,j} L_i(x) L_j(y),
\end{aligned}
\tag{2.73}
$$

where L_k are the standard Legendre polynomials, whereas $L_k^\star$ and $L_k^\diamond$ are defined according to

$$
\begin{aligned}
L_k^\star(x) &= L_k(x) - L_{k+1}(x), \quad k \geq 0, \\
L_k^\diamond(y) &= L_k(y) + L_{k+1}(y), \quad k \geq 0,
\end{aligned}
\tag{2.74}
$$

such that each $L_k^\star(x)$ satisfy a homogeneous Dirichlet boundary condition at $x = 1$, whereas each $L_k^\diamond(x)$ satisfy a homogeneous Dirichlet boundary condition at $x = -1$. The test functions are expanded in a similar way so that by plugging the expansion into the weak formulation previously derived we end up with an algebraic eigenvalue problem of the form

$$\mathbb{A}\boldsymbol{W} = \lambda\mathbb{B}\boldsymbol{W}. \tag{2.75}$$

Matrices $\mathbb{A}$ and $\mathbb{B}$ can be generally written as

$$\mathbb{A} = \begin{pmatrix} A_{ru} & A_{rv} & 0 & A_{r\phi} \\ A_{\theta u} & A_{\theta v} & 0 & A_{\theta \phi} \\ 0 & 0 & A_{zw} & A_{z\phi} \\ A_{cu} & A_{cv} & A_{cw} & A_{c\phi,} \end{pmatrix} \tag{2.76}$$

$$\mathbb{B} = \begin{pmatrix} B_{ru} & 0 & 0 & 0 \\ 0 & B_{\theta v} & 0 & 0 \\ 0 & 0 & B_{zw} & 0 \\ 0 & 0 & 0 & B_{c\phi,} \end{pmatrix} \tag{2.77}$$

being their elements still matrices of smaller size coming from evaluating the integrals appearing in the weak formulation. The array $\boldsymbol{W} = (\boldsymbol{U}, \boldsymbol{\Pi})^T$ returns the coefficients of the expansion for the velocity components and the pressure. The eigenproblem (2.75) is then solved numerically using Matlab.

Spurious modes and resolvedness condition

Spectral methods may give rise to spurious eigenvalues and eigenfunctions. These are numerical artifacts caused by highly-oscillatory eigenfunctions which are not well-resolved given a numerical resolution. That is, the eigenfunction satisfy the discretized problem (2.75) without satisfying the continuous eigenvalue problem (2.70)—(Boyd 2001, chapter 7). Here two strategies have been applied to retain only well resolved eigenvalues and eigenvectors. For the eigenvalues, let λ_i be the set of eigenvalues computed using N_x and N_y modes. (Previously we used the same N for both x and y to lighten notation. Here we do not assume they are the same.) Let λ_j be the set of eigenvalues computed with a slightly increased resolution (e.g. with $N_x + 1$ and $N_y + 1$). Then, the first resolvedness condition states that

$$\inf_{j} |\lambda_i - \lambda_j| \leq tol_1, \qquad i = 1, \ldots, N_i, \tag{2.78}$$

being N_i the total number of eigenvalues computed using the first resolution and tol_1 a prescribed tolerance. Eigenvalues satisfying the above condition are those stable under small changes to the discretization, and hence are a good eigenvalues.

The second strategy to exclude spurious modes follows what has been done in Brambley (2007, 59), and is based on the imposition of a resolvedness condition on the eigenfunctions. Given an eigenvector with spectral coefficient a_{ij}, it is well-resolved if

$$Resolvedness = \frac{\sup_{(i,j) \in \mathcal{B}} |a_{ij}|}{\sup_{\forall (i,j)} |a_{ij}|} \leq tol_2, \tag{2.79}$$

being tol_2 a prescribed tolerance and $\mathcal{B}$ an L-shaped subdomain in the $i - j$ plane denoting highly oscillatory modes, such that

$$\mathcal{B} = \{(i, j) : N_x - b_x \leq i \leq N_x, \quad or \quad N_y - b_y \leq j \leq N_y\}, \tag{2.80}$$

with b_x, b_y two prescribed borders widths. The region $\mathcal{B}$ is shown in figure 2.9. Figure 2.10 displays a well resolved pressure mode and a badly-resolved
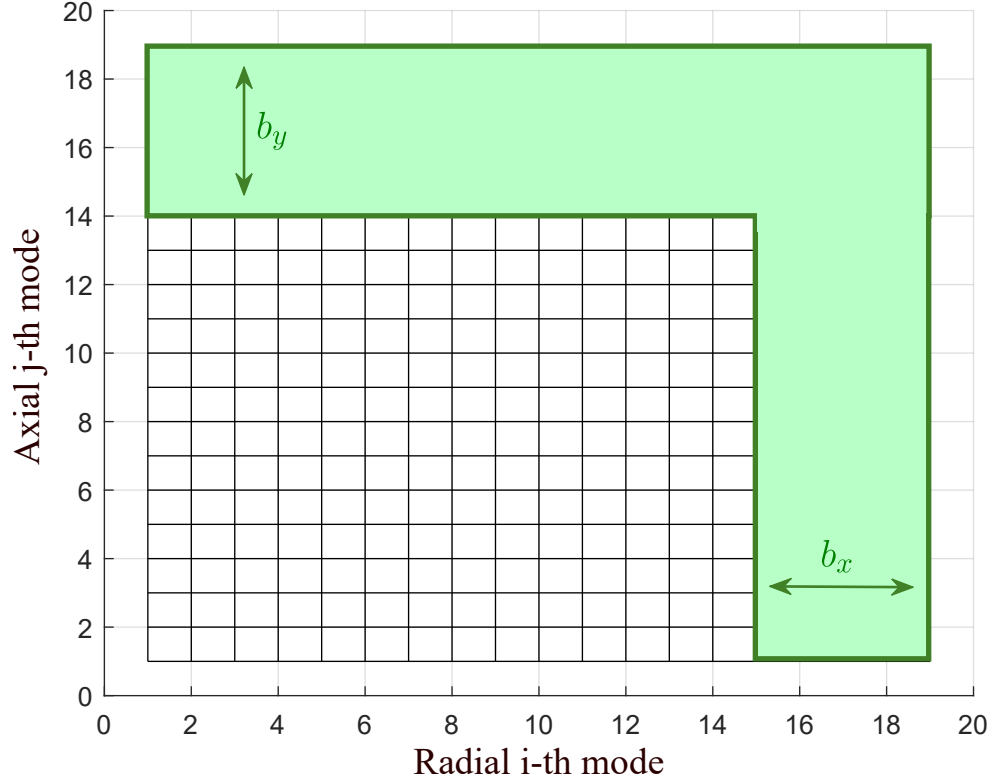
Figure 2.9: Resolvedness region for the convergence of a computational mode: the subdomain $\mathcal{B}$ is coloured in light-green.

pressure mode taking $b_x = b_y = 4$, $N_x = N_y = 19$ and a tolerance $tol_2 = 10^{-2}$. It can be seen how for a well-resolved mode, the magnitude of the spectral coefficient a_{ij} decreases very fast with mode number. By contrast, for a badly-resolved mode, the amplitude $|a_{ij}|$ does not decay.

Figure 2.10: Comparison between a badly-resolved mode (left) and a well-resolved mode (right).

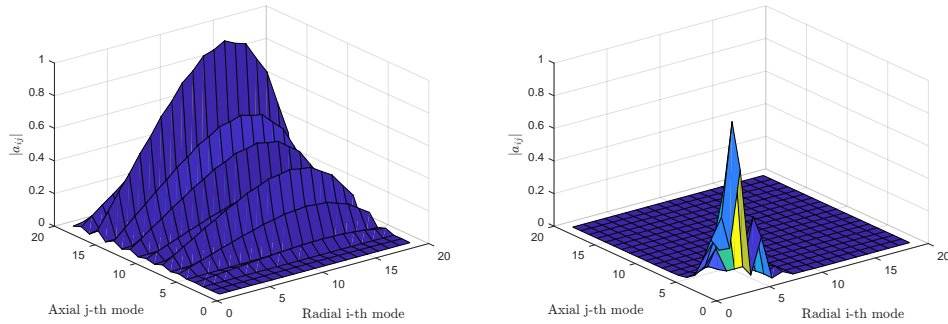| Mode	$\nu = 10^{-2}$	$\nu = 10^{-4}$	$\nu = 10^{-9}$	$\nu = 0$
(a)	$4.289 - 8 \cdot 10^{-4}\mathrm{i}$	$4.289 - 8 \cdot 10^{-6}\mathrm{i}$	$4.289 - 8 \cdot 10^{-11}\mathrm{i}$	$4.289 - 1 \cdot 10^{-14}\mathrm{i}$
(b)	$7.435 - 1 \cdot 10^{-2}\mathrm{i}$	$7.435 - 1 \cdot 10^{-4}\mathrm{i}$	$7.435 - 1 \cdot 10^{-9}\mathrm{i}$	$7.435 - 1 \cdot 10^{-14}\mathrm{i}$
(c)	$9.043 - 3 \cdot 10^{-2}\mathrm{i}$	$9.043 - 3 \cdot 10^{-4}\mathrm{i}$	$9.043 - 3 \cdot 10^{-9}\mathrm{i}$	$9.043 + 1 \cdot 10^{-15}\mathrm{i}$
(d)	$-5.201 - 3 \cdot 10^{-3}\mathrm{i}$	$-5.201 - 3 \cdot 10^{-5}\mathrm{i}$	$-5.201 - 3 \cdot 10^{-10}\mathrm{i}$	$-5.201 + 1 \cdot 10^{-14}\mathrm{i}$
(e)	$-7.458 - 1 \cdot 10^{-2}\mathrm{i}$	$-7.458 - 1 \cdot 10^{-4}\mathrm{i}$	$-7.458 - 1 \cdot 10^{-9}\mathrm{i}$	$-7.458 + 5 \cdot 10^{-14}\mathrm{i}$
(f)	$-9.034 - 4 \cdot 10^{-2}\mathrm{i}$	$-9.035 - 4 \cdot 10^{-4}\mathrm{i}$	$-9.035 - 4 \cdot 10^{-9}\mathrm{i}$	$-9.035 + 1 \cdot 10^{-14}\mathrm{i}$

Table 2.1: Variation of the eigenvalues corresponding to the surface gravity modes as function of the artificial viscosity ν. The ordering of the modes is exactly the same as in the paper by Mougel *et al.* (2015), so that it is easier to make a direct comparison with their results.

2.4.2 Numerical Results

We now present the numerical solutions of the complete generalised eigenvalue problem. For comparison purposes, our artificial viscosity has been set to $\nu = 0.01$. Figure 2.11 displays our modes; each of them can be easily compared with those in the paper by Mougel *et al.* (2015, p. 223) showing excellent agreement in terms both of the eigenvalues and the eigenfunctions.

We then lowered the artificial viscosity in order to get to the pure inviscid limit, especially focusing on surface gravity modes as these are the type of waves mostly studied in this thesis. Table 2.1 compares the eigenvalues of the six Gravity modes shown in figure 2.11 as function of the artificial viscosity ν. The real part of λ remains basically unchanged, whereas, as expected and desirable, the imaginary part becomes smaller and smaller, reaching the machine precision for $\nu = 0$. The shape of the first eigenmode–mode (a)–in our ordering, is displayed in figure 2.12 for the four values of ν used. Hence, the shape of the surface gravity modes is insensitive to ν in the limit $\nu = 0$, confirming the robustness of our numerical scheme in computing surface modes and the possibility to adapt this code to other problems, such as those we are going to present in the next chapters.

2.4.3 Newton's bucket problem in an infinitely axially extended cylinder

In this section we will solve the previous problem when the axial domain is infinite, that is there is no bottom flat boundary, however the fluid still stays below the deformable free surface $z = h_0(r)$. Particularly, we would like to provide some analytical results to be compared with the numerics. That is useful to have some fast formulas available when the computation of the oscillation frequency of the systems is needed. Moreover, we would like to test the validity of such analytical results against those computed in the case the cylindrical container is necessarily bounded.

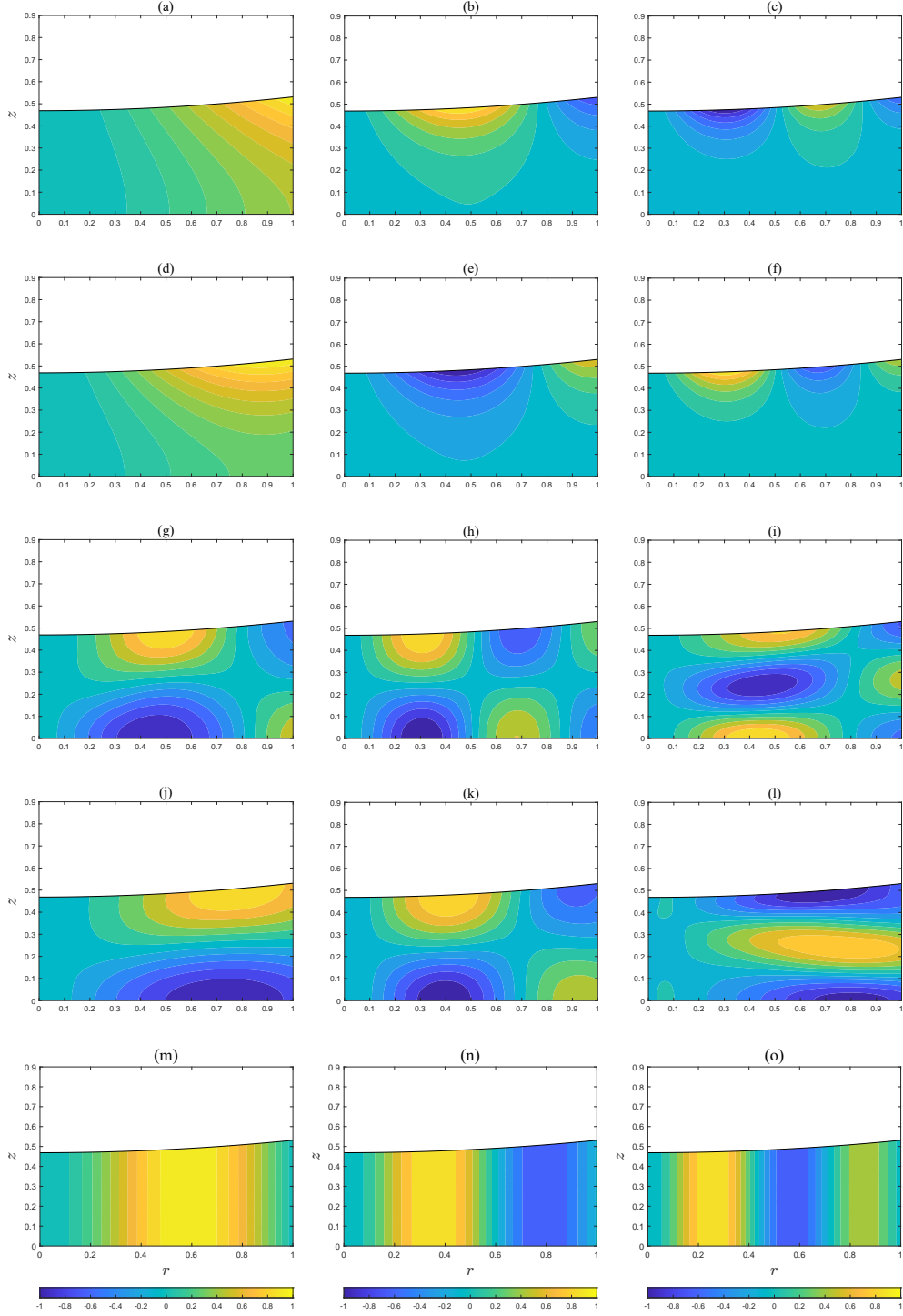We start by decomposing the pressure field into normal modes. The

Figure 2.11: Same eigenmodes as those computed in Mougel *et al.* (2015, p. 223) using the same physical parameters $m = 2$, $Fr = a = 0.5$, $R = 1$ and our artificial viscosity $\nu = 0.01$. The corresponding eigenvalues follow. (a): $\lambda = 4.2897 - 0.008i$. (b): $\lambda = 7.4359 - 0.0123i$. (c): $\lambda = 9.0436 - 0.0368i$. (d): $\lambda = -5.2014 - 0.0029i$. (e): $\lambda = -7.4580 - 0.0156i$. (f): $\lambda = -9.0349 - 0.0408i$. (g): $\lambda = 1.4077 - 0.0112i$. (h): $\lambda = 1.0974 - 0.0254i$. (i): $\lambda = 1.7833 - 0.0180i$. (j): $\lambda = -1.6985 - 0.0111i$. (k): $\lambda = -1.3292 - 0.0304i$. (l): $\lambda = -1.9142 - 0.0122i$. (m): $\lambda = -0.0346 - 0.0086i$. (n): $\lambda = -0.0124 - 0.0139i$. (o): $\lambda = -0.0077 - 0.0166i$. First two rows represent surface gravity modes. Third and fourth row inertial modes. Last row Rossby modes.
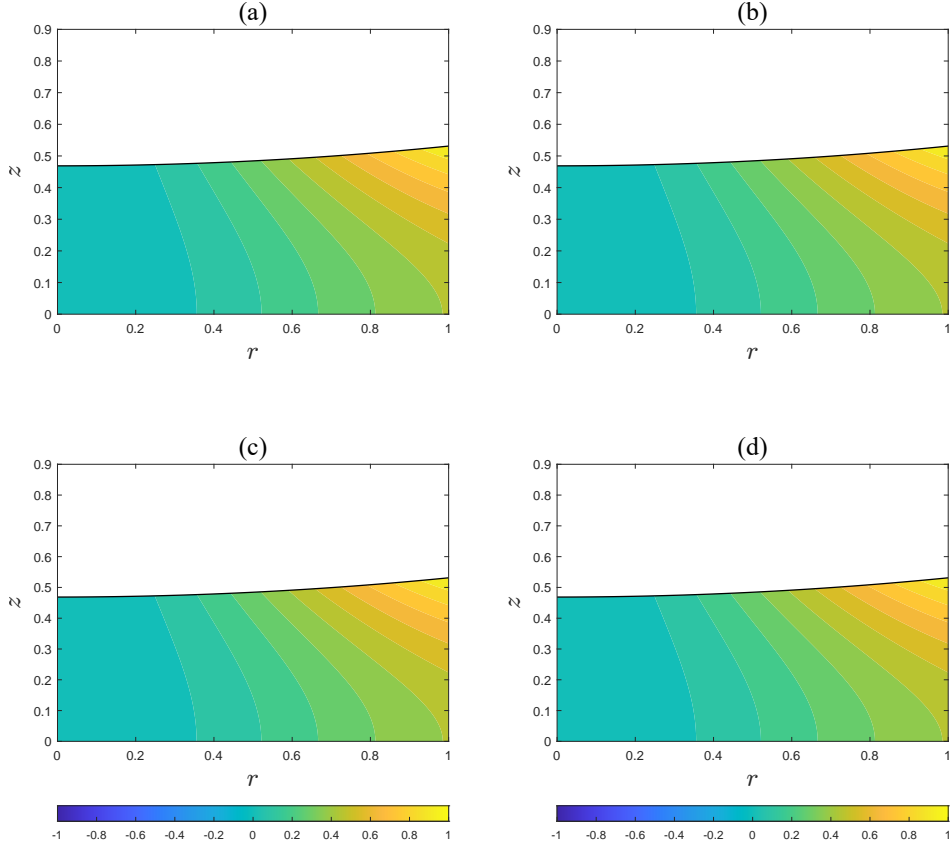
Figure 2.12: Comparison of the shape of the first surface gravity mode for $m = 2$, $R = 1$, $a = F = 0.5$ and different values of ν. (a): $\nu = 10^{-2}$. (b): $\nu = 10^{-4}$. (c): $\nu = 10^{-9}$. (d): $\nu = 0$.

equations and boundary conditions governing the eigenvalue problem are given by

$$-\lambda^2 \Delta_m \phi + 4 \frac{\partial^2 \phi}{\partial z^2} = 0, \quad (r, z) \in (0, 1) \times (-\infty, h_0(r)), \tag{2.81a}$$

$$-\lambda \frac{\partial \phi}{\partial r} + 2m\phi = 0, \quad at \quad r = 1, \tag{2.81b}$$

$$aF^2\lambda^2(\lambda^2 - 4)\phi - (\lambda^2 - 4)\frac{\partial \phi}{\partial z} - 2maF^2\lambda\phi = -aF^2\lambda^2 r \frac{\partial \phi}{\partial r}, \quad on \quad z = h_0(r), \tag{2.81c}$$

$$\phi \to 0, \quad as \quad z \to -\infty, \qquad \phi < \infty, \quad at \quad r = 0. \tag{2.81d}$$

37

Axisymmetric perturbations

When the perturbations are axisymmetric, the azimuthal wavenumber $m = 0$ and the differential problem (2.81) becomes

$$\frac{\lambda^2}{\lambda^2 - 4}\left(\frac{\partial^2 \phi}{\partial r^2} + \frac{1}{r}\frac{\partial \phi}{\partial r}\right) = -\frac{\partial^2 \phi}{\partial z^2}, \tag{2.82a}$$

$$\frac{\partial \phi}{\partial r} = 0, \quad at \quad r = 1, \tag{2.82b}$$

$$aF^2\lambda^2(\lambda^2 - 4)\phi - (\lambda^2 - 4)\frac{\partial \phi}{\partial z} = -aF^2\lambda^2 r\frac{\partial \phi}{\partial r}, \quad on \quad z = h_0(r), \tag{2.82c}$$

$$\phi \to 0, \quad as \quad z \to -\infty, \qquad \phi < \infty, \quad at \quad r = 0. \tag{2.82d}$$

We make the approximation that the right-hand side in the free surface boundary condition can be neglected. Heuristically, we can think that if there is no boundary at the bottom of the container, only gravity modes are expected to appear due to the decaying property of the solution at $z = -\infty$. We can then envision that the free surface changes slowly and its deformation becomes negligible, thus providing the aforementioned approximation. Also, in the extreme case of low rotation rate we have that $\frac{\partial \phi}{\partial z} \simeq \lambda^2 \phi$, so for $|\lambda|$ sufficiently large, the dominant terms are those on the left-hand side. The minimum value of λ^2 in this case is in fact $\lambda^2 \simeq 14.68$ which then makes terms of order λ^4 sufficiently larger than terms of order λ^2, hence allowing to neglect the right-hand side in the free surface boundary condition. Within this approximation, the differential problem we aim at solving now reads

$$\frac{\lambda^2}{\lambda^2 - 4}\left(\frac{\partial^2 \phi}{\partial r^2} + \frac{1}{r}\frac{\partial \phi}{\partial r}\right) = -\frac{\partial^2 \phi}{\partial z^2}, \tag{2.83a}$$

$$\frac{\partial \phi}{\partial r} = 0, \quad at \quad r = 1, \tag{2.83b}$$

$$aF^2\lambda^2(\lambda^2 - 4)\phi - (\lambda^2 - 4)\frac{\partial \phi}{\partial z} = 0, \quad on \quad z = h_0(r), \tag{2.83c}$$

$$\phi \to 0, \quad as \quad z \to -\infty, \qquad \phi < \infty, \quad at \quad r = 0. \tag{2.83d}$$

The structure of this system now allows to search for a solution by separation of variables, i.e. $\phi(r,z) = a(r)b(z)$, leading to the two ordinary differential problems:

$$\begin{aligned} &a''(r) + \frac{1}{r}a'(r) - \frac{m^2}{r^2}a(r) + \left(\frac{k^2}{\lambda^2}(\lambda^2 - 4)\right)a(r) = 0, \\ &a(0) < \infty, \\ &a'(1) = 0, \end{aligned} \tag{2.84}$$

$$\begin{aligned} &b''(z) - k^2 b(z) = 0, \\ &b(-\infty) = 0. \end{aligned} \tag{2.85}$$

The solution for the radial problem is given by the discrete functions:

$$a_n(r) = A_n J_0\Big(\alpha_{0,n} r\Big), \qquad (2.86a)$$

$$\frac{k_n}{\lambda_n}\sqrt{\lambda_n^2 - 4} = \alpha_{0,n}, \quad n = 1, 2, \ldots. \qquad (2.86b)$$

being $\alpha_{0,n}$ the roots of the zero-th order bessel function derivative, namely the roots of $J_1(\cdot)$. The solution for the axial function b satisfying the asymptotic condition at $z = -\infty$ yields $b_n(z) = e^{k_n z}$, with $k_n \in \mathbb{C}$ and $\Re[k_n] > 0$. Now, the final step is to use the free surface boundary condition to get the second relation between k_n and λ_n and consequently to compute the eigenvalues. This yields the simple equation

$$\frac{1}{aF^2\lambda_n^2}(\lambda_n^2 - 4)(aF^2\lambda_n^2 - k_n) = 0, \qquad (2.87)$$

which has non-trivial solutions when $k_n = aF^2\lambda_n^2$. At this point, we go back to equation (2.86b), substitute the expression for k_n and get

$$\lambda_n\sqrt{\lambda_n^2 - 4} = \alpha_{0,n}. \qquad (2.88)$$

Equation above admit four type of solutions; these are given by

$$\lambda_{1,2} = \pm\sqrt{2 + \sqrt{4 + \frac{\alpha_{0,n}^2}{a^2 F^4}}}, \qquad (2.89a)$$

$$\lambda_{3,4} = \pm i\sqrt{2 + \sqrt{4 + \frac{\alpha_{0,n}^2}{a^2 F^4}}} \qquad (2.89b)$$

Eigenvalues $\lambda_{3,4}$ have to be discarded giving rise to an increasing behaviour along z as we get towards $z = -\infty$. Thus, the only acceptable eigenvalues are $\lambda_{1,2}$. Figure 2.13 compares the approximate eigenvalues with those computed numerically by solving the full problem (figures on the left). The dimensionless depth used here is $a = 1$ and four different Froude numbers have been used, namely $F = 0.5, 0.75, 1, 1.5$ .Also, the relative error between the numerical and the theoretical eigenvalues is provided on the right part of the figures. The agreement is excellent and at most a relative error of about 4.5% only is obtained for the most extreme case $F = 1.5$.

Non-Axisymmetric perturbations

When perturbations depend on the azimuthal wavenumber m, then the differential eigenvalues problem to be solved is given by the general set of equations (2.81). In order to get analytical results also valid in this situation, we are going to make the same approximation as in the axisymmetric case, that is we neglect the right-hand side in the free surface boundary condition. The

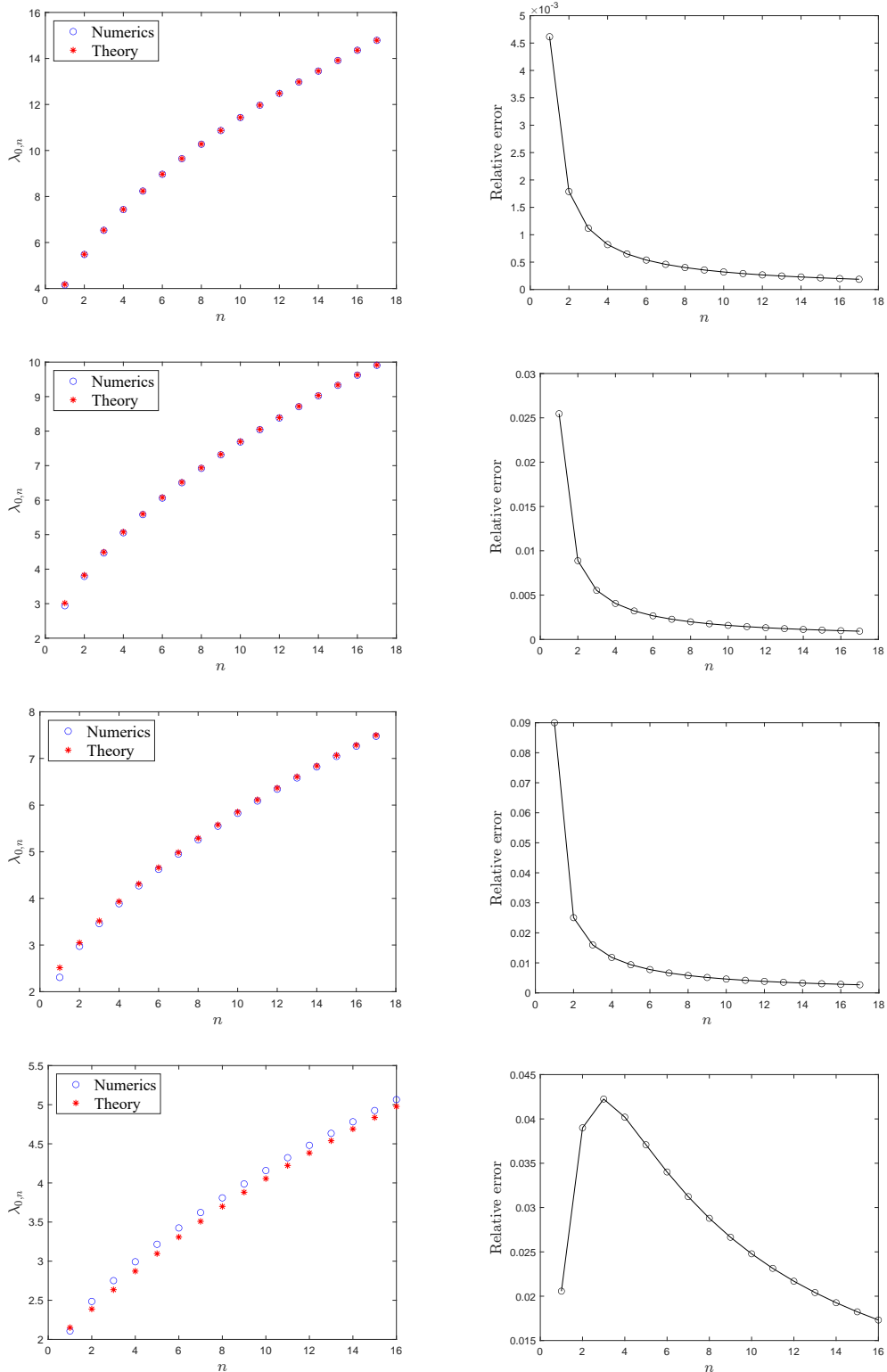Figure 2.13: Comparison of the eigenvalues computed using equation (2.89a) and those using the the numerics for $m = 0$, $a = 1$ and different Froude numbers. First row: $F = 0.5$. Second row: $F = 0.75$. Third row: $F = 1$. Fourth row: $F = 1.5$.

following problem under study reads:

$$-\lambda^2 \Delta_m \phi + 4\frac{\partial^2 \phi}{\partial z^2} = 0, \quad (r,z) \in (0,1) \times (-\infty, h_0(r)), \qquad (2.90a)$$

$$-\lambda \frac{\partial \phi}{\partial r} + 2m\phi = 0, \quad at \quad r = 1, \qquad (2.90b)$$

$$aF^2\lambda^2(\lambda^2 - 4)\phi - (\lambda^2 - 4)\frac{\partial \phi}{\partial z} - 2maF^2\lambda\phi = 0, \quad on \quad z = h_0(r), \quad (2.90c)$$

$$\phi \to 0, \quad as \quad z \to -\infty, \quad \phi < \infty, \quad at \quad r = 0. \qquad (2.90d)$$

To solve it we can apply the separation of variables again, even though $h_0(r)$ is a quadratic function of r, given that this does not enter in any terms of the differential problem. By repeating the same procedure shown in the previous paragraph we can write the general solution as

$$\phi_m(r,z) = C_m J_m\Big(\frac{k}{\lambda}\sqrt{\lambda^2 - 4}r\Big)e^{kz}. \qquad (2.91)$$

In order to find the two equations for (k, λ) we use the boundary conditions, that now are, according to the assumption made, with constant coefficients. In particular, from the boundary condition along the free surface we get

$$k = aF^2\lambda^2 - \frac{2maF^2\lambda}{\lambda^2 - 4}, \qquad (2.92)$$

so, substituting it into the lateral boundary condition we get a nonlinear algebraic equation in λ only, which reads

$$\begin{aligned} &-\lambda J'_m\Big[\Big(aF^2\lambda - \frac{2maF^2}{\lambda^2 - 4}\Big)\sqrt{\lambda^2 - 4}r\Big] \\ &+ 2mJ_m\Big[\Big(aF^2\lambda - \frac{2maF^2}{\lambda^2 - 4}\Big)\sqrt{\lambda^2 - 4}r\Big] = 0, \quad at \quad r = 1. \end{aligned} \qquad (2.93)$$

We can re-write it in a more elegant and convenient form by defining $\alpha(\lambda) = \Big(aF^2\lambda - \frac{2maF^2}{\lambda^2 - 4}\Big)\sqrt{\lambda^2 - 4}$. Then, by using recursion formulas for Bessel functions— see for example Abramowitz and Stegun (1965)—we have

$$\lambda\alpha(\lambda)J_{m+1}\Big[\alpha(\lambda)\Big] + m(2 - \lambda)J_m\Big[\alpha(\lambda)\Big] = 0. \qquad (2.94)$$

Equation (2.94) gives the eigenvalues λ of the system. In order to solve that we applied Newton-Raphson method used to solve nonlinear algebraic equations (Quarteroni *et al.* 2014). In figure 2.14, in analogy to the axisymmetric case, we show the comparison of the eigenvalues obtained by the theory and the full numerics for $m = 1, 2, 3, 4$, $a = 1$ and Froude number $F = 0.5$. The agreement is excellent, especially starting from the second mode on. The first mode seems to be the one suffering more the approximation we made, probably being it the closest to the limit $\lambda = 2$. However, the error made in that case is acceptable, especially when thinking at the possible applications of the system in terms of

estimation of the oscillation frequencies. For all other modes, the error goes to zero really quickly, so the analytical predictions work very well.

In addition we show comparison between numerical and analytical results for the case $a = 0.5$, which is the typical aspect ratio taken into account in the paper of Mougel $et\ al.$ (2015). Figures 2.15 and 2.16 in fact, compare the first six gravity modes as in the paper. The numerical eigenfunctions are displayed on the left; those coming from the theory are displayed on the right. The corresponding eigenvalues are indeed called λ_L for the numerical ones and λ_R for the theoretical ones. As can be noted, the agreement is good both in terms of the eigenvalues and of the eigenfunctions. The major discrepancy in the plot of the eigenfunctions is for modes (a) and (d); the reason for that might be given by the fact that in the numerical results pressure modes have the form of $\phi_{\mathrm{Num}} \sim \cosh(kz)$, whereas in the theoretical results they only behave as $\phi_{\mathrm{Th}} \sim e^{kz}$. Therefore, close to the bottom boundary the two solutions differ. Figure 2.17 compares the eigenvalues at different Froude numbers, particularly for $F \in [0.5, 1, 1.5, 1.9]$. The last two values are extremely high since the corresponding free surface shape is close to form a dry region. For such a reason, the agreement stops being so accurate, even though at least in the case $F = 1.5$ most of the eigenvalues are well-comparable.

2.5 Summary

In this chapter we first derived the general equations and boundary condition for studying the linear stability of a steady, axisymmetric free surface rotating flow. We then particularized those for two cases: the first without the presence of any background flow and the second for a solid-body rotation.

The case with no flow, despite being very well-known in the literature, permitted the comprehension of the surface gravity waves in terms both on their dispersion relation, their spatial structure and the two asymptotic limits of either shallow and deep water waves. In particular, considerations on the dispersion relation for deep-water waves turned out to be useful in the computation of the analytical eigenvalues for the Newton's bucket problem.

The case with a solid-body rotation has been studied both numerically and analytically. Our numerical results were in excellent agreement with those presented in Mougel $et\ al.$ (2015), thus validating the numerical code we developed. The analytical results also agreed very well with the numerics, thus providing a fast available tool for obtaining approximate solutions of this problem.
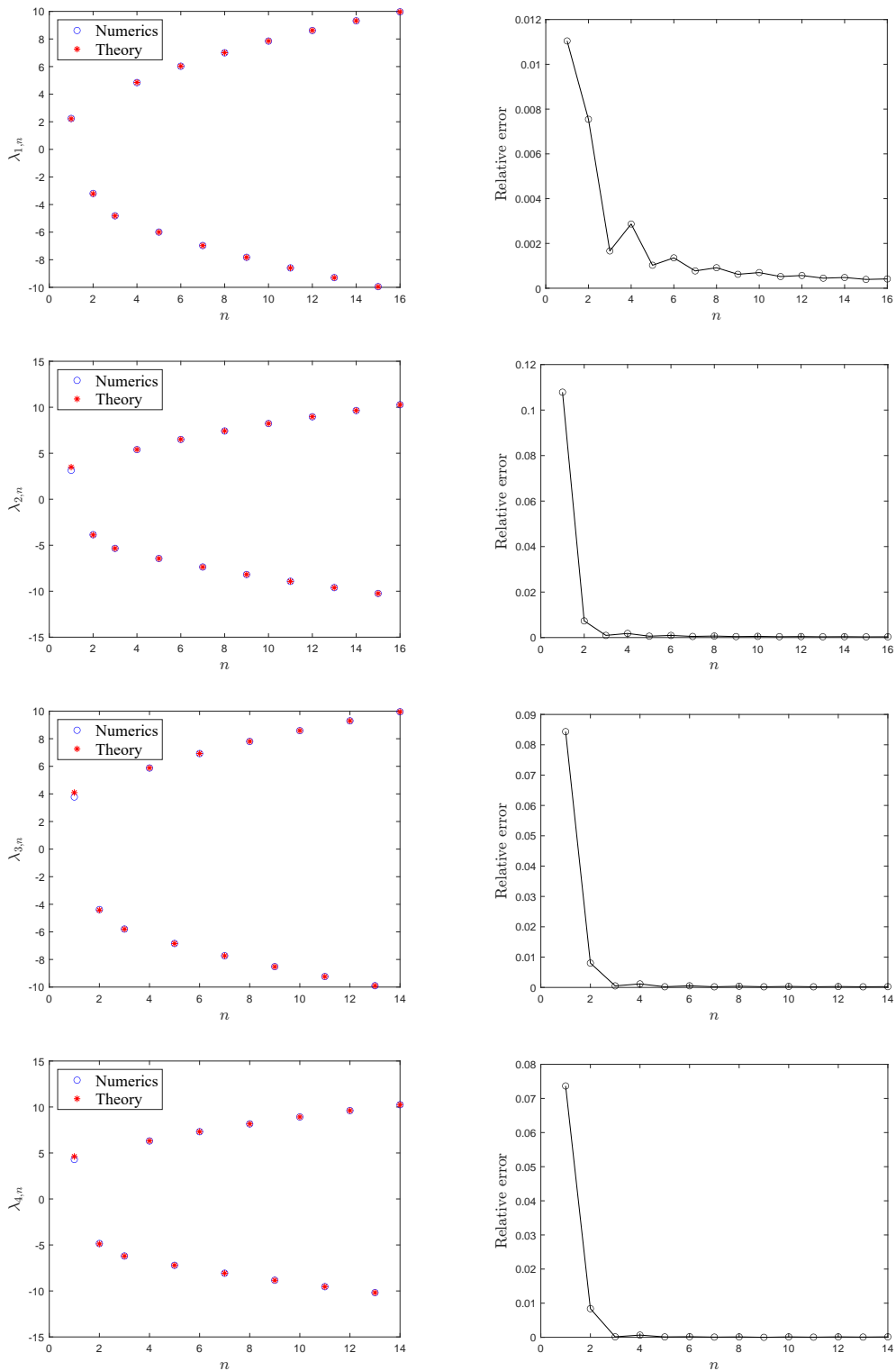
Figure 2.14: Comparison of the eigenvalues computed using equation 2.94 and those using the the numerics for $m = 1, 2, 3, 4$, $a = 1$ and $F = 0.5$. First row: $m = 1$. Second row: $m = 2$. Third row: $m = 3$. Fourth row: $m = 4$.

Figure 2.15: Comparison between the numerical eigensolutions and those coming from solving equations (2.91,2.92, 2.94). Physical parameters are the same as in Mougel's paper, namely $m = 2$ and $a = F = 0.5$. The numerical eigenfunctions are those shown on the left of the figure; the theoretical ones on the right. Accordingly, the numerical eigenvalues are denoted by λ_L, whereas the theoretical ones by λ_R, as follows: (a): $\lambda_L = 4.2897$, $\lambda_R = 4.7577$. (b): $\lambda_L = 7.4359$, $\lambda_R = 7.4523$. (c): $\lambda_L = 9.0436$, $\lambda_R = 9.0479$.
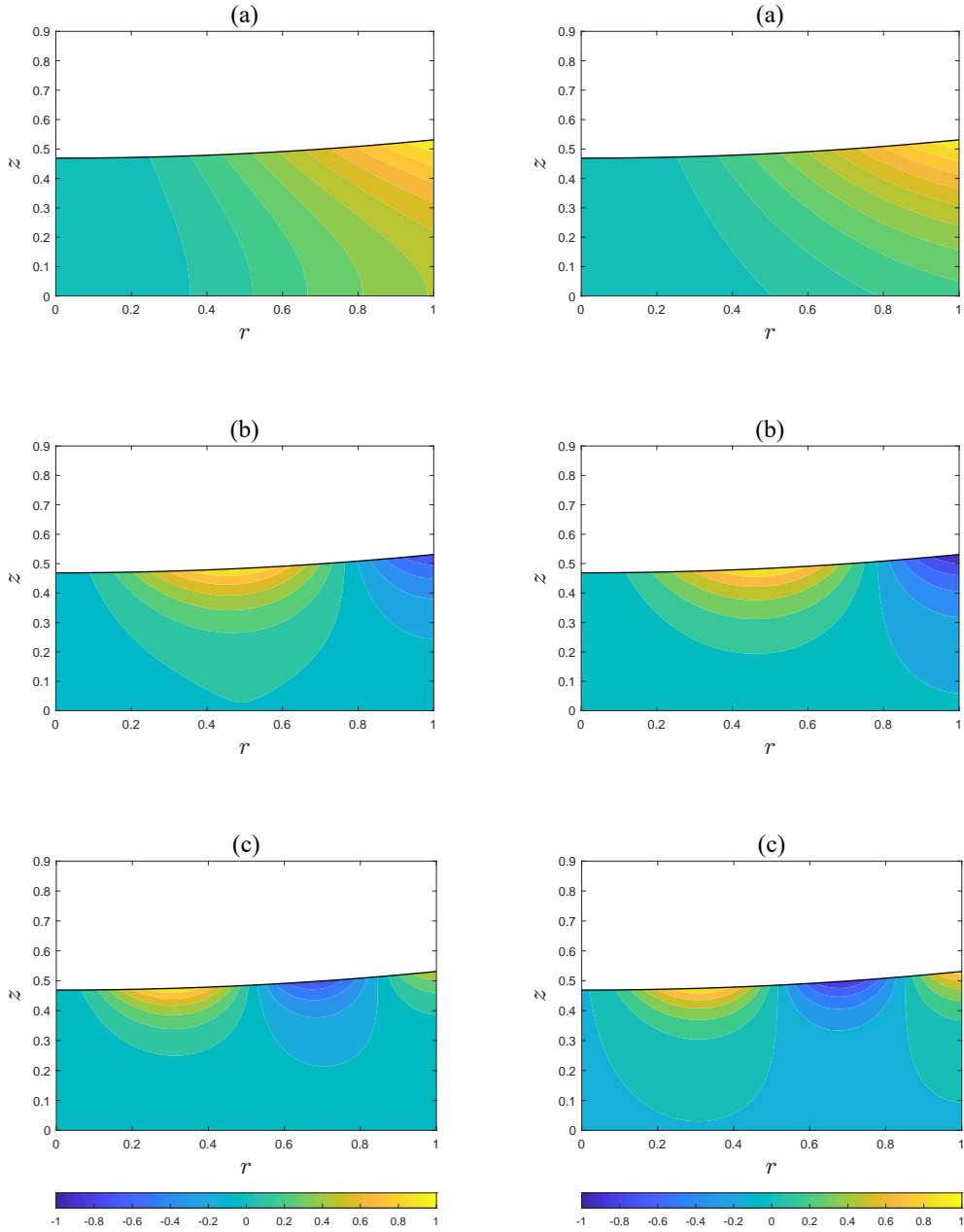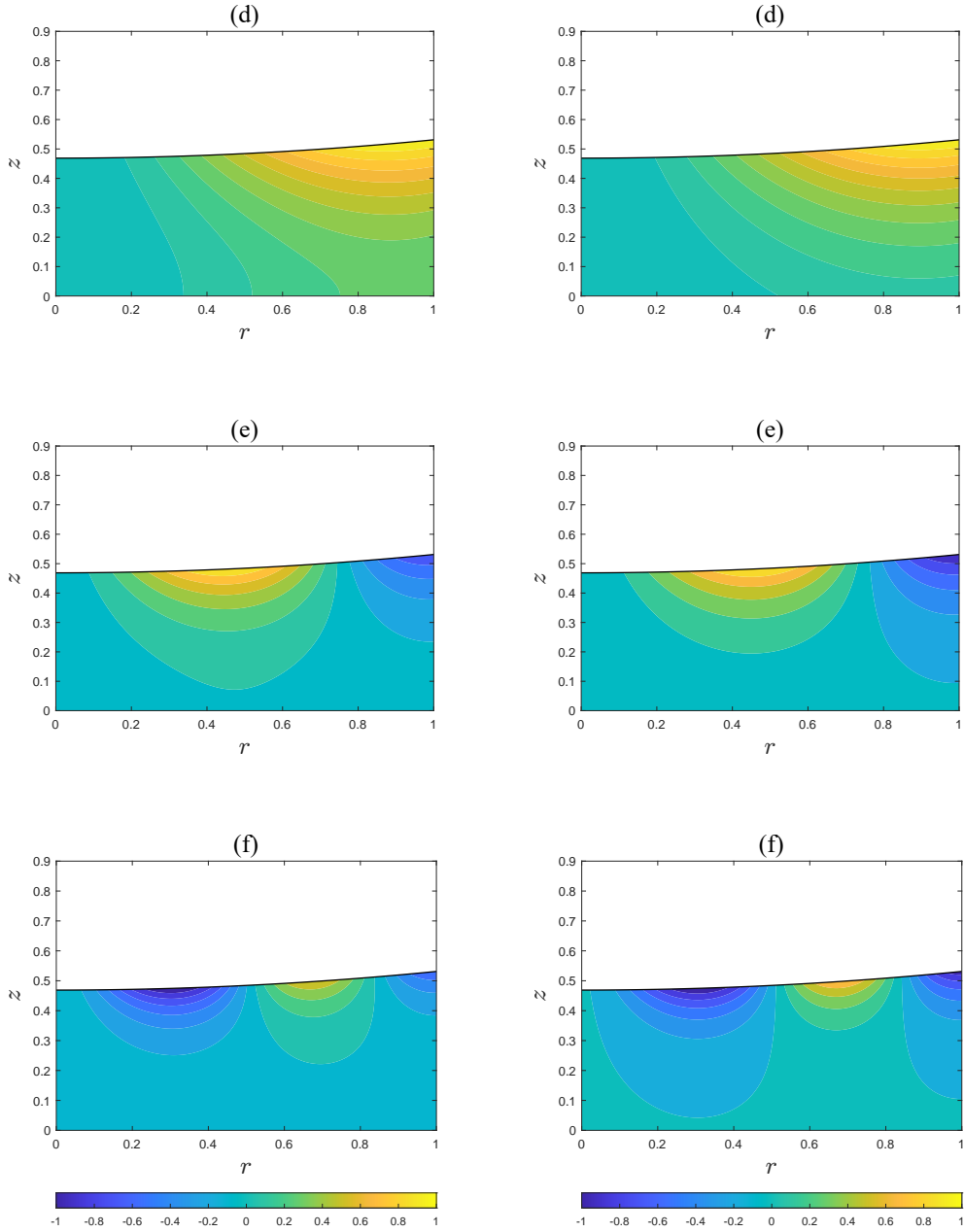
Figure 2.16: Comparison between the numerical eigensolutions and those coming from solving equations (2.91,2.92, 2.94). Physical parameters are the same as in Mougel's paper, namely $m = 2$ and $a = F = 0.5$. The numerical eigenfunctions are those shown on the left of the figure; the theoretical ones on the right. Accordingly, the numerical eigenvalues are denoted by λ_L, whereas the theoretical ones by λ_R, as follows: (d): $\lambda_L = -5.201$, $\lambda_R = -5.3497$. (e): $\lambda_L = -7.4580$, $\lambda_R = -7.4716$. (f): $\lambda_L = -9.0349$, $\lambda_R = -9.0386$.

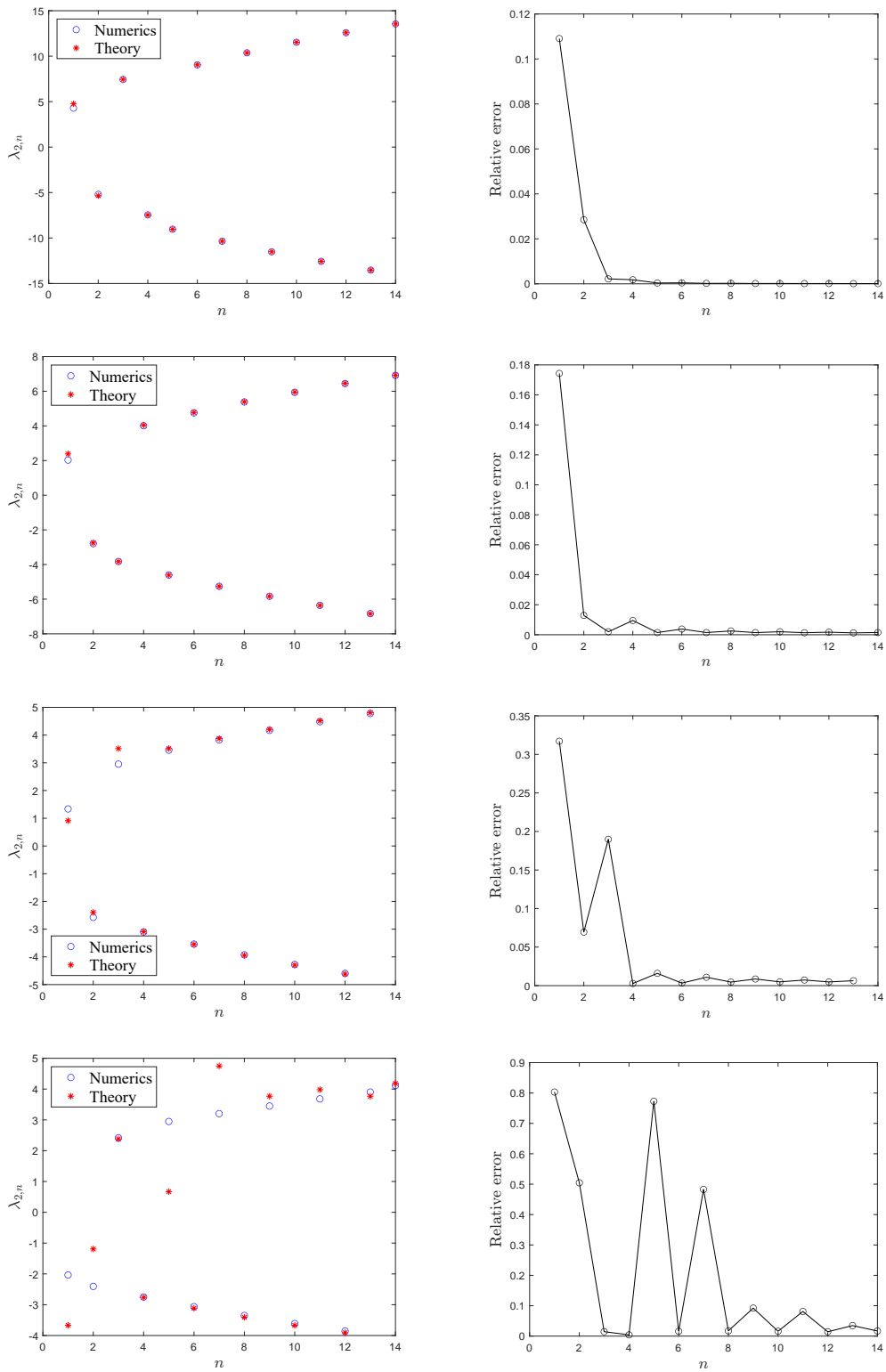Figure 2.17: Comparison of the eigenvalues computed using equation 2.94 and those using the the numerics for $m = 2$, $a = 0.5$ and $F \in [0.5, 1, 1.5, 1.9]$. First row: $F = 0.5$. Second row: $F = 1$. Third row: $F = 1.5$. Fourth row: $F = 1.9$.

46

Chapter 3

Waves on unbounded shallow-water free surface swirling flows

Wave propagation problems in unbounded domains are not usually solvable in closed form, except in very few simple cases. One of the main difficulty lies on the treatment of the boundary condition at infinity which has to be of a radiating type, that is only outgoing waves are allowed to propagate in the far-field. In this chapter we will be studying a model equation that we call the Convective Wave Equation (CWE). This model captures the essence of surface gravity waves over a prescribed vortex flow taking into account the advection contribution due to the flow. As described in the introduction (section 1.5), this kind of equation exhibits unstable modes when the background flow is a potential vortex spinning sufficiently fast. Thus, the aim of the present chapter is doubled: on one hand we want to see whether unstable modes exist even when the background vortex is not potential. On the other hand, the motivating example of two vortices travelling in the pool is out of reach with full 3D simulations, and so we would like to simulate this equation with a dipole background flow and observe the linear response of the system in presence of a pair of counter-rotating vortices.

As far as the imposition of a non-reflecting boundary condition is concerned, we are going to use the first asymptotic radiation condition derived by Engquist and Majda (1977) in polar coordinates for the monopolar vortex case. Whenever an analytical formula for imposing a NRBC cannot be applied, we are going to develop a Perfectly Matched Layer (PML) formulation. All PML formulations derived are based on the inspiring work of Sim (2010) and properly generalized depending on the problem under consideration.

The chapter is organised as follows: in section 3.1, we illustrates the advantages of Sim's PML formulation by applying it to the 1D wave equation where the efficiency of the absorbing boundary can be compared with that

given by the exact NRBC. In sections 3.2–3.3 we introduce the Convective Wave Equation. We study this model in a laterally unbounded domain, firstly in the simpler case of waves convected by a single vortex, both in frequency and time domain. Then, in section 3.6 we generalize the CWE model to the case of surface waves advected by a dipole flow.

3.1 The efficiency of PML formulations in absorbing incoming waves

In this initial section we want to show the efficiency of PML methods in providing the absorption of outgoing waves, hence avoiding spurious reflection from a fixed boundary. We trace exactly the formulation developed in Sim (2010, Ch. 3) for the classical wave equation and adapt it for the much simpler 1D case.

The PML equations read

$$
\begin{aligned}
&\frac{\partial^2 v}{\partial t^2} + \xi(x)\frac{\partial v}{\partial t} - c^2\frac{\partial^2 v}{\partial x^2} + c^2\frac{\partial w}{\partial x} = 0, \quad x \in \Omega_{PML} \equiv [0, L], \\
&\frac{\partial w}{\partial t} + \xi(x)w - \xi(x)\frac{\partial v}{\partial x} = 0, \quad x \in \Omega_{PML} \equiv [0, L],
\end{aligned}
\tag{3.1}
$$

where $v(x,t)$ is the real unknown we are interested in, $w(x,t)$ is the auxiliary variable introduced by the PML method, $\xi(x)$ is the damping function used to damp waves out, c the constant wave speed, $\Omega_{PML} = [0, L]$ the extended boundary incorporating the absorbing layer which starts at a location $x = L_c$ and extends up to $x = L$. A representation of the scenario is given in figure 3.1.

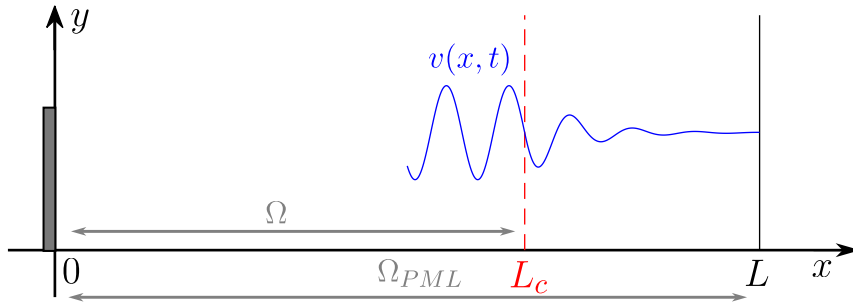Figure 3.1: Schematic representation of the domain and the behaviour of waves in the PML formulation (3.1).

For the results we are going to present, the parameters just mentioned and the damping function have been taken to be

$$
\begin{aligned}
&c = 1, \\
&L_c = 1, \qquad L = 2, \\
&\xi(x) = 10\Big[\frac{x - L_c}{L - L_c} - \frac{1}{2\pi}\sin\Big(2\pi\frac{x - L_c}{L - L_c}\Big)\Big].
\end{aligned}
\tag{3.2}
$$

48

The damping function $\xi(x)$ in (3.2) is the same one used in Sim (2010) and has the following properties:

- it is non-negative, thus it ensure damping of the waves along the spatial variables.

- The function and its first derivative are both null at $x = L_c$, location where the damping begins. This is to ensure no reflection at that point.

- It smoothly increase within the absorbing layer, providing a gradual dampening of the waves.

It is worth to mention though that the choice of the damping function $\xi(x)$ is arbitrary, provided it satisfies the three main conditions above.

We provide equations (3.1) with Neumann boundary conditions at the end points of v, that is

$$\frac{\partial v(0,t)}{\partial x} = 0, \quad \frac{\partial v(L,t)}{\partial x} = 0. \tag{3.3}$$

The Neumann boundary condition at the right-end point allows us to measure the amplitude of the reflected wave at that boundary. Finally, the initial conditions are

$$
\begin{aligned}
v(x,0) &= e^{-40(x-\frac{1}{2})^2}, \\
\frac{\partial v(x,0)}{\partial t} &= 0.
\end{aligned}
\tag{3.4}
$$

This simple case is of particular convenience because results coming from the PML formulation can be directly compared with those coming from imposing the exact non-reflecting boundary condition for the 1D wave equation at $x = L_c$ (1.7).

In figure 3.2 we give the characteristics diagram in the $x - t$ plane for the exact solution with NRBC and the PML one. In figure 3.3, a comparison of the two solutions at $x = L_c$ is shown, together with the corresponding difference $|v_{ex}(L_c,t) - v_{PML}(L_c,t)|$. The L^∞ error of the PML solution is given by $||E||_\infty = \sup_t |v_{ex}(L_c,t) - v_{PML}(L_c,t)| = 5.97 \cdot 10^{-5}$, whereas the corresponding relative error in L^∞-norm is equal to $\frac{||E||_\infty}{||v_{ex}(L_c,t)||_\infty} = 1.19 \cdot 10^{-4}$. Finally, in figure 3.4 the amplitude of the reflected wave in the PML formulation is displayed as function of time. As can be seen, the agreement between the two solutions is excellent and also the amount of reflection goes to zero quickly. The maximum amount of reflection is of order 10^{-3} which is very small given the geometrical and damping parameters used. Different damping profiles $\xi(x)$ as well as sizes/magnitudes of the damping region can be chosen leading to possible advantages in terms of further reducing the reflection at the extended boundary as well as the computational effort needed to solve the problem.
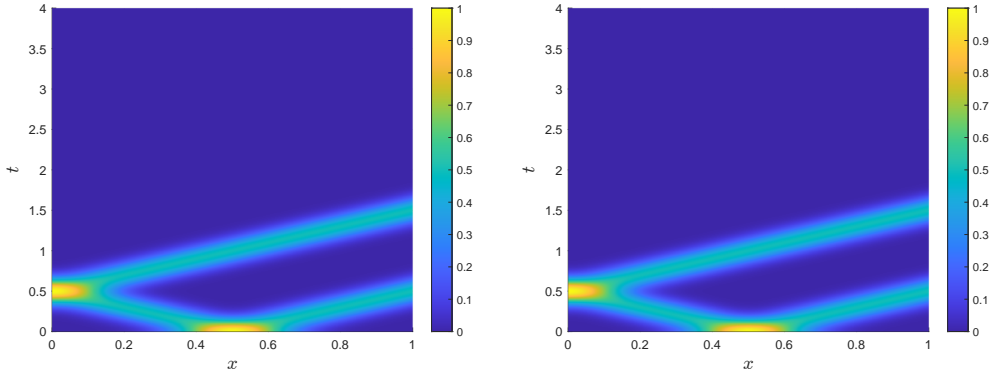
Figure 3.2: Characteristic lines in the $x - t$ plane for the solution using the exact NRBC (left) and the solution using the PML formulation (right).
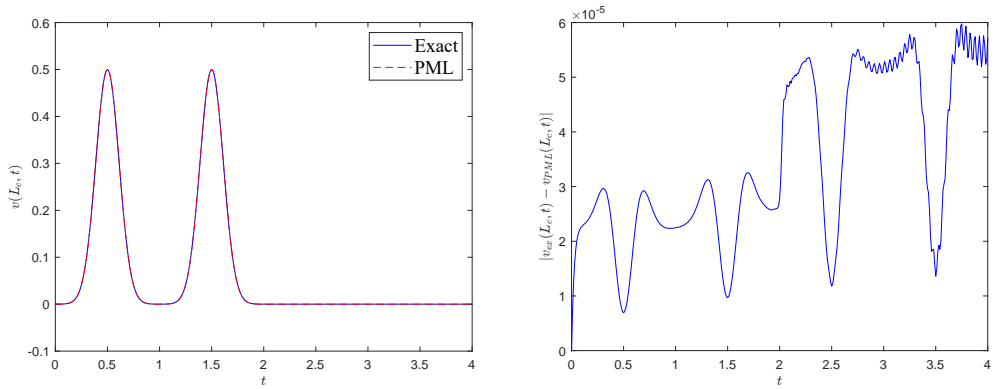
Figure 3.3: Comparison between the exact solution and the PML one at the starting point of the damping region $x = L_c$ as function of time (left). Difference in modulus between the exact and the PML solution at $x = L_c$ as function of time (right).

Figure 3.4: Rays in the $x - t$ plane for the PML solution (left) and amplitude of the reflected wave at the extended boundary $x = L$ (right).

3.2 The Convective Wave Equation for shallow-water surface waves

The previous section described how to deal with non-reflecting boundaries for hyperbolic wave equations in the absence of any background flow on which waves can propagate. Now, we want to derive a first model containing a background flow that influences how water waves move within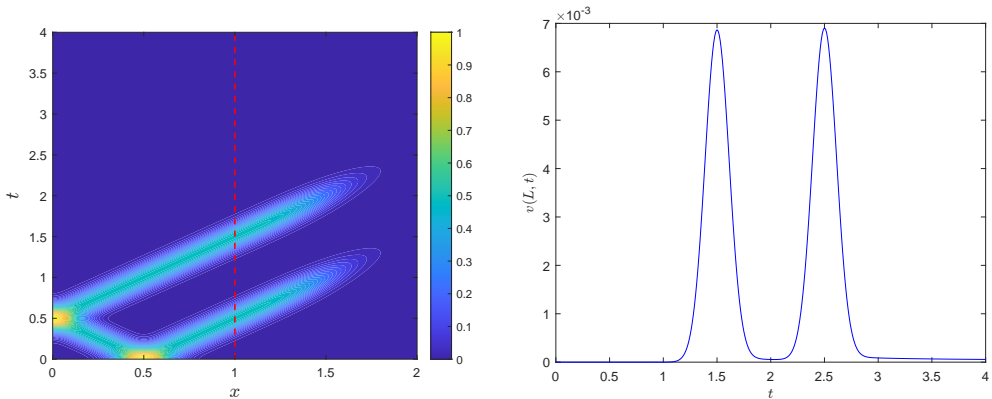 the fluid. As the model is put in the context of the shallow-water approximation (Johnson 1997, McWilliams 2006), let us start our derivation by considering the set of fully nonlinear shallow-water equations:

$$\frac{\partial \boldsymbol{u}}{\partial t} + (\boldsymbol{u} \cdot \nabla)\boldsymbol{u} + g\nabla h = 0,$$
$$\frac{\partial h}{\partial t} + \nabla \cdot (\boldsymbol{u}h) = 0,$$
(3.5)

where the first equation expresses conservation of momentum and the second equation expresses conservation of mass (continuity equation). As usual we want to linearize them around a steady equilibrium state, which we assume to be given by a generic two dimensional velocity field $\boldsymbol{U_0}$ and by a constant fluid depth H, i.e. we set

$$\boldsymbol{u} = \boldsymbol{U_0}(\boldsymbol{x}) + \varepsilon \boldsymbol{u'}, \qquad h = H + \varepsilon h'.$$
(3.6)

Plugging the linear expansion above into the governing equations, after dropping terms of order ε^2 we are left with the linear system

$$\frac{\partial \boldsymbol{u'}}{\partial t} + (\boldsymbol{U_0} \cdot \nabla)\boldsymbol{u'} + (\boldsymbol{u'} \cdot \nabla)\boldsymbol{U_0} + g\nabla h' = 0,$$
$$\frac{\partial h'}{\partial t} + \boldsymbol{U_0} \cdot \nabla h' + H(\nabla \cdot \boldsymbol{u'}) = 0.$$
(3.7)

We would like to simplify further the system. Following Patrick (2019), through a Clebsch decomposition (Seliger and Whitham 1968) we can write the perturbation velocity as

$$\boldsymbol{u'} = \nabla\phi + \boldsymbol{\xi},$$
(3.8)

so that the momentum and continuity equations (3.7) become respectively

$$\nabla(D_t\phi + gh) + \left[D_t\boldsymbol{\xi} + (\boldsymbol{\xi} \cdot \nabla)\boldsymbol{U_0} + \xi_0\tilde{\nabla}\phi \right] = 0,$$
$$D_th + H\nabla^2\phi + H\nabla \cdot \boldsymbol{\xi} = 0,$$
(3.9)

where $D_t = \partial_t + \boldsymbol{U_0} \cdot \nabla$ represents the material derivative due to the base flow, $\tilde{\nabla} = (-\partial_y, \partial_x)$ represents the co-gradient operator and ξ_0 the base vorticity. Now, still Patrick (2019, pp. 84-85) showed that the term inside the gradient

51

operator in the first equation can be set to zero, yielding $h = -\frac{1}{g}D_t\phi$. Inserting that into the continuity equation we are left with a closed system in the two unknowns $\phi, \boldsymbol{\xi}$:

$$
\begin{aligned}
D_t^2\phi - c^2\nabla^2\phi &= c^2\nabla\cdot\boldsymbol{\xi}, \\
D_t\boldsymbol{\xi} + (\boldsymbol{\xi}\cdot\nabla)\boldsymbol{U_0} + \xi_0\tilde{\nabla}\phi &= 0,
\end{aligned}
\tag{3.10}
$$

with $c = \sqrt{gH}$ being the speed of sound in the shallow-water limit. Assuming $\boldsymbol{\xi}$ forms a small perturbation to $\nabla\phi$, then the right-hand side of the first equation can be neglected and the problem reduces to studying the single PDE

$$
D_t^2\phi - c^2\nabla^2\phi = 0.
\tag{3.11}
$$

Since the vector field $\boldsymbol{\xi}$ represents the perturbation vorticity, such approximation can be justified assuming the background flow is weakly rotational, hence $\boldsymbol{\xi}$ can be seen only as a correction term to the main flow. Besides the formal justification of the equation, we will use the convective wave equation above as a model for the propagation of shallow-water waves on prescribed vortical flows, independently of the magnitude of the background vorticity.

It is more convenient to re-state the equation above in dimensionless form. To do so, let us assume the background flow to be characterised by a reference velocity U and by a reference length a. Note that the reference length can be chosen as the size of the core in the case of a monopolar vortex (such as the Lamb-Oseen flow) or could even be chosen as the distance between a pair of vortices. Recalling c to be the wave speed, we can non-dimensionalize the variables as follows:

$$
\boldsymbol{x} \to a\boldsymbol{x}, \qquad t \to \frac{a}{c}t, \qquad \boldsymbol{U_0} \to U\boldsymbol{U_0}, \qquad \phi \to (ac)\phi,
\tag{3.12}
$$

so that the resulting dimensionless Convective Wave Equation holds

$$
\left(\frac{\partial}{\partial t} + F\boldsymbol{U_0}\cdot\nabla\right)^2\phi - \nabla^2\phi = 0,
\tag{3.13}
$$

where $F = \frac{U}{c} = \frac{U}{\sqrt{gH}}$ is again the Froude number and the only parameter in the equation.

3.3 The Convective Wave Equation for a monopolar vortex

When the background flow is purely azimuthal and radially dependent only, equation (3.13) reads

$$
\left(\frac{\partial}{\partial t} + F\frac{U_0(r)}{r}\frac{\partial}{\partial\theta}\right)^2\phi - \nabla^2\phi = 0.
\tag{3.14}
$$

The boundary conditions we impose are

$$|\phi| < \infty, \quad at \quad r = 0,$$
$$\sqrt{r}\frac{\partial \phi}{\partial t} + \sqrt{r}\frac{\partial \phi}{\partial r} + \frac{1}{2\sqrt{r}}\phi = 0, \quad as \quad r \to \infty, \qquad (3.15)$$

The second boundary condition is the first order approximation of the series of non-reflecting boundary condition in polar coordinates derived by Engquist and Majda (1977). With regards to our problem, as the vortex is assumed to decay at infinity, the convective wave equation reduces to the classical wave equation and such a NRBC is exact.

Defining $\Omega_0(r) = U_0(r)/r$ and looking for normal modes solutions of the form $\phi(r, \theta, t) = \psi(r)e^{-i\omega t + im\theta}$, we obtain a single ordinary differential problem for ψ

$$(\omega - mF\Omega_0(r))^2 \psi + \psi'' + \frac{1}{r}\psi' - \frac{m^2}{r^2}\psi = 0,$$
$$\psi(0) < \infty, \qquad (3.16)$$
$$- i\omega\sqrt{r}\psi(r) + \sqrt{r}\psi'(r) + \frac{1}{2\sqrt{r}}\psi(r) = 0, \quad as \quad r \to \infty.$$

We solve the system for non-axisymmetric modes. In fact, we can already see that for $m = 0$ there are no normal modes satisfying both boundary conditions. Regularity at the origin would imply a solution of the form $\psi \sim J_m(\omega r)$. On the other hand, the non-reflecting boundary condition would imply that $\psi \sim H_m^2(\omega r)$, which is singular at the origin. As a matter of fact, looking for eigenmodes of the convective wave problem above with $m = 0$ is equivalent to solve the 1D wave equation on a semi-infinite interval with an exact non-reflecting boundary condition at one end-point. Normal modes solutions do not exist for such a problem. So, we will focus only on values of m greater than zero.

The background flow we choose here is a Lamb-Oseen vortex which takes the non-dimensional form

$$U_0(r) = \frac{1}{r}\left(1 - e^{-r^2}\right), \qquad (3.17)$$

giving an angular velocity field of the form

$$\Omega_0(r) = \frac{1}{r^2}\left(1 - e^{-r^2}\right). \qquad (3.18)$$

In the following we are going to solve problem (3.16) by means of the same numerical method used in the previous chapter, i.e. a Galerkin spectral method with linear re-mapping.

3.3.1 Numerical method

As previously stated, we are going to take values of $m > 0$. Hence, the regularity condition on $r = 0$ becomes $\psi(r = 0) = 0$, for any value of m. On the basis of what has been done in the previous chapter, we first define the following change of coordinate

$$x = \frac{2}{R}r - 1 \Rightarrow x \in [-1, 1]. \tag{3.19}$$

The differential problem (3.16) becomes

$$\frac{4}{R^2}\psi''(x) + \frac{4}{R^2(x+1)}\psi'(x) - \frac{4m^2}{R^2(x+1)^2}\psi + (\omega - mF\Omega_0(x))^2\,\psi(x) = 0,$$
$$\psi(-1) = 0,$$
$$\frac{2}{R}\psi'(1) = i\omega\psi(1) - \frac{1}{2R}\psi(1).$$
$$\tag{3.20}$$

Multiplying it by a test function v in a suitable space as ψ, integrating over $(-1, 1)$ and exploiting the boundary conditions we get

$$\omega^2 \left[\int_{-1}^{1} v\psi \right] + \omega \left[\frac{2i}{R} - 2mF \int_{-1}^{1} \Omega_0 v\psi \right]$$
$$+ m^2F^2 \int_{-1}^{1} \Omega_0^2 v\psi + \frac{4}{R^2} \int_{-1}^{1} \frac{1}{x+1} v\psi' \tag{3.21}$$
$$- \frac{4m^2}{R^2} \int_{-1}^{1} \frac{1}{(x+1)^2} v\psi - \frac{4}{R^2} \int_{-1}^{1} v'\psi' - \frac{1}{R^2} v(1)\psi(1) = 0.$$

The weak formulation above leads to a continuous polynomial eigenvalue problem of the form

$$\mathcal{M}(m, F, R)\omega^2 + \mathcal{C}(m, F, R)\omega + \mathcal{K}(m, F, R) = 0, \tag{3.22}$$

which can be discretized by expanding both ψ and v in proper basis functions. In our case we used the same modified Legendre polynomials $L^\diamond(x)$ defined in (2.74), so that the Dirichlet boundary condition at $x = -1$ is automatically satisfied.

The need of imposing a non-reflecting boundary condition at a finite radius, however, forces us to run our code twice, each time with a slightly changed finite radius. That is because we want ultimately to get rid of those modes affected by the spurious reflection coming from the truncation of the domain. In practise we run the code a first time with a NRBC at a radius $R = 30$; then running it a second time with a NRBC at an increased radius, $R = 40$. After having obtained the eigenvalues in the two cases, we then retain only those modes whose eigenvalues did not vary according to the resolvedness conditions defined in the previous chapter (2.78)–(2.79). The number of grid points has been taken as $N_x = 300$, the tolerances $tol_1 = tol_2 = 0.01$ and the

border width $b_x = 10$.

3.4 General results

In this section we present a set of complete results for the shallow-water Convective Wave Equation with the Lamb-Oseen background flow. We remind that this flow is regular at the origin and has a nonzero dimensionless vorticity given by

$$\xi_0(r) = \frac{1}{r}\frac{d}{dr}\Big(rU_0(r)\Big) = 2e^{-r^2}. \tag{3.23}$$

Our computations show the emergence of unstable modes. In figure 3.5 (top) we show the trend of the imaginary part of the eigenvalues as function of the Froude number, representing the growth rate of the modes as function of the Froude number. The low azimuthal wavenumber modes are those with higher growth rates. For moderately high azimuthal wavenumber perturbations, the growth rate is slower and there exist a plateau in the eigenvalues curve where modes are mostly neutrally stable. Such an increase in the growth rate seems to persist even at larger Froude numbers, with high azimuthal wavenumber modes crossing the neutral stability threshold and becoming unstable too. Figure 3.6 shows the range of the Froude numbers for a given azimuthal wavenumber m inside which nearly marginally stable states are found. Nearly marginally stable states are modes whose growth rate is in modulus less or equal than 10^{-4}. For $m = 1$ there is only a single marginally stable state, whereas for increasing values of m such an interval gets wider. In terms of the eigenfunctions, we can subdivide the structure of the eigenmodes into two classes: radiating modes and trapped modes. The former have a typical spiral shape, as shown in figure 3.7 (left). Such modes behave as travelling waves along the radial direction, and radiation to infinity is responsible for the dissipation of the initial energy put into the system to excite the mode. In contrast, trapped modes are confined to a bounded region in the radial direction, and without the spiraling structure seen for the radiating modes. Those modes behave as standing waves along the radial direction and either dissipate extremely slowly or emerge leading the overall dynamics. An example can be seen in 3.7 (right). The distinction between radiating and trapped modes can further be seen in the eigenvalues. Indeed, radiating modes have eigenvalues with a significant negative imaginary part, indicating exponential decay in time, whereas trapped modes have either a negligible imaginary part or a positive imaginary part, ultimately leading to an instability of the vortex.

Another interesting phenomenon concerns the propagation direction of the surface waves with respect to the rotation of the base vortex flow as its rotation rate is varied. This is shown in figure 3.5 (bottom), which shows how the real part of the eigenvalues (the oscillation frequency) varies with the Froude number for different azimuthal wavenumbers. For $\Re(\omega) < 0$, waves
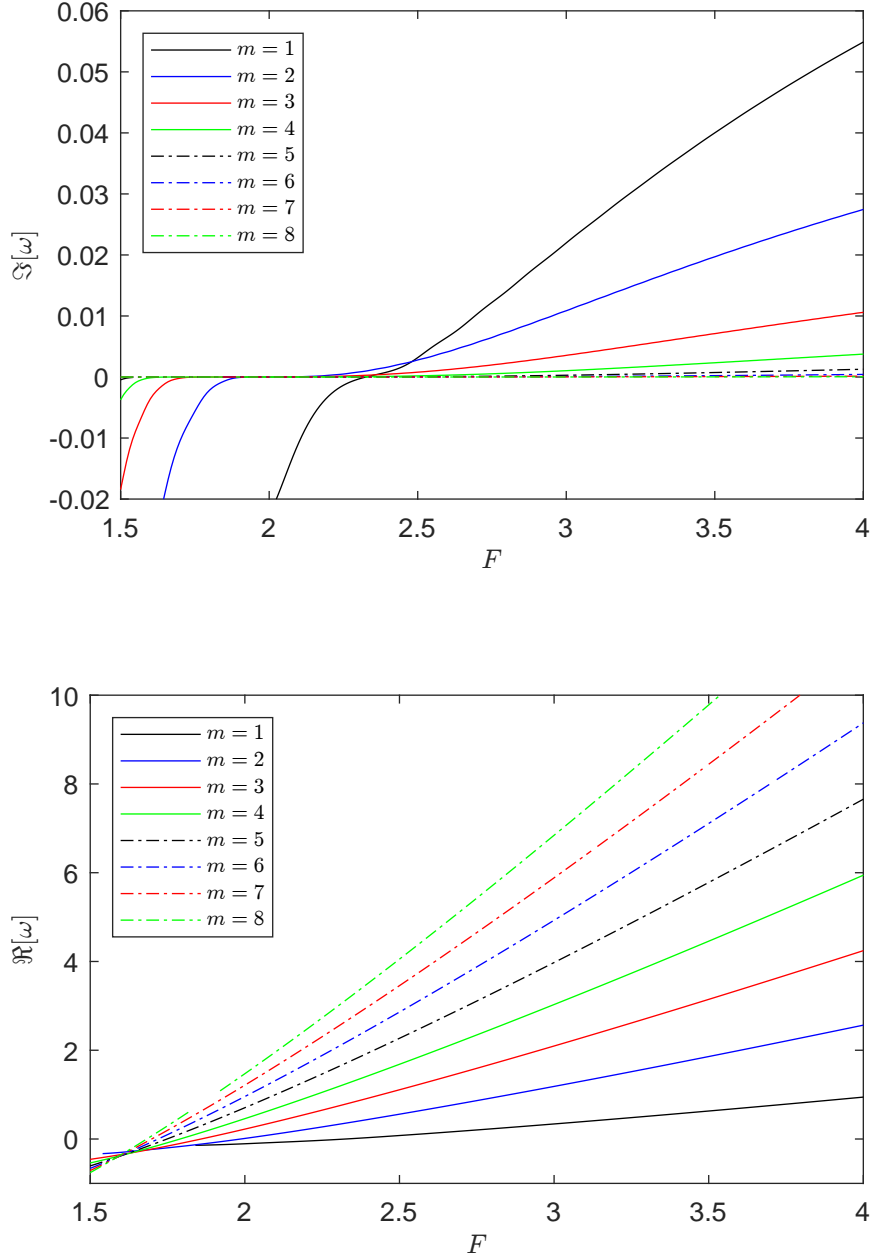
Figure 3.5: Eigenvalues curves for different azimuthal wavenumbers as function of the Froude number. Top: imaginary part of the eigenvalues, corresponding to growth rate. Bottom: real part of the eigenvalues, corresponding to oscillation frequency.

rotate opposite to the base flow (counter-rotating waves), while for $\Re(\omega) > 0$, waves rotate in the same direction as the base flow (co-rotating waves).

The mechanism triggering the instability can be associated to the presence of an ergoregion, i.e. a spatial location where the modulus of the background velocity equals the speed of sound:

$$\boldsymbol{x}_e : \quad |\boldsymbol{U_0}(\boldsymbol{x}_e)| = c = 1. \tag{3.24}$$

Together with the ergoregion there is another important boundary which is
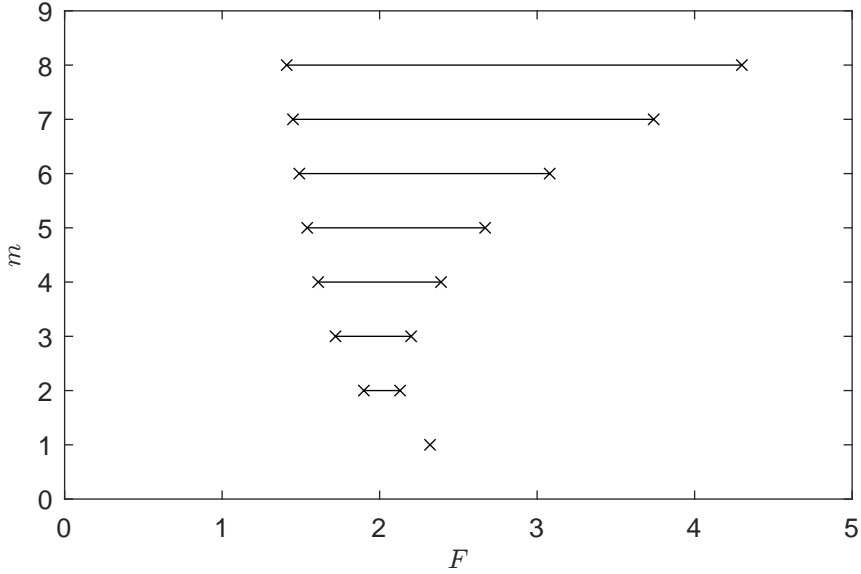
56

Figure 3.6: Range of Froude numbers for which marginally stable modes exists for a given m. A mode as been considered marginally stable if the modulus of the imaginary part of the corresponding eigenvalue is less or equal than 10^{-4}.
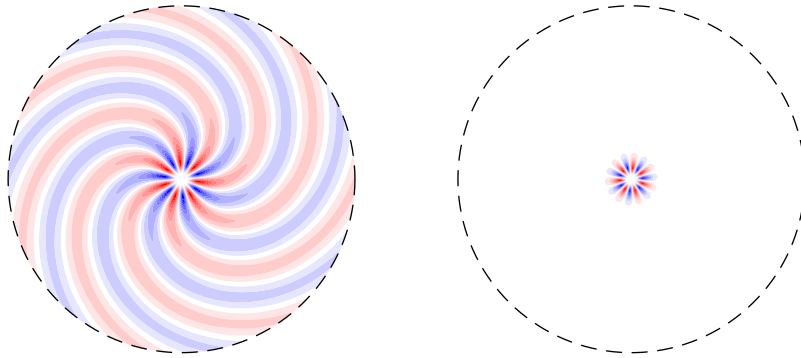

Figure 3.7: Left: Radiating mode for $m = 7$ and $F = 1.3$. Right: trapped mode for $m = 7$ and $F = 2$.

called horizon. This is the locus of points where the magnitude of the radial velocity component equals the wave speed, i.e.

$$\boldsymbol{x}_H : \quad |U_{0_r}(\boldsymbol{x}_H)| = c = 1. \tag{3.25}$$

For simple monopolar vortices, these two boundaries are simply circles centered at the origin and having different radii. In the case of the potential vortex studied by Patrick et $al.$ (2018) with background flow $\boldsymbol{U_0}(r) = -\frac{D}{r}\hat{\boldsymbol{r}} + \frac{C}{r}\hat{\boldsymbol{\theta}}$, the ergoregion is always external to the horizon. Indeed, the two curves are given by $r_H = D$ and $r_e = \sqrt{C^2 + D^2} > r_H$. The presence of an horizon is very useful in avoiding a possible instability as that boundary acts as a membrane which absorbs negative energy modes, i.e. modes having a negative energy density which might ultimately become unstable. In fact, inside the ergoregion $U_0(r) > c$ and there exist negative-energy states which become

57

positive-energy states when they leave the ergoregion. Hence, in the absence of an horizon capable of absorbing incoming waves from the ergoregion, energy conservation leads to the emergence of unstable modes whose amplitudes grow exponentially in time. Unstable modes of this type have been previously found in the case of a potential vortex by Oliveira *et al.* (2014). Since that base flow is singular at the origin, they truncated the inner boundary at a location $r = r_{min}$, where they imposed either a Dirichlet or a Neumann boundary condition. They argue, and indeed their results confirm this, that the instability is a general feature occurring in laterally unbounded wave systems possessing an ergoregion but not a horizon. Indeed, they showed that the instability mechanism is insensitive to the type of boundary condition imposed at r_{min}, for example.

Our results, in conclusion, confirm the ergoregion instability argument and show that this happen even when the flow is defined over the whole radial domain $r \in [0, \infty)$ and has a nonzero vorticity.

3.5 Analytical toy model for the Convective Wave Equation

In order to gain more insight into the appearance of neutrally stable trapped modes, we now want to simplify further the convective wave equation described previously, by making the following assumptions:

- the angular velocity field is discontinuous at a radius $r = a$ and has form:

$$\Omega_0(r) = \begin{cases} F, & 0 \leq r \leq a, \\ \Omega_2, & r > a. \end{cases} \quad , \quad F > \Omega_2 > 0, \qquad (3.26)$$

  where F is equivalent to our Froude number, and Ω_2 a generic constant.

- the Laplacian can be approximated only by using the second order derivative, i.e. $\nabla^2 \simeq \partial_r^2$.

Even though the second assumption is not necessary in order to obtain an exact solution—indeed that could be expressed in terms of Bessel functions of the first kind in the first radial sub-domain and Hankel functions in the second radial sub-domain—the emphasis here is to actually obtain an exact solution which can be written explicitly, i.e. without relying on a numerical solver. The boundary conditions remain unchanged and so are periodic in θ, Non-Reflecting at $r = \infty$ and null at the centre $r = 0$. We define $x = r$ for notation convenience, so that the differential problem we aim at solving is

given by

$$(\partial_t + \Omega_0(x)\partial_\theta)^2 u - \partial_x^2 u = 0,$$
$$u(0, \theta, t) = 0,$$
$$\lim_{x \to \infty} (\partial_t + \Omega_2 \partial_\theta) u + \partial_x u = 0,$$
$$u(x, 0, t) = u(x, 2\pi, t), \quad and \quad \partial_\theta u(x, 0, t) = \partial_\theta u(x, 2\pi, t).$$

(3.27)

being the second boundary condition an exact non-reflecting boundary condition for u. Let us define $u_1 \equiv u$ in $x \in [0, a]$ and $u_2 \equiv u$ in $x \in (a, \infty)$. We can re-write the differential problem above as

$$(\partial_t + F\partial_\theta)^2 u_1 - \partial_x^2 u_1 = 0, \quad x \in [0, a],$$
$$(\partial_t + \Omega_2 \partial_\theta)^2 u_2 - \partial_x^2 u_2 = 0, \quad x \in (a, \infty),$$
$$u_1(0, \theta, t) = 0,$$
$$u_1(a, \theta, t) = u_2(a, \theta, t),$$
$$\partial_x u_1(a, \theta, t) = \partial_x u_2(a, \theta, t),$$
$$\lim_{x \to \infty} (\partial_t + \Omega_2 \partial_\theta) u_2 + \partial_x u_2 = 0,$$
$$u_1(x, 0, t) = u_1(x, 2\pi, t), \quad and \quad \partial_\theta u_1(x, 0, t) = \partial_\theta u_1(x, 2\pi, t),$$
$$u_2(x, 0, t) = u_2(x, 2\pi, t), \quad and \quad \partial_\theta u_2(x, 0, t) = \partial_\theta u_2(x, 2\pi, t).$$

(3.28)

Solution in the inner region: $0 \leq x \leq a$

In this region the differential problem we want to solve reads

$$(\partial_t + F\partial_\theta)^2 u_1 - \partial_x^2 u_1 = 0,$$
$$u_1(0, \theta, t) = 0,$$
$$u_1(x, 0, t) = u_1(x, 2\pi, t), \quad and \quad \partial_\theta u_1(x, 0, t) = \partial_\theta u_1(x, 2\pi, t).$$

(3.29)

We look for a periodic solution of the form $u_1 = \psi_1(x)e^{-i\omega t + im\theta}$, with $\omega \in \mathbb{C}$ and $m \in \mathbb{Z}$. Substitution into equations (3.29) gives the reduced differential problem

$$\psi_1'' + (\omega - mF)^2 \psi_1 = 0,$$
$$\psi_1(0) = 0,$$

(3.30)

whose solution is

$$\psi_1(x) = -2A_1 \sinh[i(\omega - mF)x],$$

(3.31)

A_1 being an arbitrary constant.

Solution in the outer region: $x > a$

In this region the differential problem we want to solve reads

$$
\begin{aligned}
&(\partial_t + \Omega_2\partial_\theta)^2\, u_2 - \partial_x^2 u_2 = 0, \\
&\lim_{x\to\infty}\, (\partial_t + \Omega_2\partial_\theta)\, u_2 + \partial_x u_2 = 0, \\
&u_2(x, 0, t) = u_2(x, 2\pi, t), \quad and \quad \partial_\theta u_2(x, 0, t) = \partial_\theta u_2(x, 2\pi, t).
\end{aligned}
\tag{3.32}
$$

Even in this case we look for a periodic solution of the form $u_2 = \psi_2(x)e^{-i\omega t + im\theta}$. Substitution into the differential problem above yields

$$
\begin{aligned}
&\psi_2'' + (\omega - m\Omega_2)^2\psi_2 = 0, \\
&\psi_2'(\infty) = i(\omega - m\Omega_2)\psi_2(\infty),
\end{aligned}
\tag{3.33}
$$

which returns

$$
\psi_2(x) = A_2 e^{i(\omega - m\Omega_2)x},
\tag{3.34}
$$

where A_2 is a constant dependent of A_1 due to the matching condition at $x = a$. Note also that the behaviour of the solution at $x = \infty$ depends on the eigenvalues ω which in principle can be complex, therefore giving rise to either exponentially increasing or decreasing eigenfunctions as x gets larger.

Matching conditions at the interface $x = a$

We want the two solutions computed before and their first derivatives to match at point $x = a$. By imposing these two conditions we get the following system of algebraic equations

$$
\begin{aligned}
&-2A_1 \sinh[i(\omega - mF)a] = A_2 e^{i(\omega - m\Omega_2)a}, \\
&-2iA_1(\omega - mF)\cosh[i(\omega - mF)a] = i(\omega - m\Omega_2)A_2 e^{i(\omega - m\Omega_2)a}.
\end{aligned}
\tag{3.35}
$$

Re-arranging that, we end up with a single equation in the unknown ω of the form

$$
\tanh[i(\omega - mF)a] = \frac{\omega - mF}{\omega - m\Omega_2}.
\tag{3.36}
$$

The equation above is still a trascendental equation in ω, so can only be solved numerically. So as to make further progress and try to obtain an explicit solution in closed form, we notice that for sufficiently high azimuthal wavenumbers m, we can approximate the right-hand side of equation (3.36) as

$$
\frac{\omega - mF}{\omega - m\Omega_2} \simeq \frac{F}{\Omega_2},
\tag{3.37}
$$

and study the approximate eigenvalues equation

$$
\tanh[i(\omega - mF)a] = \frac{F}{\Omega_2} \Rightarrow i(\omega - mF)a = \frac{1}{2}\log\left(\frac{\Omega_2 + F}{\Omega_2 - F}\right).
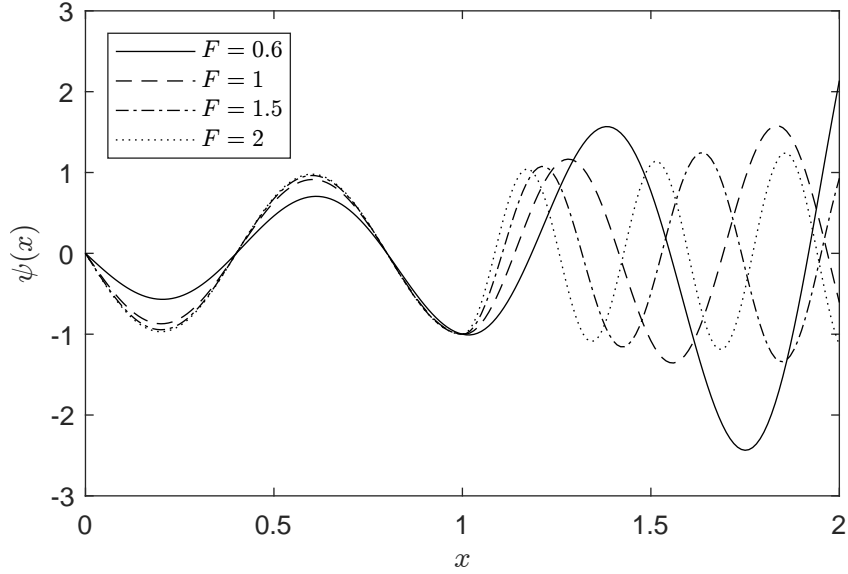\tag{3.38}
$$

Figure 3.8: Eigenfunctions of the toy model problem computed using the following parameters: $\Omega_2 = 1/2, a = 1, n = 0, m = 7$.

Now, since $F > \Omega_2$ by assumption, the argument of the logarithm is negative and leads to the following final set of discrete eigenvalues

$$\omega_n = mF + \frac{1}{2a}(\pi + 2n\pi) - \frac{i}{2a} \log\left(\frac{F + \Omega_2}{F - \Omega_2}\right), \quad n \in \mathbb{Z}. \tag{3.39}$$

The eigenvalues as function of the Froude number are displayed in figure 3.9 for the following parameters: $\Omega_2 = 1/2, a = 1, n = 0, m = 7$. The plotted curves look qualitatively similar to those obtained in the previous section for the Lamb-Oseen vortex—figure (3.5). In particular, the toy model is capable of reproducing the trend of the imaginary part of the eigenvalues as function of the Froude number, ultimately leading to nearly marginally-stable states. The higher the Froude number, the lower the decay rate of the eigenvalues, hence the lower the leakage of the waves out of the first subdomain $x \in [0, a]$. This features can be seen looking at figure 3.8. The exponential growth in x of the mode at $F = 0.6$ is larger than the corresponding growth at $F = 2$ where the mode is almost entirely sinusoidal. In this sense, at high Froude numbers, modes tend to behave more as standing waves rather than travelling waves, resembling one of the characteristics described in the previous section about trapped modes. Also, the simple model studied here shows another feature: for waves convected by a purely rotating vortex flow, solutions in the form of normal modes can be found only over a certain range of rotation rates and hence there exists a critical value below which the discrete set of modes cannot be computed. In our toy model this threshold value is exactly $F = \Omega_2$ and comes from the analytical form of the imaginary part of the spectrum in equation (3.39). For the general case described in the previous sections where the background flow varies continuously and the Laplacian
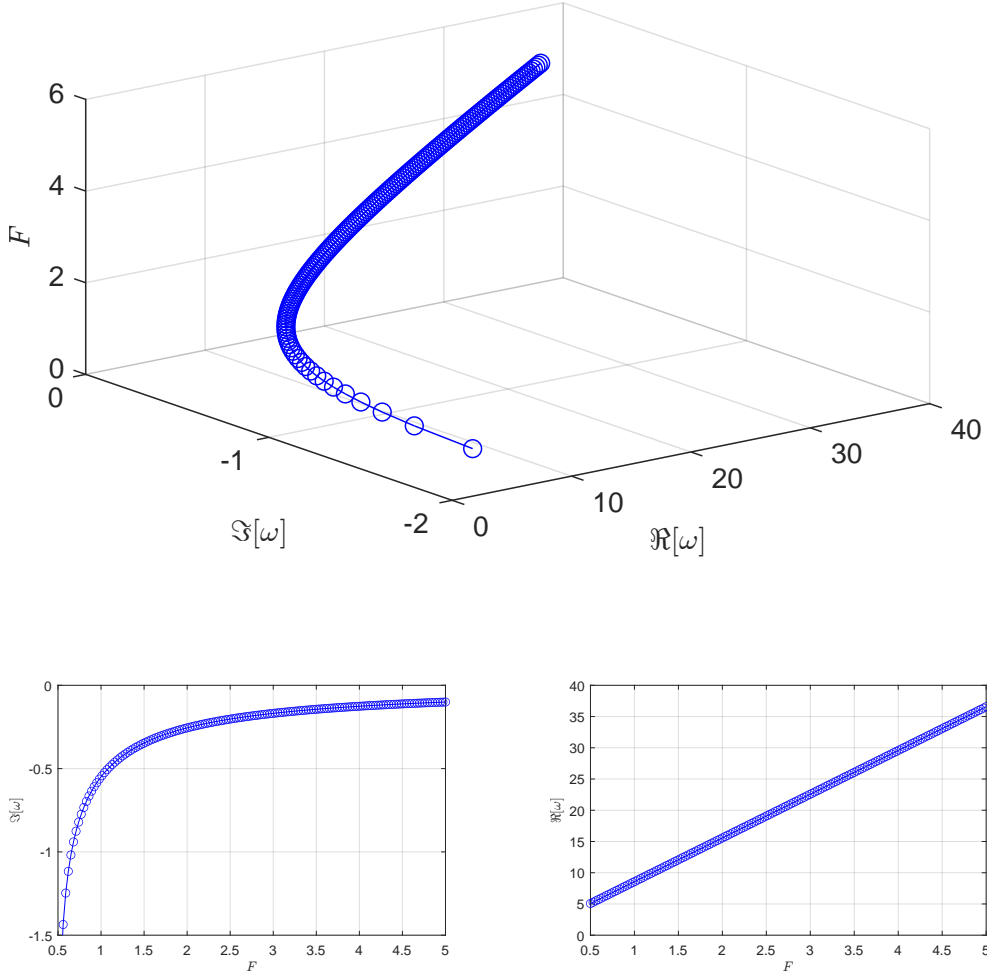
Figure 3.9: Discrete infinite set of eigenvalues for the simplified convective wave equation with a discontinuous angular velocity. Top: full 3D representation. Bottom: imaginary and real part of the eigenvalues as function of the Froude number.

contains two additional terms, an analytical solution cannot be found and the threshold Froude number can be just detected numerically. However, the toy model studied here helps in getting some qualitative characteristics for this kind of problem.

In order to explain why physically radiating and trapped modes propagate, we proceed as follows. The toy problem allows us to make an interesting analogy with the propagation of one-dimensional waves into two media having different physical properties. To show this, let us express $u_1(x, \theta, t) = v_1(x, \tau(t, \theta))$ and $u_2(x, \theta, t) = v_2(x, \tau(t, \theta))$. This dependence of the unknowns on t and θ is justified as we are looking for rotating waves. In particular, we choose the function $\tau(t, \theta) = \bar{a}t + \bar{b}\theta$, where $\bar{a}, \bar{b}$ are two constants that might be interpreted as the frequency of oscillation and the azimuthal wavenumber, respectively. Computing the partial derivatives with respect to t and θ, we

can then write

$$(\bar{a} + F\bar{b})^2 \partial_\tau^2 v_1 - \partial_x^2 v_1 = 0,$$
$$(\bar{a} + \Omega_2 \bar{b})^2 \partial_\tau^2 v_2 - \partial_x^2 v_2 = 0. \tag{3.40}$$

Defining the two speeds of sound $\bar{c}_1 = \frac{1}{\bar{a}+F\bar{b}}$ and $\bar{c}_2 = \frac{1}{\bar{a}+\Omega_2\bar{b}}$ in the first and second medium respectively, equations (3.40) become two standard 1D wave equations in two different media:

$$\partial_\tau^2 v_1 - \bar{c}_1^2 \partial_x^2 v_1 = 0,$$
$$\partial_\tau^2 v_2 - \bar{c}_2^2 \partial_x^2 v_2 = 0. \tag{3.41}$$

Following Bécherrawy (2012), we define the reflection and transmission coefficients

$$\mathcal{R} = \frac{\bar{c}_1 - \bar{c}_2}{\bar{c}_2 + \bar{c}_1}, \quad \mathcal{T} = \frac{2\bar{c}_2}{\bar{c}_2 + \bar{c}_1}, \tag{3.42}$$

which yield

$$\mathcal{R} = \frac{(\Omega_2 - F)\bar{b}}{2\bar{a} + (F + \Omega_2)\bar{b}},$$
$$\mathcal{T} = \frac{2\bar{a} + 2F\bar{b}}{2\bar{a} + (F + \Omega_2)\bar{b}}. \tag{3.43}$$

Since $F > \Omega_2$ by assumption of the model, two limiting cases are of particular interest:

1. $F \to \Omega_2$: in this case $\mathcal{R} \to 0$ and $\mathcal{T} \to 1$, thus the wave is totally transmitted and there is no reflection at the interface. The interface is a totally transparent boundary and we have a highly radiating wave propagating in the second medium. In other words we are approaching the vertical asymptote in the eigenvalue curve shown in figure 3.9.

2. $F \to \infty$: in this case $\mathcal{R} \to -1$ and the wave within the first medium is totally reflected. This is the case where a trapped mode develops; in fact, the wave remains trapped and cannot leave the first region.

3.6 The Convective Wave Equation for a dipole flow

Thus far we have considered the background flow to be a monopole vortex. However, our initial motivation showed waves propagating around the core of a pair of counter-rotating vortices. The video by Skipp (2020) indeed, shows that if a plate is dragged sufficiently slowly through the water of a swimming pool and then gradually lifted out, two pair of counter-rotating vortices are formed and travel throughout the entire swimming pool without dissipating nor interacting one another for a long time. For such a reason, in this section we examine the dynamics of linear surface gravity waves over a dipole flow which is supposed to travel at a uniform velocity U.

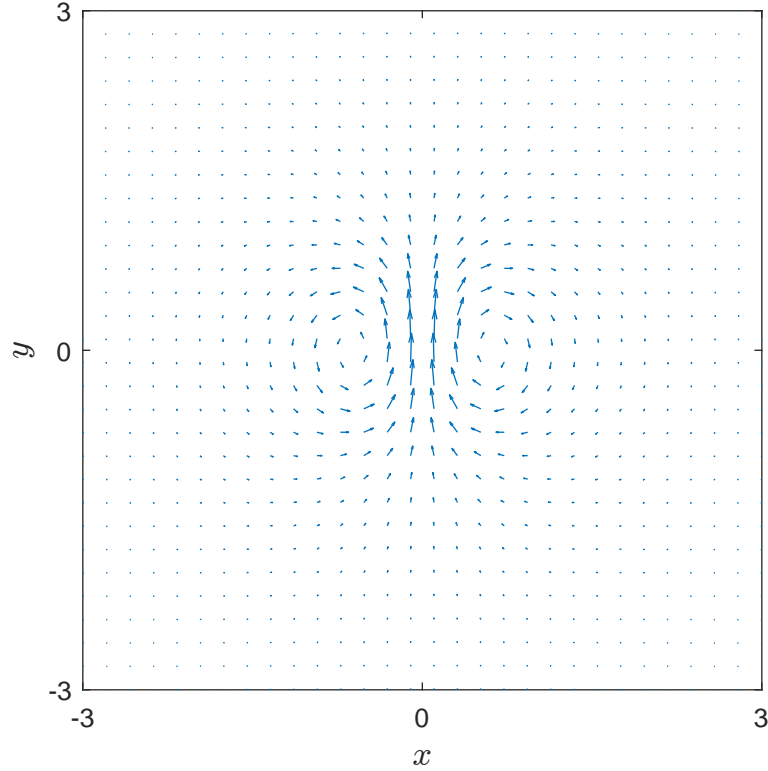In order to characterize the structure of the dipole we use the one

Figure 3.10: Velocity vector field of Lamb's dipole (3.44) for $a = 1$, $k = 3.8317$ and $U = 0.5$.

derived by Lamb in his book–Lamb (1932). Such a simple dipole model actually constitutes an exact solution of the 2D Euler equations and is composed of a vortical part within a core centered in a circle of a prescribed radius, and an exterior irrotational part. Generalizations of this dipole can be found in Saffman (1992). Lamb's dipole is usually described by its streamfunction $\psi(x, y)$ as follows

$$\psi(x, y) = \begin{cases} Ux - \frac{2U J_1(k\sqrt{x^2+y^2})}{k J_0(ka)\sqrt{x^2+y^2}}x, & x^2 + y^2 \leq a, \\ \frac{Ua^2 x}{x^2+y^2}, & x^2 + y^2 > a, \end{cases} \tag{3.44}$$

The velocity components are easily obtained by differentiating the streamfunction according to $U_0(x, y) = \frac{\partial \psi}{\partial y}$ and $V_0(x, y) = -\frac{\partial \psi}{\partial x}$. The velocity vector field is represented in figure 3.10 with parameters $U = 0.5$, $a = 1$, $k = 3.8317$.

We now get back to the convective wave equation as we aim at describing how surface waves are convected by the dipole flow. Firstly we non-dimensionalize the equation. Taking a as the characteristic length scale, U as the reference velocity of the dipole and c as the characteristic velocity of the perturbations, the convective wave equation (3.13) can be written as

$$\left(\frac{\partial}{\partial t} + FU_0(x, y)\frac{\partial}{\partial x} + FV_0(x, y)\frac{\partial}{\partial y}\right)^2 \phi - \left(\frac{\partial^2 \phi}{\partial x^2} + \frac{\partial^2 \phi}{\partial y^2}\right) = 0, \tag{3.45}$$
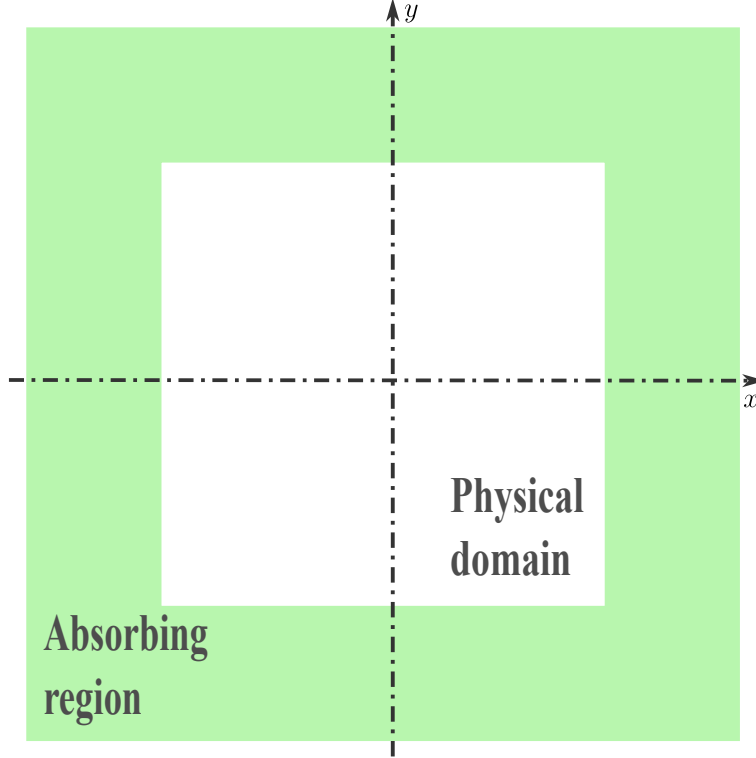
Figure 3.11: Square domain where we apply a PML formulation in order to solve equation (3.45) for a dipole background flow.

where $F = \frac{U}{c} = \frac{U}{\sqrt{gH}}$ is the Froude number, $U_0(x, y)$ and $V_0(x, y)$ the velocity components of the dipole in dimensionless form, whose streamfunction is now given by

$$\psi(x, y) = \begin{cases} x - \frac{2J_1(k\sqrt{x^2+y^2})}{kJ_0(k)\sqrt{x^2+y^2}}x, & x^2 + y^2 \leq 1, \\ \frac{x}{x^2+y^2}, & x^2 + y^2 > 1. \end{cases} \tag{3.46}$$

In the following we are going to solve equation (3.45) on a square domain $S = S_p \cup S_a$, where S_p identifies the physical domain and S_a the absorbing region–figure 3.11. To handle boundary conditions, we will use a PML formulation that later on we are going to solve by time marching using the method of lines (MOL)—see Schiesser and Griffiths (2009) for further details on this method and its implementation in Matlab.

3.6.1 PML formulation of the convective wave equation in cartesian coordinates

The PML formulation we are going to obtain is inspired by that given in Sim (2010) for the standard hyperbolic wave equation without any background flow. As stated before, in our case we have a dipole that changes the way waves are transported. The dipole is generally represented by a two-dimensional velocity field $\boldsymbol{U_0}(x, y) = U_0(x, t)\hat{\boldsymbol{x}} + V_0(x, y)\hat{\boldsymbol{y}}$. To start our derivation we first

65

re-write the convective wave equation expanding all the terms in there:

$$\frac{\partial^2 \phi}{\partial t^2} + 2FU_0 \frac{\partial^2 \phi}{\partial t \partial x} + 2FV_0 \frac{\partial^2 \phi}{\partial t \partial y}$$
$$+ F^2 U_0 \frac{\partial}{\partial x}\left(U_0 \frac{\partial \phi}{\partial x}\right) + F^2 U_0 \frac{\partial}{\partial x}\left(V_0 \frac{\partial \phi}{\partial y}\right) + F^2 V_0 \frac{\partial}{\partial y}\left(U_0 \frac{\partial \phi}{\partial x}\right) + F^2 V_0 \frac{\partial}{\partial y}\left(V_0 \frac{\partial \phi}{\partial y}\right)$$
$$- \left(\frac{\partial^2 \phi}{\partial x^2} + \frac{\partial^2 \phi}{\partial y^2}\right) = 0.$$

$$(3.47)$$

We define the Laplace transform in time of $\phi(x,y,t)$ as

$$\tilde{\phi}(x,y,s) = \int_0^\infty \phi(x,y,t)e^{-st}dt. \tag{3.48}$$

We assume the initial conditions to be non-zero in the physical domain S_p and null outside it. So, outside S_p, the convective wave equation written in terms of the Laplace variable reads

$$s^2 \tilde{\phi} + 2sFU_0 \frac{\partial \tilde{\phi}}{\partial x} + 2sFV_0 \frac{\partial \tilde{\phi}}{\partial y}$$
$$+ F^2 U_0 \frac{\partial}{\partial x}\left(U_0 \frac{\partial \tilde{\phi}}{\partial x}\right) + F^2 U_0 \frac{\partial}{\partial x}\left(V_0 \frac{\partial \tilde{\phi}}{\partial y}\right) + F^2 V_0 \frac{\partial}{\partial y}\left(U_0 \frac{\partial \tilde{\phi}}{\partial x}\right) + F^2 V_0 \frac{\partial}{\partial y}\left(V_0 \frac{\partial \tilde{\phi}}{\partial y}\right)$$
$$- \left(\frac{\partial^2 \tilde{\phi}}{\partial x^2} + \frac{\partial^2 \tilde{\phi}}{\partial y^2}\right) = 0.$$

$$(3.49)$$

At this point we introduce two stretched coordinates along x and y, namely

$$\tilde{x} = x + \frac{1}{s}\int_0^x \xi_1(x')dx',$$
$$\tilde{y} = y + \frac{1}{s}\int_0^y \xi_2(y')dy'. \tag{3.50}$$

Functions $\xi_1(x), \xi_2(y)$ are arbitrary functions having support only in the absorbing layers surrounding the actual computational domain. It will be shown later that these can be used to provide damping of the incoming waves into the layers. Their functional form can be chosen to minimize the reflection at the beginning of the damping region and clearly to smoothly damp out waves all across the damping layers up to the extended boundary. For our computations we use the same damping function for ξ_1 and ξ_2 given by

$$\xi_j(x_j) = \begin{cases} \frac{4}{3}\frac{\bar{\xi}_j}{(x_f - x_d)^2}(x_j - x_d)^2, & |x_j| \leq \frac{x_d + x_f}{2}, \\ \frac{4}{3}\frac{\bar{x}_j}{x_f - x_d}(|x_j| - x_f) + \bar{\xi}_j, & \frac{x_d + x_f}{2} < |x_j| \leq x_f, \end{cases} \tag{3.51}$$

with $j = 1, 2$ being an index here used to identify either the spatial coordinate x or y and the corresponding damping function along these directions, x_f is the end point of the domain in one particular direction (either x or y), x_d the
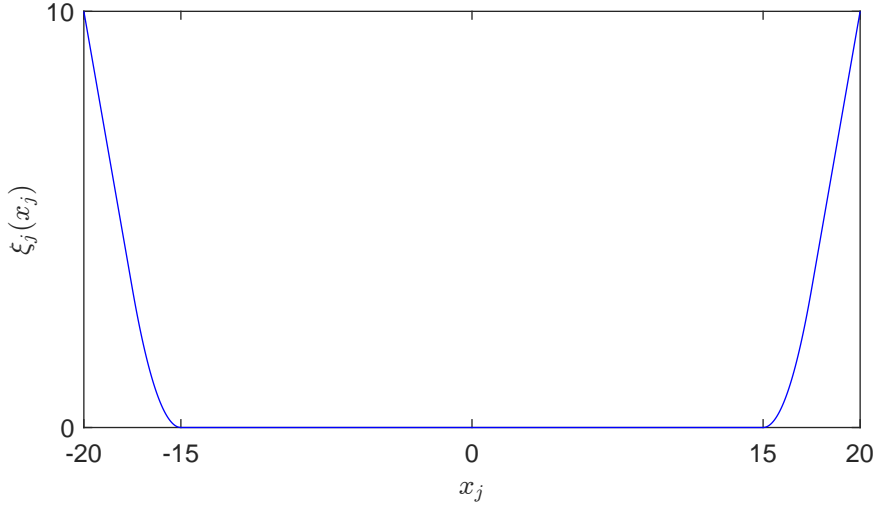
66

Figure 3.12: Function ξ_1 and ξ_2 used in the PML formulation for the CWE. Here $j = 1, 2$ is used to identify either the spatial coordinate x or y and the corresponding damping function along these directions. In this example $x_d = 15$, $x_f = 20$ and $\bar{\xi}_j = 10$.

point where the damping layer begins, $\bar{\xi}_j$ the amount of damping. Function (3.51) is quadratic at the beginning of the damping region and then becomes linear throughout the damping layer in order to avoid strong reflections. An example is shown in figure 3.12. Note that ξ_1 depends on x only, whereas ξ_2 only on y, so each function acts separately on the two spatial variables. The partial derivatives change according to

$$
\begin{aligned}
\frac{\partial}{\partial \tilde{x}} &= \frac{s}{s + \xi_1(x)} \frac{\partial}{\partial x} = \frac{1}{\gamma_1(x)} \frac{\partial}{\partial x}, \\
\frac{\partial}{\partial \tilde{y}} &= \frac{s}{s + \xi_2(y)} \frac{\partial}{\partial y} = \frac{1}{\gamma_2(y)} \frac{\partial}{\partial y},
\end{aligned}
\tag{3.52}
$$

where we have defined $\gamma_1(x) = 1 + \frac{\xi_1(x)}{s}$ and $\gamma_2(y) = 1 + \frac{\xi_2(y)}{s}$ which depend on the damping functions ξ_1 and ξ_2 respectively. Now, following Sim (2010), we impose the differential equation (3.49) to hold in the new coordinates. This does not affect the behaviour of ϕ inside the physical domain and ensures that the solution decays exponentially fast in the absorbing region S_a. To see this, let us consider a travelling wave in the single spatial direction x. Enforcing the behaviour along $\tilde{x}$ yields a solution of the form

$$
\phi \sim e^{i\omega t - i\omega \tilde{x}} = e^{i\omega t - i\omega x - \int_0^x \xi_1(x') dx'},
\tag{3.53}
$$

which decays in x as the damping function $\xi_1(x) \geq 0$. Using the derivatives (3.52) and multiplying by $\gamma_1 \gamma_2$ we then obtain

$$s^2 \gamma_1 \gamma_2 \tilde{\phi} + 2Fs\gamma_2 U_0 \frac{\partial \tilde{\phi}}{\partial x} + 2Fs\gamma_1 V_0 \frac{\partial \tilde{\phi}}{\partial y}$$
$$+ F^2 \gamma_2 U_0 \frac{\partial}{\partial x}\left(\frac{U_0}{\gamma_1}\frac{\partial \tilde{\phi}}{\partial x}\right) + F^2 \gamma_2 U_0 \frac{\partial}{\partial x}\left(\frac{V_0}{\gamma_2}\frac{\partial \tilde{\phi}}{\partial y}\right) + F^2 \gamma_1 V_0 \frac{\partial}{\partial y}\left(\frac{U_0}{\gamma_1}\frac{\partial \tilde{\phi}}{\partial x}\right) + F^2 \gamma_1 V_0 \frac{\partial}{\partial y}\left(\frac{V_0}{\gamma_2}\frac{\partial \tilde{\phi}}{\partial y}\right)$$
$$- \gamma_2 \frac{\partial}{\partial x}\left(\frac{1}{\gamma_1}\frac{\partial \tilde{\phi}}{\partial x}\right) - \gamma_1 \frac{\partial}{\partial y}\left(\frac{1}{\gamma_2}\frac{\partial \tilde{\phi}}{\partial y}\right) = 0,$$

$$(3.54)$$

which can be simplified into

$$s^2 \gamma_1 \gamma_2 \tilde{\phi} + 2Fs\gamma_2 U_0 \frac{\partial \tilde{\phi}}{\partial x} + 2Fs\gamma_1 V_0 \frac{\partial \tilde{\phi}}{\partial y}$$
$$+ F^2 U_0 \frac{\partial}{\partial x}\left(\frac{\gamma_2}{\gamma_1}U_0\frac{\partial \tilde{\phi}}{\partial x}\right) + F^2 U_0 \frac{\partial}{\partial x}\left(V_0\frac{\partial \tilde{\phi}}{\partial y}\right) + F^2 V_0 \frac{\partial}{\partial y}\left(U_0\frac{\partial \tilde{\phi}}{\partial x}\right) + F^2 V_0 \frac{\partial}{\partial y}\left(\frac{\gamma_1}{\gamma_2}V_0\frac{\partial \tilde{\phi}}{\partial y}\right)$$
$$- \frac{\partial}{\partial x}\left(\frac{\gamma_2}{\gamma_1}\frac{\partial \tilde{\phi}}{\partial x}\right) - \frac{\partial}{\partial y}\left(\frac{\gamma_1}{\gamma_2}\frac{\partial \tilde{\phi}}{\partial y}\right) = 0.$$

$$(3.55)$$

Now, a direct computation of the products between γ_1 and γ_2 yields

$$\frac{\gamma_2}{\gamma_1} = 1 + \frac{\xi_2 - \xi_1}{s + \xi_1},$$
$$\frac{\gamma_1}{\gamma_2} = 1 + \frac{\xi_1 - \xi_2}{s + \xi_2},$$
$$\gamma_1 \gamma_2 = 1 + \frac{\xi_1 + \xi_2}{s} + \frac{\xi_1 \xi_2}{s^2},$$

$$(3.56)$$

so, we can write

$$s^2 \left(1 + \frac{\xi_1 + \xi_2}{s} + \frac{\xi_1 \xi_2}{s^2}\right)\tilde{\phi} + 2Fs\left(1 + \frac{\xi_2}{s}\right)U_0\frac{\partial \tilde{\phi}}{\partial x} + 2Fs\left(1 + \frac{\xi_1}{s}\right)V_0\frac{\partial \tilde{\phi}}{\partial y}$$
$$+ F^2 U_0 \frac{\partial}{\partial x}\left(U_0\left(1 + \frac{\xi_2 - \xi_1}{s + \xi_1}\right)\frac{\partial \tilde{\phi}}{\partial x}\right) + F^2 U_0 \frac{\partial}{\partial x}\left(V_0\frac{\partial \tilde{\phi}}{\partial y}\right)$$
$$+ F^2 V_0 \frac{\partial}{\partial y}\left(U_0\frac{\partial \tilde{\phi}}{\partial x}\right) + F^2 V_0 \frac{\partial}{\partial y}\left(V_0\left(1 + \frac{\xi_1 - \xi_2}{s + \xi_2}\right)\frac{\partial \tilde{\phi}}{\partial y}\right)$$
$$- \frac{\partial}{\partial x}\left(\left(1 + \frac{\xi_2 - \xi_1}{s + \xi_1}\right)\frac{\partial \tilde{\phi}}{\partial x}\right) - \frac{\partial}{\partial y}\left(\left(1 + \frac{\xi_1 - \xi_2}{s + \xi_2}\right)\frac{\partial \tilde{\phi}}{\partial y}\right) = 0.$$

$$(3.57)$$

Let us introduce two additional unknowns $\tilde{\psi}$ and $\tilde{\sigma}$ as

$$\tilde{\psi} = \frac{\xi_2 - \xi_1}{s + \xi_1}\frac{\partial \tilde{\phi}}{\partial x},$$
$$\tilde{\sigma} = \frac{\xi_1 - \xi_2}{s + \xi_2}\frac{\partial \tilde{\phi}}{\partial y},$$

$$(3.58)$$

68

so the previous set of equations become

$$s^2\tilde{\phi} + s(\xi_1 + \xi_2)\tilde{\phi} + \xi_1\xi_2\tilde{\phi} + 2FsU_0\frac{\partial\tilde{\phi}}{\partial x} + 2FU_0\xi_2\frac{\partial\tilde{\phi}}{\partial x} + 2FsV_0\frac{\partial\tilde{\phi}}{\partial y} + 2FV_0\xi_1\frac{\partial\tilde{\phi}}{\partial y}$$

$$+ F^2U_0\frac{\partial}{\partial x}\left(U_0\frac{\partial\tilde{\phi}}{\partial x}\right) + F^2U_0\frac{\partial}{\partial x}\left(V_0\frac{\partial\tilde{\phi}}{\partial y}\right) + F^2V_0\frac{\partial}{\partial y}\left(U_0\frac{\partial\tilde{\phi}}{\partial x}\right) + F^2V_0\frac{\partial}{\partial y}\left(V_0\frac{\partial\tilde{\phi}}{\partial y}\right)$$

$$+ F^2U_0\frac{\partial}{\partial x}\left(U_0\tilde{\psi}\right) + F^2V_0\frac{\partial}{\partial y}\left(V_0\tilde{\sigma}\right) - \frac{\partial^2\tilde{\phi}}{\partial x^2} - \frac{\partial^2\tilde{\phi}}{\partial y^2} - \frac{\partial\tilde{\psi}}{\partial x} - \frac{\partial\tilde{\sigma}}{\partial y} = 0,$$

$$(s + \xi_1)\tilde{\psi} = (\xi_2 - \xi_1)\frac{\partial\tilde{\phi}}{\partial x},$$

$$(s + \xi_2)\tilde{\sigma} = (\xi_1 - \xi_2)\frac{\partial\tilde{\phi}}{\partial y}.$$

$$(3.59)$$

Finally, we inverse Laplace transform in time and obtain the final PML formulation

$$D_t^2\phi - c^2\nabla^2\phi = (\xi_1 + \xi_2)\frac{\partial\phi}{\partial t} + \xi_1\xi_2\phi + 2FU_0\xi_2\frac{\partial\phi}{\partial x} + 2FV_0\xi_1\frac{\partial\phi}{\partial y}$$

$$+ F^2U_0\frac{\partial}{\partial x}\left(U_0\psi\right) - \frac{\partial\psi}{\partial x} + F^2V_0\frac{\partial}{\partial y}\left(V_0\sigma\right) - \frac{\partial\sigma}{\partial y},$$

$$\frac{\partial\psi}{\partial t} = -\xi_1\psi + (\xi_2 - \xi_1)\frac{\partial\phi}{\partial x},$$

$$\frac{\partial\sigma}{\partial t} = -\xi_2\sigma + (\xi_1 - \xi_2)\frac{\partial\sigma}{\partial y}.$$

$$(3.60)$$

3.6.2 Discretization and numerical solution

To discretize the previous system (3.60) using the method of lines, we want first to re-write it as a first order system in time. Let us introduce four variables

$$u_1 = \phi, \qquad u_2 = D_t\phi, \qquad u_3 = \psi, \qquad u_4 = \sigma. \qquad (3.61)$$

System (3.60) can be re-written as

$$\frac{\partial u_1}{\partial t} = -FU_0\frac{\partial u_1}{\partial x} - FV_0\frac{\partial u_1}{\partial y} + u_2,$$

$$\frac{\partial u_2}{\partial t} = -FU_0\frac{\partial u_2}{\partial x} - FV_0\frac{\partial u_2}{\partial y} + \left(\frac{\partial^2 u_1}{\partial x^2} + \frac{\partial^2 u_1}{\partial y^2}\right)$$

$$- \xi_1\xi_2 u_1 + F(\xi_1 - \xi_2)U_0\frac{\partial u_1}{\partial x} + F(\xi_2 - \xi_1)V_0\frac{\partial u_1}{\partial y} - (\xi_1 + \xi_2)u_2$$

$$+ \frac{\partial u_3}{\partial x} - F^2U_0\frac{\partial}{\partial x}\left(U_0 u_3\right)$$

$$+ \frac{\partial u_4}{\partial y} - F^2V_0\frac{\partial}{\partial y}\left(V_0 u_4\right),$$

$$\frac{\partial u_3}{\partial t} = -\xi_1 u_3 + (\xi_2 - \xi_1)\frac{\partial u_1}{\partial x},$$

$$\frac{\partial u_4}{\partial t} = -\xi_2 u_4 + (\xi_1 - \xi_2)\frac{\partial u_1}{\partial y}.$$

$$(3.62)$$

Before proceeding with the actual discretization, we collect all the terms on the right-hand side of the previous equations containing x-derivatives only and in a similar way those containing y-derivatives only. This way, we can write the previous system as

$$\frac{\partial u_1}{\partial t} = \mathcal{X}_1 + \mathcal{Y}_1,$$
$$\frac{\partial u_2}{\partial t} = \mathcal{X}_2 + \mathcal{Y}_2,$$
$$\frac{\partial u_3}{\partial t} = \mathcal{X}_3, \tag{3.63}$$
$$\frac{\partial u_4}{\partial t} = \mathcal{Y}_4.$$

Let $u_{k_{i,j}}(t) = u_k(x_j, y_i, t)$ for $k = 1, 2, 3, 4$, $(x_j, y_i) = \left(x_0 + (j-1)\Delta x, y_0 + (i-1)\Delta y\right)$ be the grid points for $(i,j) \in \left([1, N_y], [1, N_x]\right)$ and $(\Delta x, \Delta y) = \left(\frac{x_f - x_0}{N_x - 1}, \frac{y_f - y_0}{N_y - 1}\right)$. We evaluate the previous equations at each point x_j, y_i. The discretization of the right-hand sides along the x-direction is given by

$$\mathcal{X}_{1_{i,j}} = -FU_0(y_i, x_j)\frac{u_{1_{i,j+1}} - u_{1_{i,j-1}}}{2\Delta x},$$

$$\mathcal{X}_{2_{i,j}} = -FU_0(y_i, x_j)\frac{u_{2_{i,j+1}} - u_{2_{i,j-1}}}{2\Delta x} + \frac{u_{1_{i,j+1}} - 2u_{1_{i,j}} + u_{1_{i,j-1}}}{\Delta x^2}$$
$$- FU_0(y_i, x_j)\left(\xi_2(y_i) - \xi_1(x_j)\right)\frac{u_{1_{i,j+1}} - u_{1_{i,j-1}}}{2\Delta x}$$
$$- F^2 U_0(y_i, x_j)\frac{U_0(y_i, x_{j+1})u_{3_{i,j+1}} - U_0(y_i, x_{j-1})u_{3_{i,j-1}}}{2\Delta x} \tag{3.64}$$
$$+ \frac{u_{3_{i,j+1}} - u_{3_{i,j-1}}}{2\Delta x},$$

$$\mathcal{X}_{3_{i,j}} = -\xi_1(x_j)u_{3_{i,j}} + (\xi_2(y_i) - \xi_1(x_j))\frac{u_{1_{i,j+1}} - u_{1_{i,j-1}}}{2\Delta x}.$$

As far as the y-contributions is concerned, we have

$$\mathcal{Y}_{1_{i,j}} = -FV_0(y_i, x_j)\frac{u_{1_{i+1,j}} - u_{1_{i-1,j}}}{2\Delta y} + u_{2_{i,j}},$$

$$\mathcal{Y}_{2_{i,j}} = -FV_0(y_i, x_j)\frac{u_{2_{i+1,j}} - u_{2_{i-1,j}}}{2\Delta y} + \frac{u_{1_{i+1,j}} - 2u_{1_{i,j}} + u_{1_{i-1,j}}}{\Delta y^2}$$
$$- FV_0(y_i, x_j)\left(\xi_1(x_j) - \xi_2(y_i)\right)\frac{u_{1_{i+1,j}} - u_{1_{i-1,j}}}{2\Delta y}$$
$$- \xi_1(x_j)\xi_2(y_i)u_{1_{i,j}} - \left(\xi_1(x_j) + \xi_2(y_i)\right)u_{2_{i,j}} \tag{3.65}$$
$$- F^2 V_0(y_i, x_j)\frac{V_0(y_{i+1}, x_j)u_{4_{i+1,j}} - V_0(y_{i-1}, x_j)u_{4_{i-1,j}}}{2\Delta y}$$
$$+ \frac{u_{4_{i+1,j}} - u_{4_{i-1,j}}}{2\Delta y},$$

$$\mathcal{Y}_{4_{i,j}} = -\xi_2(y_i)u_{4_{i,j}} + (\xi_1(x_j) - \xi_2(y_i))\frac{u_{1_{i+1,j}} - u_{1_{i-1,j}}}{2\Delta y}.$$

At the boundary points, since the type of boundary condition is unimportant, we can simply impose a Dirichlet boundary condition $\mathcal{X}_k = 0$ and $\mathcal{Y}_k = 0$, for

70

$k = 1, 2, 3, 4$. The following final system of ODEs are obtained

$$\frac{du_{1_{i,j}}}{dt} = \mathcal{X}_{1_{i,j}} + \mathcal{Y}_{1_{i,j}},$$

$$\frac{du_{2_{i,j}}}{dt} = \mathcal{X}_{2_{i,j}} + \mathcal{Y}_{2_{i,j}},$$

$$\frac{du_{3_{i,j}}}{dt} = \mathcal{X}_{3_{i,j}}, \quad (3.66)$$

$$\frac{du_{4_{i,j}}}{dt} = \mathcal{Y}_{4_{i,j}}.$$

These have been solved using the MATLAB routine "ODE45". We now proceed with a couple of numerical tests in order to check the efficiency and accuracy of our numerics.

3.6.3 Numerical experiments and comparisons

In this section we want to validate our formulation with two tests conducted on a purely rotating background flow given by the following form,

$$\boldsymbol{U_0}(\boldsymbol{x}) = re^{-r^2}\hat{\boldsymbol{\theta}}. \quad (3.67)$$

For such a monopole we can find very accurate solutions since the flow depends on r only. In fact, in this case the wave equation (3.14) can be decomposed in Fourier modes along the azimuthal direction and solved as function of r and t only, thus reducing the number of spatial variables involved. For this reason, from now on, we treat such solutions as exact. In particular, we will call them "1D exact solutions". We are going to compare our 2D PML solutions with the 1D exact ones. These results will be computed at different Froude numbers ($F = 0.5$ and $F = 4$), various number of grid points and times ranges.

The first test has been done by taking $F = 0.5$, $N_x = N_y = 400$, $\bar{\xi}_1 = \bar{\xi}_2 = 10$, $x_d = y_d = 15$ and the initial conditions

$$\phi(r, \theta, 0) = \frac{3}{2}e^{-8(r-\frac{3}{2})^2}\cos(\theta), \qquad \frac{\partial\phi(r, \theta, 0)}{\partial t} = 0. \quad (3.68)$$

Figure 3.13 compares the trend of the PML solution along the x-axis with the exact one at different times. The most stringent test is the second one, conducted at $F = 4$. In fact, from the modal analysis at $F = 4$ the Gaussian vortex profile exhibits an instability with respect to sloshing perturbations (i.e. perturbations with azimuthal wavenumber $m = 1$), with the solution growing exponentially in time. Thus, it becomes extremely important to check whether our PML method is capable of tracking unstable modes. Figure 3.14 shows the comparative results in this case with initial conditions

$$\phi(r, \theta, 0) = e^{-8(r-10)^2}\cos(\theta), \qquad \frac{\partial\phi(r, \theta, 0)}{\partial t} = 0. \quad (3.69)$$
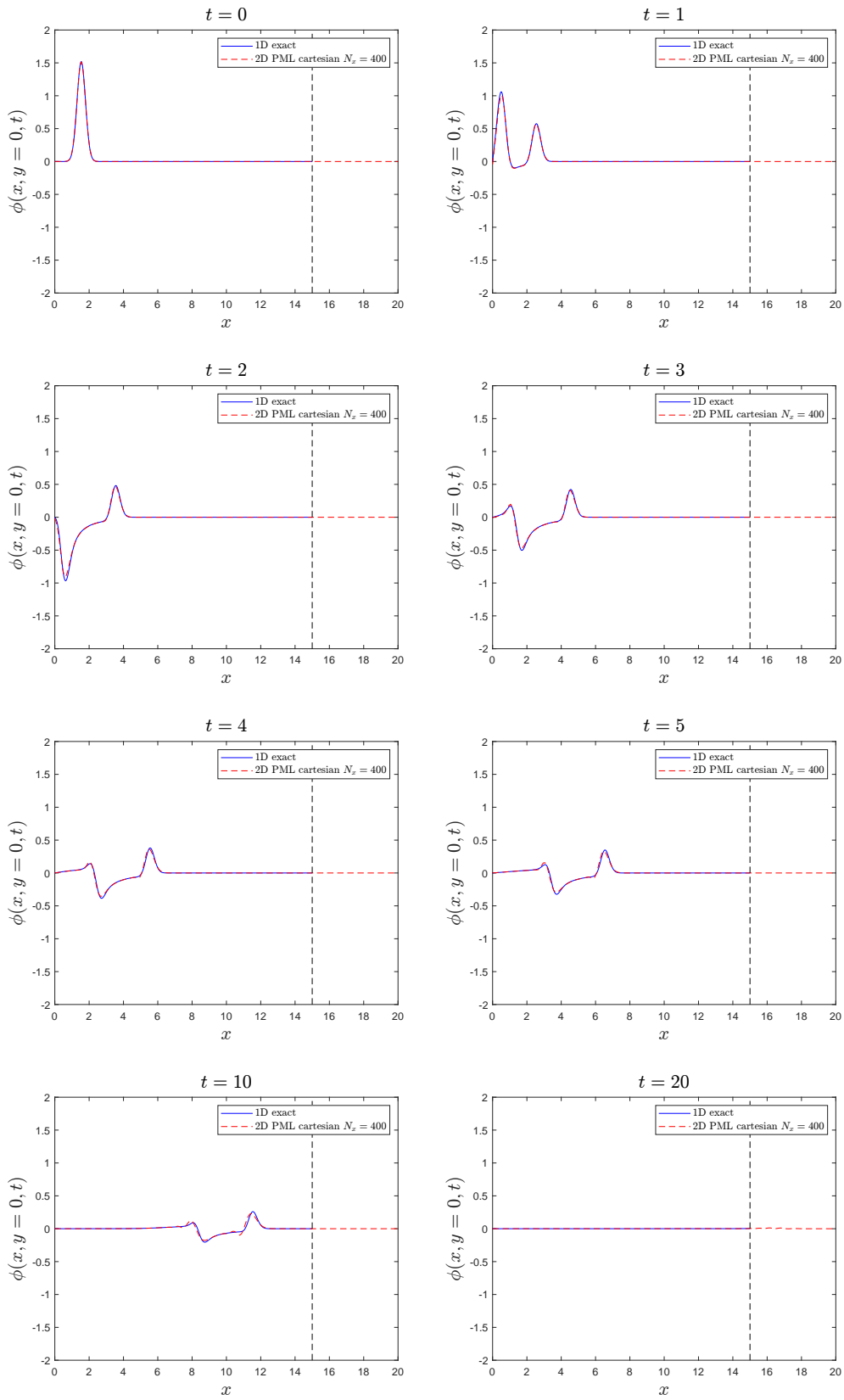
Figure 3.13: Time evolution of the 1D exact solution and the PML model in cartesian coordinates for the vortex profile in equation (3.67) with $F = 0.5$.

Particularly, the PML code has been run twice with two different spatial resolutions; the first one with $N_x = N_y = 400$ grid points and the second with $N_x = N_y = 600$ grid points. The magnitude of the damping functions as well as the locations of beginning of the damping regions have been kept unchanged with respect to the previous test. Clearly, the solution with a higher number of nodes stays closer to the exact solution for most of the time, whereas the one with $N_x = 400$ suffers of little wiggles that form as time goes on. Both approximate solutions though are able to ultimately capture the aforementioned instability. Finally, in order to give a broader picture of the scenario in this case, the propagation of the waves in the $x - y$ plane is displayed in figure 3.15 at different times.

3.6.4 Results for Lamb's dipole

We now consider the Convective Wave Equation with Lamb's dipole (3.46) as a background flow. We show hereafter results for three different Froude numbers: $F = 0.25, 0.5, 0.75$. The reason for choosing them is based on the argument made in section 3.4 that possible instabilities of the system are associated to the presence of an ergoregion. We want to verify that this argument holds in the case of a non-axisymmetric, nontrivial flow, as the dipole is. In figure 3.16 the ergoregion is shown for the three different Froude numbers considered. As can be noted, for $F = 0.25$ the ergoregion is actually absent, whereas for increasing values of F it becomes more complicated. At even larger Froude numbers (see the example for $F = 1$ in figure 3.16) it splits into two distinct regions, hence bringing further complexities that we are not going to deal in this thesis. So, we will only study the problem for three different Froude numbers $F = 0.25, 0.5, 0.75$. We therefore expect an instability to occur at $F = 0.5$ and $F = 0.75$, being these values above a critical Froude number $F_c = 0.288$ at which the ergoregion starts to appear. We used the PML formulation derived earlier. All the numerical parameters like the domain size and the amount of damping introduced have been varied from case to case and will be specified for each case. On the contrary the solution has always been initialized with the same initial conditions which read

$$\phi(x, y, 0) = e^{-4\left(r - \frac{x_f}{2}\right)^2}, \qquad \frac{\partial \phi(x, y, 0)}{\partial t} = 0. \qquad (3.70)$$

Results for $F = 0.25$

In this initial case, the domain parameters are $x_0 = y_0 = -20$, $x_f = y_f = 20$ and $x_d = y_d = 15$. The amount of damping in both direction is $\bar{\xi}_1 = \bar{\xi}_2 = 10$ and we used $N_x = N_y = 400$ grid points in both the x and y direction. In figure 3.17, the perturbation potential $\phi(x, y, t)$ is shown at different times
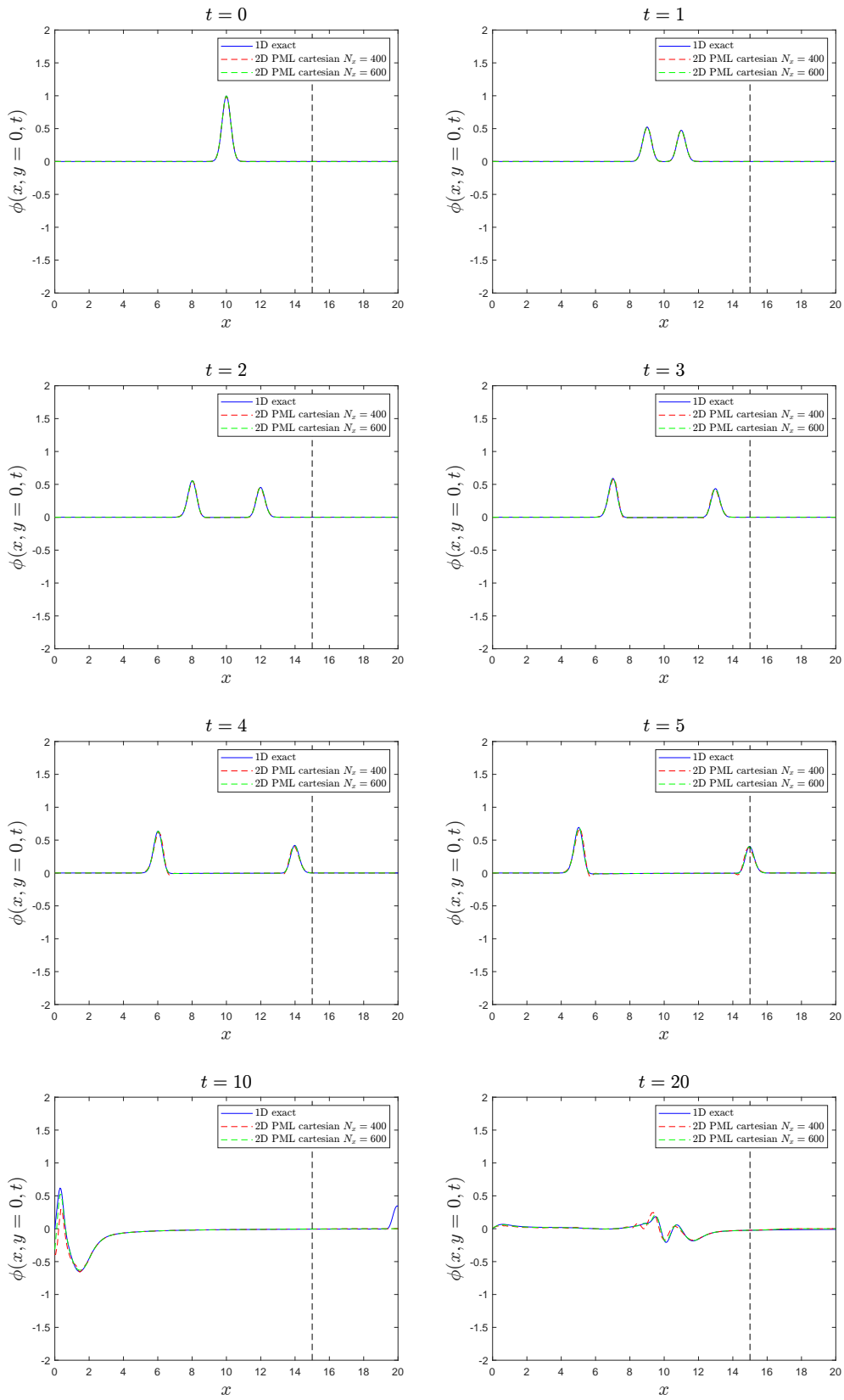
Figure 3.14: Time evolution of the 1D exact solution and the PML model in cartesian coordinates for the vortex profile in equation (3.67) with $F = 4$.
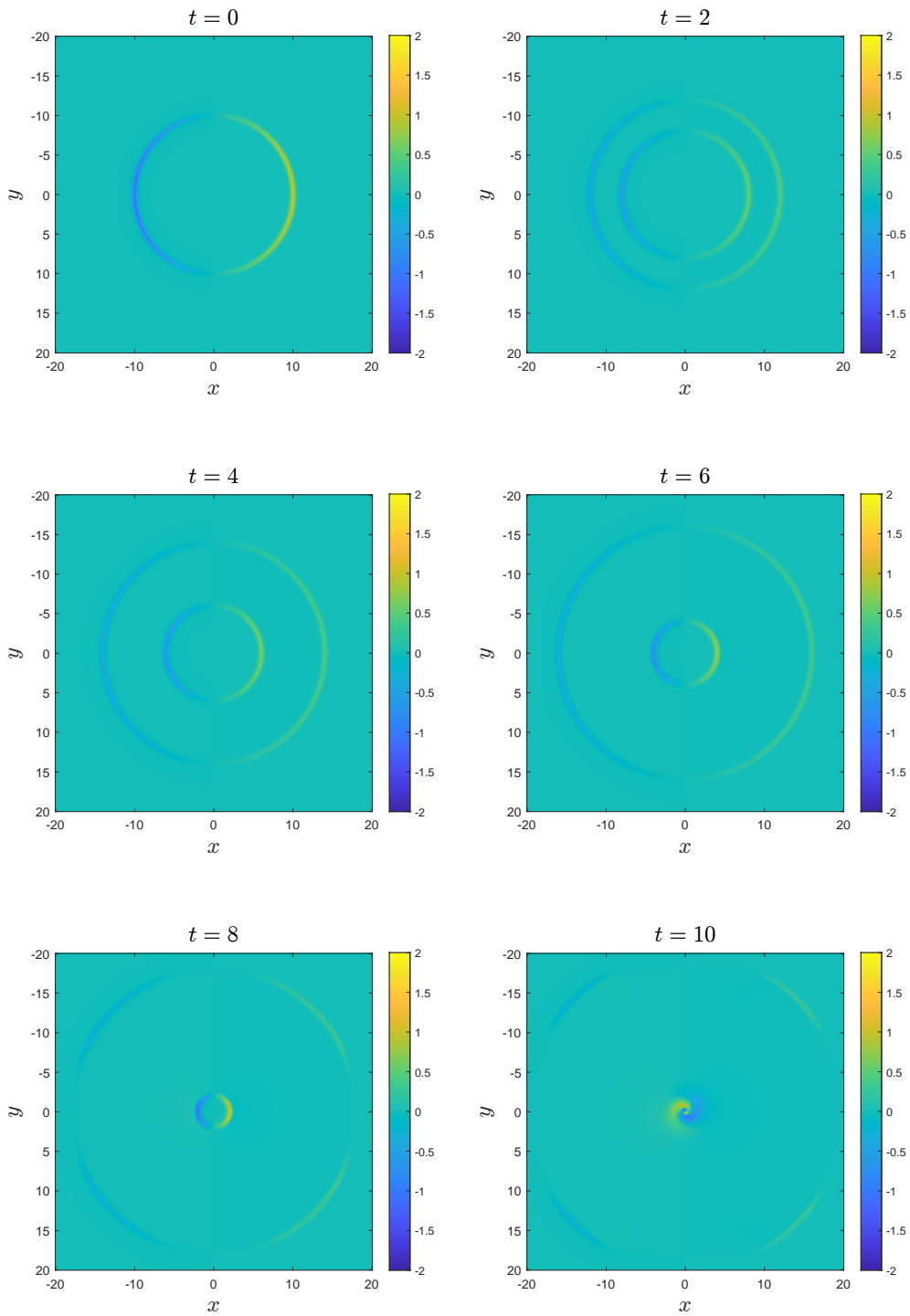
Figure 3.15: Time evolution of the PML solution in the case $F = 4$ using 400 grid points in both spatial directions.
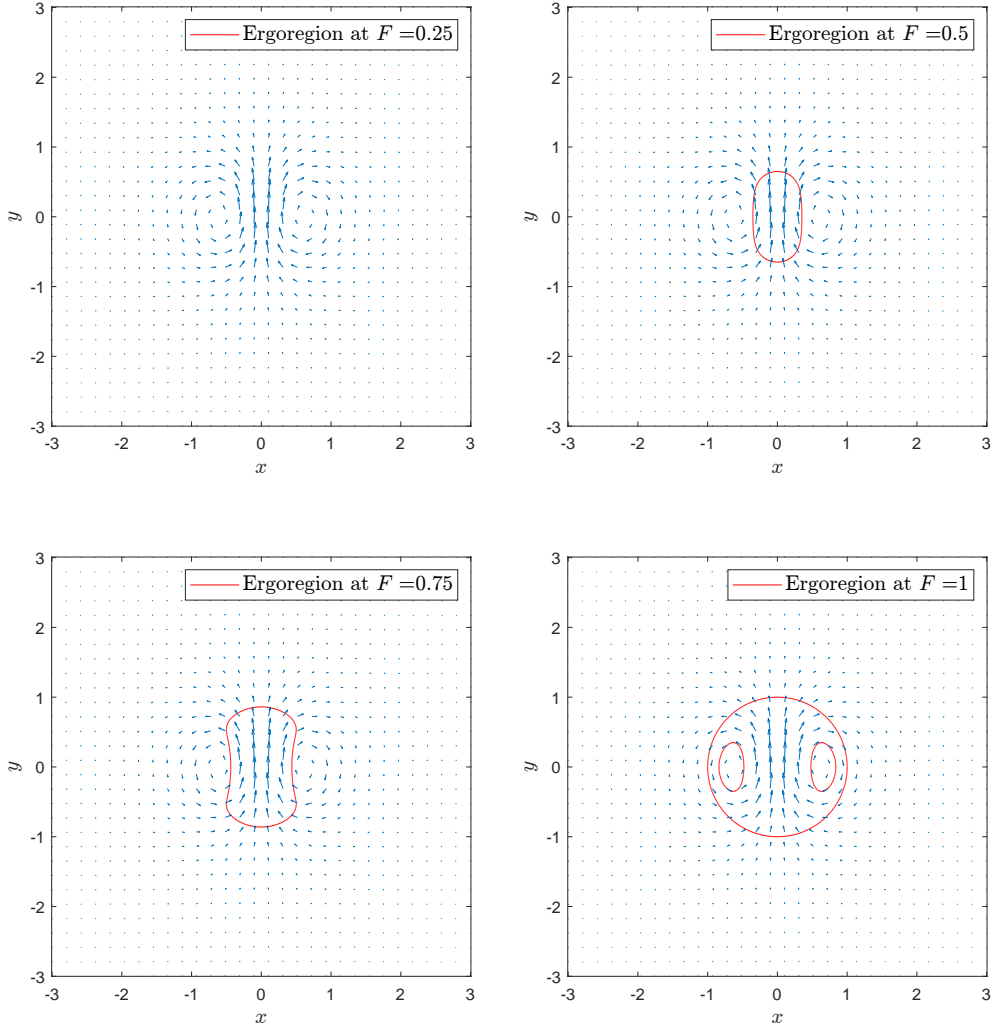
Figure 3.16: Ergoregion for Lamb's dipole at different Froude numbers over the flow. Red line: plot of the ergoregion curve. Arrows: Lamb's dipole velocity field.

together with its behaviour along the x and y directions, namely $\phi(x, 0, t)$ and $\phi(0, y, t)$. As expected no instability arises in this case and the solution dies out as time evolves. The absorbing layers work very well and provide the desired non-reflecting behaviour.

Results for F = 0.5

We repeat the computations for $F = 0.5$ and the same geometrical and artificial parameters as in the previous example. Results are shown in figure 3.18. In this case, however an instability is seen to arise after a time $t = 15$, with the solution being particularly oscillatory within the dipole's core $[x_{\text{core}}, y_{\text{core}}] = [-1, 1] \times [-1, 1]$. We discuss this phenomenon in the next paragraph.

Figure 3.17: Perturbation potential for $F = 0.25$ at different times. Left: contour plot of the solution in the $x-y$ plane. Right: corresponding behaviour along the axes. Red dotted lines indicate where the damping layers begin.
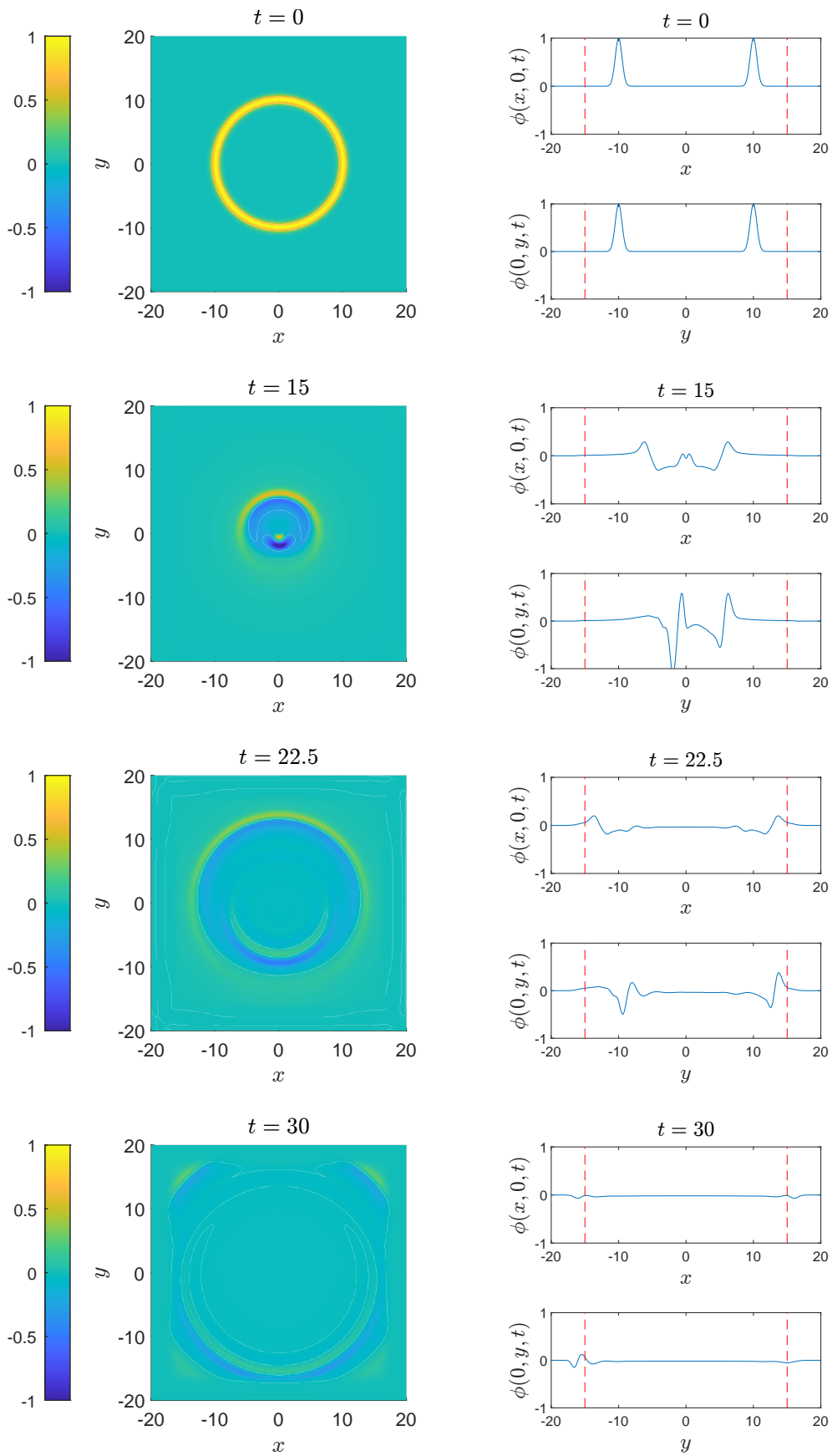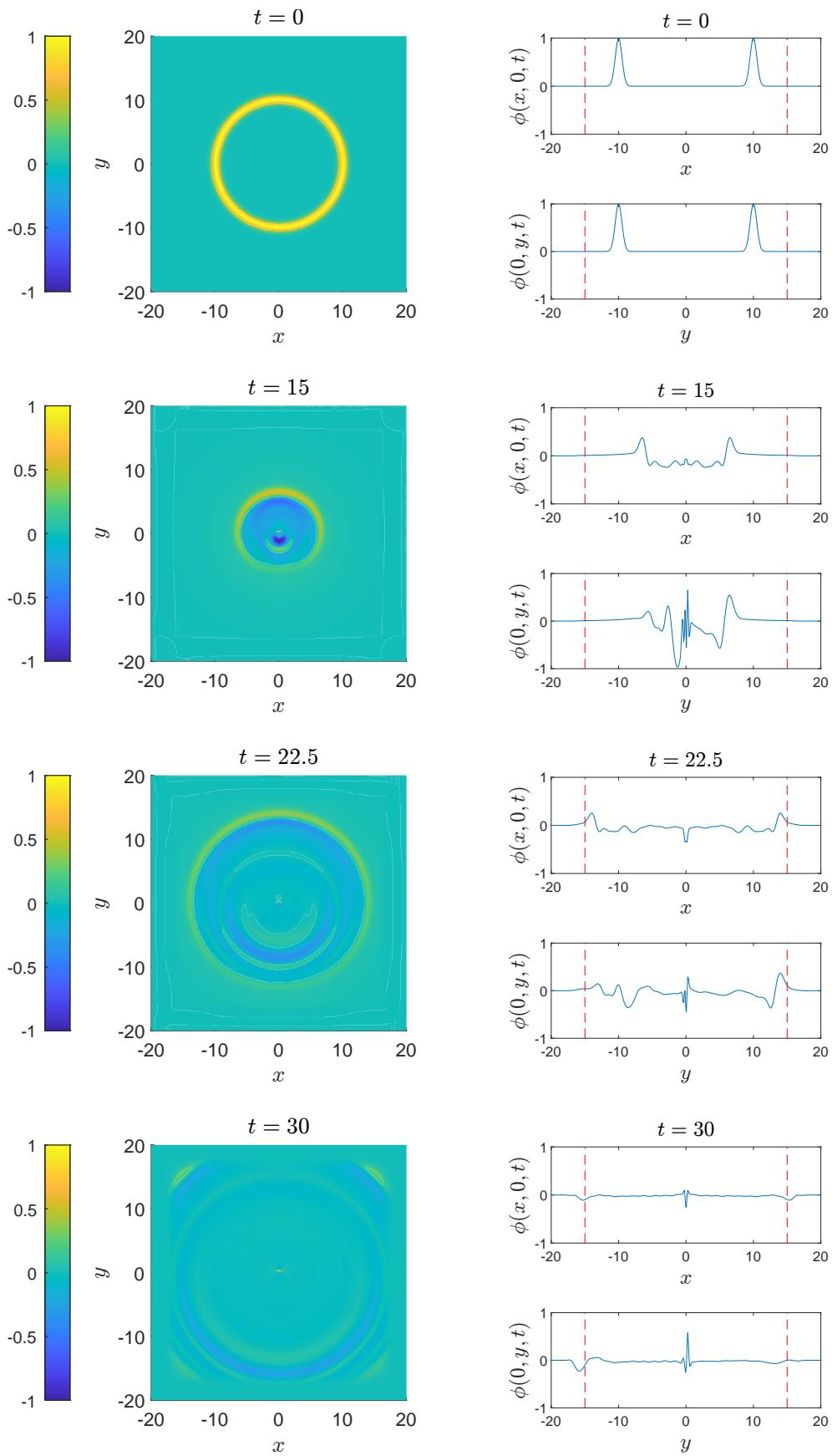
Figure 3.18: Perturbation potential for $F = 0.5$ at different times. Left: contour plot of the solution in the $x-y$ plane. Right: corresponding behaviour along the axes. Red dotted lines indicate where the damping layers begin.

Results for F = 0.75

Finally, we perform computations for $F = 0.75$ and again using the same parameters as in the previous examples. Results are shown in figure 3.19. The primarily thing to be noticed in this case is the occurrence of a stronger instability dictated both by the higher amplitude of the wave (already at a time $t = 30$) and by the highly-oscillatory behaviour of the solution in the core region. We think that this kind of instability could be generated by two different aspects: either a numerical issue due to a poorly resolved solution where the gradients are higher (the core indeed) or to a greater influence of the ergoregion; this is in fact now more extended and complex, as depicted in figure 3.16. In order to check which of the two is the correct reason, we perform a set of convergence studies. The first convergence study aims at increasing the resolution of the numerical solution by reducing the domain size. The second convergence study, instead, involves the addition of an artificial dissipative term into the governing equations.

For the first check test we take $x_0 = y_0 = -5$, $x_f = y_f = 5$ and $x_d = y_d = 4$. The number of grid points has been kept unchanged, i.e. $N_x = N_y = 400$, so that the spatial resolution is increased by four times with respect to the previous case with $x_0 = y_0 = 20$. The amount of damping in both directions has now been taken to be $\bar{\xi}_1 = \bar{\xi}_2 = 50$. The solution has been simulated until a much shorter final time, i.e. $T = 5$. Results are shown in figure 3.20. As can be seen, until approximately $t = 2.5$ the solution is smooth, but as the y-gradient becomes very large, then those little wiggles start appearing again. It is interesting to notice though that the wiggles appear only in the core where the ergoregion actually is present. Based on figure 3.20, the wavelength of these little wiggles can be estimated as $\lambda_w \simeq 0.16$, whereas the grid scale is $\Delta x = 0.025$, hence almost an order of magnitude lower than the wavelength. For such a reason, it seems reasonable to argue that the wiggles are real short waves propagating within the core of the two vortices.

For the second check test, we introduce an artificial viscous term in the governing equation. In particular, taking already the PML formulation—equation (3.62)—we add a diffusive term of the form $\eta \nabla^2 u_2$ in the second
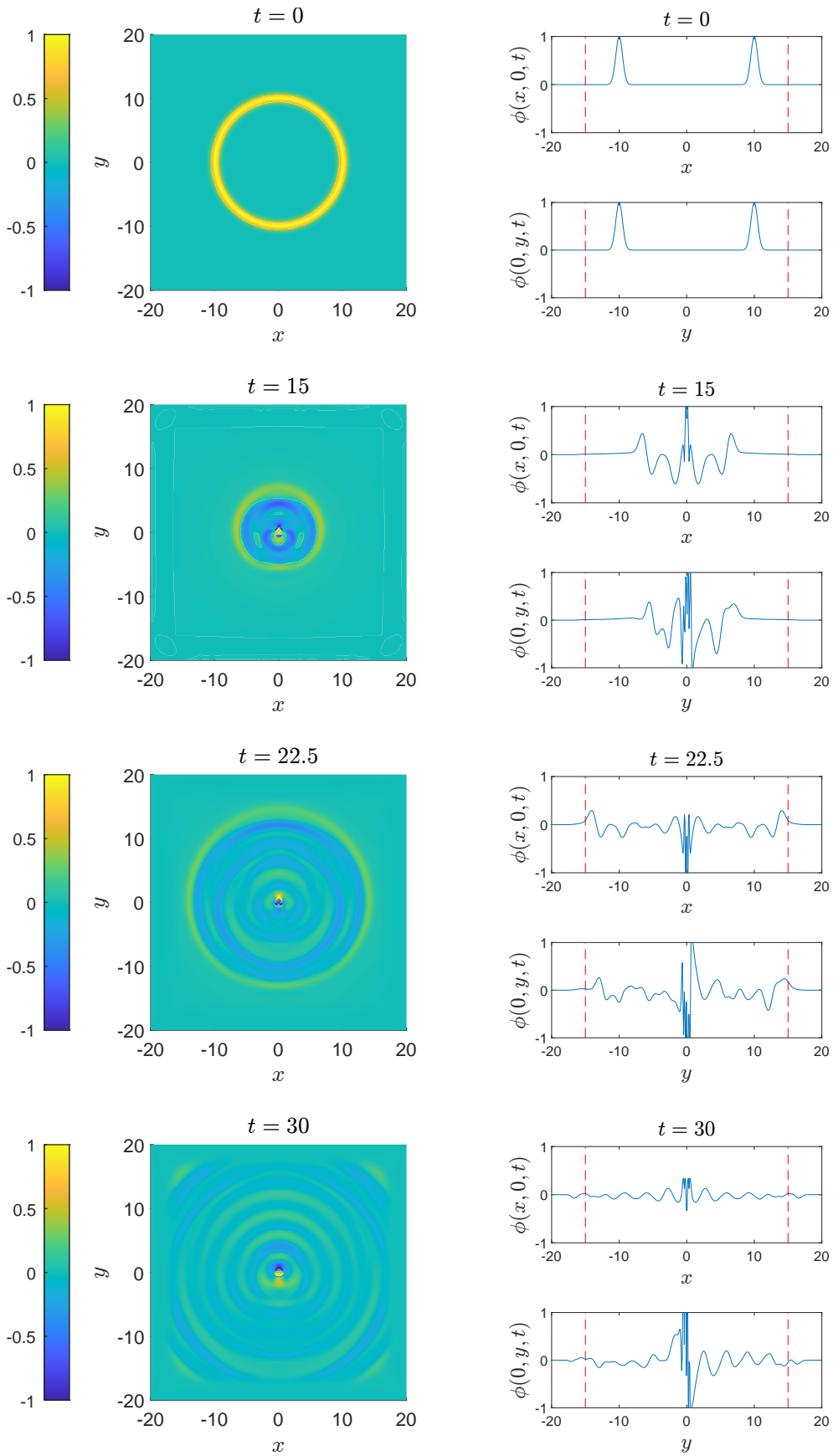
Figure 3.19: Perturbation potential for $F = 0.75$ at different times. Left: contour plot of the solution in the $x-y$ plane. Right: corresponding behaviour along the axes. Red dotted lines indicate where the damping layers begin.
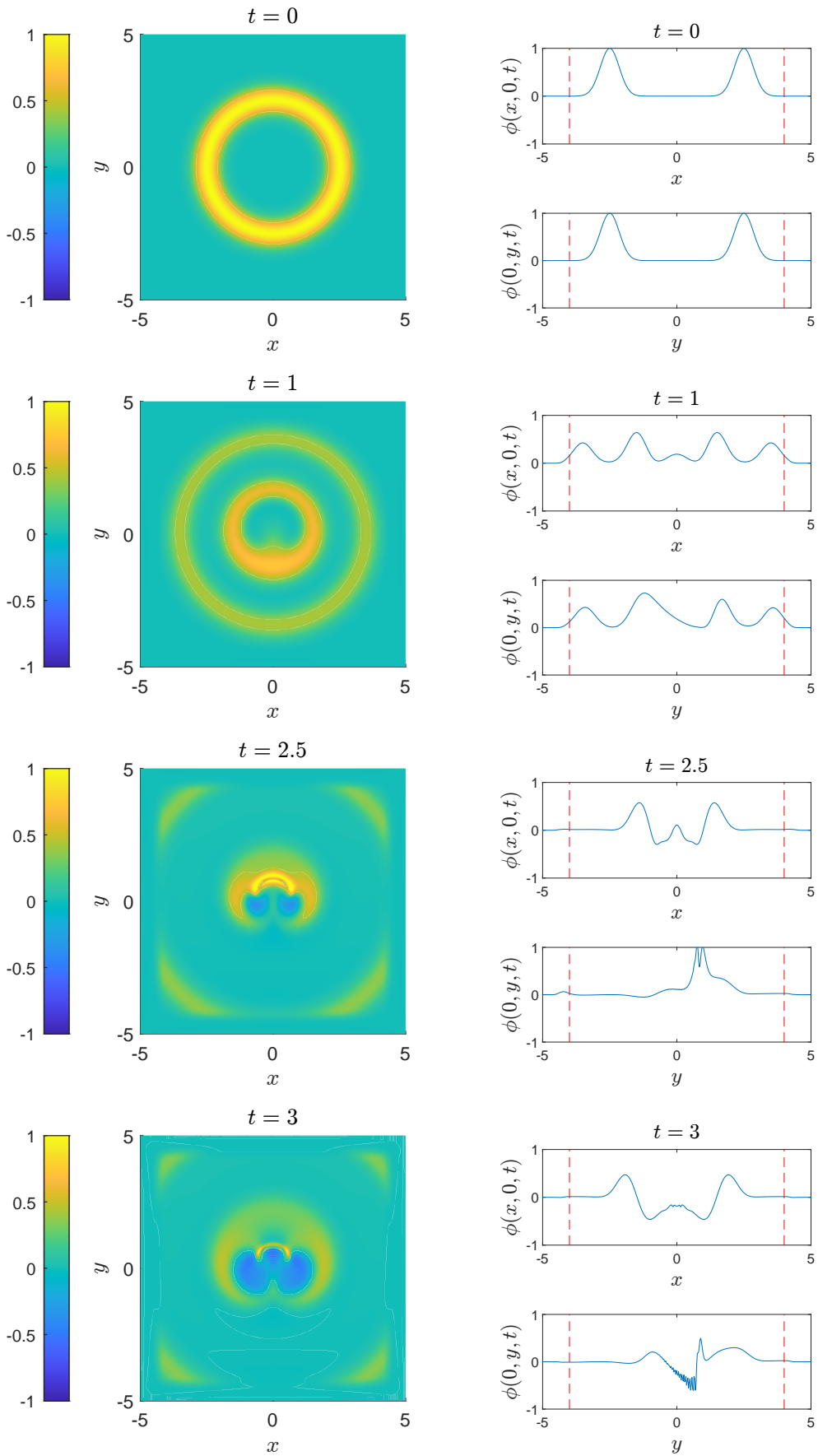
Figure 3.20: Perturbation potential for $F = 0.75$ at different times. The spatial resolution has been increased by four times with respect to the results shown in figure 3.19. Red dotted lines indicate where the damping layers begin.

81

equation, so that the resulting system now reads

$$\frac{\partial u_1}{\partial t} = -FU_0\frac{\partial u_1}{\partial x} - FV_0\frac{\partial u_1}{\partial y} + u_2,$$

$$\frac{\partial u_2}{\partial t} = -FU_0\frac{\partial u_2}{\partial x} - FV_0\frac{\partial u_2}{\partial y} + \left(\frac{\partial^2 u_1}{\partial x^2} + \frac{\partial^2 u_1}{\partial y^2}\right)$$

$$- \xi_1\xi_2 u_1 + F(\xi_1 - \xi_2)U_0\frac{\partial u_1}{\partial x} + F(\xi_2 - \xi_1)V_0\frac{\partial u_1}{\partial y} - (\xi_1 + \xi_2)u_2 + \eta\nabla^2 u_2$$

$$+ \frac{\partial u_3}{\partial x} - F^2 U_0\frac{\partial}{\partial x}\Big(U_0 u_3\Big)$$

$$+ \frac{\partial u_4}{\partial y} - F^2 V_0\frac{\partial}{\partial y}\Big(V_0 u_4\Big),$$

$$\frac{\partial u_3}{\partial t} = -\xi_1 u_3 + (\xi_2 - \xi_1)\frac{\partial u_1}{\partial x},$$

$$\frac{\partial u_4}{\partial t} = -\xi_2 u_4 + (\xi_1 - \xi_2)\frac{\partial u_1}{\partial y}.$$

$$(3.71)$$

We then simulated the problem for two different values of the artificial viscosity $\eta = 0.001$ and $\eta = 0.01$. Results are shown in figures 3.21 and 3.22 respectively. Only for $\eta = 0.01$ the oscillations almost disappear. However, $\eta = 0.01$ is still a high viscosity value and one needs to go further down to $\eta = 10^{-4} - 10^{-6}$ to simulate the inviscid problem using an artificial viscous term. Given that for $\eta = 0.001$ wiggles appear already, we now conclude that these are not numerical artefacts, but real short waves possibly caused by the complexity of the background flow and the implications this has on the structure of the convective wave equation. Such rich dynamics can be further appreciated by looking at the trend of ϕ at higher times; around point $(x, y) = (0, 1)$ something is still going on probably due to the ergoregion influence—figure 3.23). Also, it is possible that the additional presence of a sort of horizon influences the behaviour of these waves too. However, generalization of the definition of an horizon for a non-axisymmetric flow is out of the scope of the present work. Thus, we limit our analysis of the results to the possible influence of the ergoregion which, as shown, can be easily defined for any background flow. We leave to future studies the investigation of the horizon effects on the dynamics of surface waves in the dipolar case and their corresponding numerical implementation.

3.7   Summary

In this chapter we have studied the Convective Wave Equation for both a monopole and a dipole vortex flow. Regarding the monopole case, the particular Lamb-Oseen vortex has been considered and surface waves on that flow have been shown to become unstable beyond a critical Froude number. The instability shown ultimately confirmed the argument on the "ergoregion instability" mechanism proposed in previous studies (Oliveira *et al.* 2014).

Figure 3.21: Perturbation potential for $F = 0.75$ and artificial viscosity $\eta = 0.001$ at different times. Red dotted lines indicate where the damping layers begin.
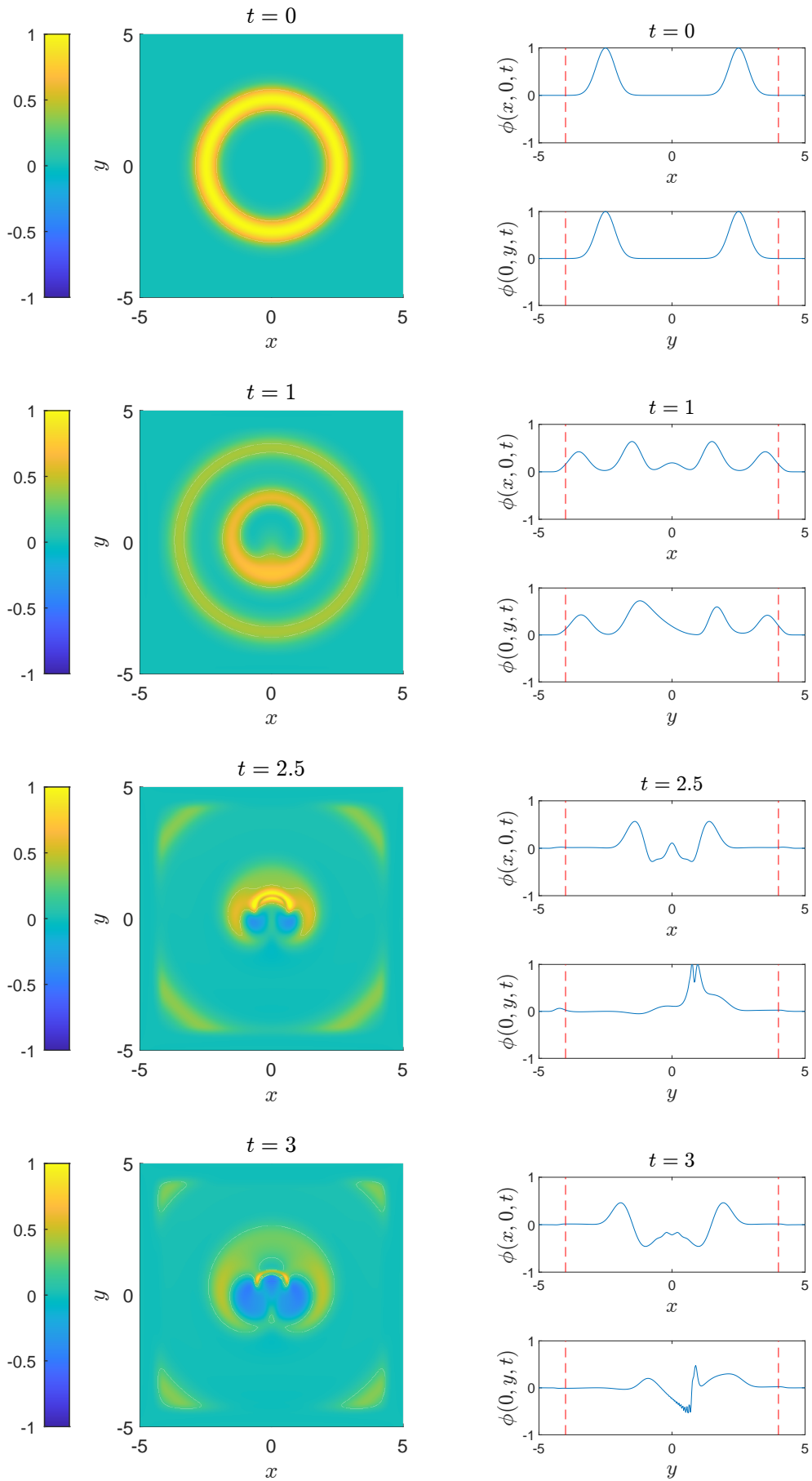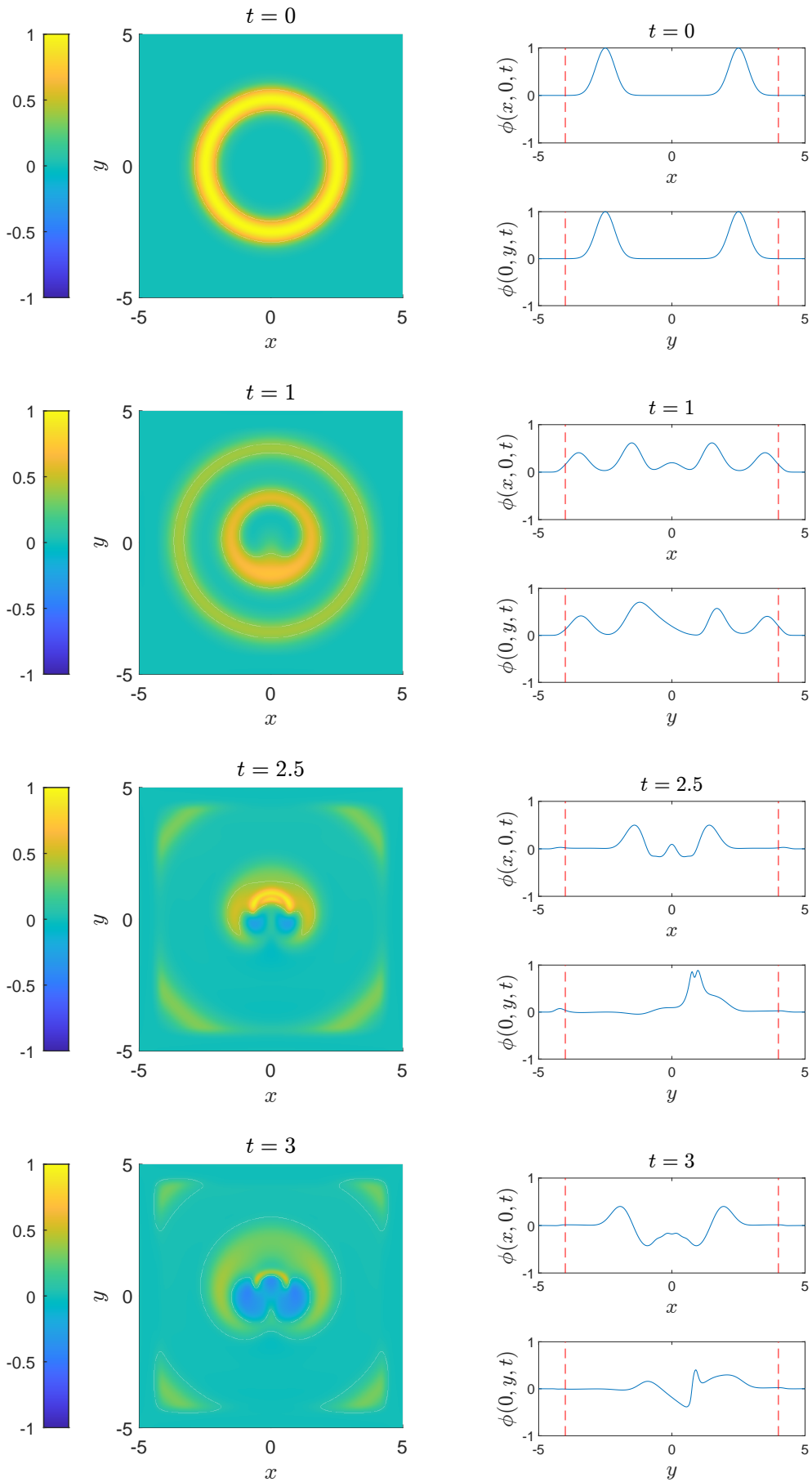
83

Figure 3.22: Perturbation potential for $F = 0.75$ and artificial viscosity $\eta = 0.01$ at different times. Red dotted lines indicate where the damping layers begin.

84
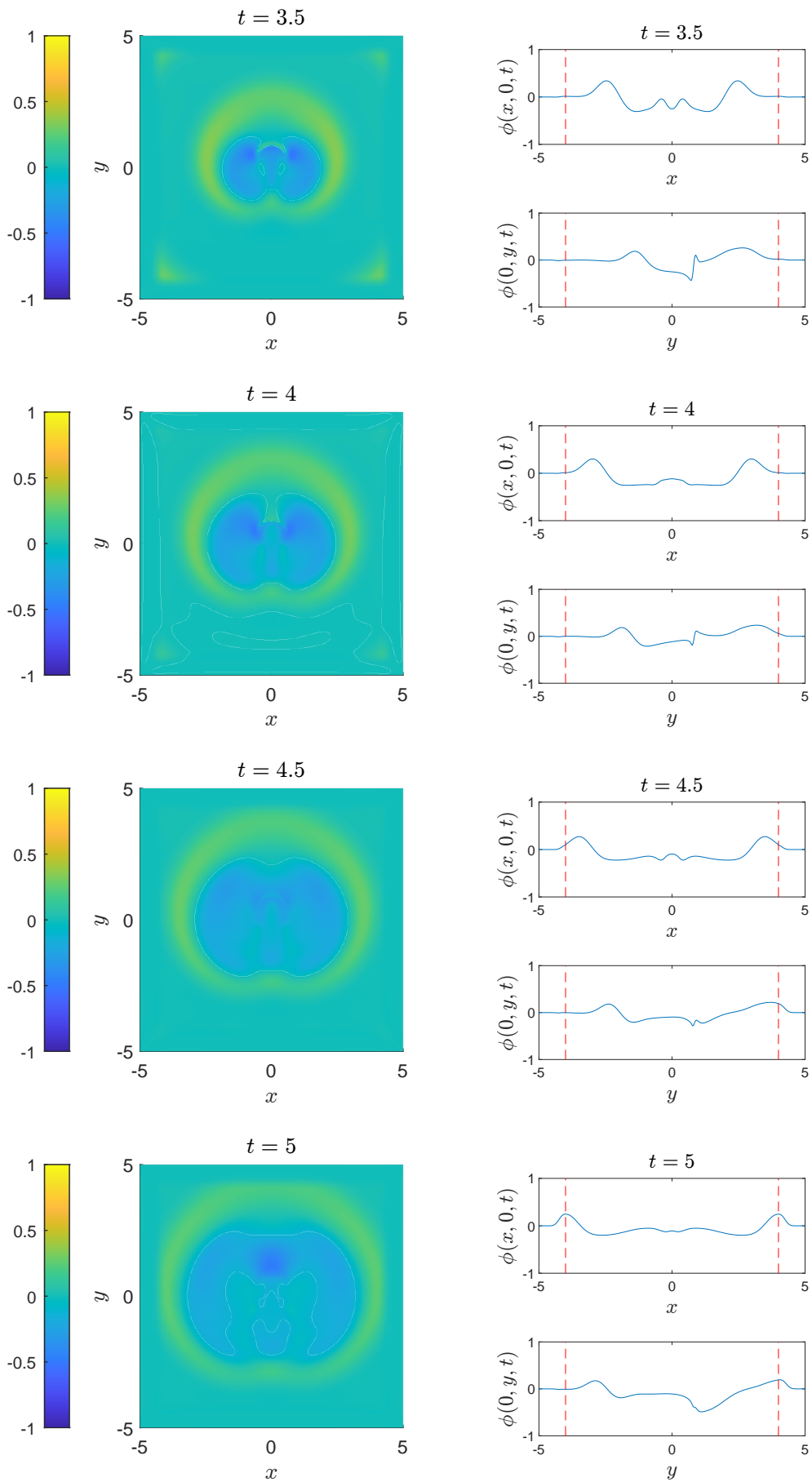
Figure 3.23: Perturbation potential for $F = 0.75$ and artificial viscosity $\eta = 0.01$ up to time $T = 5$. Red dotted lines indicate were the damping layers begin.

85

A toy problem has then been studied in order to obtain a solution in closed-form for the eigenvalue problem. This was particularly useful to get insight into the trend of the eigenvalues as function of the rotation rate of the vortex and link the behaviour of both dissipative and weakly marginally stable modes to the eigenvalues properties.

Finally, the Convective Wave Equation has been studied for Lamb's dipole. A specific PML formulation has been implemented and the problem has been solved by time marching using the method of lines. Solutions have been shown for three specific Froude numbers: $F = 0.25, 0.5, 0.75$. Dissipative waves develop for $F = 0.25$, whereas in the other two cases an instability was presumably found. However, computational costs made the achievement of accurate results impossible. We tried to overcome this difficulty by adding an artificial viscous term into the governing equations which helped in tracking a smooth solution for longer times, but additional study and analysis is still needed to obtain reliable results.

Chapter 4

Waves on unbounded non-shallow-water free surface swirling flows

Motivated by the visualization of trapped surface waves rotating around the core of vortices in the swimming pool (Skipp 2020), in this chapter we extend what has been studied in the previous chapter using the Convective Wave Equation as a prototype model. To do so, we have numerically studied the free-surface response of a Lamb–Oseen vortex to small perturbations in a fluid of finite depth, but laterally unbounded. The numerical method used is spectrally accurate, and uses a novel non-reflecting buffer region to simulate a laterally unbounded fluid. While a variety of linear waves can arise in this system, we focus here on surface gravity waves. We investigate the linear stability of the vortex as a function of the perturbation azimuthal mode number and the vortex rotation rate. While trapped modes have previously been seen in shallow water surface waves, as outlined in chapter 3, the situation considered here is qualitatively different owing to the dispersive nature of non-shallow-water waves. The chapter is organised as follows: in section 4.1, a general description is given of the mathematical model used to study perturbations to a Lamb–Oseen swirling flow in a finite-depth configuration. The mathematical description of an absorbing layer formulation implemented to prescribe the non-reflecting character of the waves, together with the numerical procedure used to solve the corresponding eigenvalue problem is described in section 4.2. The results of this numerical solutions are described in section 4.3 and 4.4.

The material presented in this chapter has been submitted to the Journal of Fluid Mechanics and it is currently under review. The corresponding ArXiv link follows: `https://arxiv.org/abs/2209.14011`

4.1 Mathematical Model

Assuming that viscosity is negligible over the timescales of interest here, the governing equations are the incompressible Euler equations,

$$\frac{\partial \boldsymbol{U}}{\partial t} + \boldsymbol{U} \cdot \boldsymbol{\nabla} \boldsymbol{U} + \frac{1}{\rho} \boldsymbol{\nabla} P + g\hat{\boldsymbol{z}} = 0, \qquad \boldsymbol{\nabla} \cdot \boldsymbol{U} = 0, \qquad (4.1)$$

where $\boldsymbol{U}$ is the fluid velocity, P is the fluid pressure, $\hat{\boldsymbol{z}}$ is a unit vector in the vertical direction, and the constants ρ and g are the fluid density and the acceleration due to gravity respectively. The fluid is contained between a bottom boundary at $z = 0$ and an upper free surface at $z = H$. The fluid must satisfy no penetration through the bottom boundary, giving $\boldsymbol{U} \cdot \hat{\boldsymbol{z}} = 0$ at $z = 0$. Two boundary conditions, a kinematic and a dynamic boundary condition, must be satisfied along the free surface itself. Here, we assume the fluid above the free surface to be dynamically passive, and in particular, to have a constant pressure $\bar{P}$. Together, these give the boundary conditions

$$\frac{\partial H}{\partial t} + \boldsymbol{U} \cdot \boldsymbol{\nabla} H = \boldsymbol{U} \cdot \hat{\boldsymbol{z}} \qquad \text{and} \qquad P = \bar{P} \qquad \text{on} \qquad z = H. \qquad (4.2)$$

We split the overall velocity and pressure into a steady purely swirling base flow and a small (magnitude ε) time-dependent perturbation, where

$$\boldsymbol{U} = U_0(r)\hat{\boldsymbol{\theta}} + \varepsilon(u_r\hat{\boldsymbol{r}} + u_\theta\hat{\boldsymbol{\theta}} + u_z\hat{\boldsymbol{z}}), \quad P = P_0(r,z) + \varepsilon p, \quad H = h_0(r) + \varepsilon h. \tag{4.3}$$

4.1.1 The steady base flow solution

A purely swirling steady base flow has a velocity given by $\boldsymbol{U_0} = U_0(r)\hat{\boldsymbol{\theta}}$. The governing equations and boundary conditions for this steady flow are satisfied provided we take

$$P_0(r,z) = \bar{P} + \rho g \left(h_0(r) - z \right), \tag{4.4a}$$

$$h_0(r) = h_\infty - \frac{1}{g} \int_r^\infty \frac{U_0^2(r')}{r'} \, \mathrm{d}r', \tag{4.4b}$$

where h_∞ is the depth of the fluid at $r = \infty$. This holds for any velocity profile $U_0(r)$. For the specific case of the Lamb–Oseen vortex considered here, we have

$$U_0(r) = \frac{\Gamma_0}{2\pi r} \left(1 - \exp\left(-r^2/a^2 \right) \right), \tag{4.5}$$

where a sets the radial size of the core and Γ_0 sets the circulation of the vortex. Note that, for the Lamb–Oseen vortex, for small r, we have $U_0(r) \approx r\Gamma_0/2\pi a^2$, so that (4.5) is a solid body rotation near the centre of the vortex, while for large r we have $U_0(r) \approx \Gamma_0/2\pi r$, so that (4.5) is a potential swirl far from the centre of the vortex. A typical steady base flow free surface for the Lamb–
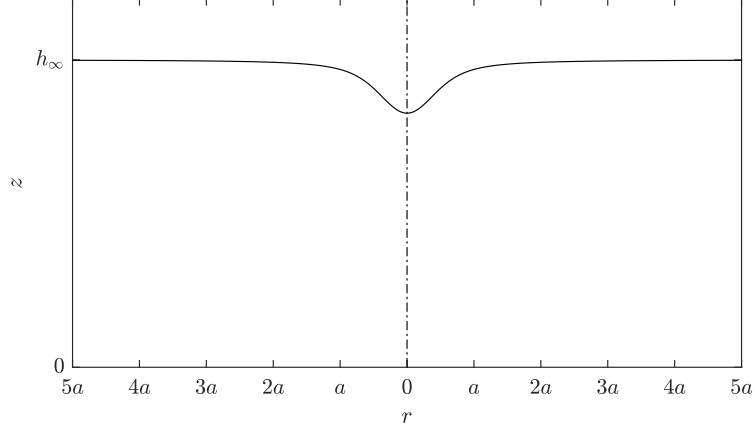
Figure 4.1: A typical section through a Lamb–Oseen vortex, showing the steady base flow free surface.

Oseen vortex is shown in figure 4.1.

4.1.2 Perturbation Dynamics

Waves arise when a small perturbation is introduced to the steady base solution. By linearizing the governing equations (4.1) about the base solution (U_0, P_0, h_0) given above, the governing equations for the perturbation are

$$D_t u_r - 2\Omega_0(r)u_\theta + \frac{1}{\rho}\frac{\partial p}{\partial r} = 0, \tag{4.6a}$$

$$D_t u_\theta + \frac{1}{r}\big(rU_0(r)\big)' u_r + \frac{1}{\rho r}\frac{\partial p}{\partial \theta} = 0, \tag{4.6b}$$

$$D_t u_z + \frac{1}{\rho}\frac{\partial p}{\partial z} = 0, \tag{4.6c}$$

$$\frac{1}{r}\frac{\partial}{\partial r}\left(ru_r\right) + \frac{1}{r}\frac{\partial u_\theta}{\partial \theta} + \frac{\partial u_z}{\partial z} = 0, \tag{4.6d}$$

where $D_t = \partial_t + \Omega_0(r)\partial_\theta$ is the convective derivative and $\Omega_0(r) = U_0(r)/r$ is the steady base flow angular velocity. (Here and throughout, primes denotes derivatives with respect to the argument for a function of only one variable). Linearizing the boundary conditions (4.2) about the steady base flow leads to

$$u_z = \frac{1}{\rho g}D_t p + h_0' u_r \quad \text{and} \quad h = \frac{p}{\rho g} \quad \text{on} \quad z = h_0(r), \tag{4.7a}$$

$$u_z = 0 \quad \text{on} \quad z = 0. \tag{4.7b}$$

Since our focus is on trapped waves and their formation, in addition to these boundary conditions there is another implicit condition, which is that there are no waves entering the domain from $r = \infty$, and thus only outgoing waves are allowed at $r = \infty$. This rather subtle condition will become more concrete when we truncate the domain to finite r in order to numerically solve

89

the above equations.

Before we progress further, we now make two changes to the governing equations for the perturbation. Firstly, since the governing equations for the perturbation are linear, we may assume a modal solution of the form

$$\boldsymbol{u} = \left[u(r,z)\hat{\boldsymbol{r}} + v(r,z)\hat{\boldsymbol{\theta}} + w(r,z)\hat{\boldsymbol{z}} \right] \exp(-\mathrm{i}\omega t + \mathrm{i}m\theta), \qquad (4.8a)$$

$$p = \phi(r,z)\exp(-\mathrm{i}\omega t + \mathrm{i}m\theta), \qquad (4.8b)$$

where m is restricted to integer values, since the solution must be 2π periodic, while ω in general will be complex, with $\mathrm{Re}(\omega)/2\pi$ being the oscillation frequency and $-\mathrm{Im}(\omega)$ being the decay rate. The eigenvalue problem that will eventually result will have ω as the eigenvalue to be found.

Secondly, we re-write the governing equations and boundary conditions in a non-dimensional form. To do so, we choose the reference lengthscale to be a, the scale of the vortex core (equation (4.5) and figure 4.1). The reference time scale is that given by this lengthscale and gravity: $\sqrt{a/g}$. The velocity scale is thus $\sqrt{ag}$. All dimensional variable may then be expressed in terms of a nondimensional variable (denoted by a tilde), as

$$(r,\theta,z) = (a\tilde{r}, \tilde{\theta}, a\tilde{z}), \qquad t = \sqrt{\frac{a}{g}}\tilde{t}, \qquad U_0(r) = \frac{\Gamma_0}{2\pi a}\tilde{U}_0(\tilde{r}), \qquad \Omega_0 = \frac{\Gamma_0}{2\pi a^2}\tilde{\Omega}_0,$$

$$h = a\tilde{h}, \qquad p = \rho a g \tilde{p}, \qquad \omega = \sqrt{\frac{g}{a}}\tilde{\omega}, \qquad \boldsymbol{u} = \sqrt{ag}\tilde{\boldsymbol{u}}.$$

$$(4.9)$$

There are two physical parameters that are not scaled to unity by this nondimensionalization: these may be thought of as the strength of the vortex and the depth of the fluid at infinity, given respectively as

$$F = \frac{\Gamma_0}{2\pi\sqrt{ga^3}}, \qquad\qquad \tilde{h}_\infty = \frac{h_\infty}{a}. \qquad (4.10)$$

F is the Froude number and sets the nondimensionalized velocity of the vortex. Hence, $F \to 0$ corresponds to a slow vortex with negligible steady surface height variation, while $F \to \infty$ corresponds to a fast vortex with significant steady surface height variation, as can be seen from $(4.13c)$ below. The dimensionless depth $\tilde{h}_\infty$ is exactly that, so that the limit $\tilde{h}_\infty \to 0$ corresponds to the shallow-water limit and $\tilde{h}_\infty \to \infty$ corresponds to the deep-water limit. Care is needed, however, in considering the shallow-water limit: in what follows, we will assume that the steady fluid height never reaches zero, so that the bottom stays wetted, and consequently the shallow water limit $\tilde{h}_\infty \to 0$ must be taken together with the slow wide vortex limit $F \to 0$ such that $\tilde{h}_\infty/F^2$ is bounded away from zero, as can also be seen from (4.13) below. The azimuthal wavenumber m is also a dimensionless parameter, and represents the rotational symmetry of the solution being investigated.

Dropping the tildes, the complete nondimensional eigenvalue problem is

$$\big(-\mathrm{i}\omega + \mathrm{i}mF\Omega_0(r)\big)u - 2F\Omega_0(r)v + \frac{\partial\phi}{\partial r} = 0, \qquad (4.11a)$$

$$\big(-\mathrm{i}\omega + \mathrm{i}mF\Omega_0(r)\big)v + \frac{F}{r}\big(rU_0(r)\big)'u + \frac{\mathrm{i}m}{r}\phi = 0, \qquad (4.11b)$$

$$\big(-\mathrm{i}\omega + \mathrm{i}mF\Omega_0(r)\big)w + \frac{\partial\phi}{\partial z} = 0, \qquad (4.11c)$$

$$\frac{1}{r}\frac{\partial}{\partial r}\big(ru\big) + \frac{\mathrm{i}m}{r}v + \frac{\partial w}{\partial z} = 0, \qquad (4.11d)$$

together with the boundary conditions of no incoming modes at $r = \infty$, and

$$w = 0, \qquad\qquad\qquad\qquad \text{on} \quad z = 0, \qquad (4.12a)$$

$$w = \big(-\mathrm{i}\omega + \mathrm{i}mF\Omega_0(r)\big)\phi + F^2 r\Omega_0^2(r)u, \qquad \text{on} \quad z = h_0(r). \qquad (4.12b)$$

For the Lamb–Oseen vortex, in dimensionless terms

$$U_0(r) = \frac{1 - \exp(-r^2)}{r}, \quad \Omega_0(r) = \frac{U_0(r)}{r}, \quad h_0(r) = h_\infty - F^2\int_r^\infty \frac{U_0^2(r')}{r'}\,\mathrm{d}r'.$$
$$(4.13a, b, c)$$

One consequence of the harmonic assumption (4.8) is the creation of a so-called "critical layer", i.e. a radial location $r = r_c$ where the background flow resonates with the waves, namely $mF\Omega_0(r_c) - \omega = 0$. It is not immediately obvious from (4.11) that anything particularly special occurs at the critical layer, as in no equation does it cause the highest derivative to vanish, and therefore our numerics described in §4.2 has no difficulty in this case. However, in fact the critical layer is related to behaviour that is not of the harmonic form assumed in (4.8); investigating the effect of the critical layer requires a different mathematical and numerical technique (such as Frobenius series; see, by way of example, King *et al.* 2022), which is beyond the scope of this thesis. However, we comment in passing that Fabre *et al.* (2006) found that disturbances related to the critical layer are necessarily damped, suggesting that the undamped trapped wave modes we are interested in here are not related to the critical layer.

4.2 Numerical methods

4.2.1 Absorbing layer for 3D incompressible Euler equations

In practice, we solve the eigenvalue problem in a finite computational domain and hence introduce an artificial boundary at finite radius R. The far-field boundary condition of no incoming waves becomes a non-reflecting boundary condition (NRBC) at this boundary. However, exact NRBCs are generally derived using the method of characteristics, but this is not available to us
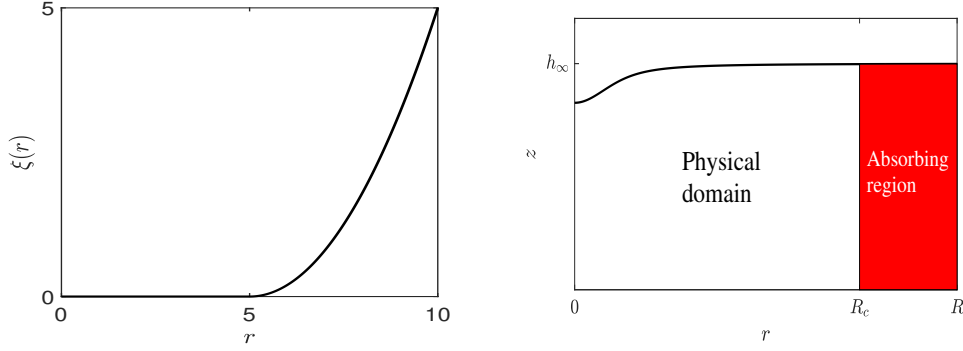
Figure 4.2: Left: profile of the quadratic damping function defined in (4.15) with parameters: $\bar{\xi} = 5$, $R_c = 5$ and $R = 10$. Right: schematic of the computational domain in the $r - z$ plane.

since (4.11d) is not hyperbolic. A widely used alternative is based on damping layers or even perfectly matched layers, as discussed in chapter 3. Here we damp waves only in the radial direction. In particular, in order to provide the damping character of the waves in the lateral absorbing region, we add a "damped compressibility" term into the continuity equation (4.11d), which then becomes

$$\xi(r)\phi + \frac{1}{r}\frac{\partial}{\partial r}(ru) + \frac{im}{r}v + \frac{\partial w}{\partial z} = 0. \tag{4.14}$$

where $\xi(r)$ is a sufficiently smooth function that is identically zero outside the damping region. This is motivated by the introduction of damping in the acoustic wave equation following Gao *et al.* (2017, pp. 81-82), and is explained in further detail in the next subsection. In what follows, we find good results using the simple form for $\xi(r)$ given by

$$\xi(r) = \begin{cases} 0, & r < R_c, \\ \bar{\xi}\left(\dfrac{r - R_c}{R - R_c}\right)^2, & R_c \leq r \leq R. \end{cases} \tag{4.15}$$

This gives a physical region, $r < R_c$, with no damping, and computational region $r \in [R_c, R]$ with a damping strength governed by the constant $\bar{\xi}$. We then impose a Dirichlet boundary condition on the pressure at an artificial boundary $r = R \gg 1$. A representation of the damping function as well as the subdivision of the numerical domain is shown in figure 4.2.

The governing equations (4.11*a–c*) together with the modified continuity equation (4.14) and boundary conditions (4.12) form an eigenvalue problem to solve for the allowable frequencies ω permitting a nonzero modal solution.

Rational derivation of the absorbing layer formulation

In the previous section 4.2.1, the continuity equation was modified by the introduction of the "damped compressibility" term $\xi(r)\phi$ in equation (4.14) in

α	0	10^{-4}	10^{-2}	10^{-1}	1
$\text{Re}(\omega)$	-1.3769	-1.3769	-1.3759	-1.3662	-1.2711
$\text{Im}(\omega)$	-0.0138	-0.0138	-0.0139	-0.0147	-0.0241

Table 4.1: Eigenvalues as function of the compressibility $\alpha = \frac{1}{c^2}$ for a radiating mode, for $m = 7$, and $F = 0.3$.

order to emulate an infinite domain using our finite computational domain, by damping out disturbances as they reach the unphysical computational boundary at $r = R$. Here, we justify the inclusion of that term by analogy with the equations of acoustics.

Small (linear) homentropic perturbations $(\boldsymbol{u}, p, \rho)$ to a static fluid $(\boldsymbol{0}, p_0, \rho_0)$ are governed by the linearized Euler Equations:

$$\rho_0 \frac{\partial \boldsymbol{u}}{\partial t} + \nabla p = 0, \qquad \frac{1}{c^2}\frac{\partial p}{\partial t} + \rho_0 \nabla \cdot \boldsymbol{u} = 0, \qquad p = c^2 \rho, \qquad (4.16)$$

where c is the speed of sound. These can be combined into a single wave equation for the pressure,

$$\frac{1}{c^2}\frac{\partial^2 p}{\partial t^2} - \nabla^2 p = 0. \qquad (4.17)$$

Following Gao *et al.* (2017, pp. 81-82), in order to introduce a sponge layer to damp outgoing waves, we add a damping term of the form $\xi(r)\partial_t p$ into the wave equation (4.17),

$$\frac{1}{c^2}\frac{\partial^2 p}{\partial t^2} + \xi(r)\frac{\partial p}{\partial t} - \nabla^2 p = 0. \qquad (4.18)$$

This wave equation can be split back into the original physical mass- and momentum-equations in the original physical variables $(\boldsymbol{u}, p, \rho)$ as

$$\rho_0 \frac{\partial \boldsymbol{u}}{\partial t} + \nabla p = 0, \qquad \frac{1}{c^2}\frac{\partial p}{\partial t} + \xi(r)p + \rho_0 \nabla \cdot \boldsymbol{u} = 0, \qquad p = c^2 \rho, \qquad (4.19)$$

If we now take the incompressible limit $1/c^2 \to 0$ in system (4.19), we obtain the modified continuity equation (4.14) introduced in section 4.2.1.

Figure 4.3 and table 4.1 show the effect of the compressibility $\alpha = 1/c^2$ on the structure of the radiating eigenmode and the eigenvalue respectively, for parameters $m = 7$ and $F = 0.3$. From both, it is clear that the eigenmode computed does not vary significantly as $\alpha \to 0$, and so we conclude that the damping properties of the $\xi(r)p$ term are carried over in the limit $\alpha \to 0$.

4.2.2 Numerical discretization

In order to solve (4.11a–c,4.12,4.14), we used a Galerkin spectral method as done in section 2.4 for the Newton's bucket problem. The differences here
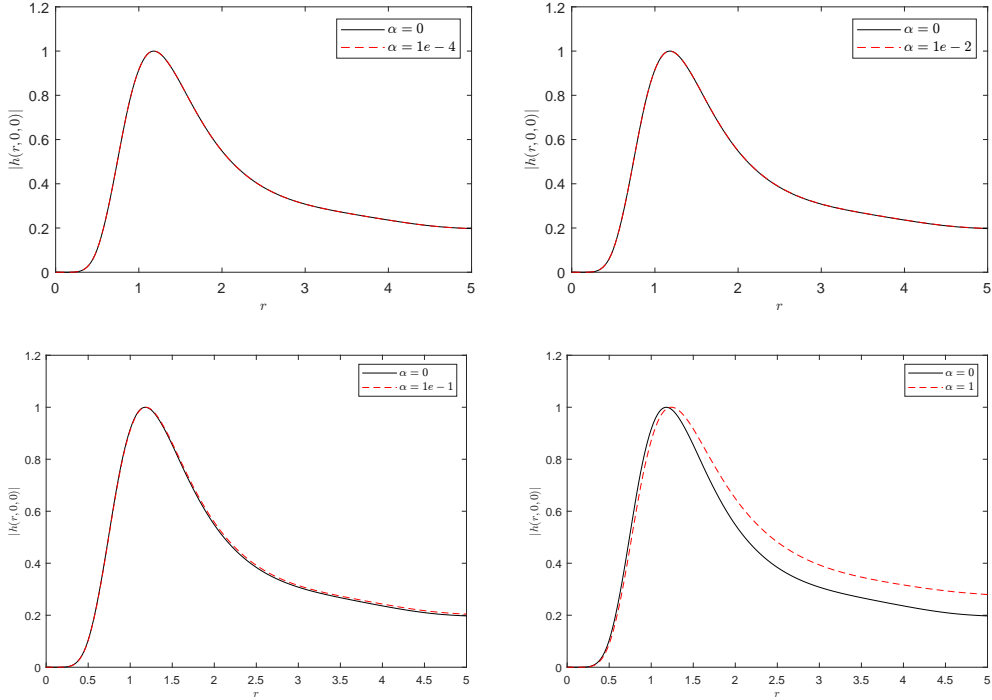
Figure 4.3: Comparison of the structure of the eigenmode $|h(r, 0, 0)|$ for $m = 7$, $F = 0.3$ and different value of the compressibility $\alpha = 1/c^2$.

are given by the Dirichlet boundary condition on the pressure (and not on the velocity) $\phi(r = R, z) = 0$ on one hand, and by the basis functions that are chosen to satisfy the Dirichlet boundary conditions on the other. We also remap the domain from the domain $D = [0, R] \times [0, h_0(r)]$ to the computational square domain $S = [-1, 1] \times [-1, 1]$ to account for the shape of the computational domain with a variable surface height $h_0(r)$. We then obtain the weak formulation of the problem as in section 2.4.1. Details are given below.

Discrete problem for non-axisymmetric perturbations

In the general case of a nonzero value of m, the weak formulation of the eigenvalue problem can be obtained in the following way. First of all, we notice the presence of singular terms at $r = 0$ for u, v, ϕ so we will require these function to be null at the origin. Consequently, even w will be so. Thus, we look at the unknowns in the following spaces:

$$[u, v, \phi] \in V_H(S) = \{(u, v, \phi) \in H^1(S) : (u, v, \phi) = 0, \quad at \quad r = 0\}, \quad \text{(4.20a)}$$

$$w \in V_v(S) = \{w \in H^1(S) : w = 0, \quad at \quad r = 0, \quad z = 0\}, \quad \text{(4.20b)}$$

where $H^1(S)$ is the usual Sobolev space (Quarteroni 2009, ch. 2). We multiply the azimuthal component of the momentum equation and the continuity equation by $(x + 1)$. Then, by multiplying each of the equations by suitable test functions (v_x, v_t, v_y, q) in the same space as the corresponding

94

unknowns, after integrating over the square S and exploiting the boundary conditions, the weak formulation of the differential problem reads: find $([u, v, \phi], w) \in V_H(S) \times V_v(S)$ such that $\forall([v_x, v_t, q], v_y) \in V_H(S) \times V_v(S)$ the following holds:

$$\int_S v_x \mathrm{im} F \Omega_0(x) u - \int_S v_x 2F \Omega_0(x) v - \int_S \frac{2}{R} \frac{\partial v_x}{\partial x} \phi - \int_S v_x \frac{2}{R} \frac{h_0'(x)}{h_0(x)} (y+1) \frac{\partial \phi}{\partial y} = \mathrm{i}\omega \int_S v_x u, \tag{4.21a}$$

$$\int_S v_t \left[\mathrm{im} F \Omega_0(x)(x+1)v + \frac{2F}{R}[(x+1)U_0(x)]u + \frac{2\mathrm{im}}{R}\phi \right] = \mathrm{i}\omega \int_S v_t(x+1)v, \tag{4.21b}$$

$$\int_S v_y \left[\mathrm{im} F \Omega_0(x) w + \frac{2}{h_0(x)} \frac{\partial \phi}{\partial y} \right] = \mathrm{i}\omega \int_S v_y w, \tag{4.21c}$$

$$\int_S \frac{2}{R} q \frac{\partial}{\partial x}[(x+1)u] + \int_S \frac{2}{R} \frac{h_0'(x)}{h_0(x)}(x+1) \left[qu + \frac{\partial q}{\partial y} u \right] + \int_S \frac{2\mathrm{im}}{R} qv$$
$$- \int_S \frac{2}{h_0(x)}(x+1) \frac{\partial q}{\partial y} w + \int_{x=-1}^{x=1} \frac{2\mathrm{im} F(x+1)\Omega_0(x)}{h_0(x)} q(x,1)\phi(x,1) \tag{4.21d}$$
$$= \mathrm{i}\omega \int_{x=-1}^{x=1} \frac{2(x+1)}{h_0(x)} q(x,1)\phi(x,1).$$

Let us define the bilinear forms $\mathcal{A} : V_H \times V_v \to \mathbb{R}$ and $\mathcal{B} : V_H \times V_v \to \mathbb{R}$ such that the generalised eigenvalue problem above can be compactly written as: find $([u, v, \phi], w) \in V_H \times V_v$ such that

$$\mathcal{A}([\boldsymbol{u}, \phi], [\boldsymbol{v}, q]) = \omega \mathcal{B}([\boldsymbol{u}, \phi], [\boldsymbol{v}, q]), \quad \forall([v_x, v_t, q], v_y) \in V_H \times V_v \tag{4.22}$$

At this point, in order to discretize the problem, we need to expand the unknowns in terms of proper basis functions. Such basis functions are taken in such a way the homogeneous Dirichlet boundary conditions are automatically satisfied in both the axial and radial coordinates. In particular, we define the following set of polynomials, $P_n^\star(x)$ as follows:

$$P_n^\star(x) = P_n(x) + P_{n-1}(x), \quad n \geq 1, \tag{4.23}$$

where $P_n(x)$ are standard Legendre polynomials. Thanks to the above definition, a Dirichlet boundary condition at $x = -1$ is automatically satisfied. Therefore, we expand the velocity components and the pressure as

$$[u, v, \phi](x, y) = \sum_{i=1}^{N_x} \sum_{j=1}^{N_y} [u_{ij}, v_{ij}, \phi_{ij}] P_i^\star(x) P_j(y),$$
$$w(x, y) = \sum_{i=1}^{N_x} \sum_{j=1}^{N_y} w_{ij} P_i^\star(x) P_j^\star(y). \tag{4.24}$$

After substituting the expansion into the weak formulation (4.22), the discretized problem ends up being of the form

$$\boldsymbol{A}\boldsymbol{w} = \omega\boldsymbol{B}\boldsymbol{w}, \tag{4.25}$$

with $\boldsymbol{w} = (u_{ij}, v_{ij}, w_{ij}, \phi_{ij})$ representing our array containing the spectral coefficients of each unknown, $\boldsymbol{A}$ and $\boldsymbol{B}$ being matrices of order $4N_x N_y \times 4N_x N_y$, where N_x and N_y are the number of Legendre polynomials used in the radial and vertical directions respectively. This discretized problem may then be solved using any numerical eigenvalue solver; here, we use the `eig` solver in MATLAB. Not all solutions to the discretized problem (4.25) correspond to solutions to the continuous problem being approximated, however. To remove under-resolved eigenmodes and spurious eigenvalues, the numerical solutions are filtered, as described here below.

Discrete problem for axisymmetric perturbations

In the axisymmetric case $(m = 0)$, the differential problem over the square S simplifies, and it can be noted that only the radial component of the velocity must go to zero as $r \to 0$, with the other unknowns allowed to take any finite value. Thus, studying the axisymmetric perturbation problem means to look for the eigensolutions in the following spaces: $u \in V_H(S)$, $(v, \phi) \in H^1(S)$ and $w \in V_{v0} = \{w \in H^1(S) : w = 0, \quad at \quad z = 0\}$. The weak formulation is then obtained as shown previously. Regarding the discretization process, we express the four unknowns (and corresponding test functions) as follows

$$u(x, y) = \sum_{i=1}^{N_x} \sum_{j=1}^{N_y} u_{ij} P_i^\star(x) P_j(y),$$

$$[v, \phi](x, y) = \sum_{i=1}^{N_x} \sum_{j=1}^{N_y} [v_{ij}, \phi_{ij}] P_i(x) P_j(y), \tag{4.26}$$

$$w(x, y) = \sum_{i=1}^{N_x} \sum_{j=1}^{N_y} w_{ij} P_i(x) P_j^\star(y).$$

After substitution into the weak formulation, in a similar way to the previous non-axisymmetric case, the resulting algebraic generalised eigenproblem is obtained.

4.2.3 Spurious numerical modes and resolvedness conditions

In order to get rid of unresolved spectral modes we used the same strategy adopted in section 2.4.1 for the Newton's Bucket problem. For the results computed in this chapter, however, we set $N_x = 50$, $N_y = 20$, $b_x = 12$, and $b_y = 4$, tol $= 10^{-1}$.
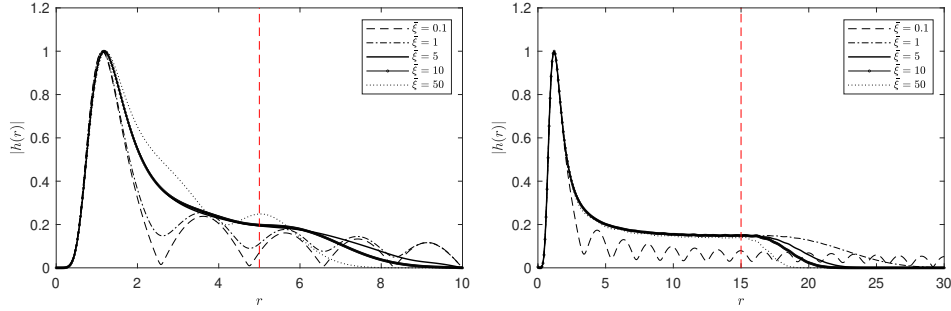
Figure 4.4: Eigenfunctions for $m = 7$, $F = 0.3$, and different values of $\bar{\xi}$. A vertical red-dashed line indicates the radial point R_c where the damping effect begins. Left: a small computational domain $R_c = 5$, $R = 10$. Right: a large computational domain $R_c = 15$, $R = 30$.

4.2.4 Spurious reflected modes

The finite numerical domain and damping region introduces another source of spurious modes besides those coming from the numerical discretization, namely those modes which are well-resolved but which include a significant reflection from either the damping boundary at $r = R_c$ or the truncation boundary at $r = R$. Such spurious eigenmodes are affected by the values of R_c and R, and by the amount of damping $\bar{\xi}$, whereas good approximations to the modes on the infinite domain should be insensitive to these values. Since $-\text{Im}(\omega)$ is the decay rate of the mode, variations in damping typically have a strong effect on $\text{Im}(\omega)$ for spurious reflected modes. We may therefore remove these spurious reflected modes by running our numerical code twice: the first time with a suitably chosen amount of damping $\bar{\xi}$, and the second time with twice that amount of damping $2\bar{\xi}$. Only those modes whose eigenvalues do not change significantly with the change in the damping coefficient are retained (as measured using the same tolerance used for the numerical resolution).

4.2.5 Numerical convergence study

The first convergence study involves varying the amount of damping in the damping layer and checking that the eigenvalues do not change, nor does the shape of the corresponding eigenfunctions in the physical domain $r < R_c$. Here we present the convergence results for $m = 7$ and $F = 0.3$, since for these parameters the system supports radiating (outwardly propagating) modes, and such modes provide the most stringent test of a non-reflecting boundary condition. For varying magnitudes of damping $\bar{\xi}$, the radiating eigenfunction is plotted in figure 4.4, and the corresponding eigenvalues are given in table 4.2. Two domain sizes are shown in figure 4.4: $R_c = 5$ and $R = 10$ are the values used for the results in section §4.3; and $R_c = 15$ and $R = 30$ give an extended domain so that the effects of damping and resonance can be seen more clearly. The damping clearly influences the eigenfunction

97

$\bar{\xi}$	0.1	1	5	10	50
$\mathrm{Re}(\omega)$	-1.3911	-1.3894	-1.3766	-1.3769	-1.3688
$\mathrm{Im}(\omega)$	-8×10^{-4}	-0.0085	-0.0133	-0.0138	- 0.0123

Table 4.2: Eigenvalues as function of the amount of damping for $m = 7$ and $F = 0.3$, $R_c = 5$ and $R = 10$.
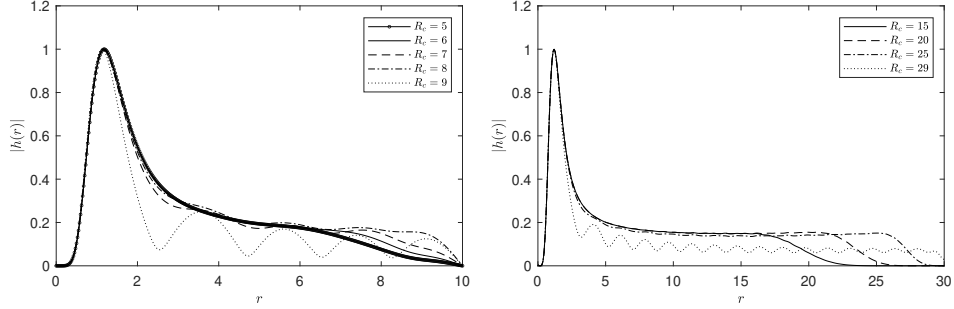

Figure 4.5: Eigenfunctions for $m = 7$, $F = 0.3$, $\bar{\xi} = 5$, and different values of R_c, computed using a small domain $R = 10$ (left) and a larger domain $R = 30$ (right).

shape, and for $\bar{\xi} \in \{0.1, 1\}$ a clear standing wave shape is seen in figure 4.4. For $\bar{\xi} \in \{5, 10\}$, the eigenfunctions are practically identical in the physical domain $0 < r < R_c$, and only differ in the damping layer $R_c \leq r \leq R$. For $\bar{\xi} = 50$, however, the damping is too strong, and little oscillations can be seen for $r < R_c$, suggesting wave reflection by the edge of the damping layer. This is also supported by the eigenvalues in table 4.2, which show the sensitivity of $\mathrm{Im}(\omega)$ to variations in damping strength, as expected.

The second convergence study involves varying the width of the damping layer whilst maintaining the same size of the computational domain and a fixed damping strength $\bar{\xi} = 5$. The eigenfunctions are displayed in figure 4.5, and the corresponding eigenvalues in table 4.3. For most results in figure 4.5 the eigenfunctions can be seen to be very similar in the physical domain $0 < r < R_c$ and to decay smoothly in r in the damping layer, while for a damping layer of width $R - R_c = 1$ a standing wave pattern can be seen for both domain sizes, implying significant wave reflection from the domain boundary at $r = R$. Again, this is also seen for the variations in the eigenvalue in table 4.3, with again $\mathrm{Im}(\omega)$ being particularly sensitive.

Finally, in figure 4.6 we compare the radiating mode for $m = 7$, $F = 0.3$

R_c	5	6	7	8	9
$\mathrm{Re}(\omega)$	-1.3766	-1.3767	-1.3802	-1.3788	-1.3918
$\mathrm{Im}(\omega)$	-0.0133	-0.0131	-0.0133	- 0.0143	-0.0045

Table 4.3: Eigenvalues as function of the initial position of the absorbing layer for $m = 7$ and $F = 0.3$, $\bar{\xi} = 5$ and $R = 10$.
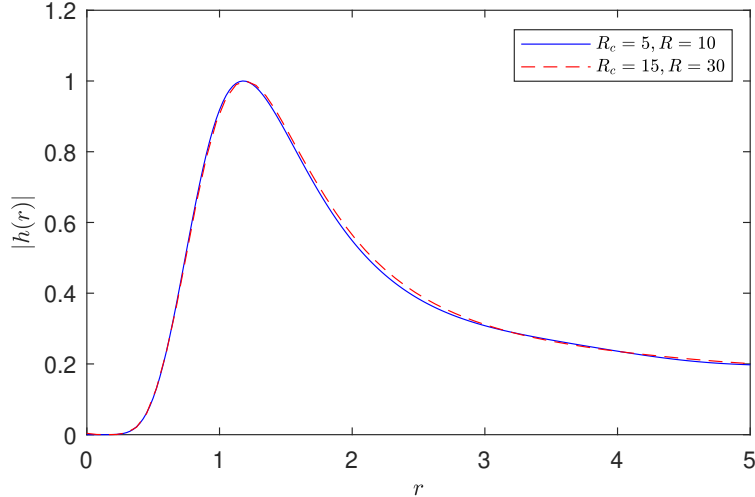
Figure 4.6: Eigenfunction for $m = 7$, $F = 0.3$, $\bar{\xi} = 10$ computed using two different domain sizes: $R_c = 5$ and $R = 10$ for the blue solid curve; and $R_c = 15$, $R = 30$ for the red dashed curve.

computed using two different size of the domain; $R_c = 5$, $R = 10$ on one hand and $R_c = 15$, $R = 30$ on the other. The two modes match very well over the physical interval $r \in [0, 5]$. This good match demonstrates that the damping layer successfully allows our numerical simulation on a small interval to reproduce results that would have been obtained using a larger interval, thus allowing our numerics to emulate an infinite unbounded domain using a finite computational domain.

4.2.6 Choice of numerical parameters

Based on numerical convergence studies, for the results that follow we take $R = 10$ and $R_c = 5$, with $\bar{\xi} = 5$ (to which results are compared to $\bar{\xi} = 10$). This choice is motivated by the need for sufficiently high resolution to resolve all modes of interest in the range of Froude numbers and azimuthal wavenumbers considered. The eigenvalue tolerance and eigenfunction resolvedness tolerance are taken to be $tol_1 = 10^{-2}$ and $tol_2 = 10^{-1}$ respectively, whereas other numerical parameters are taken to be $N_x = 50$, $N_y = 20$, $b_x = 12$ and $b_y = 4$. For the majority of results presented here, we use a fluid depth of $h_\infty = 5$. This is the depth shown in figure 4.1. This value is large enough to allow for a wide range of Froude numbers ($0 \leq F < \sqrt{h_\infty / \log(2)} \simeq 2.68$) without forming a dry region near $r = 0$, while small enough to exhibit finite-depth effects.

4.3 Results

We compute leading (i.e. least damped) eigenmodes for a range of Froude numbers and for a range of azimuthal wave numbers as large as $m = 20$, and find that above $m = 6$ surface gravity waves dominate. We shall first present

the surface waves for a representative case, wavenumber $m = 7$, and discuss in detail how the modes and eigenvalues depend on Froude number for this case. Following this, we consider the dependence of modes and eigenvalues on the azimuthal wave number.

4.3.1   Representative case $m = 7$

We begin with a detailed description of the case azimuthal wavenumber $m = 7$. The reason for taking such value of m is dictated both by the explanatory picture in Patrick *et al.* (2018, pp.6), who show a picture of the spiral structure of a normal mode solution for sufficiently high azimuthal wavenumber, as well as by the reasonable amount of computational time needed to get the leading surface waves eigenmodes. Indeed, we find numerically that the spatial structure of surface gravity waves becomes thinner and more localized close to the free surface as m increases. Following particularly the latest argument, the case of $m = 7$ has been taken as a reference study case and in the following we are going to show most of the interesting features applied to this case.

One of the key results of our study is the change in character of modes as function of the rotation rate of the vortex. Specifically, we characterize two extremes of modes: radiating modes and trapped modes. These have been previously discussed in section 3.4 both in terms of eigenvalues and structure of the corresponding eigenfunctions. The same features are therefore recovered here.

Figures 4.7 and 4.8 show representative examples of the continuous, but rapid, transition from radiating modes to trapped modes as the Froude number (the dimensionless rotation rate of the vortex), increases. This transition between radiating and trapped modes is also seen in figure 4.9 where the modulus of the free surface height is plotted as a function of r for different Froude numbers.

To look more closely at the trend in the eigensolutions, let us first denote by n an integer representing the number of peaks in radial direction of the modulus of the pressure eigenfunctions, as displayed in figure 4.10. In this way each eigensolution will be indexed by both m and n, with corresponding eigenvalues $\omega = \omega_{mn}$. In figure 4.11a, the two types of modes can be seen: radiating modes with a significant negative $\text{Im}(\omega)$, and trapped modes having an almost null $\text{Im}(\omega)$. There is no sharp transition between radiating and trapped modes. Accordingly, here we set an arbitrary threshold to separate the two sets of modes by considering a mode to be trapped when its eigenvalue has an imaginary part smaller than 10^{-5} in modulus (although our results are relatively insensitive to this threshold; see figure 4.14 discussed below). Hence, while the trapped modes considered here are almost neutrally stable, they have eigenvalues with small negative imaginary part and so radiate very slightly. Interestingly, none of the modes computed here are observed to become linearly
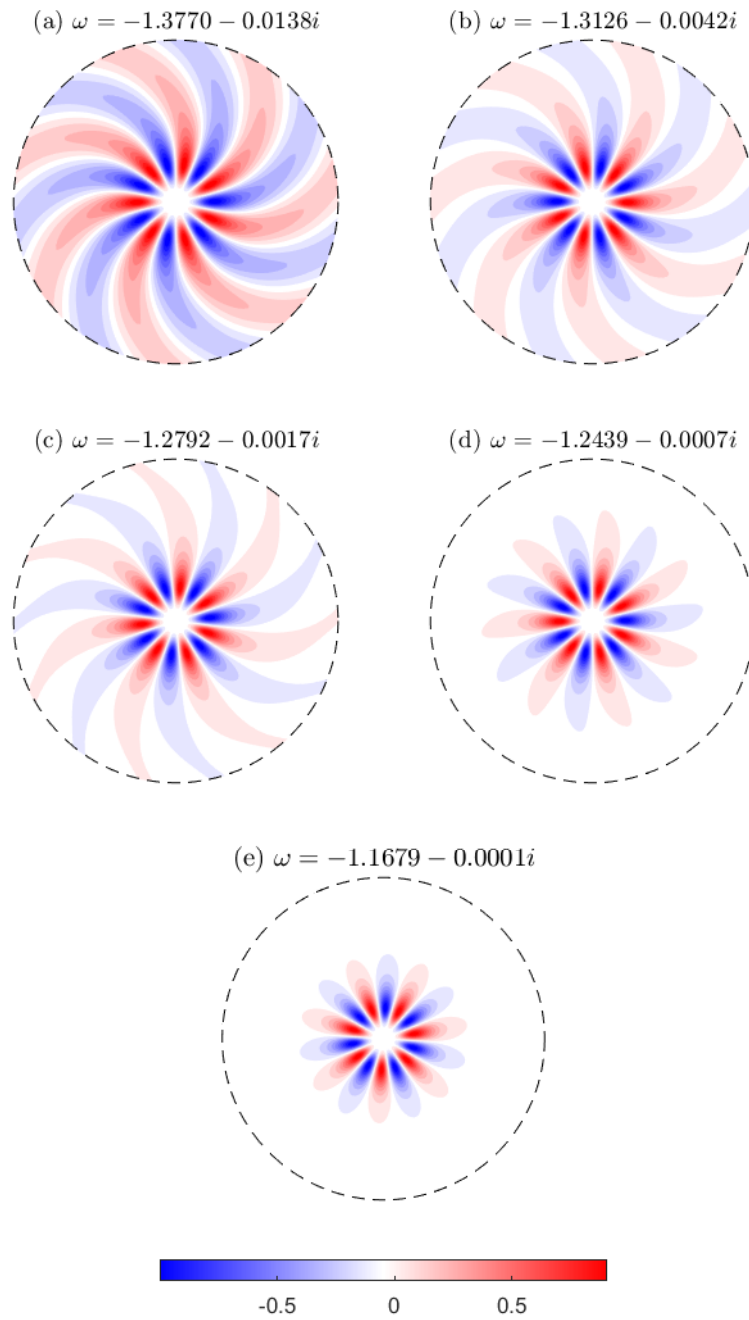
Figure 4.7: Plots of the free surface height $h(r, \theta, t = 0) = \mathrm{Re}[\phi(r, h_0(r)) \exp\{im\theta\}]$ for $m = 7$. (a) $F = 0.3$. (b) $F = 0.32$. (c) $F = 0.33$. (d) $F = 0.34$. (e) $F = 0.36$. All modes displayed rotate clockwise, i.e. against the vortex flow.
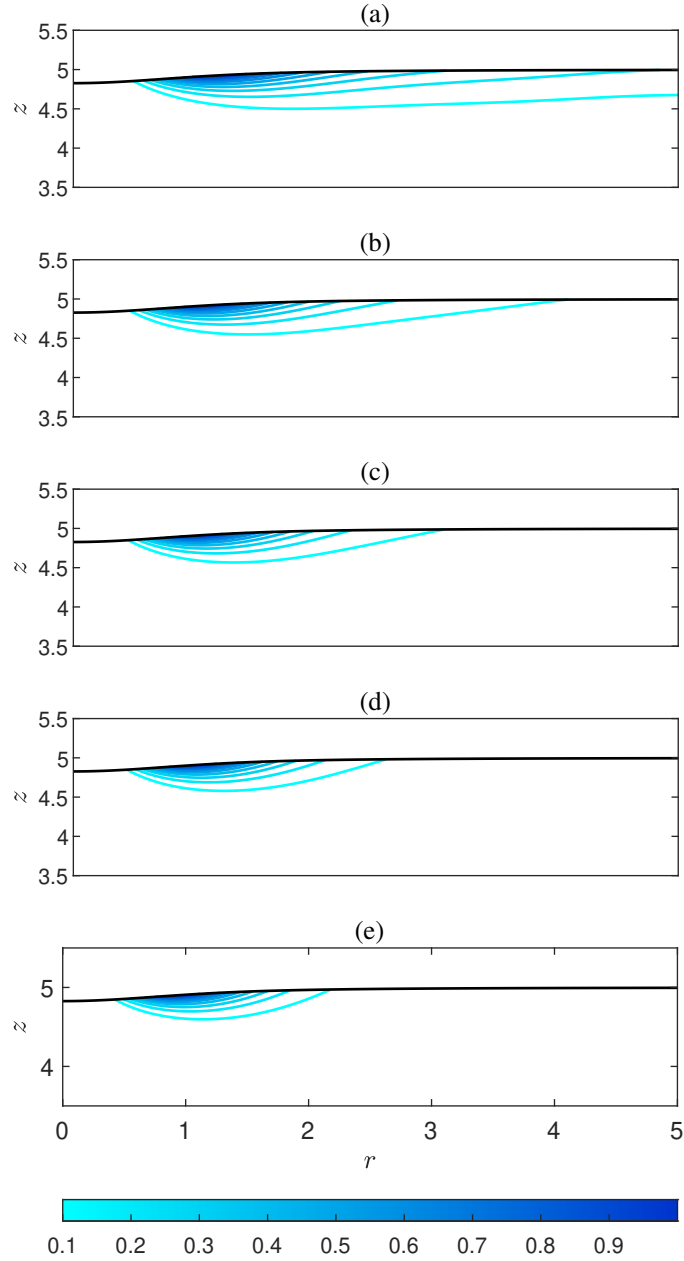
Figure 4.8: Plots of the pressure distribution $|\phi_m(r,z)|$ for $m = 7$. (a) $F = 0.3$. (b) $F = 0.32$. (c) $F = 0.33$. (d) $F = 0.34$. (e) $F = 0.36$. The black line represents the base free surface.

unstable, and we hypothesise that the base solution is at most marginally stable, but not unstable, to linear perturbations of this type at large Froude number. This stability can be viewed as a manifestation of the robustness of the Lamb–Oseen vortex (Fabre *et al.* 2006), even in the presence of a free surface.

In our calculations, the eigenmodes for sufficiently low Froude numbers become dependent on the amount of damping introduced in the system, and are therefore discarded. A similar result has been obtained in Oliveira *et al.*
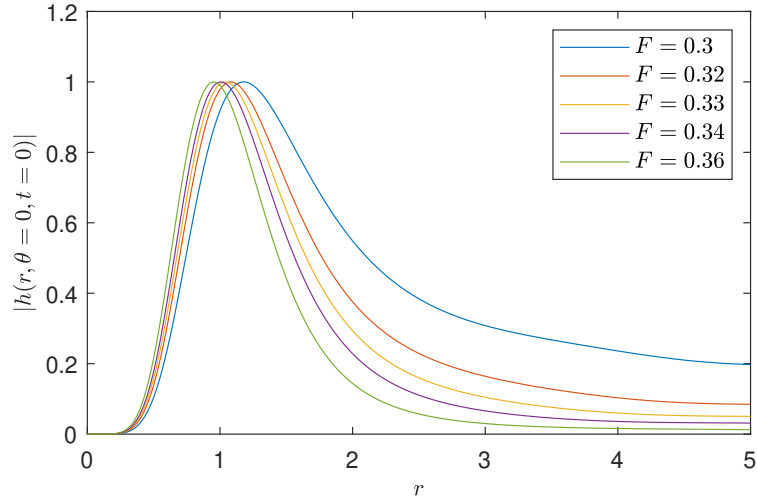
Figure 4.9: Modulus of the free surface height along the radius for $m = 7$ in the transition regime from radiating to trapped modes.
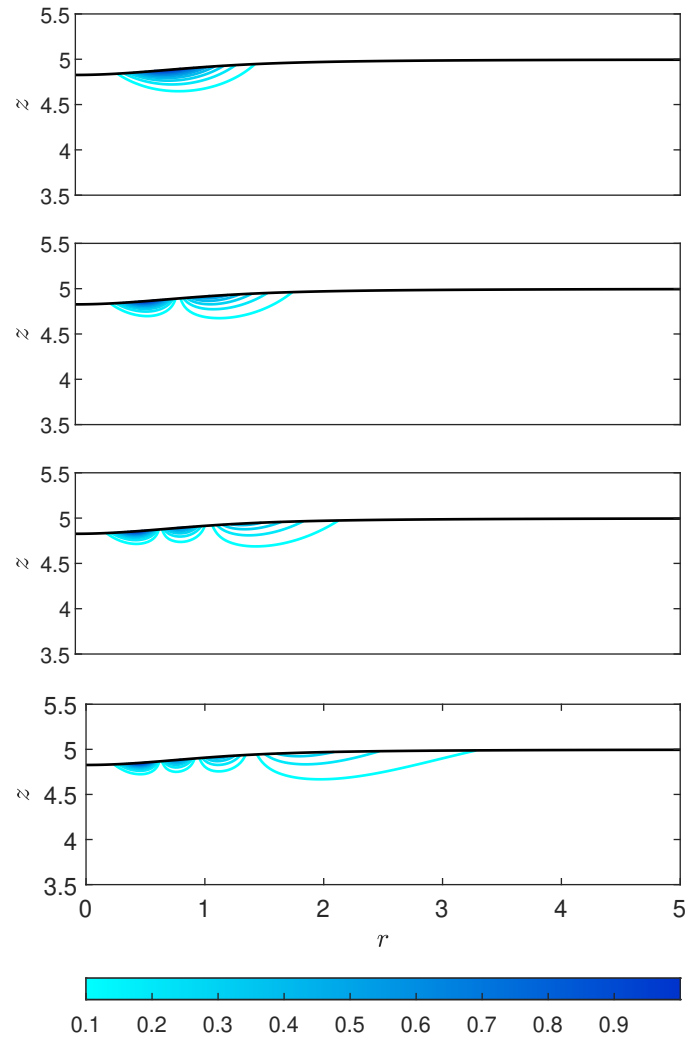

Figure 4.10: Modulus of the pressure $|\phi_m(r, z)|$ for $m = 7$ and $F = 0.5$. We show the four least stable eigenmodes for such parameters, having one, two, three and four peaks respectively.
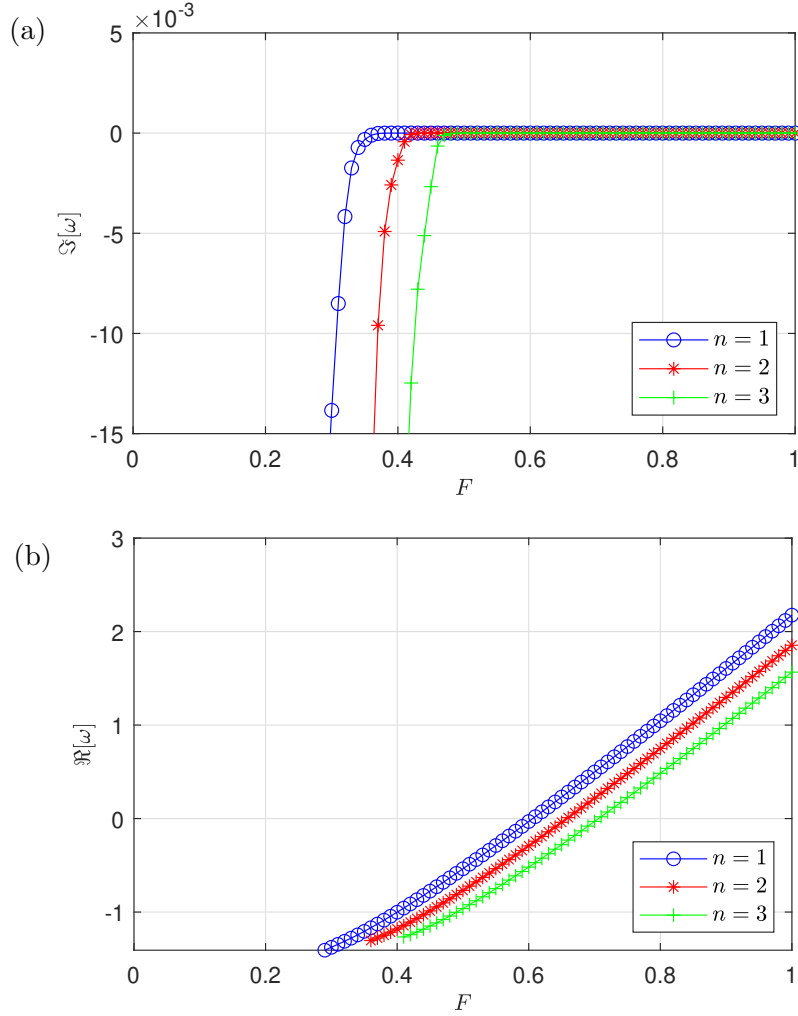
Figure 4.11: Imaginary (top) and real (bottom) parts of the eigenvalue ω_{mn} as function of the Froude number F for $m = 7$ and varying n.

(2014) studying a model wave equation describing the vortex-waves interaction in the shallow-water limit. Mathematically, this can be justified by considering the extreme case of $F = 0$; in that case, a regularity condition of the modes at $r = 0$ together with a radiating boundary condition at infinity cannot be satisfied simultaneously, thus leading to the non-existence of solutions in terms normal modes. We leave to future studies the possibility of tracking the trend of the spectrum curve as the Froude number goes to zero. It should be noted, that modes having a large negative decay rate in time do not play a relevant role in the dynamics of the system.

Another interesting phenomenon concerns the propagation direction of the surface waves with respect to the rotation of the base vortex flow as its rotation rate is varied. This is shown in figure 4.11b, which shows how the real part of the eigenvalues varies with the Froude number, again for $m = 7$. For $\text{Re}(\omega) < 0$, waves rotate opposite to the base flow (counter-rotating waves), while for $\text{Re}(\omega) > 0$, waves rotate in the same direction as the base flow (co-
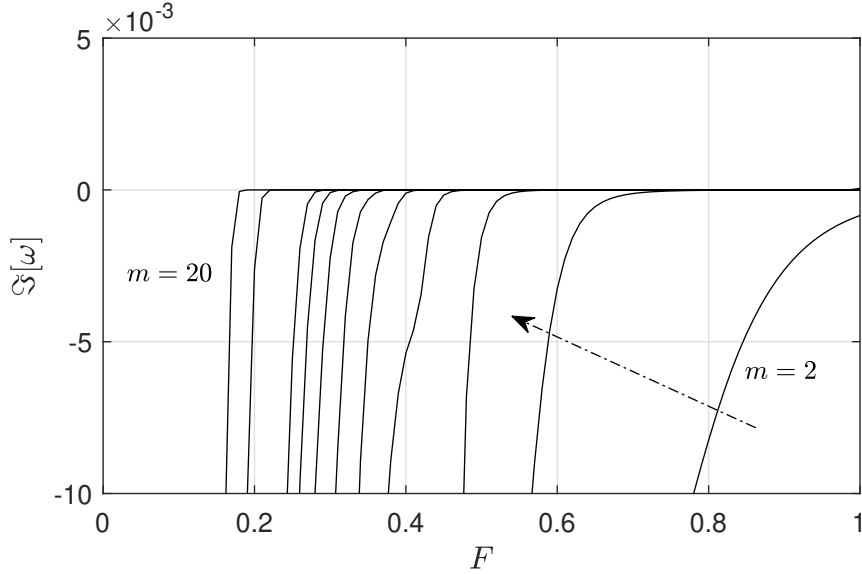
Figure 4.12: Imaginary part of the eigenvalues as functions of F for $m = 2, 3, 4, 5, 6, 7, 8, 9, 10, 15, 20$, with the arrow indicating the direction of increasing m.

rotating waves). It is clear that for each n, there is a value of Froude number separating counter-rotating from co-rotating surface waves.

4.3.2 Extension to other azimuthal wavenumbers.

The results described above for $m = 7$ are found to be typical at larger azimuthal wavenumbers. Figure 4.12 shows the trend of the imaginary part of the eigenvalues as a function of the Froude number. The results are qualitatively similar to the $m = 7$ case. Eigenvalue branches shift to lower F with increasing m, thus shifting to lower F the value of F separating radiating and trapped modes. This suggests that for very high azimuthal wavenumber perturbations we expect to get radiating eigenmodes at lower and lower Froude numbers, as shown in figure 4.13 for the example cases of $m = 15$ and $m = 20$.

We have computed the range of Froude numbers in which modes radiate and transition towards a neutrally stable state for different values of m. This is summarized in figure 4.14 showing the classes of solutions previously described over a wide range of azimuthal orders m and Froude numbers F. The contour lines plotted separate the regions of parameter space where waves are radiating and where waves are trapped, with the arrow indicating the direction of better trapping. While the individual contours range from $\mathrm{Im}(\omega) = 10^{-2}$ to $\mathrm{Im}(\omega) = 10^{-5}$, their close spacing shows that the exact threshold value of $\mathrm{Im}(\omega)$ separating trapped and radiating behaviour is not that important, with all contours giving a similar boundary. Also plotted in figure 4.14 is a dashed line showing $\mathrm{Re}(\omega) = 0$, which is the boundary between counter-rotating and co-rotating trapped waves. Two notable features of the
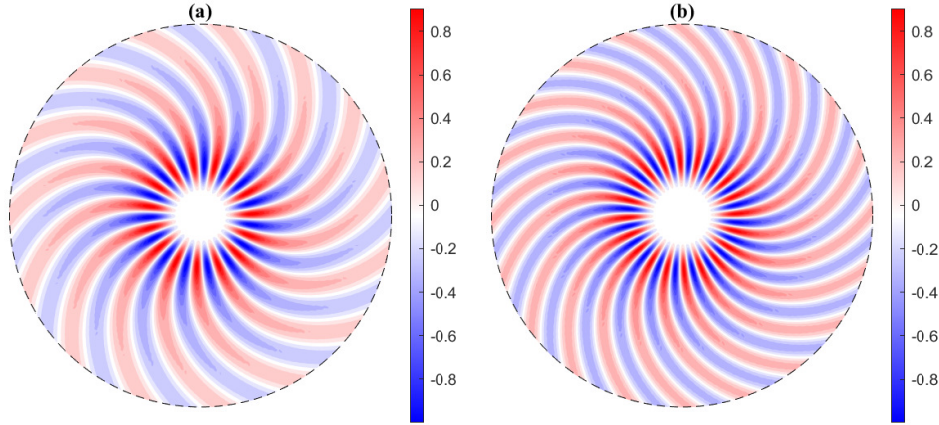
Figure 4.13: Shape of the free surface height $h(r, \theta, t = 0) = \text{Re}[\phi(r, h_0(r)) \exp\{im\theta\}]$ in two high azimuthal wavenumber cases. (a): $m = 15, F = 0.19$. (b): $m = 20, F = 0.16$.
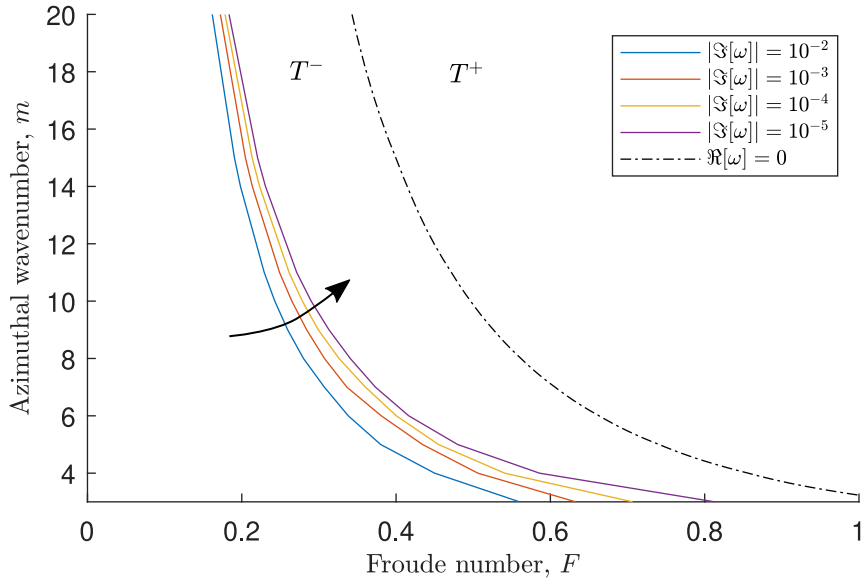

Figure 4.14: Regimes of radiating (large $|\text{Im}(\omega)|$) and trapped (small $|\text{Im}(\omega)|$) modes for different azimuthal wavenumbers m and Froude numbers F. Solid lines are contours of $|\text{Im}(\omega)|$, with the arrow indicating the direction of more perfectly trapped behaviour. The dash-dot line separates counter-rotating modes (T^-) with $\text{Re}(\omega) < 0$ from co-rotating modes (T^+) with $\text{Re}(\omega) > 0$.

plot as m is decreased are the shift of contours to larger F and the widening of the separation between contours. Both of these features are consistent with figure 4.12, where one sees not only a shift in the eigenvalue curves with m, but also a steepening of the transition between radiating and trapped modes with increasing m.

While this section considers a wide range of values of $m \geq 3$, we find $m = 0, 1$ and 2 to be dominated by inertial waves rather than surface waves, which are discussed further in section 4.3.4.

106

4.3.3 Effect of the free-surface height on the eigenmodes

In this subsection we investigate the effects associated to a variation in the fluid depth, exploring the regime between shallow and deep water. We again focus on modes with azimuthal modenumber $m = 7$ and show how the structure of eigenmodes and corresponding eigenvalues vary with fluid depth, and hence how the transition between radiating and trapped modes changes with depth.

The variation in the structure of the surface gravity eigenmodes with fluid depth h_∞ is displayed in figure 4.15 for a typical trapped mode computed at Froude number $F = 0.5$. The same type of analysis is carried out for a radiating mode at $F = 0.3$, whose spatial structures are shown in figure 4.16. Finally, in figure 4.17, the transition between radiating and trapped mode is shown as the fluid depth is varied between $h_\infty = 0.25, 0.5, 1$. Figure 4.18 shows the variation in eigenvalue as the Froude number is varied, for different fluid depths. The trend in $\text{Im}(\omega)$ shown suggests that more shallow systems require a faster rotating vortex in order to get the same wave trapping as a deeper water configuration. The variation with depth of $\text{Re}(\omega)$ is less significant. For $h_\infty = 1$, the eigenvalues are essentially identical to those computed for even higher depths, for example, in this case $h_\infty = 5$. Hence, in this regard, for a trapped mode a fluid with $h_\infty \in [0.5, 1]$ can already be considered deep water.

4.3.4 Inertial modes

While the focus of this study is surface gravity waves, our numerics finds modal solutions to the governing equations (4.11) without any assumption about the modes being surface gravity waves. By way of contrast, therefore, in this section we briefly discuss another type of mode, namely inertial modes. These modes persist even at low rotation rates, and are characterised by being neutrally stable as well as being concentrated within the vortex core and not being localized close to the free surface. Our results are therefore similar to the numerical results presented by Mougel *et al.* (2015) for a solid-body rotation, since the Lamb–Oseen vortex is very close to solid-body rotation close to the centre. Figure 4.19 shows two inertial modes computed for $m = 2$, $h_\infty = 1$, and $F = 0.2, 0.8$. The corresponding eigenvalues are purely real, and are also plotted as function of the Froude number in figure 4.19.

4.4 Results without the base free surface deformation

In this section, we demonstrate that the dominant contribution to the trapping of modes by the vortex shown in section §4.3 is the swirl of the base flow, and that the deformation of the base free surface has little effect itself. As the free surface deformation becomes more and more important through its gradient—
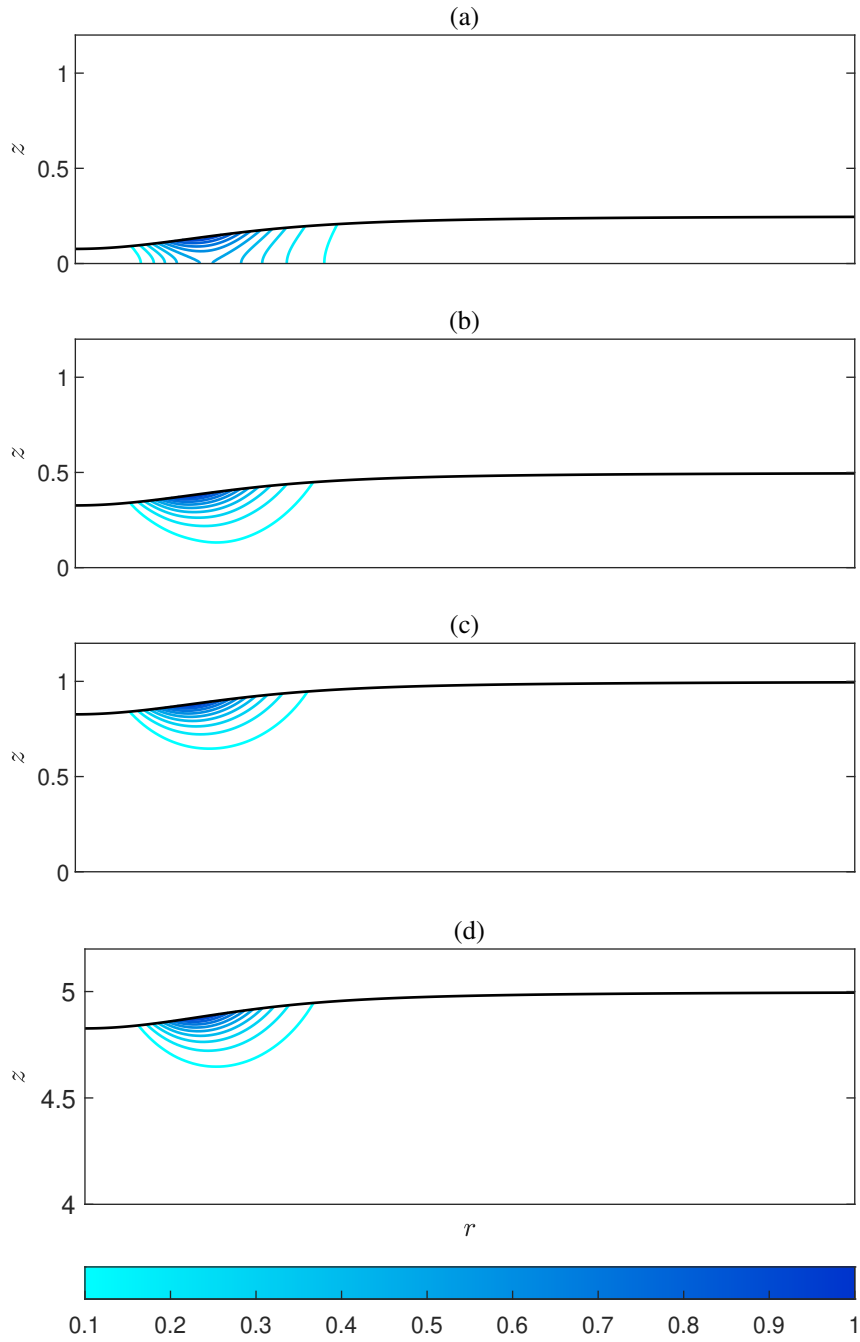
Figure 4.15: Effect of the fluid height variation on a single peak ($n = 1$) trapped pressure mode $|\phi_m(r, z)|$ computed for $m = 7$, and $F = 0.5$. (a): $\omega = -0.3058$, $h_\infty = 0.25$. (b): $\omega = -0.5316$, $h_\infty = 0.5$ (c): $\omega = -0.5366$, $h_\infty = 1$ (d): $\omega = -0.5370$, $h_\infty = 5$. The imaginary part of the eigenvalues reported here is at least of order 10^{-9}, hence can be considered as purely real.
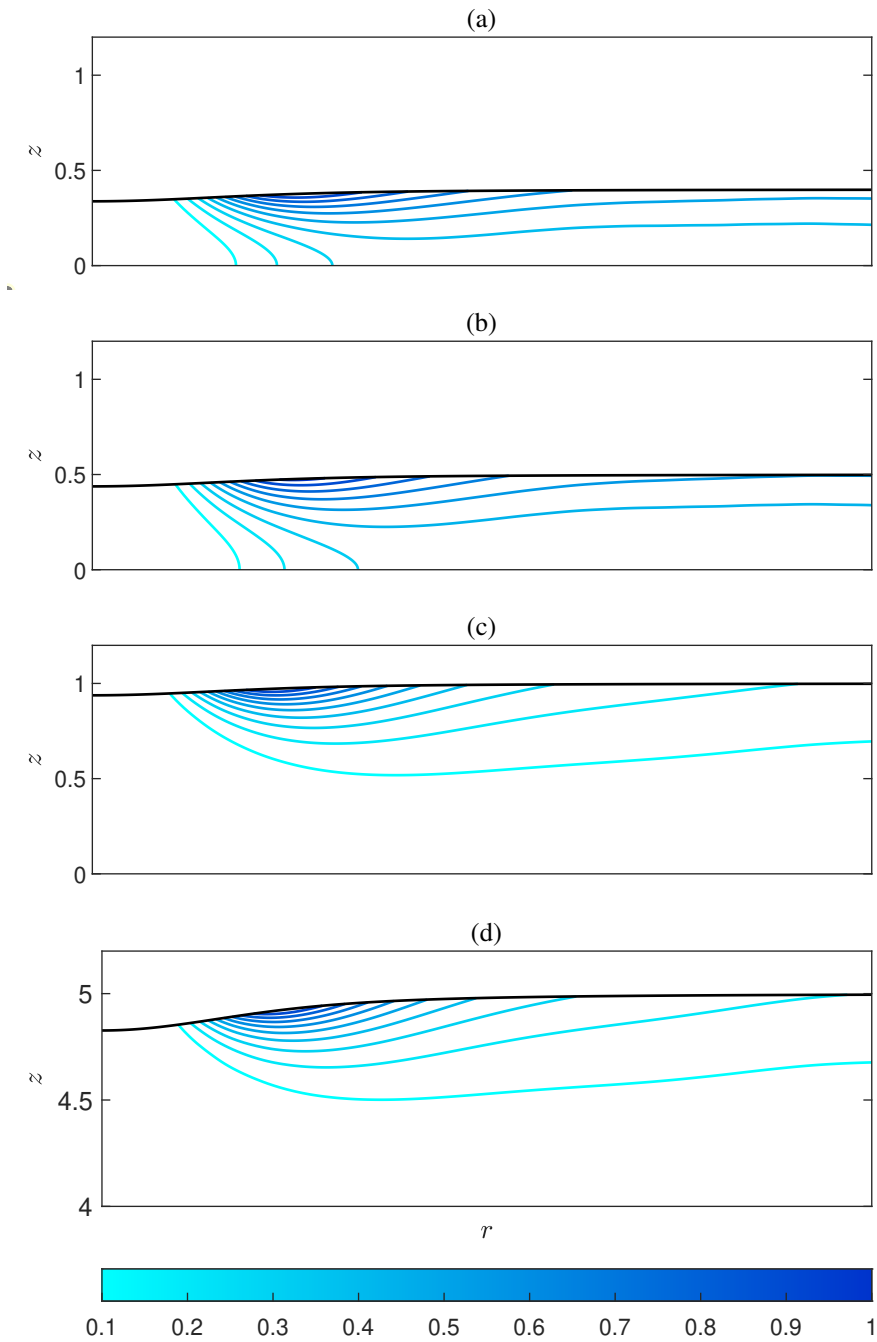
Figure 4.16: Effect of the fluid height variation on a radiating pressure mode $|\phi_m(r,z)|$ computed for $m = 7$, and $F = 0.3$. (a): $\omega = -1.3371 - 0.0530\mathrm{i}$, $h_\infty = 0.4$. (b): $\omega = -1.3633 - 0.0320\mathrm{i}$, $h_\infty = 0.5$ (c): $\omega = -1.3772 - 0.0140\mathrm{i}$, $h_\infty = 1$ (d): $\omega = -1.3770 - 0.0138\mathrm{i}$, $h_\infty = 5$.
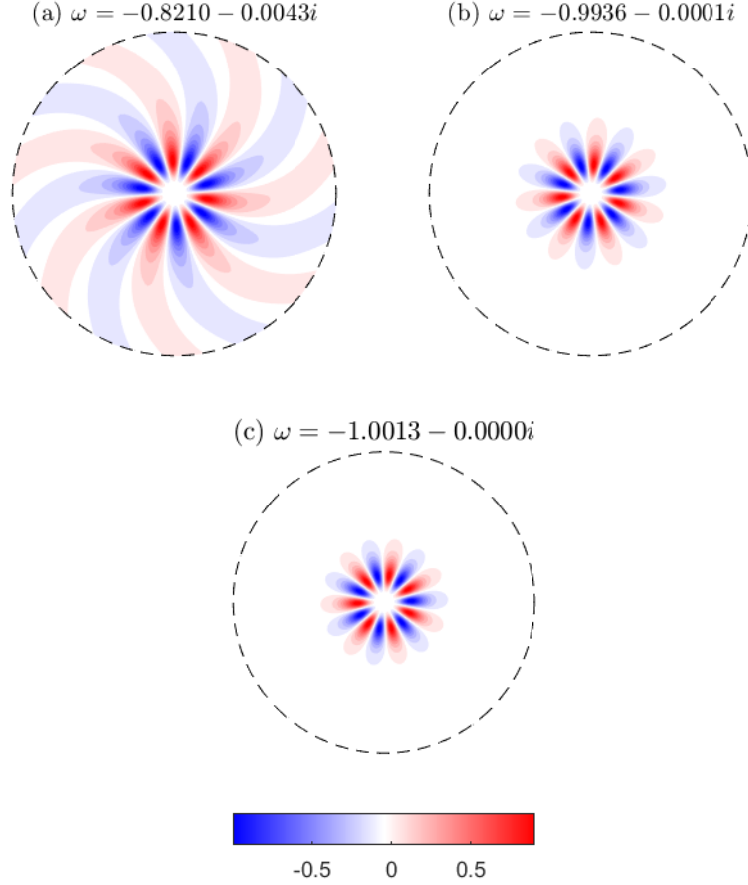
Figure 4.17: Free surface height for $m = 7$, $F = 0.4$ and different fluid depths. (a): $h_\infty = 0.25$. (b): $h_\infty = 0.5$. (c): $h_\infty = 1$.

as shown in the last term of the free surface boundary condition (2.32)— in the following we artificially assume the base free surface to be flat, meaning that $h_0(r) = h_\infty$ and $h_0'(r) = 0$. All the remaining terms in the governing equations and boundary conditions do not change. Solving the eigenvalue problem in this case, we compare the eigenvalues to the complete case where the base free surface deformation has been taken into account in figure 4.20. Little difference is seen between the two. Indeed, figure 4.21 plots the difference in eigenvalues as function of the Froude number; i.e. $|\omega - \omega_{\text{flat}}|$, where ω_{flat} are the eigenvalues without the free surface variation. It is clear that for the range of Froude numbers considered, the two agree remarkably closely.

In terms of the eigenfunctions, the free surface perturbation is displayed in figure 4.22, which should be compared against the free surface perturbation with a base free surface height variation plotted in figure 4.7; the two figures can be seen to be almost identical. The corresponding structure in the $r - z$ plane is shown in figure 4.23, which should be compared against figure 4.8 in the results section; again, the two figures are almost identical apart from the base flow height.

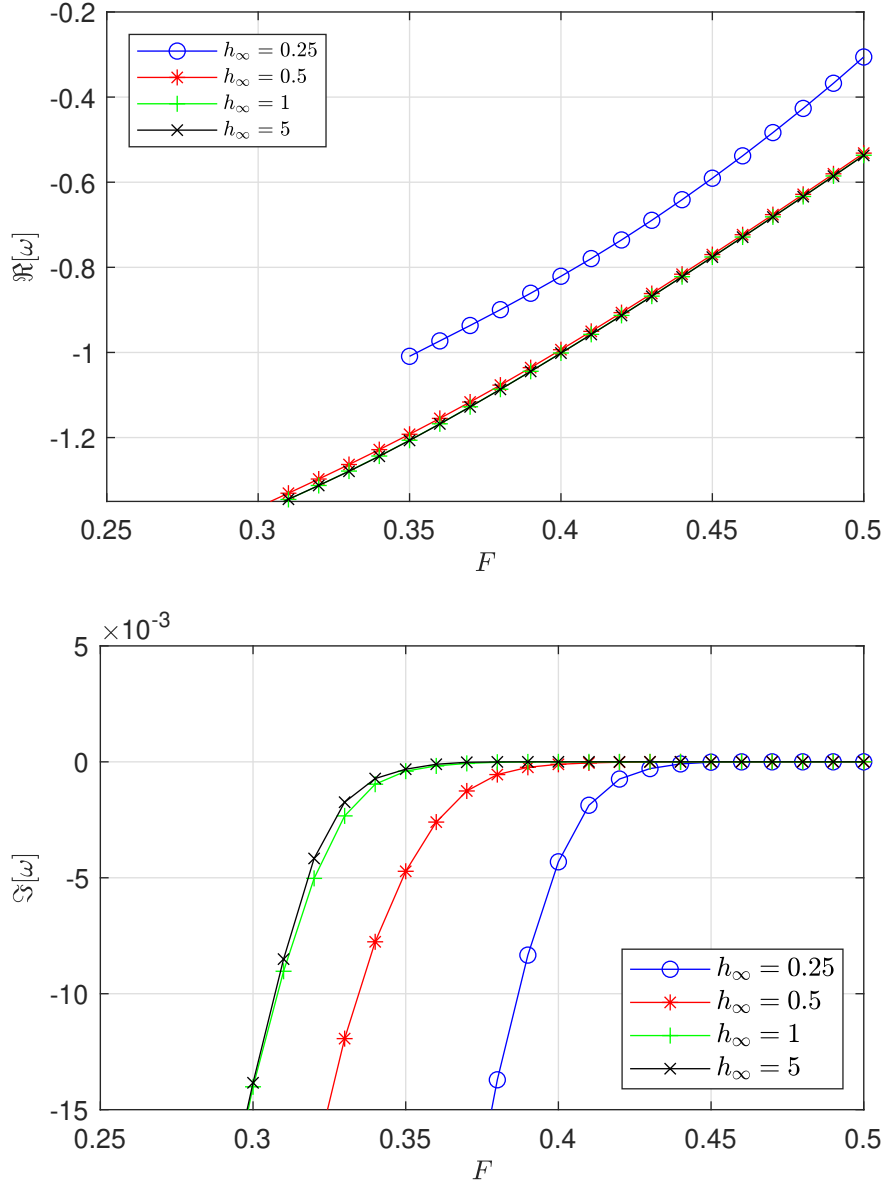We therefore conclude that the driving mechanism behind the trapping

Figure 4.18: Effect of the fluid height variation on the spectrum curves for the least damped set of eigenmodes obtained for $m = 7$.

of modes by the vortex is the rotation of the base flow, and not the free surface deformation.

4.5   Summary

In this chapter we derived and studied in detail the equations governing the propagation of linear waves in a laterally unbounded Lamb-Oseen flow with a free surface.

We conducted a parametric study on the vortex stability by varying the Froude number, the azimuthal wavenumbers and the fluid depth. We have shown that for low Froude numbers modes are radiating and decay in time; on
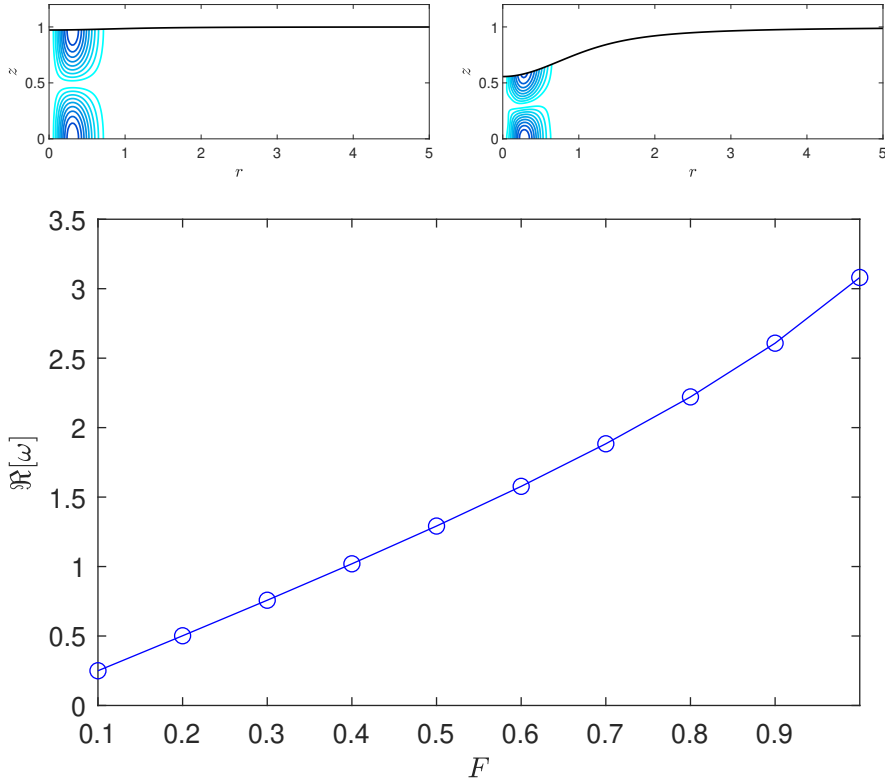
Figure 4.19: Inertial modes for $m = 2$, $h_\infty = 1$ and $F = 0.2$ (left); $F = 0.8$ (right). Eigenvalues curve as function of the Froude number for the same parameters (bottom figure).
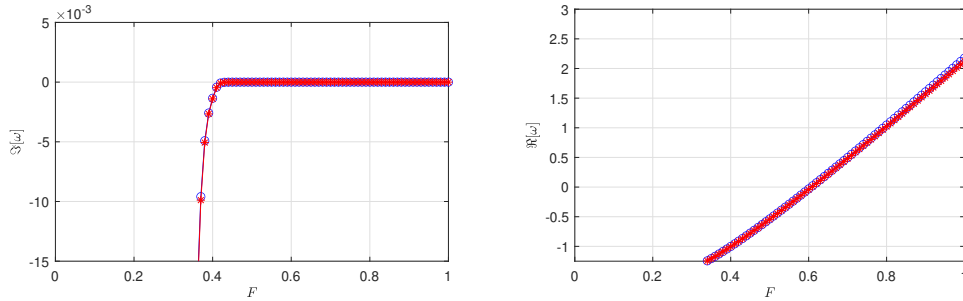
Figure 4.20: Imaginary and real part of the eigenvalues as function of the Froude number for modes with $m = 7$ and $n = 1$. Blue-circle curve: full numerics; red-asterisk curve: without the free surface contribution.

the contrary, as the Froude number increases their decay rate becomes closer and closer to zero leading to the appearance of trapped, nearly neutrally stable modes. The system, however, never becomes unstable.

The influence of the free surface deformation has been shown to give only a minor contribution in the eigenmodes found in the range $F \in [0, 1]$. Thus, the most important driving mechanism leading to the emergence of the trapped modes within the vortex is the advection of the swirling flow and not the corresponding free surface shape.
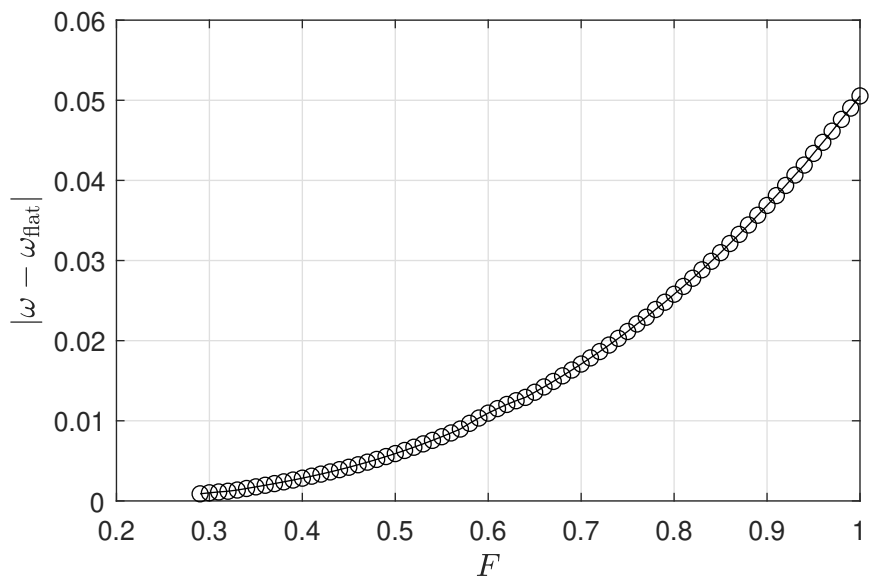
Figure 4.21: Absolute difference between eigenvalues computed with and without the free surface contribution, $|\omega - \omega_{\text{flat}}|$, for the first radial mode $n = 1$ and $m = 7$.
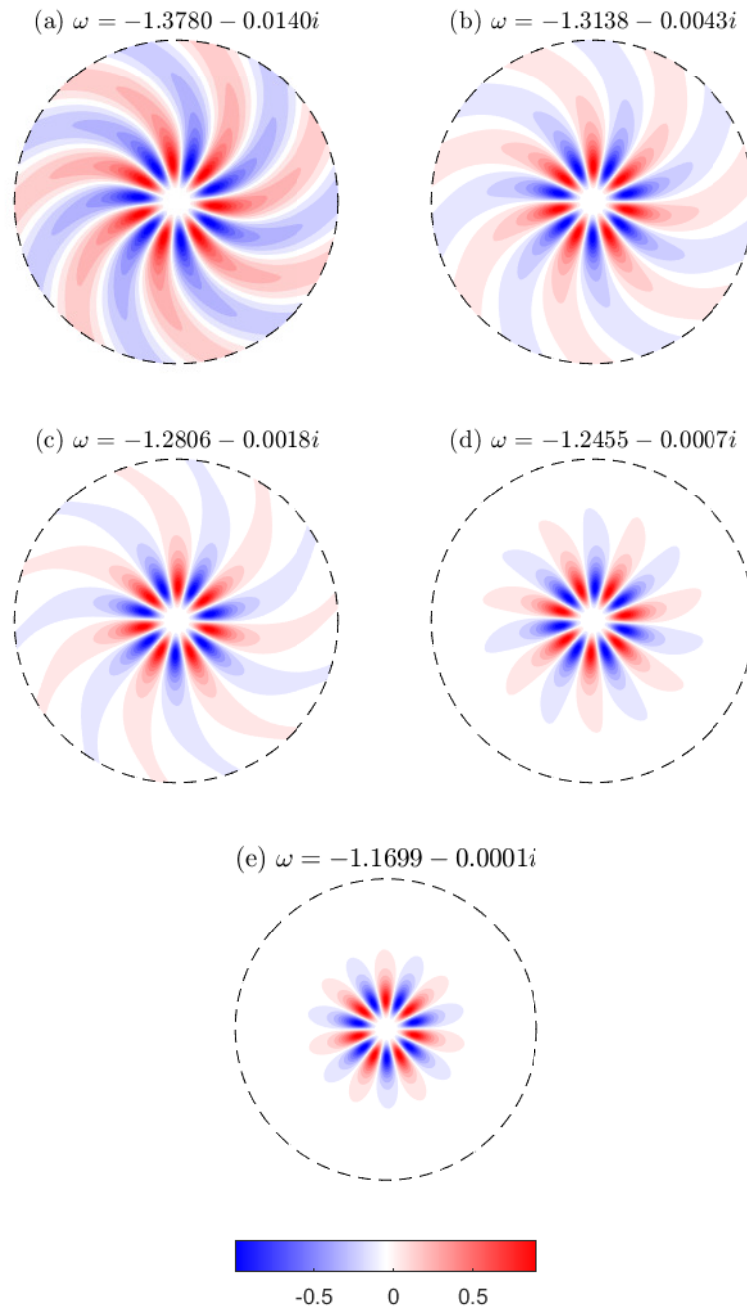
Figure 4.22: Plots of the perturbation free surface height $h(r, \theta, t = 0) = \mathrm{Re}[\phi(r, h_0(r)) \exp\{im\theta\}]$ for $m = 7$ without the base free surface deformation, to be compared against figure 4.7. (a) $F = 0.3$. (b) $F = 0.32$. (c) $F = 0.33$. (d) $F = 0.34$. (e) $F = 0.36$. All modes displayed rotate clockwise, i.e. against the vortex flow.
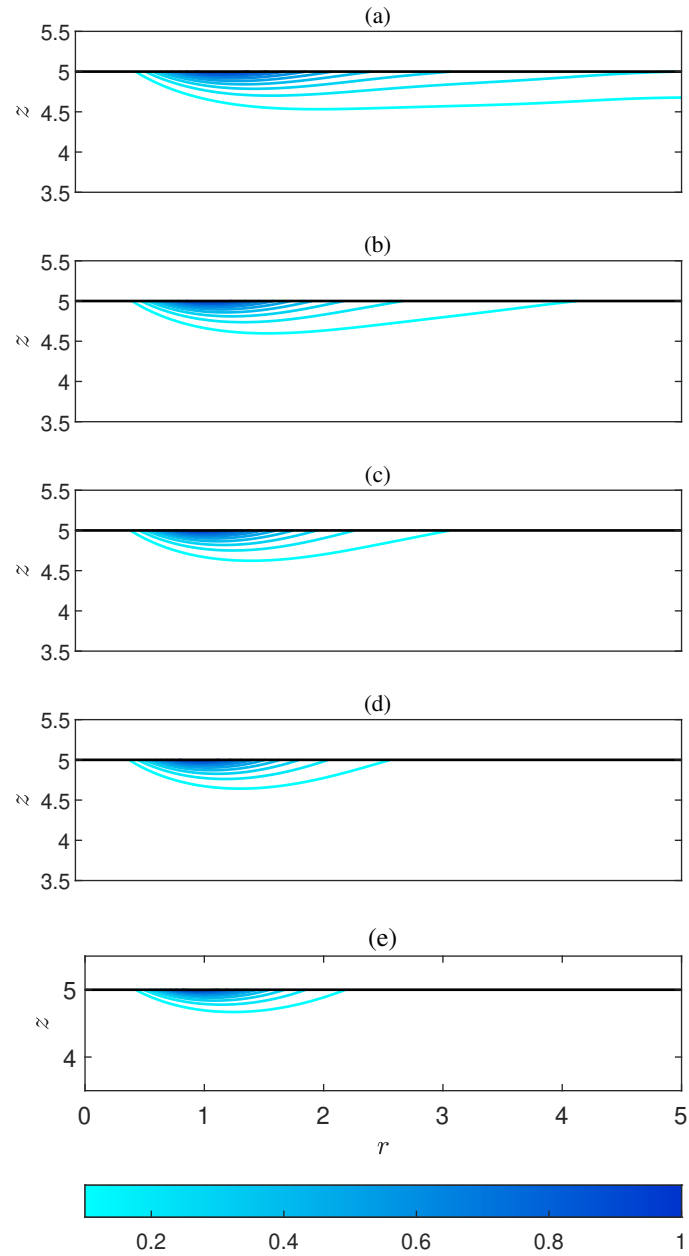
Figure 4.23: Plots of the pressure distribution $|\phi_m(r,z)|$ for $m = 7$ without the base free surface deformation, to be compared against figure 4.8. (a) $F = 0.3$. (b) $F = 0.32$. (c) $F = 0.33$. (d) $F = 0.34$. (e) $F = 0.36$.

Chapter 5

A reduced model for deep-water waves on free surface swirling flows

In this chapter we derive a novel set of two-dimensional equations to study the vortex-surface waves in the deep-water limit. As shown in figure 2.6, for example, it is clear how in real applications and phenomena the dispersive effects associated to a non-shallow fluid become important in the propagation of the waves. It is indeed sufficient the height of the fluid to be comparable to the wavelength of the waves in order the shallow-water approximation to fail. This motivates primarily the present model. Moreover, the equations we are going to derive overcome the two main assumptions used in Boussinesq-type models described in the introduction (section 1.6) and allow for the effects associated to the deformation of the base free surface and the non-zero vorticity of the background flow.

There are additional reasons to derive new reduced models in this context. The first one is numerical computations; indeed, faster computations would permit the exploration of more extreme regimes (for example higher Froude numbers limit). The second reason is the possibility of making predictions about the propagation of deep-water waves on more complicated and nontrivial flows, e.g. a dipole or a quadrupole flow.

The key point in our derivation is the introduction of a closure boundary condition imposed along the base free surface. This closure leads naturally to a closed set of equations valid in the horizontal spatial domain and involving the horizontal velocity components and the fluid elevation only. We justify the validity of our closure boundary condition by means of numerical results and comparisons with full three-dimensional calculations from (Zuccoli *et al.* 2023) for the case of a Lamb–Oseen vortex. Finally, we use the reduced system derived to make predictions on the propagation of deep-water modes over a periodic array of vortices.

5.1 Mathematical Model

We present the derivation of a reduced two-dimensional model. The equations will be derived in a cartesian reference frame, assuming a steady background flow of the form $\boldsymbol{U}_0(x,y) = U_0(x,y)\hat{\boldsymbol{x}} + V_0(x,y)\hat{\boldsymbol{y}}$, such that $\boldsymbol{U}_0 \cdot \nabla H_0 = 0$ due to the kinematic boundary condition on the free surface of the fluid. As far as the pressure field is concerned, that is given by $P_0(x,y,z) = -g(z-H_0(x,y)) + \bar{P}$, where $\bar{P}$ is the ambient atmospheric pressure. The governing equations are given by the linearized incompressible Euler equations with free surface boundary condition, involving the velocity components and the pressure. In particular, let $\boldsymbol{u}(x,y,z,t) = u_x(x,y,z,t)\hat{\boldsymbol{x}} + u_y(x,y,z,t)\hat{\boldsymbol{y}} + u_z(x,y,z,t)\hat{\boldsymbol{z}}$ be the perturbation velocity, $p(x,y,z,t)$ the perturbation pressure and $h(x,y,t)$ the perturbation height of the fluid, the linear equations read

$$D_t u_x + \frac{\partial U_0}{\partial x} u_x + \frac{\partial U_0}{\partial y} u_y + \frac{\partial p}{\partial x} = 0, \tag{5.1a}$$

$$D_t u_y + \frac{\partial V_0}{\partial x} u_x + \frac{\partial V_0}{\partial y} u_y + \frac{\partial p}{\partial y} = 0, \tag{5.1b}$$

$$D_t u_z + \frac{\partial p}{\partial z} = 0, \tag{5.1c}$$

$$\frac{\partial u_x}{\partial x} + \frac{\partial u_y}{\partial y} + \frac{\partial u_z}{\partial z} = 0, \tag{5.1d}$$

$$u_z - D_t h - \frac{\partial H_0}{\partial x} u_x - \frac{\partial H_0}{\partial y} u_y = 0, \quad on \quad z = H_0(x,y), \tag{5.1e}$$

$$p - gh = 0, \quad on \quad z = H_0(x,y). \tag{5.1f}$$

In equations above, $D_t = \partial_t + \boldsymbol{U}_0 \cdot \nabla$ is the convective derivative due to the background flow and g the acceleration of gravity. Now, let us define the unknowns on the base free surface as $u = u_x|_{H_0}$, $v = u_y|_{H_0}$, $w = u_z|_{H_0}$ and $h = \frac{1}{g} p|_{H_0}$. Moreover, let $f(x,y,z,t)$ represent any of these four unknowns. Then, the following relationships hold

$$\left.\frac{\partial f}{\partial x}\right|_{H_0} = \frac{\partial f(x,y,H_0(x,y),t)}{\partial x} - \frac{\partial H_0}{\partial x} \left.\frac{\partial f}{\partial z}\right|_{H_0},$$

$$\left.\frac{\partial f}{\partial y}\right|_{H_0} = \frac{\partial f(x,y,H_0(x,y),t)}{\partial y} - \frac{\partial H_0}{\partial y} \left.\frac{\partial f}{\partial z}\right|_{H_0}, \tag{5.2}$$

$$D_t f|_{H_0} = D_t\left(f|_{H_0}\right) - \left(\boldsymbol{U}_0 \cdot \nabla H_0\right) \left.\frac{\partial f}{\partial z}\right|_{H_0} = D_t\left(f|_{H_0}\right).$$

Evaluation of the linearized Euler equations on the background free surface and using of equations (5.2) yields

$$D_t u + \frac{\partial U_0}{\partial x} u + \frac{\partial U_0}{\partial y} v + g\frac{\partial h}{\partial x} - \frac{\partial H_0}{\partial x} \frac{\partial p}{\partial z}\bigg|_{H_0} = 0, \tag{5.3a}$$

$$D_t v + \frac{\partial V_0}{\partial x} u + \frac{\partial V_0}{\partial y} v + g\frac{\partial h}{\partial y} - \frac{\partial H_0}{\partial y} \frac{\partial p}{\partial z}\bigg|_{H_0} = 0, \tag{5.3b}$$

$$D_t w + \frac{\partial p}{\partial z}\bigg|_{H_0} = 0, \tag{5.3c}$$

$$\frac{\partial u}{\partial x} + \frac{\partial v}{\partial y} + \frac{\partial u_z}{\partial z}\bigg|_{H_0} - \frac{\partial H_0}{\partial x} \frac{\partial u_x}{\partial z}\bigg|_{H_0} - \frac{\partial H_0}{\partial y} \frac{\partial u_y}{\partial z}\bigg|_{H_0} = 0, \tag{5.3d}$$

$$w = D_t h + \frac{\partial H_0}{\partial x} u + \frac{\partial H_0}{\partial y} v, \quad on \quad z = H_0(x, y). \tag{5.3e}$$

By exploiting the momentum equation along $\hat{z}$ and the kinematic boundary condition, the momentum equations along the horizontal coordinates can be modified into

$$D_t u + \frac{\partial U_0}{\partial x} u + \frac{\partial U_0}{\partial y} v + g\frac{\partial h}{\partial x} + \frac{\partial H_0}{\partial x} D_t \left[D_t h + \frac{\partial H_0}{\partial x} u + \frac{\partial H_0}{\partial y} v \right] = 0, \tag{5.4a}$$

$$D_t v + \frac{\partial V_0}{\partial x} u + \frac{\partial V_0}{\partial y} v + g\frac{\partial h}{\partial y} + \frac{\partial H_0}{\partial y} D_t \left[D_t h + \frac{\partial H_0}{\partial x} u + \frac{\partial H_0}{\partial y} v \right] = 0. \tag{5.4b}$$

At this point equations above are written in terms of the three unknowns u, v, h. We need a third equation to close the system. To do so, let us start by looking at the functional form of the boundary condition on the free surface. We can define a functional $\Psi[u_x, u_y, u_z, p](x, y, z, t)$ such that

$$\Psi[u_x, u_y, u_z, p](x, y, z, t) = u_z - \frac{\partial H_0}{\partial x} u_x - \frac{\partial H_0}{\partial y} u_y - \frac{1}{g} D_t p, \tag{5.5}$$

where the last term comes from the dynamic boundary condition. By definition, we have that along the free surface the functional is null, i.e. $\Psi(x, u, H_0(x, y), t) = 0$. Now, Let us evaluate Ψ along a surface infinitesimally lower than $H_0(x, y)$, i.e. along $z = H_0(x, y) - \delta z$. We then get

$$\Psi(x, y, H_0(x, y) - \delta z, t) \approx \Psi(x, y, H_0(x, y), t) - \frac{\partial \Psi}{\partial z}\bigg|_{H_0} \delta z. \tag{5.6}$$

We assume that $\Psi(x, y, H_0(x, y) - \delta z, t) = 0$, so that even $\frac{\partial \Psi}{\partial z}\big|_{H_0} = 0$ and we can write

$$\frac{\partial \Psi}{\partial z}\bigg|_{H_0} = \frac{\partial u_z}{\partial z}\bigg|_{H_0} - \frac{\partial H_0}{\partial x} \frac{\partial u_x}{\partial z}\bigg|_{H_0} - \frac{\partial H_0}{\partial y} \frac{\partial u_y}{\partial z}\bigg|_{H_0} - \frac{1}{g} \frac{\partial (D_t p)}{\partial z}\bigg|_{H_0} = 0, \tag{5.7}$$

which means

$$\frac{\partial u_z}{\partial z}\bigg|_{H_0} - \frac{\partial H_0}{\partial x}\frac{\partial u_x}{\partial z}\bigg|_{H_0} - \frac{\partial H_0}{\partial y}\frac{\partial u_y}{\partial z}\bigg|_{H_0} = \frac{1}{g}D_t\frac{\partial p}{\partial z}\bigg|_{H_0}$$

$$= -\frac{1}{g}D_t^2 w = -\frac{1}{g}D_t^2\left(D_t h + \frac{\partial H_0}{\partial x}u + \frac{\partial H_0}{\partial y}v\right). \tag{5.8}$$

We define equation above as the closure boundary condition. It should be emphasized that the ansatz (5.7) has been assumed here heuristically. In Section 5.2, we validate the resulting closure boundary condition 5.8 by presenting numerical evidence that it holds for linear waves on the free surface of vortices in deep water. Substituting equation (5.8) into the continuity equation (5.3d), we get a reduced two-dimensional system of equations in the unknowns u, v, h

$$D_t u + \frac{\partial U_0}{\partial x}u + \frac{\partial U_0}{\partial y}v + g\frac{\partial h}{\partial x} + \frac{\partial H_0}{\partial x}D_t\left[D_t h + \frac{\partial H_0}{\partial x}u + \frac{\partial H_0}{\partial y}v\right] = 0, \tag{5.9a}$$

$$D_t v + \frac{\partial V_0}{\partial x}u + \frac{\partial V_0}{\partial y}v + g\frac{\partial h}{\partial y} + \frac{\partial H_0}{\partial y}D_t\left[D_t h + \frac{\partial H_0}{\partial x}u + \frac{\partial H_0}{\partial y}v\right] = 0, \tag{5.9b}$$

$$\frac{\partial u}{\partial x} + \frac{\partial v}{\partial y} - \frac{1}{g}D_t^2\left(D_t h + \frac{\partial H_0}{\partial x}u + \frac{\partial H_0}{\partial y}v\right) = 0. \tag{5.9c}$$

Adopting the same scaling as done in chapter 4, the dimensionless equations now read

$$D_t u + F\frac{\partial U_0}{\partial x}u + F\frac{\partial U_0}{\partial y}v + \frac{\partial h}{\partial x} + F^2\frac{\partial H_0}{\partial x}D_t\left[D_t h + F^2\frac{\partial H_0}{\partial x}u + F^2\frac{\partial H_0}{\partial y}v\right] = 0,$$
$$\tag{5.10a}$$

$$D_t v + F\frac{\partial V_0}{\partial x}u + F\frac{\partial V_0}{\partial y}v + \frac{\partial h}{\partial y} + F^2\frac{\partial H_0}{\partial y}D_t\left[D_t h + F^2\frac{\partial H_0}{\partial x}u + F^2\frac{\partial H_0}{\partial y}v\right] = 0,$$
$$\tag{5.10b}$$

$$\frac{\partial u}{\partial x} + \frac{\partial v}{\partial y} - D_t^2\left(D_t h + F^2\frac{\partial H_0}{\partial x}u + F^2\frac{\partial H_0}{\partial y}v\right) = 0, \tag{5.10c}$$

where again F is the Froude number and $D_t = \partial_t + F\boldsymbol{U_0}\cdot\nabla$.

5.1.1　2D model for a single vortex

If the base flow is a simple radially dependent vortex of the form $\boldsymbol{U}_0(x,y) = U_0(r)\hat{\boldsymbol{\theta}}$, with $r = \sqrt{x^2+y^2}$, $H_0(x,y) = h_0(r)$ and such that $U_0(\infty) = 0$, then working accordingly in a cylindrical reference frame, the previous set of equations reduces to

$$\left(1 + F^4 h_0'^2\right)D_t u - 2F\Omega_0 v + \frac{\partial h}{\partial r} + F^2 h_0' D_t^2 h = 0, \tag{5.11a}$$

$$D_t v + F\Gamma_0 u + \frac{1}{r}\frac{\partial h}{\partial\theta} = 0, \tag{5.11b}$$

$$\frac{1}{r}\frac{\partial}{\partial r}(ru) + \frac{1}{r}\frac{\partial v}{\partial\theta} - D_t^2\left(D_t h + F^2 h_0' u\right) = 0, \tag{5.11c}$$

where now $u = u_r|_{h_0}$, $v = u_\theta|_{h_0}$, $h = p|_{h_0}$, $\Omega_0(r) = \frac{U_0(r)}{r}$ and $\Gamma_0(r) = 2\Omega_0(r) + r\Omega_0'(r)$. Note that the prime symbol here denotes differentiation with respect to the single spatial variable r. We tried different methods in order to rigorously justify the correctness of the ansatz (5.7) leading to our closure boundary condition. Details of each of them are outlined in the appendix C, however, none of them was totally successful, thus we can justify our closure by numerical predictions and comparisons.

5.2 Application of the model to a monopolar vortex in unbounded domain

5.2.1 Comparison with 3D finite-depth results for a single vortex

We want to provide evidence of the accuracy of the closure boundary condition on the free surface (5.7). For the results section we will show results for the single vortex case; in particular we will compare those obtained using the present novel model with those obtained in Zuccoli *et al.* (2023) with full three dimensional simulations. We fix the azimuthal wavenumber to $m = 7$ and the Froude number at $F = 0.5$. Then, we are going to vary the depth of the fluid at infinity and check the accuracy of our closure boundary condition.

Figures 5.1, 5.2, 5.3 show the two contributions appearing in (5.7) written for a single vortex for different set of normal mode solutions. In particular, the two contributions are $\partial_z w|_{h_0} - h_0'\partial_z u|_{h_0}$ on one side and $(i\omega - imF\Omega_0)\partial_z\phi|_{h_0}$ on the other. Moreover, next to the free surface contributions, the pressure distribution in the $r - z$ plane is displayed, suggesting how much the bottom boundary might influence the accuracy of the closure. From those figures, it can be noted that the two curves of the free surface contributions become indistinguishable as the height at infinity h_∞ grows. As a matter of fact, the accuracy of the closure boundary condition gets better as the bottom boundary ceases to influence the structure of the modes far away from the free surface. It is surprising, however, to see how the closure gives good results for $h_\infty = 1$ already. Thus, as soon as the horizontal and vertical reference scales become of the same order, the model we derived is valid and can be easily used.

Figure 5.4 instead displays the trend of the eigenvalues as function of the Froude number, for $h_\infty = 5$. The agreement is excellent, especially until $F = 0.6$ when the deformation of the surface starts to become dominant, implying a more influence of the bottom boundary too on the structure of modes.

The model we derived gives us exactly surface gravity modes and not the other type of waves that arise (see for example Mougel *et al.* (2015), Mougel
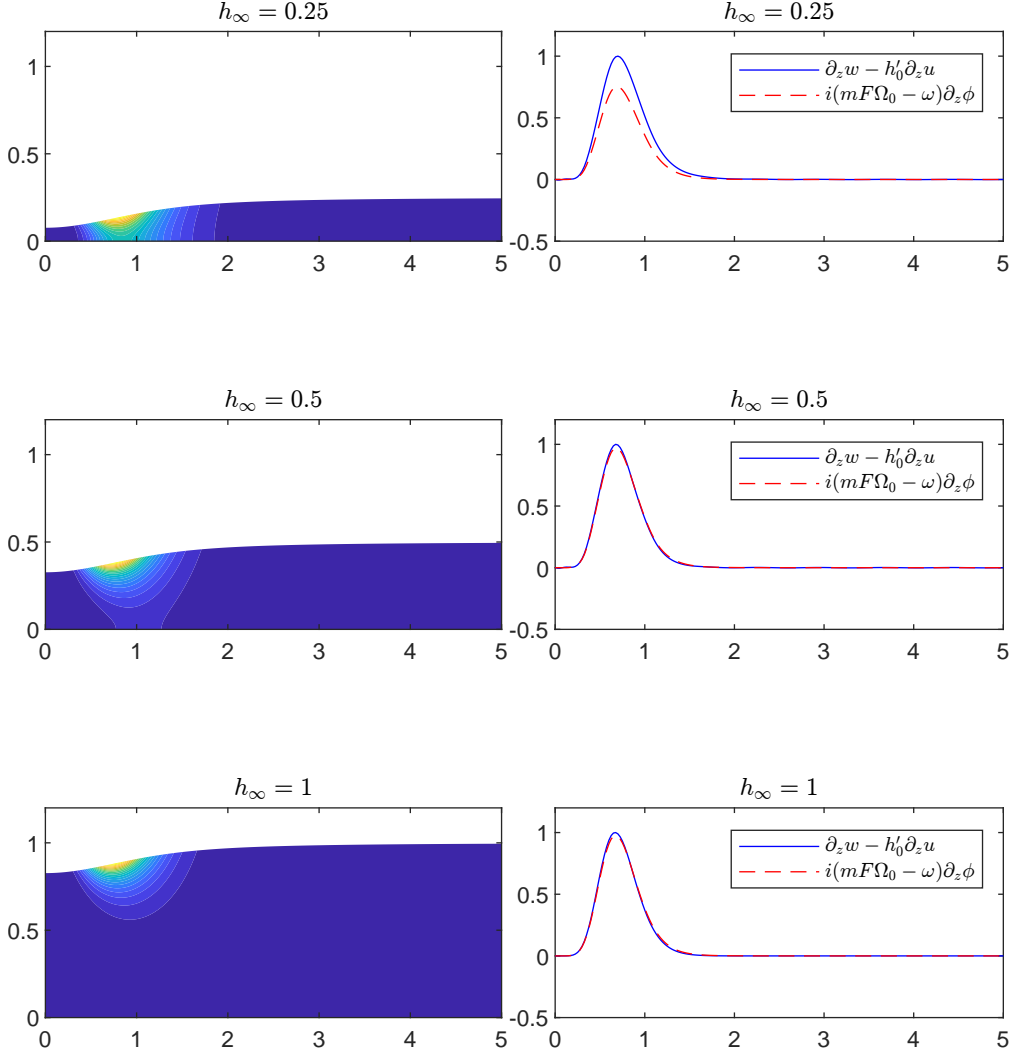
120

Figure 5.1: Accuracy of the closure boundary condition for the case of a Lamb-Oseen vortex. The mode considered here has a single peak in the modulus of the pressure $n = 1$, azimuthal wavenumber $m = 7$ and Froude number $F = 0.5$. The fluid depth at infinity has progressively been increased.

et al. (2017)) for further details on those. Hence, we would like to establish that our closure boundary condition works well for surface modes only. In figure 5.5 we compare the terms in the closure for a gravity and inertial mode respectively. It can be clearly seen our prediction is satisfied.

We have tested the accuracy of our closure for other type of vortices in addition to the Lamb-Oseen one. The only assumption in considering other single vortex profile is that the velocity field is zero at the origin and decays to zero at infinity. In particular, we have considered the following velocity profiles:

$$\Omega_0(r) = \frac{r}{4} \exp[2 - r], \tag{5.12}$$

and

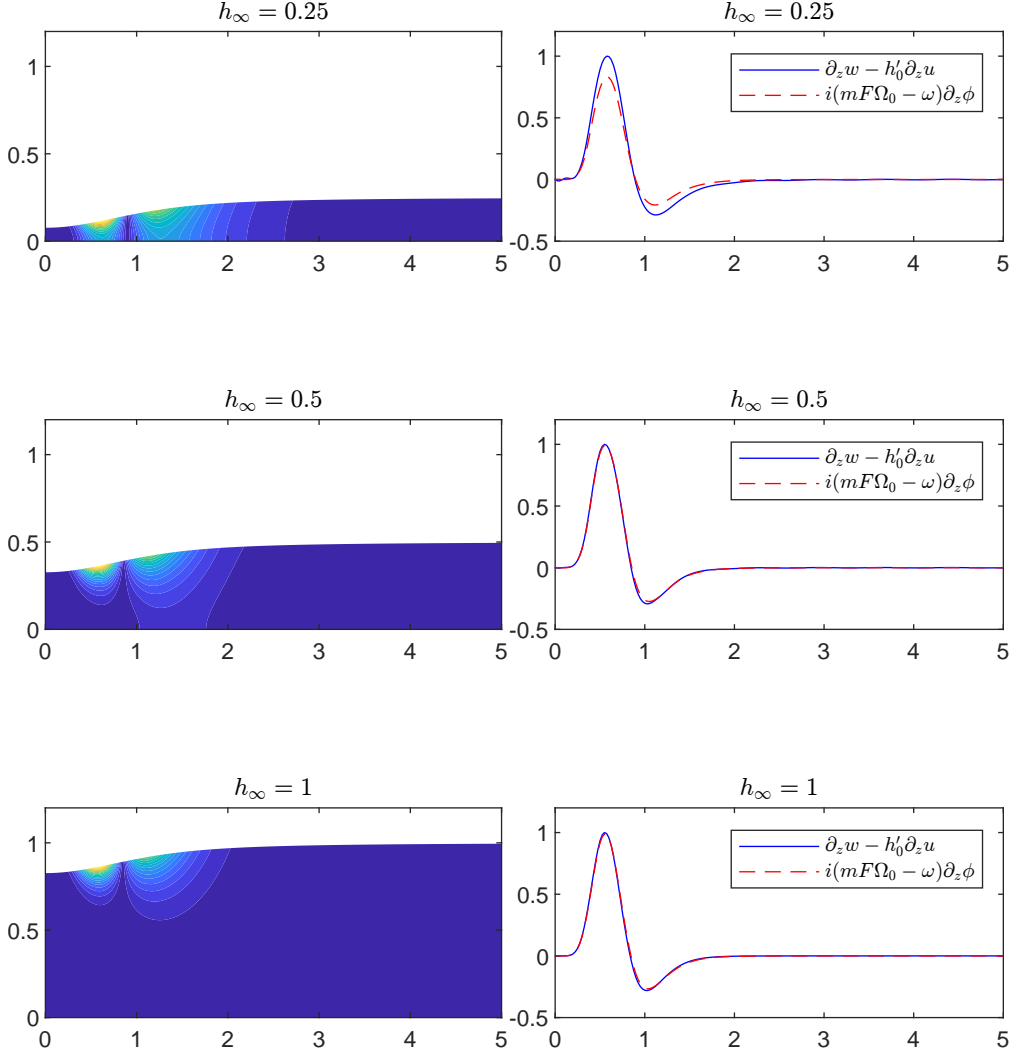$$\Omega_0(r) = \frac{1}{r^2 + 1}, \tag{5.13}$$

Figure 5.2: Accuracy of the closure boundary condition for the case of a Lamb-Oseen vortex. The mode considered here has two peaks in the modulus of the pressure $n = 2$, azimuthal wavenumber $m = 7$ and Froude number $F = 0.5$. The fluid depth at infinity has progressively been increased.

which is the same used as in Patrick *et al.* (2018). In figures 5.6 and 5.7 we plot the corresponding diagram as shown for the Lamb-Oseen profile, outlining the two contributions in the closure boundary condition.

Both base flows give again good agreement.

5.3 Application of the model to a periodic array of vortices

In this last section of the thesis we want use equations (5.10) to make predictions about the behaviour of deep-water surface waves over a more complicated, non-standard background flow, namely a periodic array of vortices. The flow is defined in a squared box of width 2π, i.e. $(x, y) \in [-\pi, \pi] \times [-\pi, \pi]$
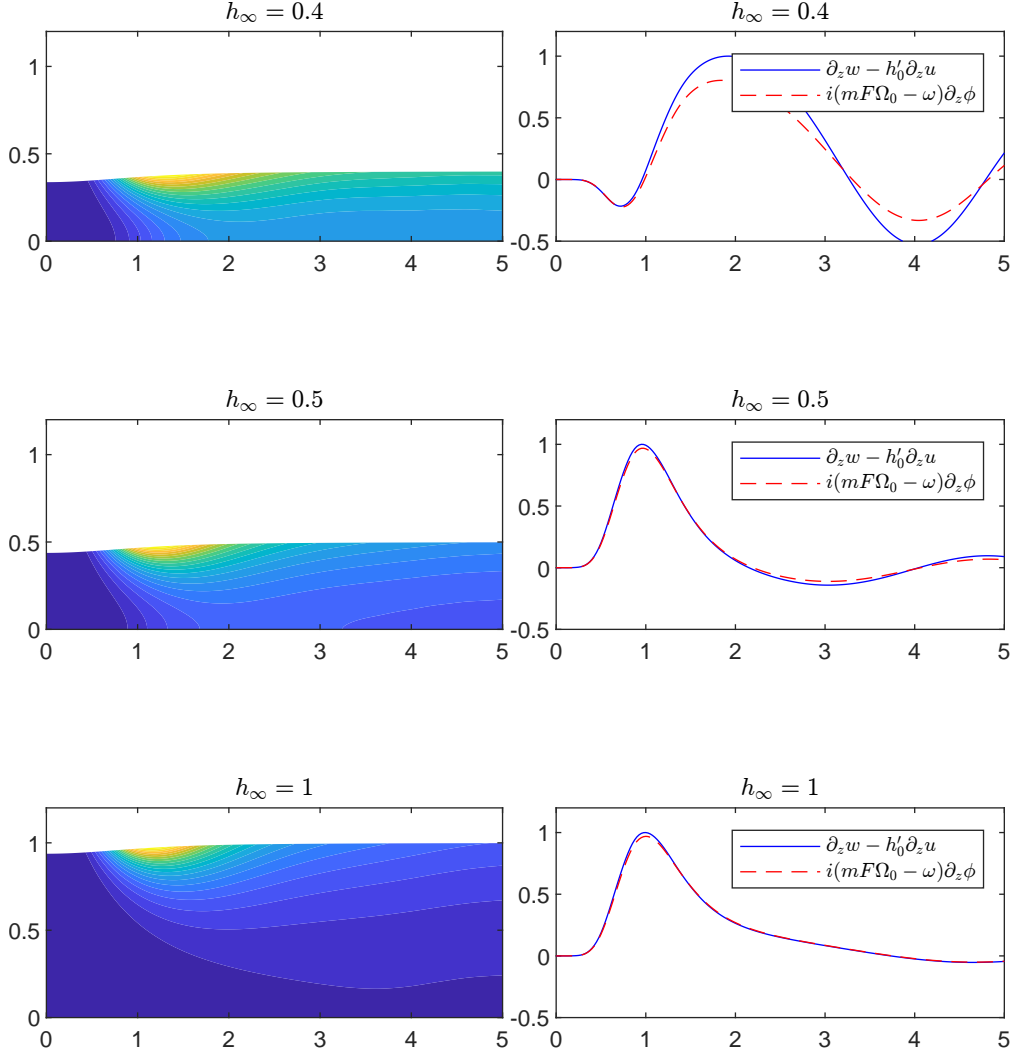
Figure 5.3: Accuracy of the closure boundary condition for the case of a Lamb-Oseen base vortex. The mode considered here is a radiating mode with azimuthal wavenumber $m = 7$ and Froude number $F = 0.3$. The fluid depth at infinity has progressively been increased.

and its velocity components are given by

$$U_0(x,y) = \sin(x)\cos(y), \qquad V_0(x,y) = -\cos(x)\sin(y). \qquad (5.14)$$

The velocity field is shown in figure 5.8.

Since the flow is periodic, the perturbations will also be so. However, before showing results for this specific problem, we first generalize the set of equations (5.9) in order to include the shallow-water regime too. This is convenient not only because it allows comparison in the two distinct regimes, but also because it eases the numerical treatment of the problem. The generalized
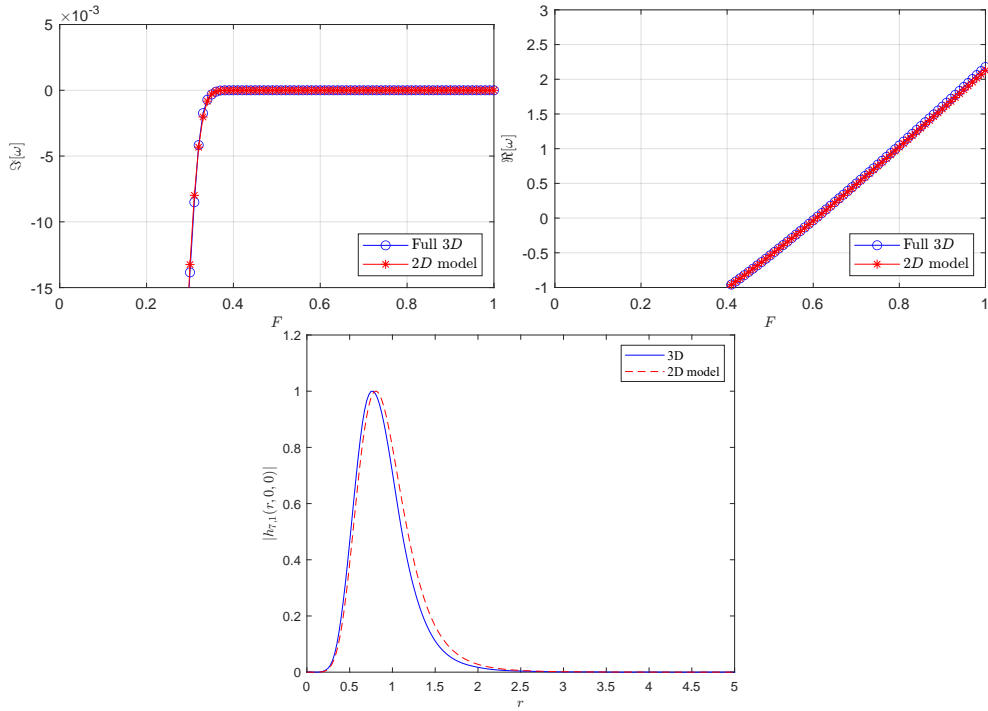
Figure 5.4: Top: comparison of the spectrum as function of the Froude numebr for the same vortex flow between the 3D simulations and the model. Bottom: comparison of least stable mode for the Lamb-Oseen vortex between the 3D results and the model for $F = 0.5$. Parameters have been taken as $m = 7$ and $h_\infty = 5$.

Figure 5.5: Comparison of the terms appearing in the closure boundary condition for a Surface Gravity mode (Top) and an Inertial mode (Bottom).
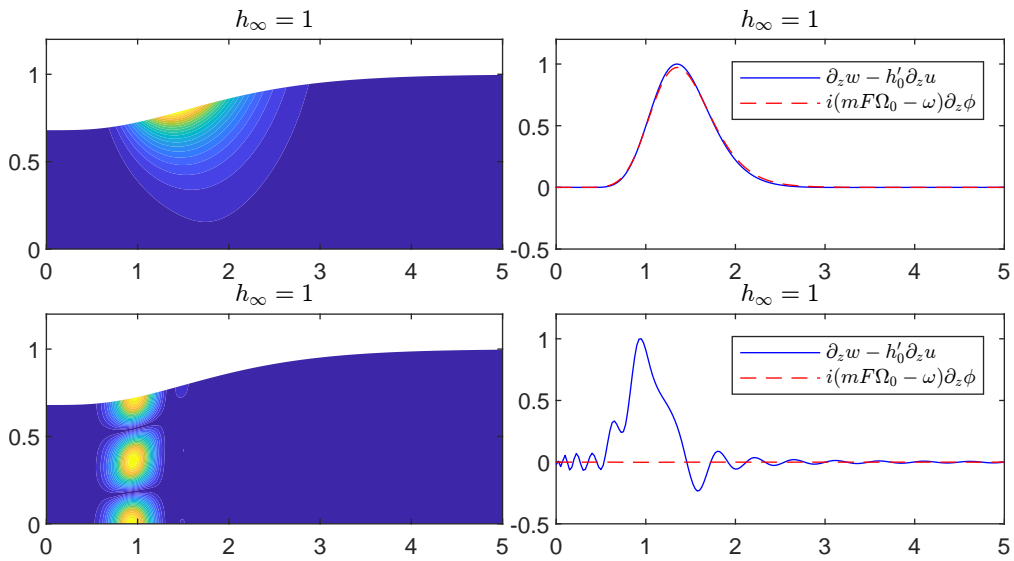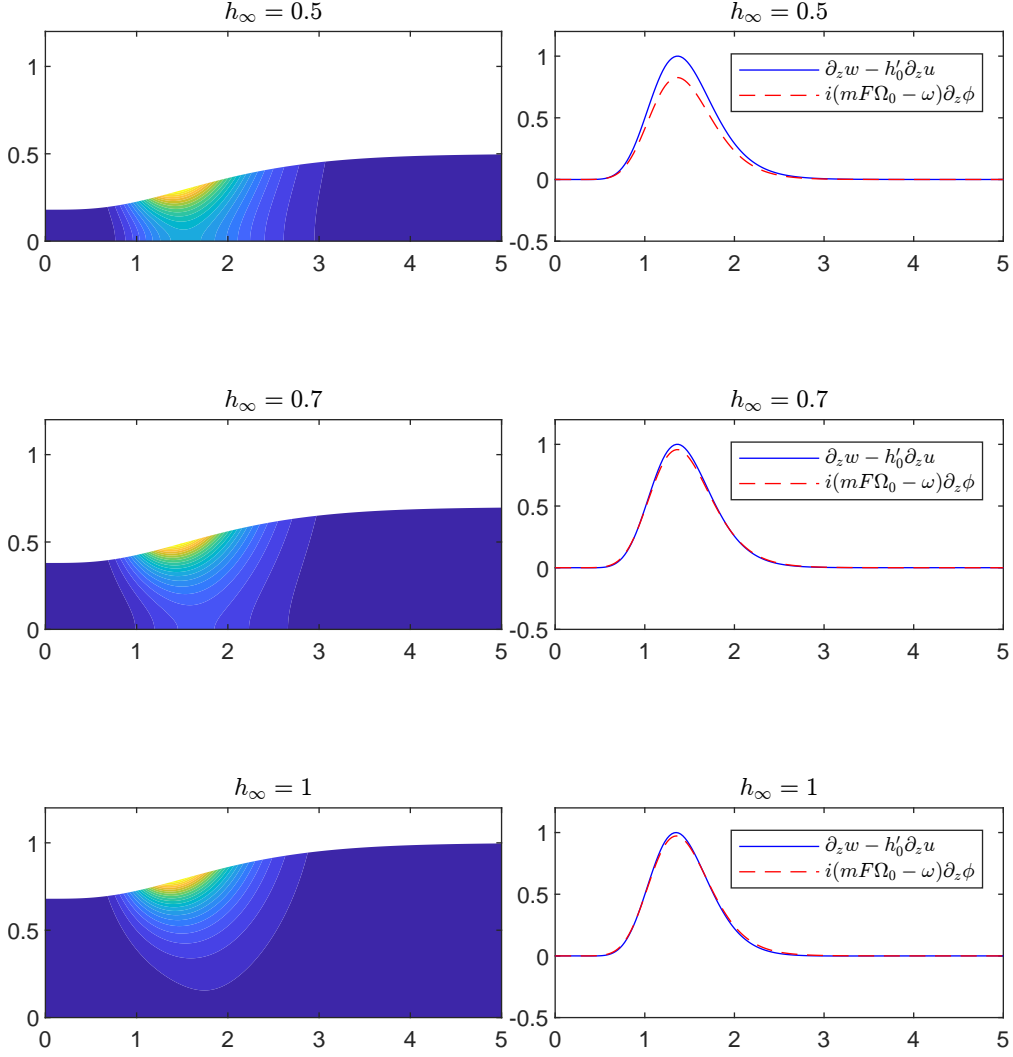
Figure 5.6: Accuracy of the closure boundary condition for the case of the vortex profile given by (5.12). The mode considered here is trapped with a single peak in the structure, azimuthal wavenumber $m = 7$ and Froude number $F = 0.5$. The fluid depth at infinity has progressively been increased.

equations read

$$D_t u + F\frac{\partial U_0}{\partial x}u + F\frac{\partial U_0}{\partial y}v + \frac{\partial h}{\partial x} + \delta F^2 \frac{\partial H_0}{\partial x}D_t\left[D_t h + F^2\frac{\partial H_0}{\partial x}u + F^2\frac{\partial H_0}{\partial y}v\right] = 0,$$
$$(5.15a)$$

$$D_t v + F\frac{\partial V_0}{\partial x}u + F\frac{\partial V_0}{\partial y}v + \frac{\partial h}{\partial y} + \delta F^2 \frac{\partial H_0}{\partial y}D_t\left[D_t h + F^2\frac{\partial H_0}{\partial x}u + F^2\frac{\partial H_0}{\partial y}v\right] = 0,$$
$$(5.15b)$$

$$\frac{\partial u}{\partial x} + \frac{\partial v}{\partial y} - \delta D_t^2\left(D_t h + F^2\frac{\partial H_0}{\partial x}u + F^2\frac{\partial H_0}{\partial y}v\right) + (1-\delta)D_t h = 0, \qquad (5.15c)$$

with $\delta \in [0,1]$ being the shallowness parameter. For $\delta = 0$, the linearized shallow water waves equations are recovered, whereas for $\delta = 1$, our model is re-obtained. In order to discretize the equations above, we want to re-write

125
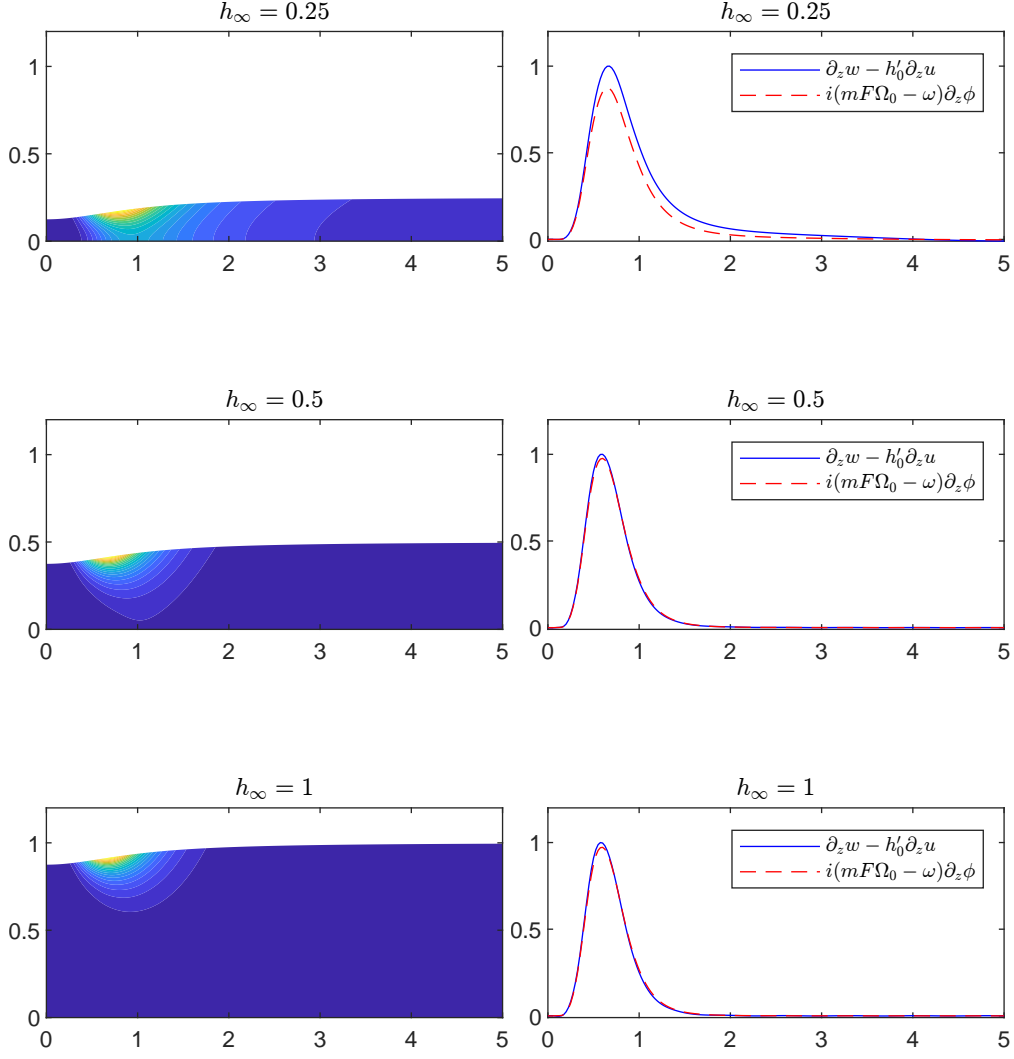
Figure 5.7: Accuracy of the closure boundary condition for the case of the vortex profile given by (5.13). The mode considered here is trapped with a single peak in the structure, azimuthal wavenumber $m = 7$ and Froude number $F = 0.5$. The fluid depth at infinity has progressively been increased.

them as a first order system in time. We define

$$
\begin{aligned}
w &= D_t h + F^2 \frac{\partial H_0}{\partial x} u + F^2 \frac{\partial H_0}{\partial y} v, \\
Q &= -\delta D_t w + (1 - \delta) h,
\end{aligned}
\tag{5.16}
$$
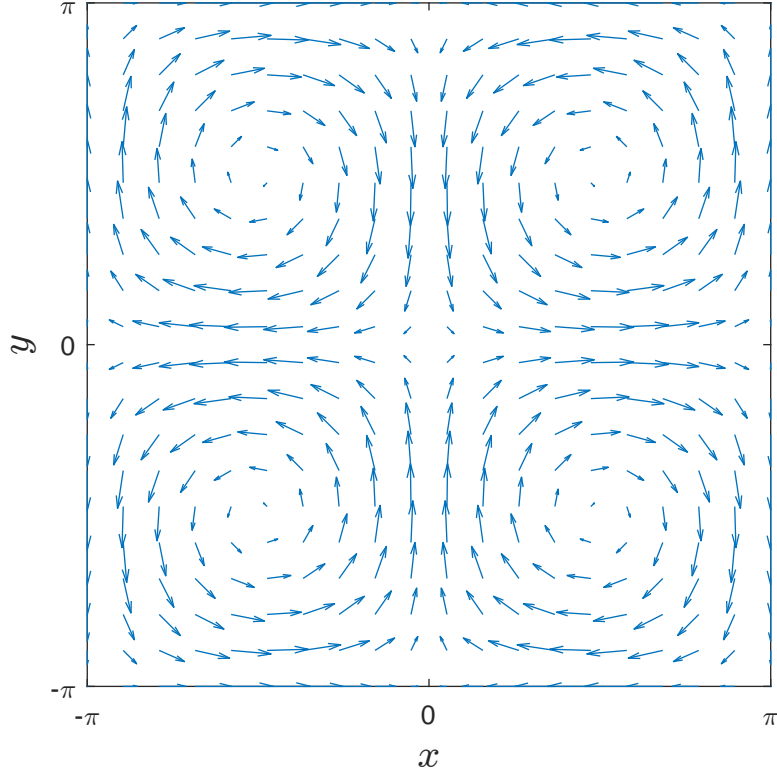
Figure 5.8: Velocity vector field for the flow defined by (5.14).

so that we obtain the following differential problem

$$D_t u + F \frac{\partial U_0}{\partial x} u + F \frac{\partial U_0}{\partial y} v + \frac{\partial h}{\partial x} - F^2 \frac{\partial H_0}{\partial x} \left[Q - (1 - \delta)h \right] = 0, \qquad (5.17a)$$

$$D_t v + F \frac{\partial V_0}{\partial x} u + F \frac{\partial V_0}{\partial y} v + \frac{\partial h}{\partial y} - F^2 \frac{\partial H_0}{\partial y} \left[Q - (1 - \delta)h \right] = 0, \qquad (5.17b)$$

$$D_t w + \frac{1}{\delta} \left[Q - (1 - \delta)h \right] = 0, \qquad (5.17c)$$

$$D_t h + F^2 \frac{\partial H_0}{\partial x} u + F^2 \frac{\partial H_0}{\partial y} v - w = 0, \qquad (5.17d)$$

$$D_t Q + \frac{\partial u}{\partial x} + \frac{\partial v}{\partial y} = 0, \qquad (5.17e)$$

in the five unknowns u, v, h, w, Q.

5.3.1 Numerical discretization

To solve equations (5.17) numerically we add some sort of artificial viscosity ν in the first two equations. This helps in getting rid of spurious unresolved eigenmodes when a finite difference scheme is applied. The system we want

to discretize then reads

$$D_t u + F\frac{\partial U_0}{\partial x}u + F\frac{\partial U_0}{\partial y}v + \frac{\partial h}{\partial x} - F^2\frac{\partial H_0}{\partial x}[Q - (1-\delta)h] - \nu\nabla^2 u = 0,$$

<div align="right">(5.18a)</div>

$$D_t v + F\frac{\partial V_0}{\partial x}u + F\frac{\partial V_0}{\partial y}v + \frac{\partial h}{\partial y} - F^2\frac{\partial H_0}{\partial y}[Q - (1-\delta)h] - \nu\nabla^2 v = 0, \quad \text{(5.18b)}$$

$$D_t w + \frac{1}{\delta}[Q - (1-\delta)h] = 0, \quad \text{(5.18c)}$$

$$D_t h + F^2\frac{\partial H_0}{\partial x}u + F^2\frac{\partial H_0}{\partial y}v - w = 0, \quad \text{(5.18d)}$$

$$D_t Q + \frac{\partial u}{\partial x} + \frac{\partial v}{\partial y} = 0. \quad \text{(5.18e)}$$

We look for normal modes $[u, v, w, h, Q](x, y, t) \to [u, v, w, h, Q](x, y)e^{\sigma t}$, with $\sigma \in \mathbb{C}$ being complex in principle; in particular $\Re[\sigma]$ represents the growth rate and $\Im[\sigma]$ the oscillation frequency. This transforms equations (5.18) into an eigenvalue problem of the form

$$\mathcal{L}\boldsymbol{v} = \sigma\boldsymbol{v}, \quad (5.19)$$

with $\boldsymbol{v} = [u, v, w, h, Q]^T$ and σ the eigenvalues to be determined. The aim now is to discretize the linear operator $\mathcal{L}$. To do so we use a centered finite difference scheme as the one used in section 3.6.2 for the Convective Wave Equation. However, here we apply periodic boundary conditions in both x and y. Let us explain how to deal with them by looking only at u in the x-direction. The first derivative is discretize as

$$\frac{\partial u(x_j, y)}{\partial x} = \frac{u(j+1, y) - u(j-1, y)}{2\Delta x}, \qquad j = 0, 1, 2, \ldots, N_x. \quad (5.20)$$

At the boundary points we impose $u(0, y) = u(N_x, y)$ and $u(N_x + 1, y) = u(1, y)$. The same rule holds for the derivative along y, as well as for both $v(x, y)$ and $h(x, y)$.

5.3.2   Results

In this section we present results of the eigenvalue problem coming from solving equations (5.18) for $\delta = 1$, i.e. in the deep-water limit. First, in figure 5.9 we present the structure of the first least stable modes computed for a slow rotation of the four vortices, namely for $F = 0.1$. The value of the artificial viscosity has been set equal to $\nu = 0.01$. By keeping the same value of artificial viscosity we then varied the Froude number in the range $F \in [0.1, 1.5]$ and found that the array of vortices undergoes an instability. The trend of both the real and imaginary part of the eigenvalues is shown in figure 5.10. It is interesting to notice that the first mode gets unstable at very low rotation
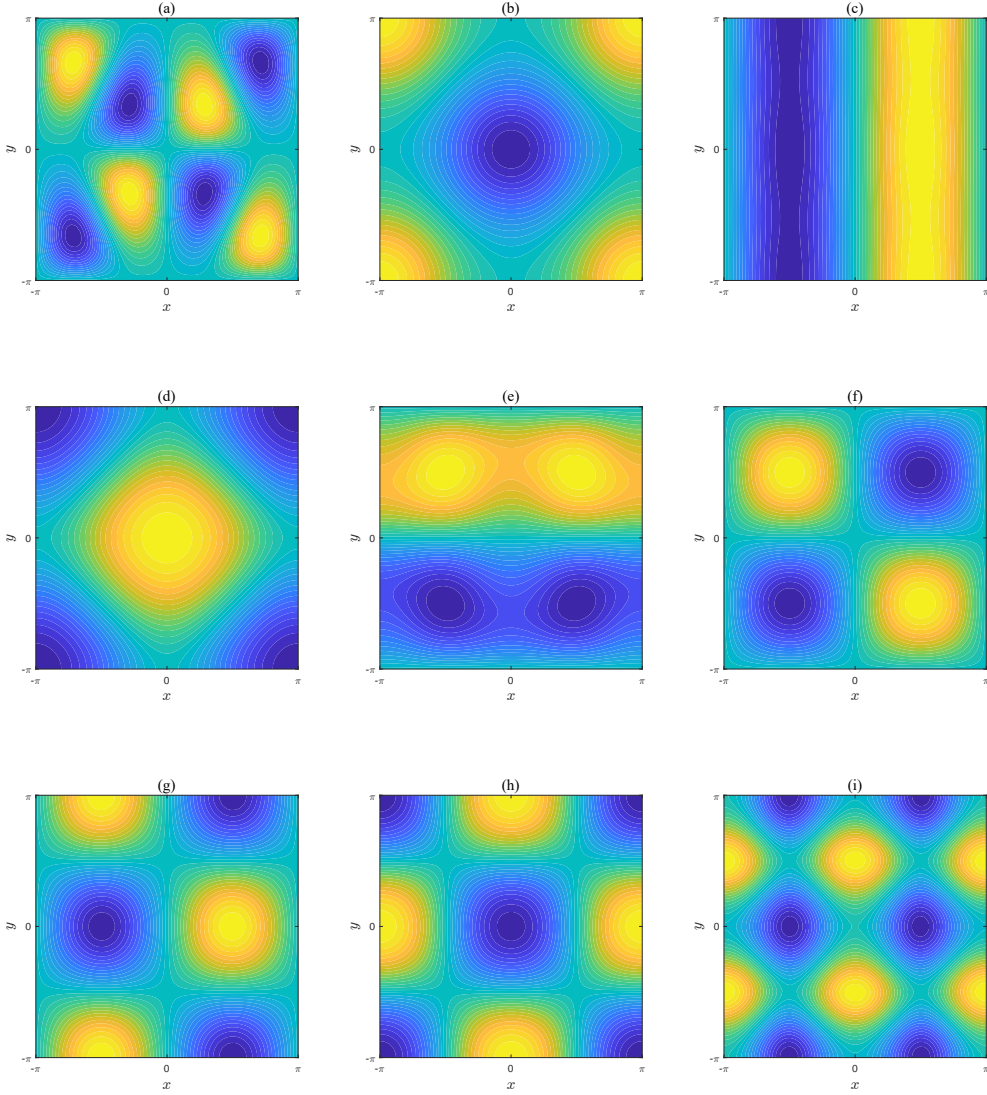
Figure 5.9: Least stable eigenmodes for $F = 0.1$, and $\nu = 0.01$. The real part of the surface height is plotted: $\Re[h(x,y)]$. Corresponding eigenvalues follow. (a): $\sigma = -0.0014 + 0.0509i$. (b): $\sigma = -0.0024 + 1.0226i$. (c): $\sigma = -0.0026 + 0.9974i$. (d): $\sigma = -0.0028 + 0.9740i$. (e): $\sigma = -0.0044 + 0.0000i$. (f): $\sigma = -0.0051 + 1.1901i$. (g): $\sigma = -0.0055 + 1.1738i$. (h): $\sigma = -0.0057 + 1.1593i$. (i): $\sigma = -0.0101 + 1.4246i$

rates, but becomes stable again at higher Froude numbers. Moreover, there is a precise Froude number $F = 0.9864$ where the two modes have the same growth rate, but they oscillates at different frequencies.

Figures 5.11 and 5.12 show the modulus of the perturbation height eigenfunctions at different Froude numbers, both for the first and the second unstable modes.

In accordance to what is shown in chapter 4 for the case of a monopolar vortex, we now want to show the direction along which waves rotate with respect to the periodic background flow. In figure 5.13 we show the time dependent evolution of the first unstable mode for $F = 0.2$. It emerges that this mode co-rotates with the flow. (The second mode also co-rotates with the

129
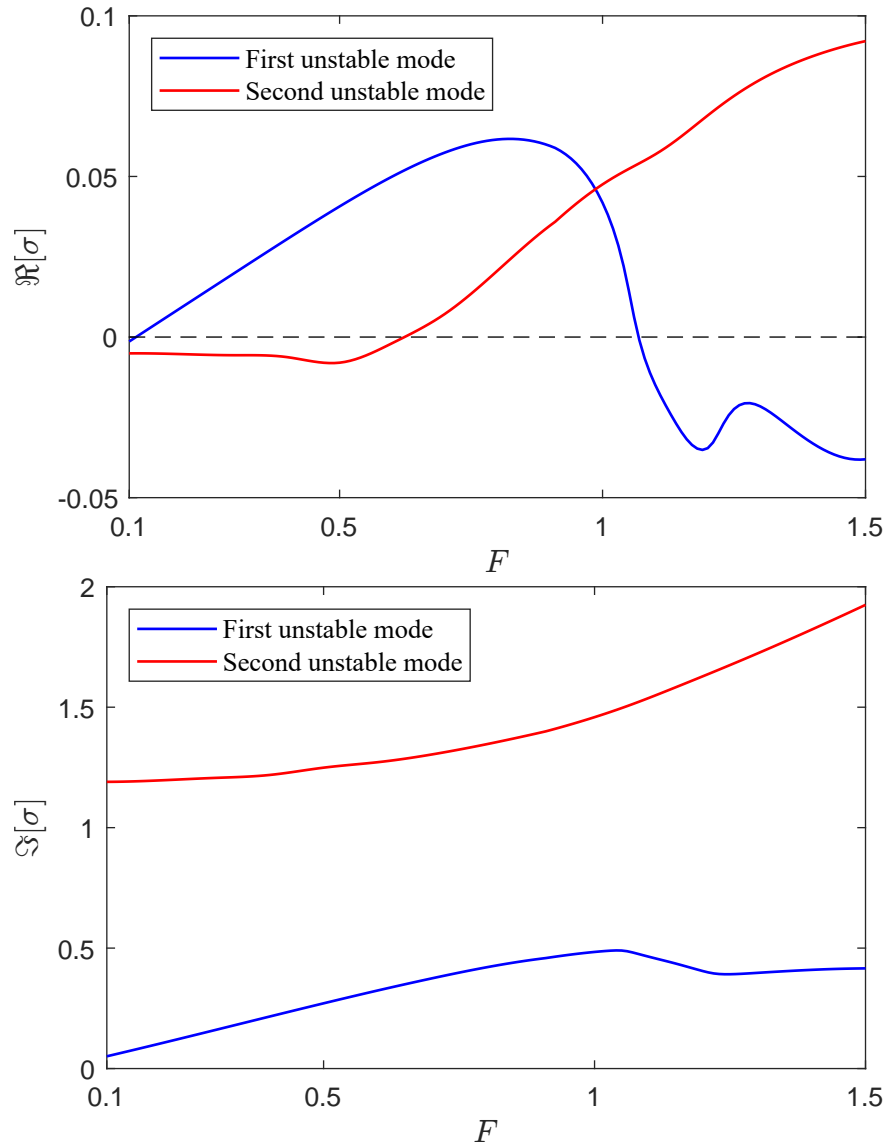
Figure 5.10: Trend of the eigenvalues of the first two unstable modes as function of the Froude number. Top: real part of the eigenvalues representing the growth rates as function of the Froude number. Bottom: imaginary part of the eigenvalues representing the oscillation frequencies as function of the Froude number.

flow, but for brevity this is not shown.)

Finally, the last set of results we show is about the trend of the eigenvalues as the artificial viscosity ν is decreased, for the fixed Froude number $F = 0.1$. The trend of both the real part and the imaginary part of the eigenvalues is shown in figure 5.14. The real part is plotted on a log-log scale and shows a linear dependence, hence it goes as a power law with the viscosity. The imaginary part, as expected, remains unchanged.

Clearly, it would be interesting to track most of the other eigenvalues
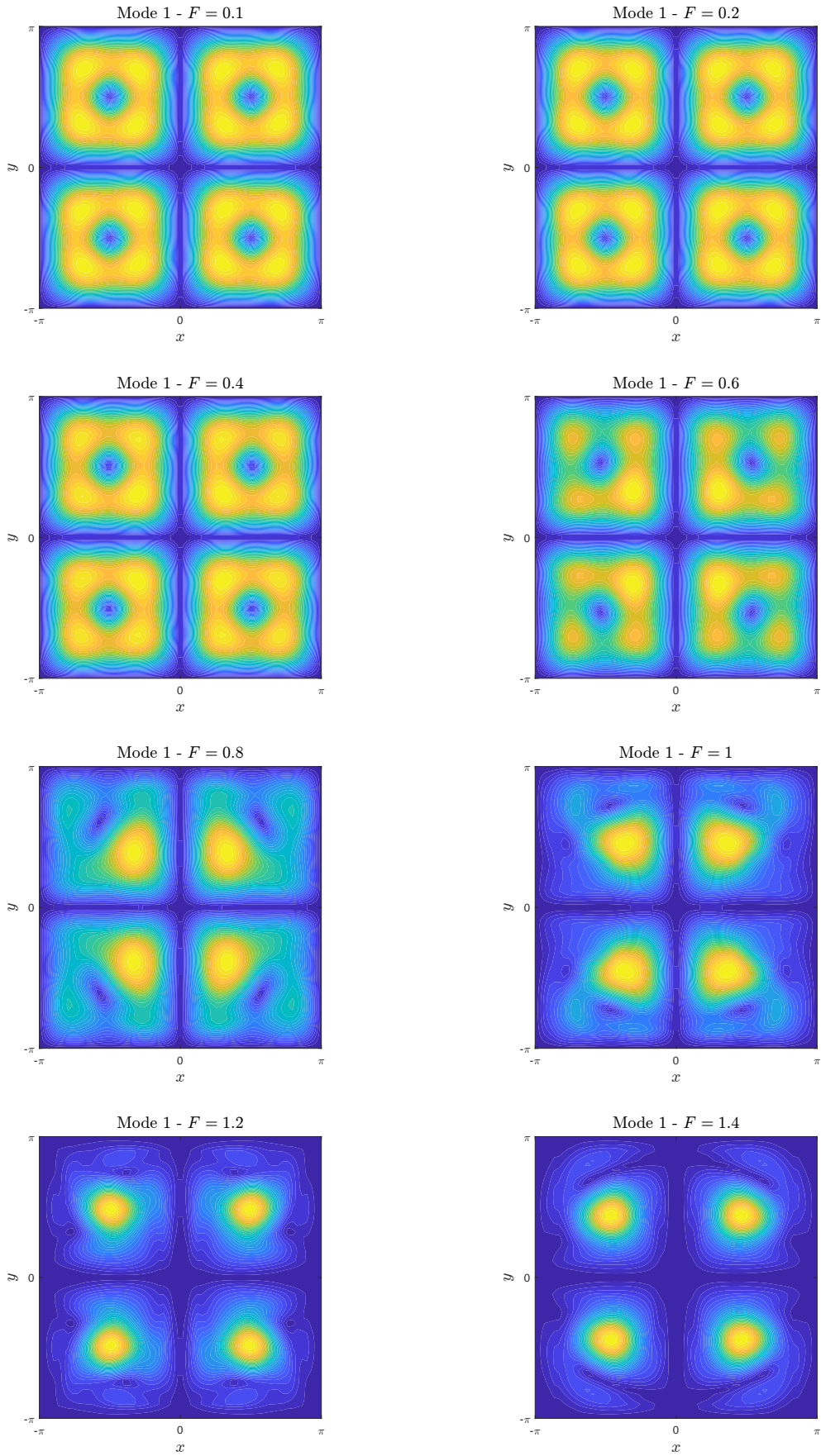
Figure 5.11: Evolution of the structure of the first unstable mode for the following Froude numbers: $F = [0.1, 0.2, 0.4, 0.6, 0.8, 1, 1.2, 1.4]$.

131
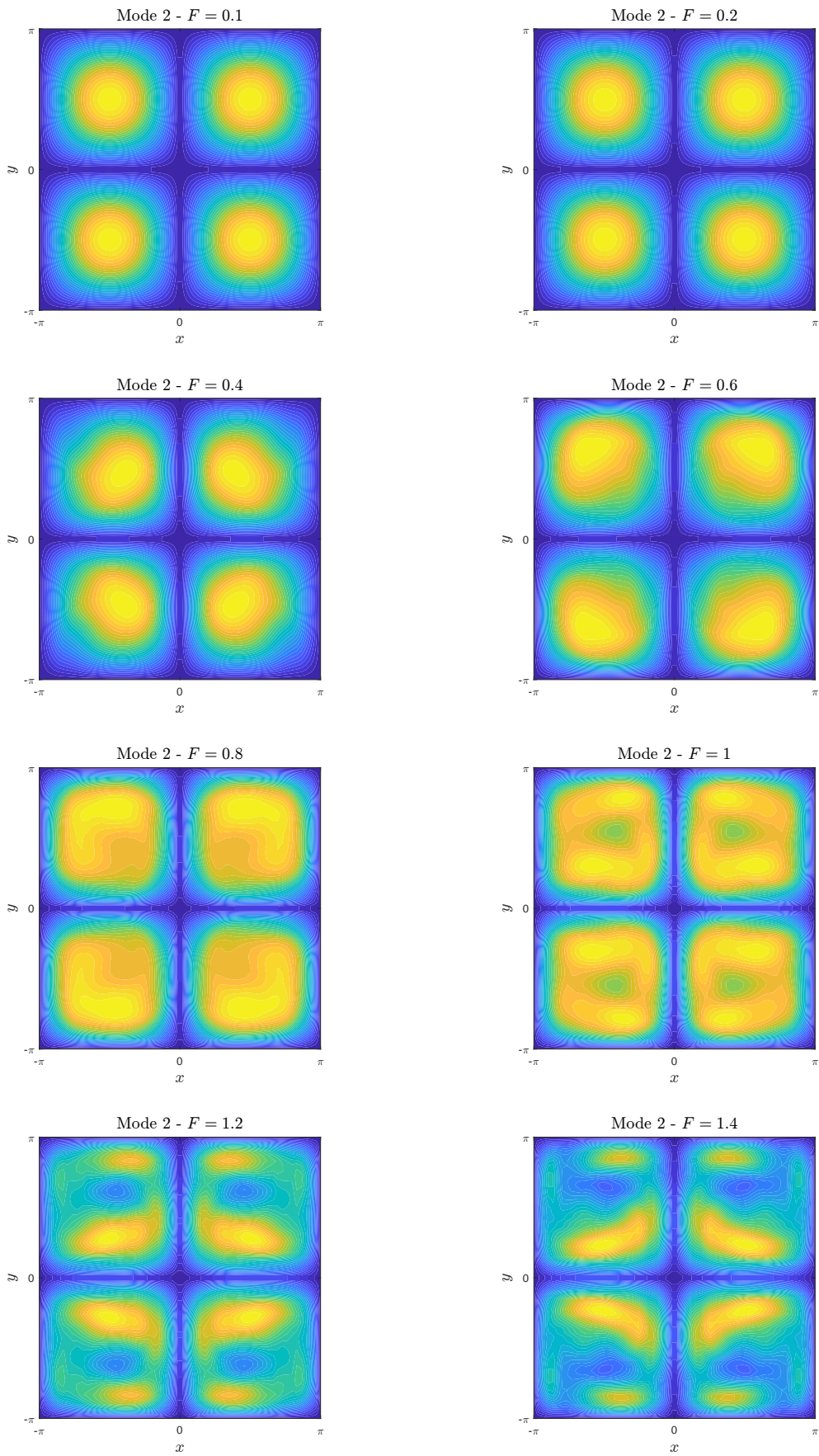
Figure 5.12: Evolution of the structure of the second unstable mode for the following Froude numbers: $F = [0.1, 0.2, 0.4, 0.6, 0.8, 1, 1.2, 1.4]$.

shown in the previous figures as function of the artificial viscosity. However, time availability limited the computations of this set of additional results, thus we leave to future studies the achievement of this goal and a full characterization of the eigenmodes in the proper inviscid limit.

5.4 Summary

In this chapter we presented a novel two-dimensional system of equations to study the vortex-surface waves in the deep water limit. The novelty of the model lies in the introduction of a closure boundary condition that has to be satisfied along the free surface shape, which leads naturally to a reduced set of equations valid in a horizontal domain.

The validity of the closure boundary condition has been tested for different type of modes and base vortex flows and compared with the full 3D results from Zuccoli *et al.* (2023).

Finally, we used the reduced model to make predictions on the eigenmodes arising from an array of vortices in a periodic square domain. Computations gave interesting results as the appearance of unstable modes.
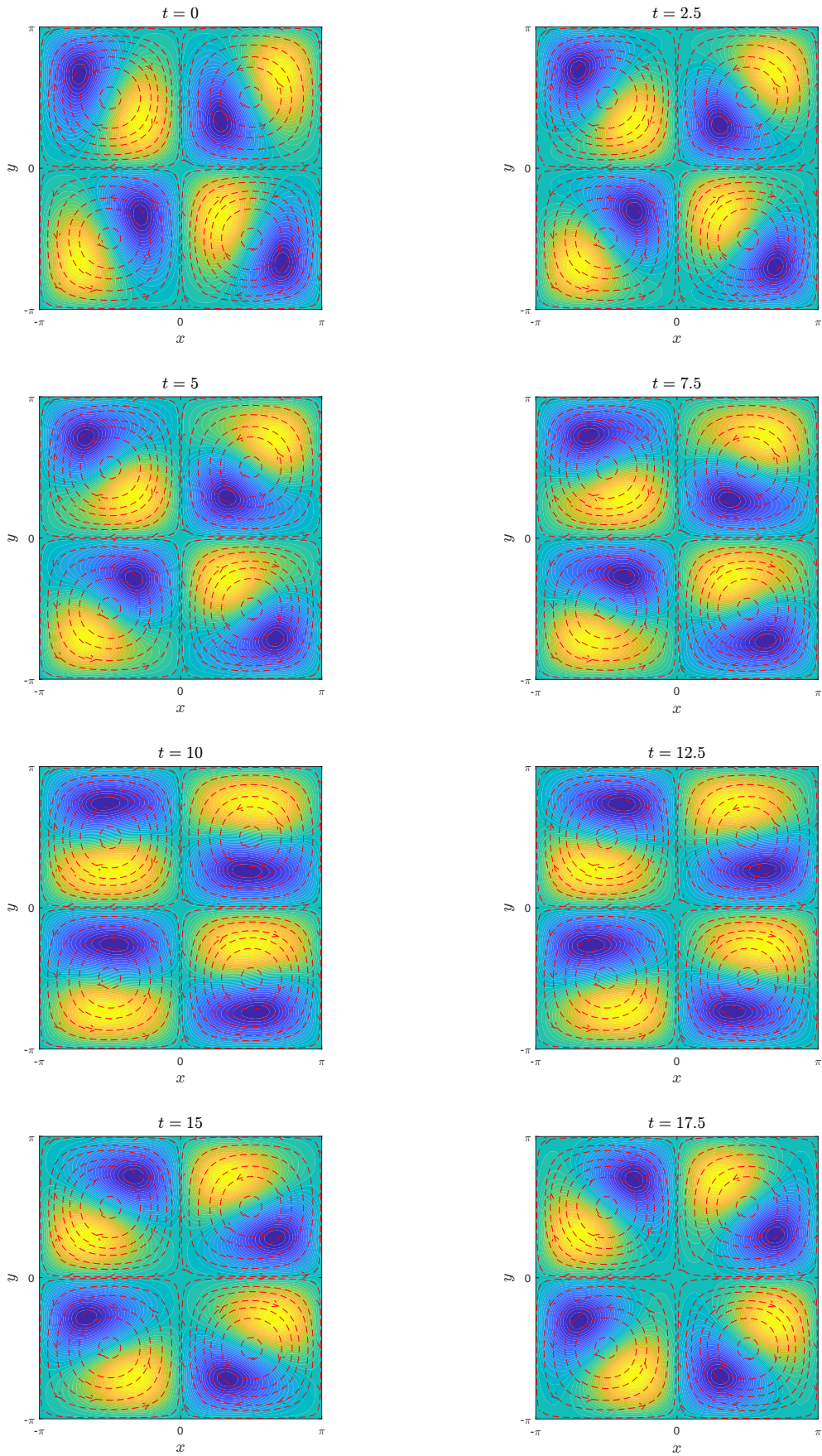
Figure 5.13: Time evolution of the first unstable mode ($\sigma = 0.0093 + 0.1047i$) arising at $F = 0.2$ and with $\nu = 0.01$ for different times: $t = [0, 2.5, 5, 7.5, 10, 12.5, 15, 17.5]$. Red-dotted lines represent the streamlines of the periodic array of vortices.

134
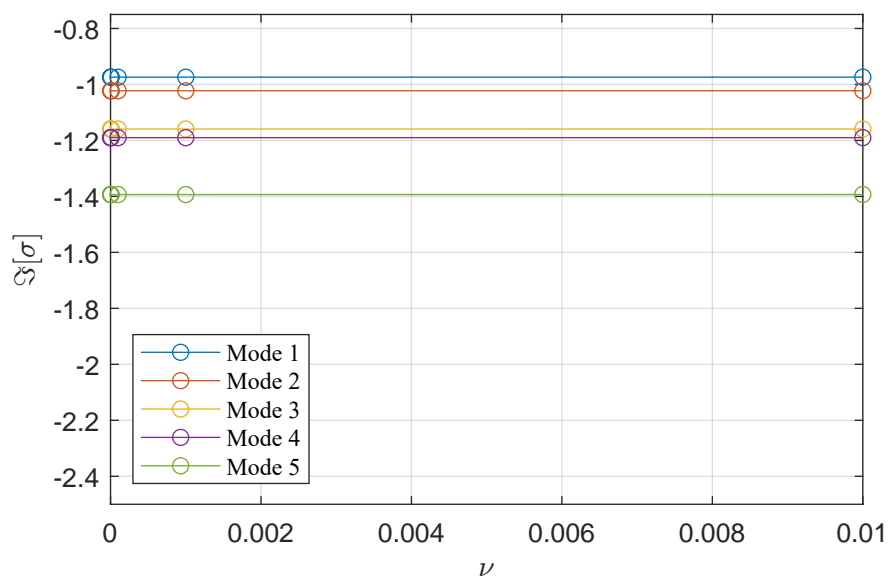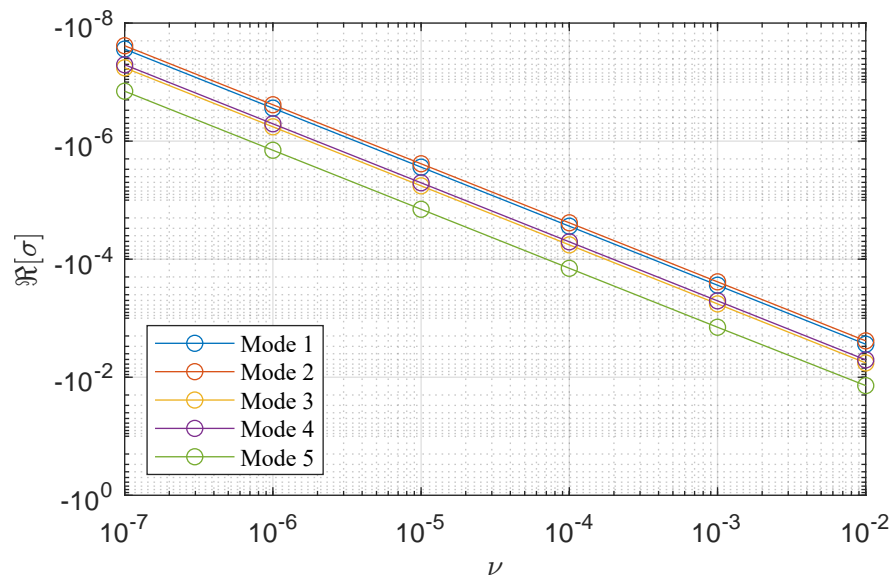
Figure 5.14: Eigenvalues trend as function of the artificial viscosity ν for $F = 0.1$. Top: real part of σ on a log-log scale. Bottom: imaginary part of σ on a linear scale.

Chapter 6

Conclusions and future research

We have considered the linear response to small perturbations of several free surface swirling flows in different configurations and under different approximations. The perturbations are generally seen as waves of various type propagating at precise frequencies and having a defined spatial structure. The specific kind of wave and its features depends both on the geometry of the system and on the particular background flow considered. The main results of this thesis concern the modelling of surface waves within different approximations. From a more technical point of view, the major difficulty we had to address is the implementation of non-reflecting boundary conditions for the simulation of such waves in a laterally unbounded region. We now give a detailed summary of what has been done throughout the chapters of the thesis together with aspects that can be further investigated in the future.

In chapter 2 we studied waves forming in a laterally confined flow. The specific cases of no flow and solid-body rotation were considered exhaustively, with the aim of highlighting the major features in terms of wave-flow interaction and implementing some numerical schemes. Whenever the base flow is absent, or negligible, only one type of waves is formed and these are surface gravity waves. The only restoring force in that case is gravity and those modes have an oscillatory behaviour in the radial direction, but an exponential behaviour in the axial direction. The dispersion relation in the general finite-depth case is highly nonlinear, but reduces to a linear one in the shallow-water regime (confirming the non-dispersive characters of these waves) and to a quadratic one in the deep-water regime. It has been shown, however, that the shallow-water limit ceases to be valid very soon as function of fluid depths reasonably employed in applications, hence giving motivation to study these kind of problems in deeper-water configurations. In particular, in chapter 2 we considered extensively the prototype Newton's Bucket problem and studied it both numerically and analytically. No instability is found in this configuration

(consistent with Mougel *et al.* (2015)). We have been able to provide excellent analytical results to help getting the oscillation frequencies of modes in the very deep-water limit as function of the rotation rate of the flow. Given the simplicity of the base flow in this case, it would be a good starting point for investigating the effects of both viscosity and surface tension, as well as the equivalent of a Faraday Waves problem (Benjamin and Ursell 1954), i.e. the response of the system to a prescribed vertical oscillation. Moreover, comparison with experimental studies would be beneficial to validate the theory developed.

In chapter 3 the Convective Wave Equation arising from the shallow-water limit was studied. This model is the first attempt to include the advection process in wave propagation over a prescribed swirling flow in an unbounded region. It shows two classes of modes that we also consider in chapter 4, namely radiating modes and trapped modes. Radiating modes are dissipative, and have a spatial structure which extends in the horizontal plane, therefore behaving as radially-travelling waves. By contrast, trapped modes, by virtue of their near zero growth rate, persist for long times with little dissipation and remain localized within the core region of the vortex and hence could be expected to be observed on the surface of a rotating vortex after all damped modes have dissipated. The spatio-temporal behaviour of these modes resembles that of a radially-standing wave instead of a radially-travelling wave. Our numerical predictions show the appearance of trapped modes provided the Froude number F (the dimensionless rotation rate) is above a threshold value, with the threshold depending on the azimuthal mode number m. For both a Lamb-Oseen vortex and a Gaussian vortex our computations also showed the appearance of an instability, with higher growth rates at low azimithal wavenumbers and a wider range of nearly neutrally stable states for large m, as summarized in figures 3.5–3.6. This confirms the "Ergoregion Instability" argument proposed in Oliveira *et al.* (2014) for waves on a potential vortex.

We then studied the same equation, but changing the background flow to a dipole solution. The idea indeed was to mimic more closely the interaction between the two vortices travelling in the swimming pool and the surface waves around them. We carried out a time-dependent simulation on a square domain in cartesian coordinates. We investigated the response to axisymmetric perturbations for three different Froude numbers $F = 0.25, 0.5, 0.75$. Our computations showed the appearance of a complex dynamics at both $F = 0.5$ and $F = 0.75$ due to the possible generalization of the ergoregion and horizon arguments from the monopolar vortex case. However, the numerical costs needed to get accurate results were too high, thus implementation of alternative strategies to get more insight into this problem is left as a future research. In particular, the polar grid with a reduced number of grid points used in sections A.1 and A.2 to test the code with a monopolar vortex, might be extended

to the dipole case, bringing a reduction in the computational costs. Another approach would be that of adding a filter in the spatial discretization applied in the cartesian formulation—see for example Bogey and Bailly (2003). This would help in obtaining smooth solutions whenever high gradients are present, as shown in figure 3.20.

In chapter 4 we have considered the linear response to small perturbations of a free surface Lamb–Oseen vortex flow in a laterally unbounded domain. We focused our attention primarily on surface waves, as it was these waves that were seen in the motivating experiment; although the numerical procedure also captures other types of modes which we briefly report on. Our study found that surface waves fall into two distinct classes: radiating modes and trapped modes. While these have been previously discovered for shallow water vortices with an inflow (such as a bathtub vortex), and for purely rotating flows—as done in chapter 3 of the present work—here we have shown that they arise in a fully 3D non-shallow-water problem without the need for an inflow to help trap the modes. The same features regarding both radiating and trapped modes are recovered here, as explained previously for the results of chapter 3. The major difference in this case, however, is that trapped modes apparently asymptotically approach a neutrally stable state in the limit of large Froude number without becoming unstable. We have ultimately confirmed what has been seen in the initial motivating experiment of the pool, namely that trapped surface wave modes in finite-depth configurations exist, are nearly neutrally stable, and can propagate with or against the base swirling flow (as also summarized in figure 4.14). That initial motivating experiment, in fact, is a real case where finite-depth effects are non-negligible and the typical wavelengths of the surface waves is lower than the reference height of the free surface.

As pointed out many times in this work, to numerically simulate a (horizontally-)unbounded fluid on a bounded numerical domain, a far-field non-reflecting boundary condition or buffer region is needed. Here, a novel additional term is introduced into the governing equations, to provide damping of the surface waves in the buffer region only. This method has proved more accurate than any non-reflecting boundary condition we implemented while remaining computationally viable. Indeed, introduction of additional unknowns in the mathematical formulation was not needed, thus overcoming the main drawback of PML methods. Furthermore, given that the background vortex flow vanishes in the far-field, the same absorbing layer formulation can be employed with other similar vortex distributions. The numerical expense of our eigenvalue problem (which is a two-dimensional spatial problem involving both r and z coordinates) might be reduced by investigating a one-dimensional approximation along the radial coordinate only; for example in either the deep- or shallow-water limits. Moreover, new methods and formulations for the im-

position of a non-reflecting boundary condition in the far-field would certainly lead to a saving in the computational time as it will avoid, for example, the need to numerically resolve the unphysical buffer region. Due to the computational expense, we have left to future studies the extension of our parametric study of waves to extreme Froude numbers. In particular it would be interesting to investigate the trend of modes for very small and very large Froude numbers.

Throughout chapter 4, we assumed a harmonic dependence $\exp\{-\mathrm{i}\omega t + \mathrm{i}m\theta\}$ (equation 4.8) and looked for modal solutions, and alternative approaches, such as time-domain simulation, may give additional insight. This is particularly in relation to the critical layer, which is where there is a radial location $r = r_c$ for which $D_t = -\mathrm{i}\omega + \mathrm{i}mF\Omega_0(r_c) = 0$; this possibility has been neglected here, and investigating it would require a different numerical and mathematical method (such as has been done for aeroacoustic waves; e.g. King *et al.* 2022). Even with the assumption of harmonic dependence $\exp\{-\mathrm{i}\omega t + \mathrm{i}m\theta\}$, a different but related problem would be to investigate the scattering of an incoming wave encountering the vortex, which would require a different far-field boundary condition to introduce the incoming wave as well as to allow outgoing waves to propagate through the far-field boundary without reflection. Finally, our model also neglects both nonlinear and surface tension effects; while this is justified for the swimming pool application we model here, these assumptions break down for either large amplitudes or short wavelengths. Therefore, it would be interesting to investigate whether their inclusion could lead to an instability of the base vortex flow.

In chapter 5 we derived a new reduced two-dimensional model in order to compute surface wave modes on any arbitrary two-dimensional flow. The model overcomes the most widely used approximations of neglecting the free surface deformation and of considering potential background flows. The idea behind the derivation of the model is in principle very simple and consists of evaluating the linearized Euler equations on the base free surface and then introduce a closure equation to close the reduced system. The closure is represented by a closure boundary condition and the way it has been derived is based on a heuristic argument, as well as on the numerical results presented in chapter 4. Results presented in chapter 5 can be categorized into two main sections: in the first part we justify the validity of our closure boundary condition. We tested it for both radiating and trapped modes in the case of a Lamb-Oseen vortex and extend this test for two other vortex profiles. Moreover, we directly compare the curve showing the trend of the eigenvalues as function of the Froude number with that obtained from the full 3D computations shown in chapter 4 for the specific parameters $m = 7$ and $h_\infty = 5$. The overall comparison results are excellent and confirm the efficiency of our reduced model. In the second part of the chapter we tried to make a predic-

tion about the dynamics of deep-water waves on a periodic array of vortices. Since the system cannot be compared with previous results, this is a prediction of how those waves interact with a non-classical vortical flow. The problem has been studied in a periodic domain and brought some interesting results and dynamics, as for example the emergence of unstable modes. More care and development is still needed in this case, hence this could certainly be the source of future investigations on the topic. Another very useful development on the study carried out in this chapter is represented by a possible rigorous derivation of the closure boundary condition. In fact, we tried to justify it rigorously in appendix C using three different strategies, but none of them gave the desired result. It would therefore be useful to come up with new ideas to justify our closure model.

Appendix A

The Convective Wave Equation for a general two-dimensional flow in polar coordinates

In this appendix we consider the two-dimensional CWE introduced in chapter 3 for an arbitrary background flow in polar coordinates. The flow is given by $\boldsymbol{U_0}(r,\theta) = U_r(r,\theta)\hat{\boldsymbol{r}} + U_\theta(r,\theta)\hat{\boldsymbol{\theta}}$, and the governing equation reads

$$\left(\frac{\partial}{\partial t} + U_r\frac{\partial}{\partial r} + \frac{U_\theta}{r}\frac{\partial}{\partial \theta}\right)\left(\frac{\partial}{\partial t} + U_r\frac{\partial}{\partial r} + \frac{U_\theta}{r}\frac{\partial}{\partial \theta}\right)\phi - c^2\left(\frac{\partial^2\phi}{\partial r^2} + \frac{1}{r}\frac{\partial\phi}{\partial r} + \frac{1}{r^2}\frac{\partial^2\phi}{\partial \theta^2}\right) = 0.$$

$$\text{(A.1)}$$

We assume the base flow to decay at large distance from the centre, so that as $r \to \infty$ we can impose the exact non-reflecting boundary condition

$$\lim_{r\to\infty} \sqrt{r}\left(\frac{\partial\phi}{\partial t} + c\frac{\partial\phi}{\partial r}\right) + \frac{c}{2\sqrt{r}}\phi = 0. \qquad \text{(A.2)}$$

At the origin, a regularity condition is needed, whereas along the angular direction we impose the solution to be periodic, independently of the background flow considered. The complete differential problem under study reads

$$\left(\frac{\partial}{\partial t} + U_r\frac{\partial}{\partial r} + \frac{U_\theta}{r}\frac{\partial}{\partial \theta}\right)\left(\frac{\partial}{\partial t} + U_r\frac{\partial}{\partial r} + \frac{U_\theta}{r}\frac{\partial}{\partial \theta}\right)\phi - c^2\left(\frac{\partial^2\phi}{\partial r^2} + \frac{1}{r}\frac{\partial\phi}{\partial r} + \frac{1}{r^2}\frac{\partial^2\phi}{\partial \theta^2}\right) = 0,$$

$$\phi(0,\theta,t) < \infty,$$

$$\lim_{r\to\infty} \sqrt{r}\left(\frac{\partial\phi}{\partial t} + c\frac{\partial\phi}{\partial r}\right) + \frac{c}{2\sqrt{r}}\phi = 0,$$

$$\phi(r,0,t) = \phi(r,2\pi,t),$$

$$\frac{\partial\phi(r,0,t)}{\partial \theta} = \frac{\partial\phi(r,2\pi,t)}{\partial \theta}.$$

$$\text{(A.3)}$$

In the following sections we numerically solve the equation both by simply applying the exact NRBC at a finite truncated radius $r = R \gg 1$ and by using a PML method. The solutions are tested against the same Gaussian vortex 3.67 and the "1D exact solution" introduced in chapter 3.

A.1 Comparison between the 2D-Exact-NRBC solution and the 1D exact solution

We recall the background flow to be

$$U_0(r) = Fre^{-r^2}. \tag{A.4}$$

For the following results, parameters have been taken as $c = 1$, $F = 4$, $R = 20$, $T_f = 120$, $n_r = 400$, $n_\theta = 200$. It is known from the modal analysis that at $F = 4$ the vortex gets unstable, with the solution growing exponentially in time. In order to test the accuracy of our numerical time-dependent scheme, we show in figure A.1 the time evolution of a initial sloshing mode (the $m = 1$ Fourier component) in both the 1D exact case and in the 2D-Exact-NRBC model. The initial condition is taken as

$$\phi(r, \theta, 0) = e^{-8(r-10)^2} \cos(\theta). \tag{A.5}$$

As can be seen, the agreement is excellent even up to high final times $t = 120$.

A.2 PML formulation for the Convective Wave Equation in polar coordinates

We start by deriving a PML formulation for our problem in polar coordinates by exploiting all terms in the convective wave equation. For notation convenience, let us define $\Omega_0 = \frac{U_\theta}{r}$. This represents the angular velocity field generated by the swirl component U_θ of the background flow. By doing so we have

$$
\begin{aligned}
&\frac{\partial^2 \phi}{\partial t^2} + 2U_r \frac{\partial^2 \phi}{\partial t \partial r} + 2\Omega_0 \frac{\partial^2 \phi}{\partial t \partial \theta} \\
&+ U_r \frac{\partial}{\partial r}\left(U_r \frac{\partial \phi}{\partial r}\right) + U_r \frac{\partial}{\partial r}\left(\Omega_0 \frac{\partial \phi}{\partial \theta}\right) + \Omega_0 \frac{\partial}{\partial \theta}\left(U_r \frac{\partial \phi}{\partial r}\right) + \Omega_0 \frac{\partial}{\partial \theta}\left(\Omega_0 \frac{\partial \phi}{\partial \theta}\right) \\
&- \frac{c^2}{r}\frac{\partial}{\partial r}\left(r \frac{\partial \phi}{\partial r}\right) - \frac{c^2}{r^2}\frac{\partial^2 \phi}{\partial \theta^2} = 0.
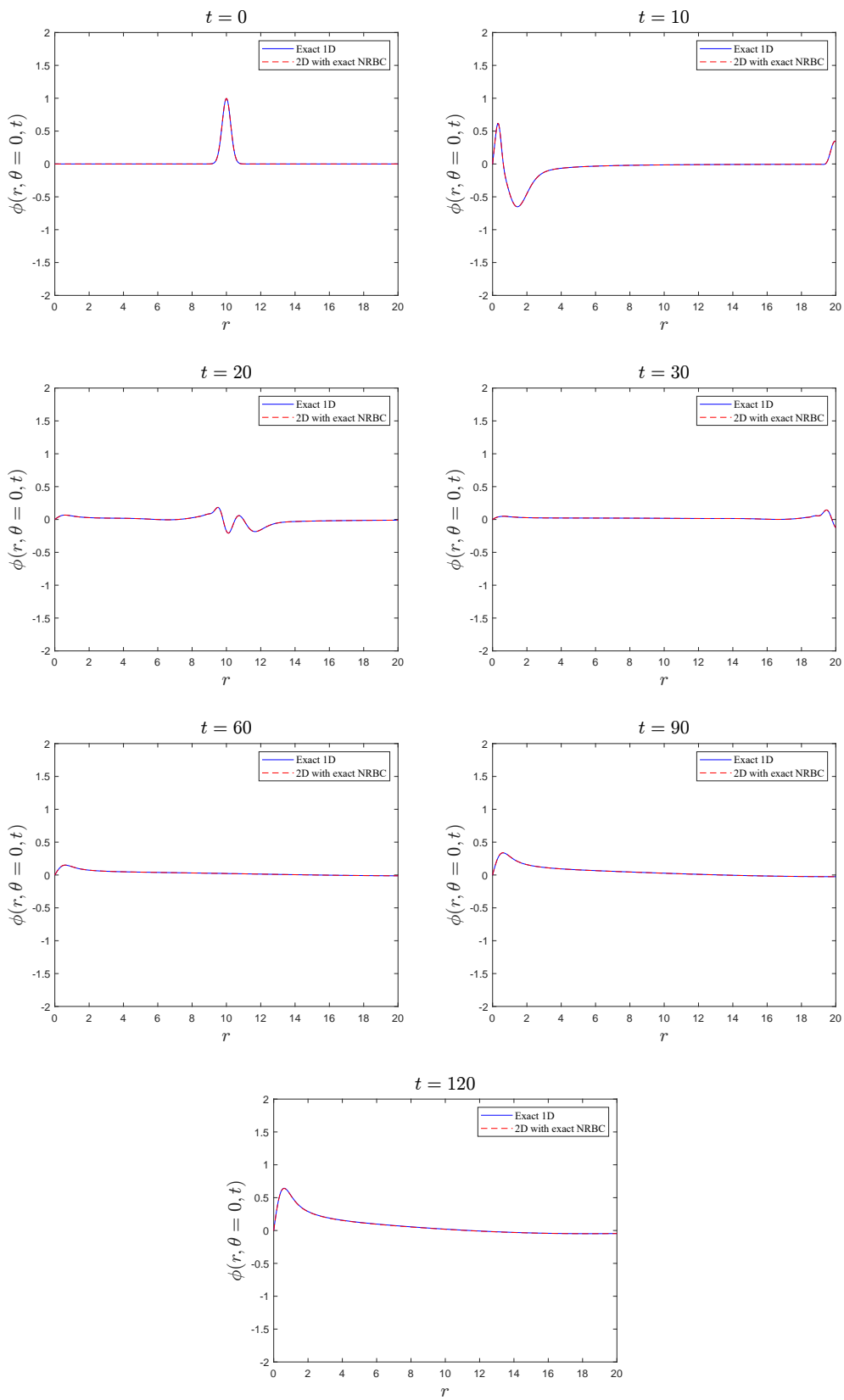\end{aligned}
\tag{A.6}
$$

Figure A.1: Time evolution of the solution for the 1D exact model and the 2D-NRBC model. Times shown here are $t = 0, 10, 20, 30, 60, 90, 120$.

Adopting a similar approach to what has been done 3.6.1, we first take the Laplace transform in time of the equation yielding

$$
s^2\tilde{\phi} + 2sU_r\frac{\partial\tilde{\phi}}{\partial r} + 2s\Omega_0\frac{\partial\tilde{\phi}}{\partial\theta}
$$
$$
+ U_r\frac{\partial}{\partial r}\left(U_r\frac{\partial\tilde{\phi}}{\partial r}\right) + U_r\frac{\partial}{\partial r}\left(\Omega_0\frac{\partial\tilde{\phi}}{\partial\theta}\right) + \Omega_0\frac{\partial}{\partial\theta}\left(U_r\frac{\partial\tilde{\phi}}{\partial r}\right) + \Omega_0\frac{\partial}{\partial\theta}\left(\Omega_0\frac{\partial\tilde{\phi}}{\partial\theta}\right)
$$
$$
- \frac{c^2}{r}\frac{\partial}{\partial r}\left(r\frac{\partial\tilde{\phi}}{\partial r}\right) - \frac{c^2}{r^2}\frac{\partial^2\tilde{\phi}}{\partial\theta^2} = 0.
$$

(A.7)

Secondly, we define a new stretched radial coordinate

$$
\tilde{r} = r + \frac{1}{s}\int_0^r \xi(r')dr',
$$

(A.8)

where $\xi(r)$ is a damping function acting only in the layer surrounding the actual domain. The radial derivative transforms according to

$$
\frac{\partial}{\partial\tilde{r}} = \frac{s}{s + \xi(r)}\frac{\partial}{\partial r} = \frac{1}{\gamma(r)}\frac{\partial}{\partial r}.
$$

(A.9)

At this point we impose equation (A.7) to be satisfied in the new stretched coordinate as well, producing

$$
s^2\tilde{\phi} + \frac{2sU_r}{\gamma}\frac{\partial\tilde{\phi}}{\partial r} + 2s\Omega_0\frac{\partial\tilde{\phi}}{\partial\theta}
$$
$$
+ \frac{U_r}{\gamma}\frac{\partial}{\partial r}\left(\frac{U_r}{\gamma}\frac{\partial\tilde{\phi}}{\partial r}\right) + \frac{U_r}{\gamma}\frac{\partial}{\partial r}\left(\Omega_0\frac{\partial\tilde{\phi}}{\partial\theta}\right) + \Omega_0\frac{\partial}{\partial\theta}\left(\frac{U_r}{\gamma}\frac{\partial\tilde{\phi}}{\partial r}\right) + \Omega_0\frac{\partial}{\partial\theta}\left(\Omega_0\frac{\partial\tilde{\phi}}{\partial\theta}\right)
$$
$$
- \frac{c^2}{\gamma r}\frac{\partial}{\partial r}\left(\frac{r}{\gamma}\frac{\partial\tilde{\phi}}{\partial r}\right) - \frac{c^2}{r^2}\frac{\partial^2\tilde{\phi}}{\partial\theta^2} = 0.
$$

(A.10)

Multiplication by γ gives

$$
s^2\gamma\tilde{\phi} + 2sU_r\frac{\partial\tilde{\phi}}{\partial r} + 2s\gamma\Omega_0\frac{\partial\tilde{\phi}}{\partial\theta}
$$
$$
+ U_r\frac{\partial}{\partial r}\left(\frac{U_r}{\gamma}\frac{\partial\tilde{\phi}}{\partial r}\right) + U_r\frac{\partial}{\partial r}\left(\Omega_0\frac{\partial\tilde{\phi}}{\partial\theta}\right) + \Omega_0\frac{\partial}{\partial\theta}\left(U_r\frac{\partial\tilde{\phi}}{\partial r}\right) + \gamma\Omega_0\frac{\partial}{\partial\theta}\left(\Omega_0\frac{\partial\tilde{\phi}}{\partial\theta}\right)
$$
$$
- \frac{c^2}{r}\frac{\partial}{\partial r}\left(\frac{r}{\gamma}\frac{\partial\tilde{\phi}}{\partial r}\right) - \gamma\frac{c^2}{r^2}\frac{\partial^2\tilde{\phi}}{\partial\theta^2} = 0,
$$

(A.11)

and recalling the definition of $\gamma = 1 + \frac{\xi(r)}{s}$, we can re-arrange the equation above as

$$s^2 \left(1 + \frac{\xi}{s} \right) \tilde{\phi} + 2sU_r \frac{\partial \tilde{\phi}}{\partial r} + 2s \left(1 + \frac{\xi}{s} \right) \Omega_0 \frac{\partial \tilde{\phi}}{\partial \theta}$$

$$+ U_r \frac{\partial}{\partial r} \left(U_r \left(1 - \frac{\xi}{s+\xi} \right) \frac{\partial \tilde{\phi}}{\partial r} \right) + U_r \frac{\partial}{\partial r} \left(\Omega_0 \frac{\partial \tilde{\phi}}{\partial \theta} \right) + \Omega_0 \frac{\partial}{\partial \theta} \left(U_r \frac{\partial \tilde{\phi}}{\partial r} \right) + \left(1 + \frac{\xi}{s} \right) \Omega_0 \frac{\partial}{\partial \theta} \left(\Omega_0 \frac{\partial \tilde{\phi}}{\partial \theta} \right)$$

$$- \frac{c^2}{r} \frac{\partial}{\partial r} \left(r \left(1 - \frac{\xi}{s+\xi} \right) \frac{\partial \tilde{\phi}}{\partial r} \right) - \left(1 + \frac{\xi}{s} \right) \frac{c^2}{r^2} \frac{\partial^2 \tilde{\phi}}{\partial \theta^2} = 0,$$

$$\text{(A.12)}$$

i.e.

$$\left(s^2 + s\xi \right) \tilde{\phi} + 2sU_r \frac{\partial \tilde{\phi}}{\partial r} + 2s\Omega_0 \frac{\partial \tilde{\phi}}{\partial \theta} + U_r \frac{\partial}{\partial r} \left(U_r \frac{\partial \tilde{\phi}}{\partial r} \right) + U_r \frac{\partial}{\partial r} \left(\Omega_0 \frac{\partial \tilde{\phi}}{\partial \theta} \right) + \Omega_0 \frac{\partial}{\partial \theta} \left(U_r \frac{\partial \tilde{\phi}}{\partial r} \right)$$

$$+ \Omega_0 \frac{\partial}{\partial \theta} \left(\Omega_0 \frac{\partial \tilde{\phi}}{\partial \theta} \right) - \frac{c^2}{r} \frac{\partial}{\partial r} \left(r \frac{\partial \tilde{\phi}}{\partial r} \right) - \frac{c^2}{r^2} \frac{\partial^2 \tilde{\phi}}{\partial \theta^2} - U_r \frac{\partial}{\partial r} \left(U_r \frac{\xi}{s+\xi} \frac{\partial \tilde{\phi}}{\partial r} \right) + \frac{c^2}{r} \frac{\partial}{\partial r} \left(r \frac{\xi}{s+\xi} \frac{\partial \tilde{\phi}}{\partial r} \right)$$

$$+ 2\xi\Omega_0 \frac{\partial \tilde{\phi}}{\partial \theta} + \frac{\xi}{s} \left[\Omega_0 \frac{\partial}{\partial \theta} \left(\Omega_0 \frac{\partial \tilde{\phi}}{\partial \theta} \right) - \frac{c^2}{r^2} \frac{\partial \tilde{\phi}}{\partial \theta^2} \right] = 0.$$

$$\text{(A.13)}$$

As the damping function varies along r only, in order not to introduce two auxiliary unknowns as for the formulation in cartesian coordinates, we assume that the effect associated to the damping only affects the radial derivatives, so we neglect the last term in square brackets. By doing so, we can just define one auxiliary variable, given by $\tilde{\psi} = \frac{\xi}{s+\xi} \frac{\partial \tilde{\phi}}{\partial r}$. Finally, we inverse Laplace transform in time the previous equation and obtain the PML formulation

$$D_t^2 \phi - c^2 \nabla^2 \phi + \xi \frac{\partial \phi}{\partial t} + 2\xi\Omega_0 \frac{\partial \phi}{\partial \theta} + \frac{c^2}{r} \frac{\partial}{\partial r} (r\psi) - U_r \frac{\partial}{\partial r} (U_r \psi) = 0,$$

$$\frac{\partial \psi}{\partial t} + \xi\psi - \xi \frac{\partial \phi}{\partial r} = 0.$$

$$\text{(A.14)}$$

As already discussed a few times, the final differential problem above can be combined with any boundary conditions at the extended radial boundary.

A.2.1 Discretization and numerical solution

We again solve the set of equations by means of the Method of Lines. As done for the cartesian coordinates problem, we re-write it in a more convenient form via the three variables:

$$u_1 = \phi, \qquad u_2 = D_t \phi, \qquad u_3 = \psi. \qquad \text{(A.15)}$$

The PML formulation in polar coordinates can be then written as

$$\frac{\partial u_1}{\partial t} = -U_r \frac{\partial u_1}{\partial r} - \Omega_0 \frac{\partial u_1}{\partial \theta} + u_2,$$

$$\frac{\partial u_2}{\partial t} = -U_r \frac{\partial u_2}{\partial r} - \Omega_0 \frac{\partial u_2}{\partial \theta} + c^2 \nabla^2 u_1 - \xi \left(u2 - U_r \frac{\partial u_1}{\partial r} - \Omega_0 \frac{\partial u_1}{\partial \theta} \right) - 2\xi\Omega_0 \frac{\partial u_1}{\partial \theta} + U_r \frac{\partial}{\partial r} \left(U_r u_3 \right)$$

$$- \frac{c^2}{r} \frac{\partial}{\partial r} \left(r u_3 \right),$$

$$\frac{\partial u_3}{\partial t} = -\xi u_3 + \xi \frac{\partial u_1}{\partial r}.$$

$$(A.16)$$

Before proceeding with the actual discretization, we collect all the terms on the right-hand sides of the previous equations containing radial derivatives only and in a similar way those containing angular derivatives only. This way, we can write the previous system as

$$\frac{\partial u_1}{\partial t} = \mathcal{R}_1 + \mathcal{T}_1,$$
$$\frac{\partial u_2}{\partial t} = \mathcal{R}_2 + \mathcal{T}_2, \qquad (A.17)$$
$$\frac{\partial u_3}{\partial t} = \mathcal{R}_3 + \mathcal{T}_3.$$

This splitting is much more convenient for imposing the boundary conditions in r and θ once the spatial contributions have been discretized. So, we now proceed with the discretization of the spatial terms appearing in (A.16) using a finite difference scheme. The grid points are taken to be $(r_j, \theta_i) = \left((j - 1)\Delta r, (i - 1)\Delta\theta \right)$ for $(i, j) \in \left([1, N_\theta], [1, N_r] \right)$ and $(\Delta r, \Delta\theta) = \left(\frac{R}{N_r - 1}, \frac{2\pi}{N_\theta - 1} \right)$. Proceeding term by term we have

$$\mathcal{R}_{1_{i,j}} = -U_r(\theta_i, r_j) \frac{u_{1_{i,j+1}} - u_{1_{i,j-1}}}{2\Delta r},$$

$$\mathcal{R}_{2_{i,j}} = -U_r(\theta_i, r_j) \frac{u_{2_{i,j+1}} - u_{2_{i,j-1}}}{2\Delta r} + c^2 \left(\frac{u_{1_{i,j+1}} - 2u_{1_{i,j}} + u_{1_{i,j-1}}}{\Delta r^2} + \frac{1}{r_j} \frac{u_{1_{i,j+1}} - u_{1_{i,j-1}}}{2\Delta r} \right)$$

$$+ \xi(r_j) U_r(\theta_i, r_j) \frac{u_{1_{i,j+1}} - u_{1_{i,j-1}}}{2\Delta r} + U_r(\theta_i, r_j) \frac{U_r(\theta_i, r_{j+1}) u_{3_{i,j+1}} - U_r(\theta_i, r_{j-1}) u_{3_{i,j-1}}}{2\Delta r}$$

$$- c^2 \frac{u_{3_{i,j+1}} - u_{3_{i,j-1}}}{2\Delta r} - \frac{c^2}{r_j} u_{3_{i,j}},$$

$$\mathcal{R}_{3_{i,j}} = \xi(r_j) \frac{u_{1_{i,j+1}} - u_{1_{i,j-1}}}{2\Delta r}.$$

$$(A.18)$$

for the radial part, and

$$\mathcal{T}_{1_{i,j}} = -\Omega_0(\theta_i, r_j) \frac{u_{1_{i+1,j}} - u_{1_{i-1,j}}}{2\Delta\theta} + u_{2_{i,j}},$$

$$\mathcal{T}_{2_{i,j}} = -\Omega_0(\theta_i, r_j) \frac{u_{2_{i+1,j}} - u_{2_{i-1,j}}}{2\Delta\theta} + \frac{c^2}{r_j^2} \frac{u_{2_{i+1,j}} - 2u_{2_{i,j}} + u_{2_{i-1,j}}}{\Delta\theta^2} - \xi(r_j)\Omega_0(\theta_i, r_j) \frac{u_{1_{i+1,j}} - u_{1_{i-1,j}}}{2\Delta\theta},$$

$$\mathcal{T}_{3_{i,j}} = -\xi(r_j) u_{3_{i,j}},$$

$$(A.19)$$

for the angular contributions. Regarding the boundary conditions along the radial direction, these they can be of any type so we can simply impose

$$\mathcal{R}_{1_{i,1}} = 0, \qquad \mathcal{R}_{2_{i,1}} = 0,, \qquad \mathcal{R}_{3_{i,1}} = 0, \qquad \forall i \in [1, N_\theta],$$
$$\mathcal{R}_{1_{i,N_r}} = 0, \qquad \mathcal{R}_{2_{i,N_r}} = 0, \qquad \mathcal{R}_{3_{i,N_r}} = 0, \qquad \forall i \in [1, N_\theta]. \qquad (A.20)$$

On the other hand, along θ, the periodic boundary conditions are implemented as follows

$$u_{1_{0,j}} = u_{1_{N_\theta,j}}, \qquad u_{1_{N_\theta+1,j}} = u_{1_{1,j}}, \qquad \forall j \in [1, N_r],$$
$$u_{2_{0,j}} = u_{2_{N_\theta,j}}, \qquad u_{2_{N_\theta+1,j}} = u_{2_{1,j}}, \qquad \forall j \in [1, N_r]. \qquad (A.21)$$

Finally, The final discrete formulation using the MOL is given by

$$\frac{du_{1_{i,j}}}{dt} = \mathcal{R}_{1_{i,j}} + \mathcal{T}_{1_{i,j}},$$
$$\frac{du_{2_{i,j}}}{dt} = \mathcal{R}_{2_{i,j}} + \mathcal{T}_{2_{i,j}}, \qquad \forall (i,j) \in \Big([1, N_\theta], [1, N_r]\Big), \qquad (A.22)$$
$$\frac{du_{3_{i,j}}}{dt} = \mathcal{R}_{3_{i,j}} + \mathcal{T}_{3_{i,j}}.$$

A.2.2 Comparison between the solution using the PML formulation in polar coordinates and the 1D exact solution

In this paragraph we do the same kind of comparison we did in both section 3.6.3 and A.1, i.e. we test our code with the purely gaussian rotating flow at two Froude numbers. The first set of results is shown in figure A.2, having taken the initial condition

$$\phi(r, \theta, 0) = 1.5 e^{-8(r-1.5)^2} \cos(\theta), \qquad (A.23)$$

and with the following physical and numerical parameters: $c = 1$, $F = 0.5$, $R_c = 15$, $R = 20$, $T_f = 20$, $n_r = 400$, $n_\theta = 100$, where R_c is the radial position where the damping layer begins and R is the actual end of the discretization domain. It can be noted that the agreement is really good at all times considered. we turn now to the second example considered, which is computed using the the same set of parameters, but $F = 4$ and $T_f = 60$, in order to allow the initial perturbation to develop the expected instability at a sufficiently long time. Moreover, the initial condition now has been taken as

$$\phi(r, \theta, 0) = e^{-8(r-10)^2} \cos(\theta). \qquad (A.24)$$

Results are shown in figure A.3. The 2D PML model captures well the instability at higher times and overall the two solutions matches pretty well. Also, it can be noted that the damping layer works well as in there the red-dotted curve vanishes sufficiently fast, therefore providing good absorption of

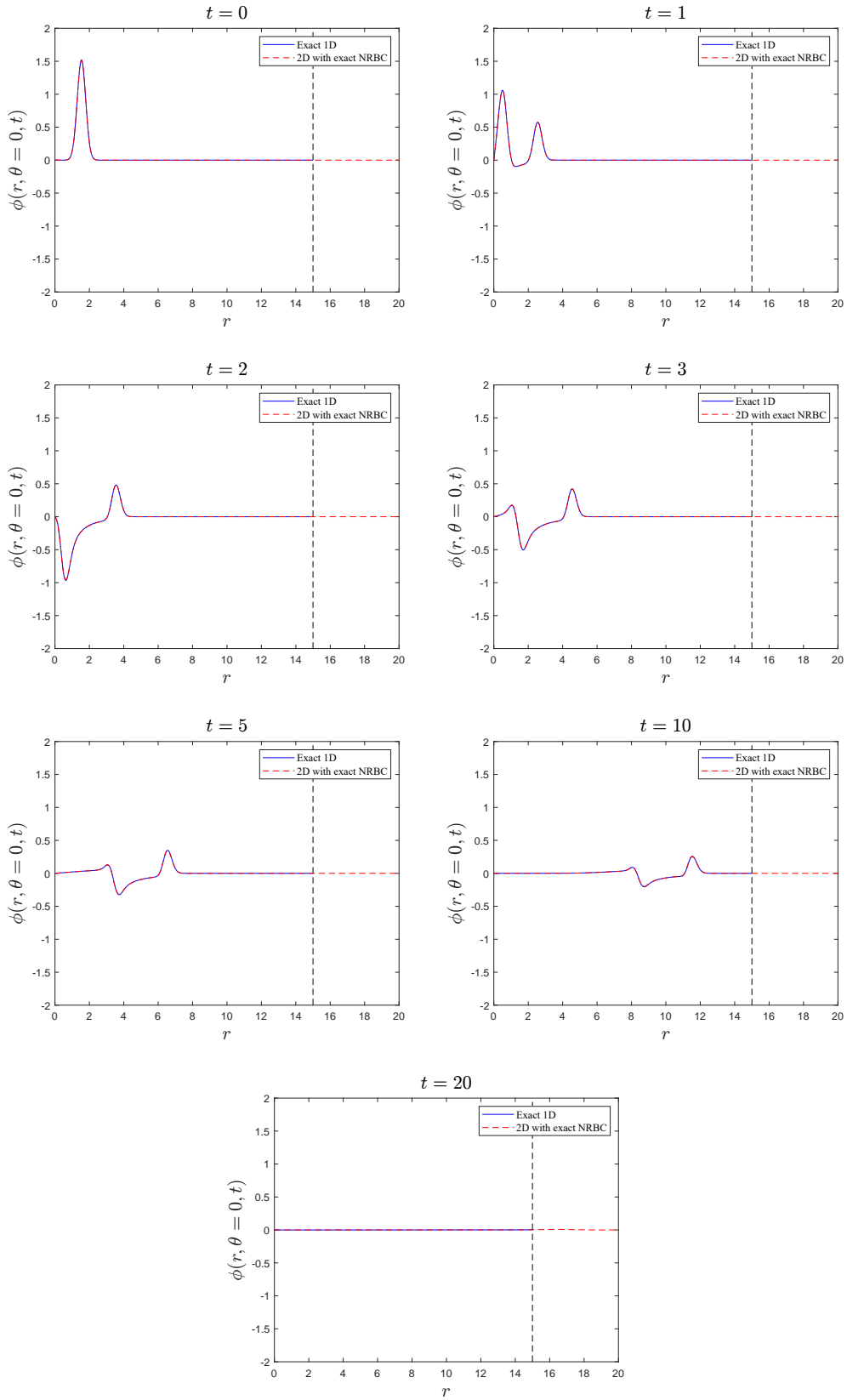Figure A.2: Time evolution of the solution for the 1D exact model and the PML model in polar coordinates for $F = 0.5$. Times are taken to be $t = 0, 1, 2, 3, 5, 10, 20$.
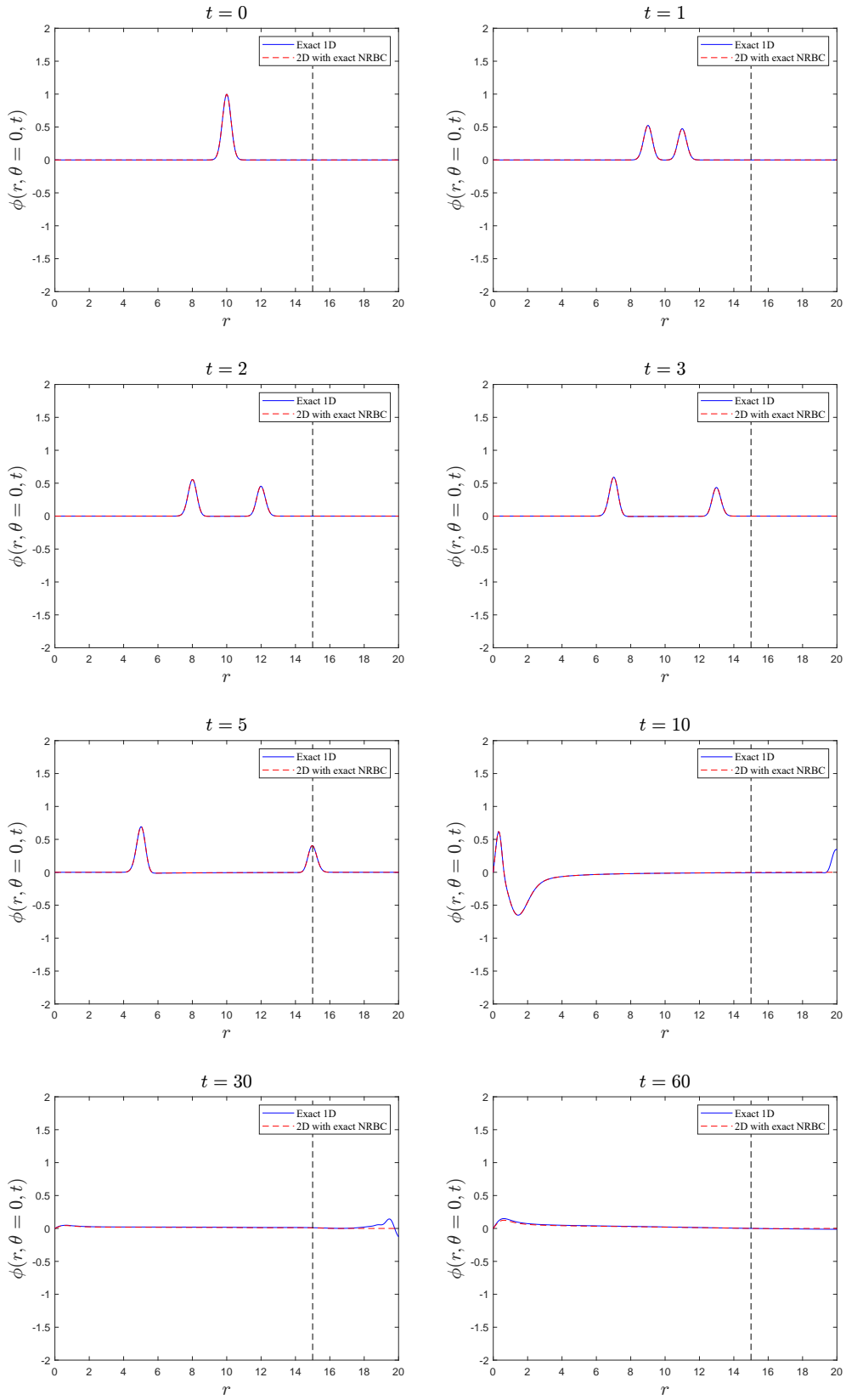
Figure A.3: Time evolution of the solution for the 1D exact model and the PML model in polar coordinates for $F = 4$. Times shown in here are $t = 0, 1, 2, 3, 5, 10, 30, 60$.

the incoming wave at the artificial boundary $R_c = 15$.

Appendix B

An analytical dipole solution of the unsteady Oseen equations

Oseen first derived an improved set of equations for studying the problem of a slow viscous flow around a infinitely extended cylinder, known as Stokes Paradox—see Batchelor (2000, Chapter 4). He accounted in the momentum equation for a transport term proportional to the uniform velocity of the fluid at infinity. In addition, we are going to include the temporal derivative term into the momentum equation. Our goal is to find a dipole solution for the following unsteady Oseen equations:

$$
\begin{aligned}
&\frac{\partial \boldsymbol{u}}{\partial t} + (U\hat{\boldsymbol{y}} \cdot \nabla)\boldsymbol{u} + \nabla p - \nu \nabla^2 \boldsymbol{u} = 0, \\
&\nabla \cdot \boldsymbol{u} = 0,
\end{aligned}
\tag{B.1}
$$

where $U\hat{\boldsymbol{y}}$ represents the uniform velocity at which the dipole moves and, as usual, ν the kinematic viscosity of the fluid. The additional convective term can be re-arranged as $(U\hat{\boldsymbol{y}} \cdot \nabla)\boldsymbol{u} = U\frac{\partial \boldsymbol{u}}{\partial y}$, so the momentum equation becomes

$$
\frac{\partial \boldsymbol{u}}{\partial t} + U\frac{\partial \boldsymbol{u}}{\partial y} + \nabla p - \nu \nabla^2 \boldsymbol{u} = 0.
\tag{B.2}
$$

Since the flow is two-dimensional, by taking the curl of the momentum equation we obtain the vorticity-stream function system:

$$
\begin{aligned}
&\frac{\partial \omega}{\partial t} + U\frac{\partial \omega}{\partial y} - \nu \nabla^2 \omega = 0, \\
&\nabla^2 \psi = -\omega.
\end{aligned}
\tag{B.3}
$$

The two equations above are decoupled and we can start by solving that for the vorticity. As a first step we reduce the diffusion-transport equation in $\omega(x, y, t)$ into a purely diffusion equation by making the following variables

transformations:

$$\omega(x, y, t) = q(x, \xi, \tau),$$
$$\tau = at + by, \tag{B.4}$$
$$\xi = ct + dy,$$

with a, b, c, d constants to be determined. The derivatives transform according to

$$\frac{\partial \omega}{\partial t} = a\frac{\partial q}{\partial \tau} + c\frac{\partial q}{\partial \xi},$$
$$\frac{\partial \omega}{\partial y} = b\frac{\partial q}{\partial \tau} + d\frac{\partial q}{\partial \xi},$$
$$\frac{\partial^2 \omega}{\partial y^2} = b^2\frac{\partial^2 q}{\partial \tau^2} + 2bd\frac{\partial^2 q}{\partial \tau \partial \xi} + d^2\frac{\partial^2 q}{\partial \xi^2}, \tag{B.5}$$
$$\frac{\partial^2 \omega}{\partial x^2} = \frac{\partial^2 q}{\partial x^2}.$$

Substitution into the governing equation yields

$$(a+Ub)\frac{\partial q}{\partial \tau} + (c+Ud)\frac{\partial q}{\partial \xi} - \nu b^2\frac{\partial^2 q}{\partial \tau^2} - 2\nu bd\frac{\partial^2 q}{\partial \tau \partial \xi} - \nu d^2\frac{\partial^2 q}{\partial \xi^2} - \nu\frac{\partial^2 q}{\partial x^2} = 0. \tag{B.6}$$

Since we want to eliminate the transport term, the second derivative in τ and the mixed derivative, we impose

$$b = 0,$$
$$d = 1, \tag{B.7}$$
$$c = -Ud = -U,$$

leading to the diffusion equation

$$\frac{\partial q}{\partial \tau} - \eta\Big(\frac{\partial^2 q}{\partial x^2} + \frac{\partial^2 q}{\partial \xi^2}\Big) = 0, \tag{B.8}$$

with $\eta = \frac{\nu}{a}$ being a new diffusivity coefficient.

A dipole solution satisfies the periodicity property along the azimuthal direction $q(r, \theta, \tau) = \tilde{q}(r, \tau)\cos(\theta)$, so it is more convenient to express the Laplacian in polar coordinates through the transformation $x = r\cos(\theta)$ and $\xi = r\sin(\theta)$. After a bit of algebra, the remaining equation for $\tilde{q}(r, \tau)$ reads

$$\frac{\partial \tilde{q}}{\partial \tau} - \eta\Big[\frac{1}{r}\frac{\partial}{\partial r}\Big(r\frac{\partial \tilde{q}}{\partial r}\Big) - \frac{1}{r^2}\tilde{q}\Big] = 0. \tag{B.9}$$

In order to re-arrange the equation in a more convenient way we define $\Gamma = r\tilde{q}$, so that we have

$$\frac{\partial \Gamma}{\partial \tau} - \eta r\frac{\partial}{\partial r}\Big[\frac{1}{r}\frac{\partial \Gamma}{\partial r}\Big] = 0. \tag{B.10}$$

This is the same equation that leads to Lamb-Oseen vortex for example, and hence we try to look for a similarity solution—see for example Drazin and Riley (2006, sec. 5.6). In particular, we set $\Gamma(r, \tau) = a(\tau)\gamma(s)$, with $s = \frac{r^2}{\delta(\tau)}$

152

being the similarity variable. Plugging the ansatz above into equation (B.10), we get the following system of ODEs

$$\dot{a}(\tau)\delta(\tau) = -4\eta a(\tau),$$
$$\dot{\delta}(\tau)a(\tau) = 4\eta a(\tau), \qquad \text{(B.11)}$$
$$s\gamma''(s) + s\gamma'(s) + \gamma(s) = 0,$$

which returns the general solutions

$$\delta(\tau) = 4\eta\tau + a_0^2,$$
$$a(\tau) = \frac{B}{4\eta\tau + a_0^2}, \qquad \text{(B.12)}$$
$$\gamma(s) = se^{-s}.$$

Thus, $\Gamma(r, \tau)$ is given by

$$\Gamma(r, \tau) = \frac{Br^2}{(4\eta\tau + a_0^2)^2} e^{-\frac{r^2}{4\eta\tau + a_0^2}}, \qquad \text{(B.13)}$$

and consequently the vorticity

$$q(r, \theta, \tau) = \left[\frac{Br}{(4\eta\tau + a_0^2)^2} e^{-\frac{r^2}{4\eta\tau + a_0^2}} \right] \cos(\theta). \qquad \text{(B.14)}$$

At this point, we turn to the Poisson equation for the streamfunction. Given the functional form of the vorticity just derived, we have

$$\nabla^2\psi = -\left[\frac{Br}{(4\eta\tau + a_0^2)^2} e^{-\frac{r^2}{4\eta\tau + a_0^2}} \right] \cos(\theta). \qquad \text{(B.15)}$$

We set $\psi(r, \theta, \tau) = \phi(r, \tau)\cos(\theta)$ to get an equation for ϕ:

$$\frac{\partial^2\phi}{\partial r^2} + \frac{1}{r}\frac{\partial\phi}{\partial r} - \frac{1}{r^2}\phi = -\frac{Br}{\delta^2(\tau)} e^{-\frac{r^2}{\delta(\tau)}}. \qquad \text{(B.16)}$$

Now, the left-hand side can be re-written as $\frac{\partial}{\partial r}\left[\frac{1}{r}\frac{\partial}{\partial r}(r\phi)\right]$, so that we have

$$\frac{\partial}{\partial r}\left[\frac{1}{r}\frac{\partial}{\partial r}(r\phi)\right] = -\frac{Br}{\delta^2(\tau)} e^{-\frac{r^2}{\delta(\tau)}}. \qquad \text{(B.17)}$$

A double integration gives us the general solution

$$\phi(r, \tau) = \frac{1}{r}\left[K(\tau) - \frac{B}{4} e^{-\frac{r^2}{\delta(\tau)}} \right] + \frac{H(\tau)}{2} r, \qquad \text{(B.18)}$$

where $H(\tau)$ and $K(\tau)$ are function to be determined by imposing the boundary conditions. In particular, we impose $\phi(\infty, \tau) = 0$ and $\phi(0, \tau) < \infty$, which yield $H(\tau) = 0$ and $K(\tau) = \frac{B}{4}$. Therefore, the streamfunction in polar coordinates
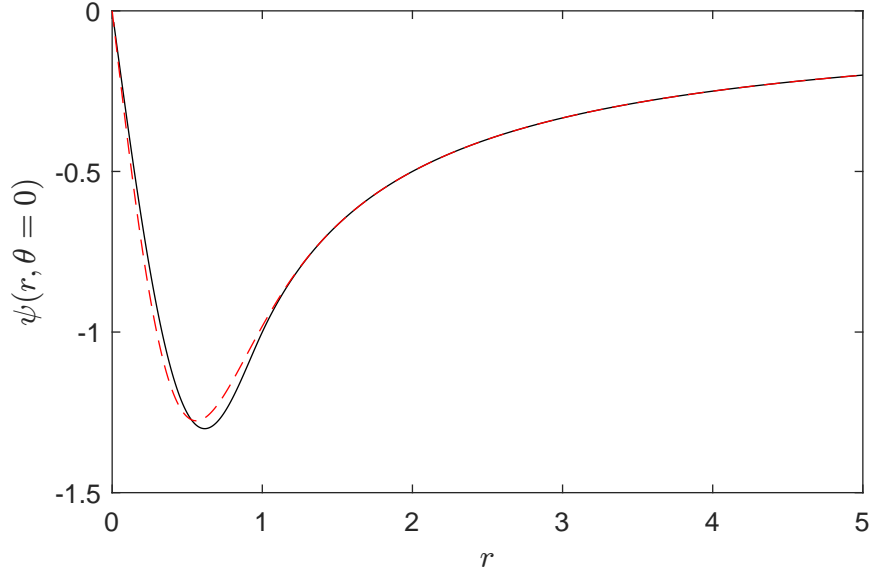
Figure B.1: Comparison between Lamb's streamfunction (black line) and the analytical streamfunction according to equation (B.19)—red dotted line. The parameters have been taken as: $U = 0.5$, $B = 4$, $\delta(\tau) = const. = 0.5$.

is given by

$$\psi(r, \theta, \tau) = \frac{B}{4r}\left(1 - e^{-\frac{r^2}{\delta(\tau)}}\right)\cos(\theta). \tag{B.19}$$

Recalling the definition of (x, ξ) in terms of (r, θ) and finally $\xi = y - Ut$, the final expression for the time-dependent streamfunction in cartesian coordinates is

$$\psi(x, y, t) = \frac{Bx}{4[x^2 + (y - Ut)^2]}\left(1 - e^{-\frac{[x^2 + (y - Ut)^2]}{4\nu t + a_0^2}}\right). \tag{B.20}$$

In figure B.1 a comparison between the streamfunction of the solution just derived and the one of Lamb's dipole Lamb (1932) is shown. For the latter, the matching radius has been taken to be of unitary value.

In figure B.2, moreover, we show the time evolution of the two vortices along the y-direction for four times $t = 0, 5, 10, 15$. This feature indeed mimics very well the representation of the two vortices travelling in a swimming pool, thus providing a good analytical model capable of describing that situation.
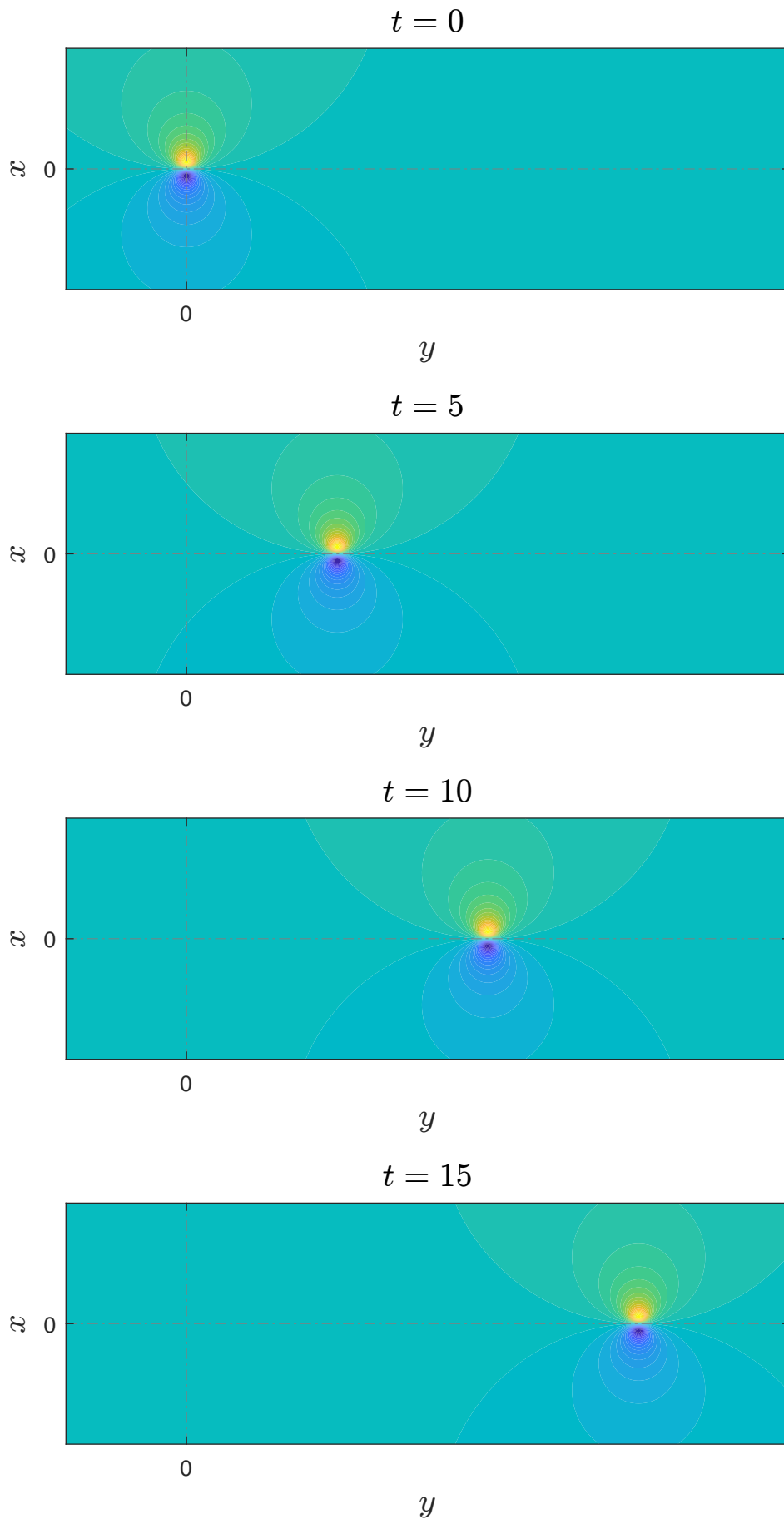
Figure B.2: Travelling in time of the two pair of vortices, according to the analytical solution derived—equation (B.20). Parameters have been set to $U = 0.5$, $B = 1$, $\nu = 10^{-5}$, $a_0 = 0.1$. 155

Appendix C

Attempts to formally justify the closure boundary condition for the 2D deep-water waves model

In this appendix we show three methods that we applied in order to justify rigorously our closure 2D deep-water waves model derived in chapter 5. Each method's ideas are outlined below, however none of them gave naturally the correct argument to being able to justify the closure. Therefore, as explained in chapter 5, we just validated our closure by means of numerical results and comparisons, and we leave to possible future studies the possibility to find an exact way to derive it.

C.1 Derivation assuming axial exponential dependence

In this section we tried to derive the reduced set of equations (5.11) rigorously in the case of a monopolar vortex. The derivation is based on the assumption of an exponential dependence of the unknowns along the axial coordinate; in particular

$$\boldsymbol{u} = \left[u(r,\theta,t)\hat{\boldsymbol{r}} + v(r,\theta,t)\hat{\boldsymbol{\theta}} + w(r,\theta,t)\hat{\boldsymbol{z}}\right] \exp[\alpha(r)(z - h_0(r))], \qquad \text{(C.1a)}$$

$$p = h(r,\theta,t) \exp[\alpha(r)(z - h_0(r))], \qquad \text{(C.1b)}$$

with $\alpha(r)$ being a generic function of r to be determined. Notice that, under the functional form written above, the dynamic boundary condition for the pressure is automatically satisfied. Substituting into the dimensionless

linearized Euler equations and dropping the common exponential term yields

$$D_t u - 2F\Omega_0 v + \frac{\partial h}{\partial r} + \alpha'(z - h_0)h - \alpha h_0' h = 0, \qquad \text{(C.2a)}$$

$$D_t v + F\Gamma_0 u + \frac{1}{r}\frac{\partial h}{\partial \theta} = 0, \qquad \text{(C.2b)}$$

$$D_t w + \alpha h = 0, \qquad \text{(C.2c)}$$

$$\frac{1}{r}\frac{\partial}{\partial r}(ru) + \frac{1}{r}\frac{\partial v}{\partial \theta} + \alpha(w - h_0'u) + \alpha'(z - h_0)u = 0, \qquad \text{(C.2d)}$$

together with the free surface boundary condition that now simplifies into

$$w - h_0'u = D_t h. \qquad \text{(C.3)}$$

Now, as the unknowns u, v, w, h do not depend on the axial coordinate, the only possibility for system (C.2) to be valid is that $\alpha' = 0 \Rightarrow \alpha(r) = const. = k$. In such case, we obtain five equations in the five unknowns u, v, w, h, k:

$$D_t u - 2F\Omega_0 v + \frac{\partial h}{\partial r} - kh_0' h = 0, \qquad \text{(C.4a)}$$

$$D_t v + F\Gamma_0 u + \frac{1}{r}\frac{\partial h}{\partial \theta} = 0, \qquad \text{(C.4b)}$$

$$D_t w + kh = 0, \qquad \text{(C.4c)}$$

$$\frac{1}{r}\frac{\partial}{\partial r}(ru) + \frac{1}{r}\frac{\partial v}{\partial \theta} + k(w - h_0'u) = 0, \qquad \text{(C.4d)}$$

$$w - h_0'u = D_t h. \qquad \text{(C.4e)}$$

At this point, however, we stop our further computations as our numerics showed that actually $\alpha(r)$ is not a constant, but varies in r, as can be seen in figure C.1. In particular, we plot the following quantities in modulus:

$$\left.\frac{\partial_z u_r}{u_r}\right|_{h_0}, \qquad \left.\frac{\partial_z u_z}{u_z}\right|_{h_0}, \qquad \left.\frac{\partial_z p}{p}\right|_{h_0}. \qquad \text{(C.5)}$$

The figure shows that all the three quantities in C.5 have—net of numerical resolution errors—the same trend of along the free surface; this is indeed a measure of $\alpha(r)$. However, this is not constant, hence contradicts the hypothesis made at the beginning.

C.2 Derivation by means of Laplace transform

Let us define the shifted coordinate

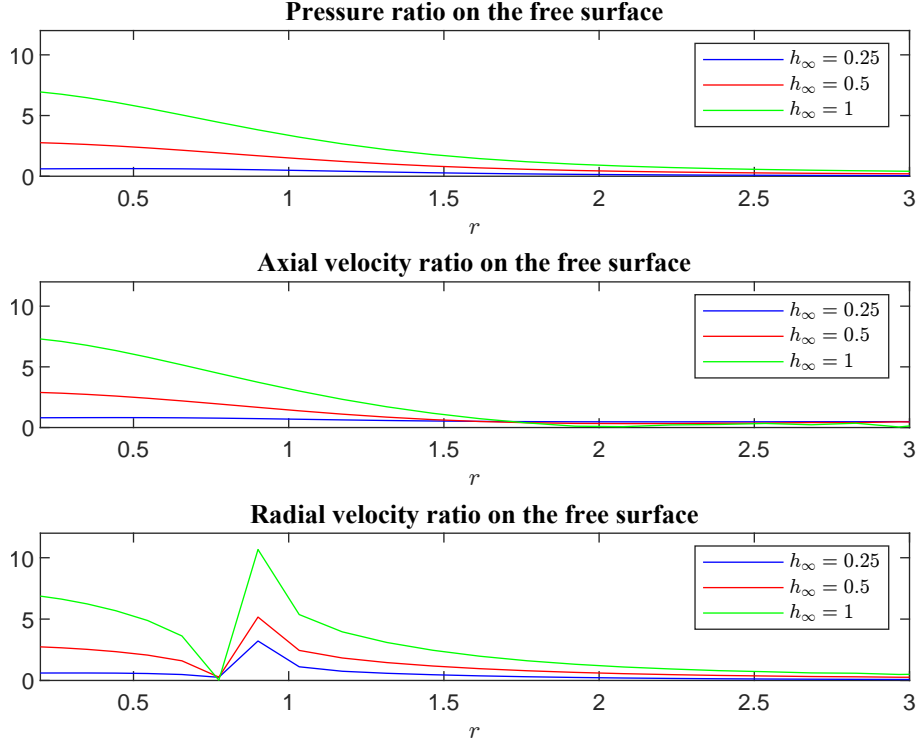$$\xi = h_0(r) - z, \qquad \text{(C.6)}$$

Figure C.1: Trend of the modulus the three quantities appearing in (C.5) as function of the radial coordinate. The mode used to plot these graphs have been computed for $m = 7$ and $F = 0.5$.

so that the free surface is now located at $\xi = 0$, and when $z \to -\infty$ $\xi \to \infty$. Let the velocity and pressure fields vary with ξ according to

$$\boldsymbol{u} = \boldsymbol{u}(r, \theta, \xi, t), \qquad p = p(r, \theta, \xi, t). \tag{C.7}$$

The linearized Euler differential problem becomes

$$D_t u_r - 2F\Omega_0 u_\theta + \frac{\partial p}{\partial r} + h_0' \frac{\partial p}{\partial \xi} = 0, \tag{C.8a}$$

$$D_t u_\theta - 2F\Gamma_0 u_r + \frac{1}{r}\frac{\partial p}{\partial \theta} = 0, \tag{C.8b}$$

$$D_t u_z - \frac{\partial p}{\partial \xi} = 0, \tag{C.8c}$$

$$\frac{1}{r}\frac{\partial}{\partial r}(r u_r) + \frac{1}{r}\frac{\partial u_\theta}{\partial \theta} + h_0' \frac{\partial u_r}{\partial \xi} - \frac{\partial u_z}{\partial \xi} = 0, \tag{C.8d}$$

$$D_t p + h_0' u_r - u_z = 0, \quad on \quad \xi = 0, \tag{C.8e}$$

plus a decay condition as $\xi \to \infty$. Firstly we deal with the continuity equation; in particular we add and subtract the quantity $D_t \frac{\partial p}{\partial \xi}$. Hence, we get

$$\frac{1}{r}\frac{\partial}{\partial r}(r u_r) + \frac{1}{r}\frac{\partial u_\theta}{\partial \theta} - D_t \frac{\partial p}{\partial \xi} + \left[D_t \frac{\partial p}{\partial \xi} + h_0' \frac{\partial u_r}{\partial \xi} - \frac{\partial u_z}{\partial \xi} \right] = 0. \tag{C.9}$$

Now, let us define a functional $\psi[u_r, u_z, p]$, such that

$$\psi[u_r, u_z, p](r, \theta, \xi, t) = D_t p + h_0' u_r - u_z. \tag{C.10}$$

It is clear that due to the free surface boundary condition $\psi(r, \theta, 0, t) = 0$. At this point, let us introduce the Laplace transform; for any function $f = f(r, \theta, \xi, t)$, its Laplace transform along the axial direction is given by

$$\hat{f}(r, \theta, s, t) = \mathcal{L}[f] = \int_0^\infty f(r, \theta, \xi, t) \exp(-s\xi) d\xi. \tag{C.11}$$

Thus, by taking the Laplace transform of the Euler equations we obtain

$$D_t \hat{u}_r - 2F\Omega_0 \hat{u}_\theta + \frac{\partial \hat{p}}{\partial r} + h_0' \left(s\hat{p} - p|_0 \right) = 0, \tag{C.12a}$$

$$D_t \hat{u}_\theta + F\Gamma_0 \hat{u}_r + \frac{1}{r} \frac{\partial \hat{p}}{\partial \theta} = 0, \tag{C.12b}$$

$$D_t \hat{u}_z - (s\hat{p} - p|_0) = 0, \tag{C.12c}$$

$$\frac{1}{r} \frac{\partial}{\partial r} (r\hat{u}_r) + \frac{1}{r} \frac{\partial \hat{u}_\theta}{\partial \theta} - D_t (s\hat{p} - p|_0) + \mathcal{L}\left[\frac{\partial \psi}{\partial \xi} \right] = 0, \tag{C.12d}$$

being $\mathcal{L}\left[\frac{\partial \psi}{\partial \xi} \right]$ the Laplace transform of the derivative of the functional with respect to ξ. In particular, we have that

$$\mathcal{L}\left[\frac{\partial \psi}{\partial \xi} \right] = s\hat{\psi} - \psi|_0 = s\hat{\psi}. \tag{C.13}$$

So, by inserting this expression into the previous equations and exploiting the term $s\hat{p} - p|_0$ as function of $\hat{u}_z$, we get

$$D_t \hat{u}_r - 2F\Omega_0 \hat{u}_\theta + \frac{\partial \hat{p}}{\partial r} + h_0' D_t \hat{u}_z, \tag{C.14a}$$

$$D_t \hat{u}_\theta + F\Gamma_0 \hat{u}_r + \frac{1}{r} \frac{\partial \hat{p}}{\partial \theta} = 0, \tag{C.14b}$$

$$\frac{1}{r} \frac{\partial}{\partial r} (r\hat{u}_r) + \frac{1}{r} \frac{\partial \hat{u}_\theta}{\partial \theta} - D_t^2 \hat{u}_z + s\hat{\psi} = 0. \tag{C.14c}$$

In order to obtain our final system of equations (5.11) we would need to assume that $\hat{\psi} = 0$. However, this is not true in principle so we do not have enough arguments to make this assumption. Indeed, we started with the hypothesis that the unknowns vary exponentially in ξ (given implicitly by the Laplace transformation) and came to another assumption that $\hat{\psi} = 0$. Hence, even by using the Laplace transform method we are not able to justify our closure model.

C.3 Derivation through the method of Multiple Scales

Let us start with the linearized Euler equations:

$$D_t u_r - 2F\Omega_0(r)u_\theta + \frac{\partial p}{\partial r} = 0, \tag{C.15a}$$

$$D_t u_\theta + F\xi_0(r)u_r + \frac{1}{r}\frac{\partial p}{\partial \theta} = 0, \tag{C.15b}$$

$$D_t u_z + \frac{\partial p}{\partial z} = 0, \tag{C.15c}$$

$$\frac{1}{r}\frac{\partial}{\partial r}(ru_r) + \frac{1}{r}\frac{\partial u_\theta}{\partial \theta} + \frac{\partial u_z}{\partial z} = 0, \tag{C.15d}$$

Let us define a slow axial variable: $\xi = \epsilon(z - h_0(r))$, with $\epsilon \ll 1$. Then, we look for a solution in the following form

$$
\begin{aligned}
u_r(r,\theta,z,t) &= \tilde{u}_r(r,\theta,\xi,t)e^{k(r)(z-h_0(r))}, \\
u_\theta(r,\theta,z,t) &= \tilde{u}_\theta(r,\theta,\xi,t)e^{k(r)(z-h_0(r))}, \\
u_z(r,\theta,z,t) &= \tilde{u}_z(r,\theta,\xi,t)e^{k(r)(z-h_0(r))}, \\
p(r,\theta,z,t) &= \tilde{p}(r,\theta,\xi,t)e^{k(r)(z-h_0(r))},
\end{aligned}
\tag{C.16}
$$

with $k(r)$ a function to be determined as well. Plugging the ansatz above into the equations, we obtain

$$D_t\tilde{u}_r - 2F\Omega_0(r)\tilde{u}_\theta + \frac{\partial\tilde{p}}{\partial r} - h_0'(r)k(r)\tilde{p} - \epsilon h_0'(r)\frac{\partial\tilde{p}}{\partial\xi} + k'(r)(z-h_0(r))\tilde{p} = 0,$$
$$\tag{C.17a}$$

$$D_t\tilde{u}_\theta + F\xi_0(r)\tilde{u}_r + \frac{1}{r}\frac{\partial\tilde{p}}{\partial\theta} = 0, \tag{C.17b}$$

$$D_t\tilde{u}_z + \epsilon\frac{\partial\tilde{p}}{\partial z} + k(r)\tilde{p} = 0, \tag{C.17c}$$

$$\frac{1}{r}\frac{\partial}{\partial r}(r\tilde{u}_r) + \frac{1}{r}\frac{\partial\tilde{u}_\theta}{\partial\theta} + k(r)(\tilde{u}_z - h_0'(r)\tilde{u}_r) + \epsilon\left(\frac{\partial\tilde{u}_z}{\partial\xi} - h_0'(r)\frac{\partial\tilde{u}_r}{\partial\xi}\right) + k'(r)(z-h_0(r))\tilde{u}_r = 0,$$
$$\tag{C.17d}$$

Now, $z - h_0(r) = \frac{\xi}{\epsilon}$, so the previous system can be written entirely in terms of ξ as

$$D_t\tilde{u}_r - 2F\Omega_0(r)\tilde{u}_\theta + \frac{\partial\tilde{p}}{\partial r} - h_0'(r)k(r)\tilde{p} - \epsilon h_0'(r)\frac{\partial\tilde{p}}{\partial\xi} + \frac{k'(r)}{\epsilon}\xi\tilde{p} = 0, \tag{C.18a}$$

$$D_t\tilde{u}_\theta + F\xi_0(r)\tilde{u}_r + \frac{1}{r}\frac{\partial\tilde{p}}{\partial\theta} = 0, \tag{C.18b}$$

$$D_t\tilde{u}_z + \epsilon\frac{\partial\tilde{p}}{\partial z} + k(r)\tilde{p} = 0, \tag{C.18c}$$

$$\frac{1}{r}\frac{\partial}{\partial r}(r\tilde{u}_r) + \frac{1}{r}\frac{\partial\tilde{u}_\theta}{\partial\theta} + k(r)(\tilde{u}_z - h_0'(r)\tilde{u}_r) + \epsilon\left(\frac{\partial\tilde{u}_z}{\partial\xi} - h_0'(r)\frac{\partial\tilde{u}_r}{\partial\xi}\right) + \frac{k'(r)}{\epsilon}\xi\tilde{u}_r = 0. \tag{C.18d}$$

with the boundary condition on the free surface

$$\tilde{u}_z = D_t\tilde{p} + h_0'(r)\tilde{u}_r, \qquad on \quad \xi = 0. \tag{C.19}$$

We proceed by making the formal expansion in powers of ϵ:

$$\begin{aligned}
\tilde{u}_r &= \tilde{u}_{r,0} + \epsilon\tilde{u}_{r,1} + \mathcal{O}(\epsilon^2),\\
\tilde{u}_\theta &= \tilde{u}_{\theta,0} + \epsilon\tilde{u}_{\theta,1} + \mathcal{O}(\epsilon^2),\\
\tilde{u}_z &= \tilde{u}_{z,0} + \epsilon\tilde{u}_{z,1} + \mathcal{O}(\epsilon^2),\\
\tilde{p} &= \tilde{p}_0 + \epsilon\tilde{p}_1 + \mathcal{O}(\epsilon^2),\\
k(r) &= k_0(r) + \epsilon k_1(r) + \mathcal{O}(\epsilon^2).
\end{aligned} \tag{C.20}$$

Collecting terms with the same power of ϵ we get the following systems cascade:

- ϵ^{-1}:

$$\begin{aligned}
k_0'(r)\xi\tilde{p}_0 &= 0,\\
k_0'(r)\xi\tilde{u}_{r,0} &= 0,
\end{aligned} \tag{C.21}$$

which returns $k_0(r) = const. = \bar{k}_0$.

- ϵ^0:

$$\begin{aligned}
&D_t\tilde{u}_{r,0} - 2F\Omega_0(r)\tilde{u}_{\theta,0} + \frac{\partial\tilde{p}_0}{\partial r} - \bar{k}_0 h_0'(r)\tilde{p}_0 + \xi k_1'(r)\tilde{p}_0 = 0,\\
&D_t\tilde{u}_{\theta,0} + F\xi_0(r)\tilde{u}_{r,0} + \frac{1}{r}\frac{\partial\tilde{p}_0}{\partial\theta} = 0,\\
&D_t\tilde{u}_{z,0} + \bar{k}_0\tilde{p}_0 = 0,\\
&\frac{1}{r}\frac{\partial}{\partial r}\left(r\tilde{u}_{r,0}\right) + \frac{1}{r}\frac{\partial\tilde{u}_{\theta,0}}{\partial\theta} + \bar{k}_0(\tilde{u}_{z,0} - h_0'(r)\tilde{u}_{r,0}) + \xi k_1'(r)\tilde{u}_{r,0} = 0,
\end{aligned} \tag{C.22}$$

From the set of equations (C.22) it has to be $k_1'(r) = 0$ in order it to be uniformly valid in $\xi \in (-\infty, 0)$. However, such a condition leads back to the interruption made in section C.1 of the present appendix, therefore we conclude here a justification based on the Multiple Scales approach.

Bibliography

M. Abramowitz and I. A. Stegun (1965). *Handbook of Mathematical Functions: With Formulas, Graphs, and Mathematical Tables*. Dover Pubblications Inc. ISBN 0486612724.

D. J. Acheson (1976). "On over-reflexion". *Journal of Fluid Mechanics*, **77** 433–472. doi: 10.1017/S0022112076002206.

A. Andersen, T. Bohr, B. Stenum, J. J. Rasmussen, and B. Lautrup (2006). "The bathtub vortex in a rotating container". *Journal of Fluid Mechanics*, **556** 121–146. doi: 10.1017/S0022112006009463.

B. Bach, E. C. Linnartz, M. H. Vested, A. Andersen, and T. Bohr (2014). "From Newton's bucket to rotating polygons: Experiments on surface instabilities in swirling flows". *Journal of Fluid Mechanics*, **759** 386–403. doi: 10.1017/jfm.2014.568.

U. Basu and A. K. Chopra (2007). "Perfectly matched layers for transient elastodynamics of unbounded domains". *International Journal for Numerical Methods in Engineering*, **59** 1039–1074. doi: 10.1002/nme.896.

G. K. Batchelor (2000). *An Introduction to Fluid Dynamics*. Cambridge University Press. ISBN 9780511800955.

A. Bayliss and E. Turkel (1980). "Radiation boundary conditions for wave-like equations". *Communications on Pure and Applied Mathematics*, **33** 707–725. doi: 10.1002/cpa.3160330603.

T. Bécherrawy (2012). *Mechanical and Electromagnetic Vibrations and Waves*. John Wiley and Sons, Inc. ISBN 9781118586525.

T. B. Benjamin and F. Ursell (1954). "The stability of the plane free surface of a liquid in vertical periodic motion". *Proceedings of the Royal Society of London. Series A. Mathematical and Physical Sciences*, **225** 505–515. https://www.jstor.org/stable/99519.

J. P. Berenger (1994). "A perfectly matched layer for the absorption of electromagnetic waves". *Journal of Computational Physics*, **114** 185–200. doi: 10.1006/jcph.1994.1159.

C. Bogey and C. Bailly (2003). "A family of low dispersive and low dissipative explicit schemes for flow and noise computations". *Journal of Computational Physics.*, pages 194–214. doi: 10.1016/j.jcp.2003.09.003.

J. Boussinesq (1871). "Theorie de l'intumescence liquide, applelee onde solitaire ou de translation, se propageant dans un canal rectangulaire". *Comptes Rendus de l'Academie des Sciences*, **72** 755–759.

J.P. Boyd (2001). *Chebyshev and Fourier spectral methods. 2nd revised edn. Mineola.* NY: Dover Publications. ISBN 9780486411835.

E. J. Brambley (2007). *The Acoustics of Curved and Lined Cylindrical Ducts with Mean Flow.* PhD thesis, University of Cambridge. doi: 10.17863/CAM.16086.

O. Bühler (2014). *Waves and mean Flows.* Cambridge University Press. ISBN 9781107478701.

O. Bühler and M. E. McIntyre (2005). "Wave capture and wave-vortex duality". *Journal of Fluid Mechanics*, **534** 67–95. doi: 10.1017/S0022112005004374.

V. Cardoso, O. J. C. Dias, J. P. S. Lemos, and S. Yoshida (2004). "Black-hole bomb and superradiant instabilities". *Physical Review D - Particles, Fields, Gravitation and Cosmology*, **70**. doi: 10.1103/PhysRevD.70.044039.

E. Cerda and F. Lund (1993). "Interaction of surface waves with vorticity in shallow water". *Physical Review Letters*, **70** 3896–3899. doi: 10.1103/PhysRevLett.70.3896.

W. C. Chew and Q. H. Liu (1996). "Perfectly matched layers for elastodynamics: a new absorbing boundary condition". *Journal of Computational Acoustics*, **4** 341–359. doi: 10.1142/S0218396X96000118.

B. Cushman-Roisin and J. M. Beckers (2011). *Introduction to Geophysical Fluid Dynamics.* Academic Press. ISBN 978-0-12-088759-0.

S. R. Dolan, L. A. Oliveira, and L. C. B. Crispino (2012). "Resonances of a rotating black hole analogue". *Physical Review D - Particles, Fields, Gravitation and Cosmology*, **85**. doi: 10.1103/PhysRevD.85.044031.

P. G. Drazin and N. Riley (2006). *The Navier-Stokes equations: a classification of flows and exact solutions.* Cambridge University Press. ISBN 9780521681629.

B. Engquist and A. Majda (1977). "Absorbing boundary conditions for the numerical simulation of waves". *Mathematics of Computation*, **31** 629–651. doi: 10.1090/S0025-5718-1977-0436612-4.

D. Fabre, D. Sipp, and L. Jacquin (2006). "Kelvin waves and the singular modes of the Lamb-Oseen vortex". *Journal of Fluid Mechanics.*, **551** 235–274. doi: 10.1017/S0022112005008463.

A. L. Fetter (1964). "Scattering of sound by a classical vortex". *Physical Review*, **136** A1488–A1493. doi: 10.1103/PhysRev.136.A1488.

J.B. Flòr (2010). *Fronts, Waves and Vortices in Geophysical Flows.* Springer-Verlag Berlin, Heidelberg. ISBN 978-3-642-11587-5.

R. Ford (1994). "The instability of an axisymmetric vortex with monotonic potential vorticity in rotating shallow water.". *Journal of Fluid Mechanics*, **280** 303–334. doi: 10.1017/S0022112094002946.

J. Fritz (1978). *Partial differential equations.* Springer-Verlag. ISBN 9781468400618.

Y. Gao, H. Song, J. Zhang, and Z. Yao (2017). "Comparison of artificial absorbing boundaries for acoustic wave equation modelling". *Exploration Geophysics*, **48** 76–93. doi: 10.1071/EG15068.

D. Givoli and B. Neta (2003). "High-order non-reflecting boundary scheme for time-dependent waves". *Journal of Computational Physics*, **186** 24–46. doi: 10.1016/S0021-9991(03)00005-6.

H. P. Greenspan (1969). *The theory of rotating fluids.* Cambridge University Press. ISBN 9780521051479.

M. J. Grote (2000a). "Non-reflecting boundary conditions for time dependent wave propagation". *Research Report/Seminar für Angewandte Mathematik.* doi: 10.3929/ethz-a-004288373.

M. J. Grote (2000b). "Nonreflecting boundary conditions for elastodynamic scattering". *Journal of Computational Physics*, **161** 331–353. doi: 10.1006/jcph.2000.6509.

M. J. Grote (2006). "Local nonreflecting boundary condition for Maxwell's equations". *Computer Methods in Applied Mechanics and Engineering*, **195** 3691–3708. doi: 10.1016/j.cma.2005.02.029.

M. J. Grote and J. B. Keller (1995). "Exact nonreflecting boundary conditions for the time dependent wave equation". *SIAM Journal on Applied Mathematics*, **55(2)** 280–297. doi: 10.1137/S0036139993269266.

M. J. Grote and J. B. Keller (1996). "Nonreflecting boundary conditions for time-dependent scattering". *Journal of Computational Physics*, **127** 52–65. doi: 10.1006/jcph.1996.0157.

M. J. Grote and J. B. Keller (2000). "Exact nonreflecting boundary condition for elastic waves". *SIAM Journal on Applied Mathematics*, **60** 803–819. doi: 10.1137/s0036139998344222.

M. J. Grote and I. Sim (2009). "On local nonreflecting boundary conditions for time dependent wave propagation". *Chines Annals of Mathematics. Series B*, **30** 589–606. doi: 10.1007/s11401-009-0203-5.

T. Hagstrom and S. I. Hariharan (1998). "A formulation of asymptotic and exact boundary conditions using local operators". *Applied Numerical Mathematics*, **27** 403–416. doi: 10.1016/S0168-9274(98)00022-1.

R. L. Higdon (1986). "Absorbing boundary conditions for difference approximations to the multi-dimensional wave equation". *Mathematics of Computation*, **47** 437–459. doi: 10.1090/S0025-5718-1986-0856696-4.

R. L. Higdon (1987). "Numerical absorbing boundary conditions for the wave equation". *Mathematics of Computation*, **49** 65–90. doi: 10.1090/S0025-5718-1987-0890254-1.

R. L. Higdon (1994). "Radiation boundary conditions for dispersive waves". *SIAM Journal of Numerical Analysis*, **31** 64–100. doi: 10.1137/0731004.

M. Hunt (2019). "Two-dimensional surface waves in magnetohydrodynamics". *Journal of Plasma Physics*, **85**. doi: 10.1017/S0022377819000497.

M. Hunt, E. Parau, J.-M. Vanden-Broeck, and D. Papageorgiou (2015). "Linear and nonlinear surface waves in electrohydrodynamics". *arXiv*, **:1501.02783**. doi: 10.48550/arXiv.1501.02783.

M. J. Hunt and D. Dutykh (2021). "Free surface flows in electrohydrodynamics with a constant vorticity distribution". *Water Waves*, **3** 297–317. doi: 10.1007/s42286-020-00043-9.

M. J. Hunt and J.-M. Vanden-Broeck (2015). "A study of the effects of electric field on two-dimensional inviscid nonlinear free surface flows generated by moving disturbances". *Journal of Engineering Mathematics*, **92** 1–13. doi: 10.1007/s10665-014-9766-6.

T. R. N. Jansson, M. P. Haspang, K. H. Jensen, P. Hersen, and T. Bohr (2006). "Polygons on a rotating fluid surface". *Physical Review Letters*, **96**. doi: 10.1103/PhysRevLett.96.174502.

R. S. Johnson (1997). *A Modern Introduction to the Mathematical Theory of Water Waves*. Cambridge University Press. ISBN 9780521598323.

M. J. King, E. J. Brambley, R. Liupekevicius, M. Radia, P. Lafourcade, and T. H. Shah (2022). "The critical layer in quadratic flow boundary layers over acoustic linings". *Journal of Fluid Mechanics.*, **950** A8. doi: 10.1017/jfm.2022.753.

R. C. Kloosterziel and G. J. F. Van Heijst (1992). "The evolution of stable barotropic vortices in a rotating free-surface fluid". *Journal of Fluid Mechanics*, **239** 607–629. doi: 10.1017/S0022112092004543.

V. F. Kopiev and I. V. Belyaev (2010). "On long-wave sound scattering by a Rankine vortex: Non-resonant and resonant cases". *Journal of Sound and Vibration*, **329** 1409–1421. doi: 10.1016/j.jsv.2009.10.028.

H. Lamb (1932). *Hydrodynamics*. Cambridge University Press, 6th edition.

J. M. Lindquist, B. Neta, and F. X. Giraldo (2012). "High-order non-reflecting boundary conditions for dispersive waves in polar coordinates using spectral elements". *Applied Mathematics and Computation*, **218** 6666–6676. doi: 10.1016/j.amc.2011.12.023.

F. Lund and C. Rojas (1989). "Ultrasound as a probe of turbulence". *Physica D: nonlinear phenomena*, **37** 508–514. doi: 10.1016/0167-2789(89)90155-3.

A. Mager (1972). "Dissipation and breakdown of a wing-tip vortex". *Journal of Fluid Mechanics.*, **55** 609–628. doi: 10.1017/S0022112072002046.

M. H. Makhmalbaf, T. Liu, and P. Merati (2017). "A vortex flow intensified by thermal convection". *Physics of Fluids*, **29**. doi: 10.1063/1.4974754.

G. R. Mamatsashvili and W. K. M. Rice (2009). "Vortices in self-gravitating gaseous discs". *Monthly Notices of the Royal Astronomical Society*, **394** 2153–2163. doi: 10.1111/j.1365-2966.2009.14481.x.

J. C. McWilliams (2006). *Fundamentals of Geophysical Fluid Dynamics*. Cambridge University Press. ISBN 978052185637.

P. A. Milewski and J. B. Keller (1996). "Three-dimensional water waves". *Studies in Applied Mathematics*, **97** 149–166. doi: 10.1002/sapm1996972149.

J. Mougel, D. Fabre, and L. Lacaze (2014). "Waves and instabilities in rotating free surface flows". *Mechanics and Industry*, **15** 107–112. doi: 10.1051/meca/2014007.

J. Mougel, D. Fabre, and L. Lacaze (2015). "Waves in Newton's bucket". *Journal of Fluid Mechanics*, **783** 211–250. doi: 10.1017/jfm.2015.527.

J. Mougel, D. Fabre, L. Lacaze, and T. Bohr (2017). "On the instabilities of a potential vortex with a free surface". *Journal of Fluid Mechanics.*, **824** 230–264. doi: 10.1017/jfm.2017.341.

S. V. Nazarenko, N. J. Zabusky, and T. Scheidegger (1995). "Nonlinear sound-vortex interactions in an inviscid isentropic fluid: A two-fluid model". *Physics of Fluids*, **7** 2407–2419. doi: 10.1063/1.868769.

L. A. Oliveira, V. Cardoso, and L. C. B. Crispino (2014). "Ergoregion instability: the hydrodynamic vortex". *Physical Review D - Particles, Fields, Gravitation and Cosmology*, **89**. doi: 10.1103/PhysRevD.89.124008.

S. Patrick (2019). *On the analogy between black holes and bathtub vortices.* PhD thesis, School of Mathematical Sciences - University of Nottingham. `https://arxiv.org/abs/2009.02133`.

S. Patrick and S. Weinfurtner (2020). "Superradiance in dispersive black hole analogues". *Physical Review D*, **102**. doi: 10.1103/PhysRevD.102.084041.

S. Patrick, A. Coutant, M. Richartz, and S. Weinfurtner (2018). "Black hole quasibound states from a draining bathtub vortex flow". *Physical Review Letters*, **121**. doi: 10.1103/PhysRevLett.121.061101.

A. Quarteroni (2009). *Numerical models for differential problems.* Springer-Verlag Italia. ISBN 9788847010710.

A. Quarteroni, F. Saleri, and P. Gervasio (2014). *Scientific computing with MATLAB and Octave.* Springer Berlin, Heidelberg. ISBN 978-3-642-45367-0.

M. Richartz, A. Prain, S. Liberati, and S. Weinfurtner (2015). "Rotating black holes in a draining bathtub: superradiant scattering of gravity waves". *Physical Review D - Particles, Fields, Gravitation and Cosmology*, **91**. doi: 10.1103/PhysRevD.91.124018.

P. G. Saffman (1992). *Vortex Dynamics.* Cambridge University Press. ISBN 0-521-42058-X.

V. M. Sauer, F. F. Fachini, and D. Dunn-Rankin (2018). "Non-premixed swirl-type tubular flames burning liquid fuels". *Journal of Fluid Mechanics.*, **846** 210–239. doi: 10.1017/jfm.2018.248.

W. E. Schiesser and G. W. Griffiths (2009). *A Compendium of Partial Differential Equations Models: Method of Lines Analysis with Matlab.* Cambridge University Press. ISBN 978-0-521-51986-1.

R. S. Scorer and L. J. Davenport (1970). "Contrails and aircraft downwash". *Journal of Fluid Mechanics.*, **43** 451–464. doi: 10.1017/S0022112070002501.

R. L. Seliger and G. B. Whitham (1968). "Variational principles in continuum mechanics". *Proceedings of the Royal Society of London. Series A. Mathematical and Physical Sciences*, **305**(1480) 1–25. doi: 10.1098/rspa.1968.0103.

J. Shen (1997). "Efficient spectral-galerkin methods iii: polar and cylindrical geometries". *SIAM Journal on Scientific Computing*, **18** 1583–1604. doi: 10.1137/S1064827595295301.

I. Sim (2010). *Non-Reflecting Boundary Conditions for Time-Dependent Wave Propagation*. PhD thesis, University of Basel. doi: 10.5451/unibas-005269594.

J. M. Skipp (2020). "Single vortex ring". `https://youtube.com/shorts/ApwCq7UkCfY`. Accessed 2021-11-09.

A. Söderstrom, M. Karlsson, and K. Museth (2010). "A PML-based nonreflective boundary for free surface fluid animation". *ACM Transactions on Graphics*, **29**. doi: 10.1145/1857907.1857912.

L. Tophoj, J. Mougel, T. Bohr, and D. Fabre (2013). "Rotating polygon instability of a swirling free surface flow". *Physical Review Letters*, **110**. doi: 10.1103/PhysRevLett.110.194502.

T. Torres (2019). *Hydrodynamic simulations of black holes*. PhD thesis, School of Mathematical Sciences - University of Nottingham. `https://doi.org/10.48550/arXiv.2111.02282`.

T. Torres, S. Patrick, A. Coutant, M. Richartz, E. W. Tedford, and S. Weinfurtner (2017). "Rotational superradiant scattering in a vortex flow". *Nature Physics*, **13** 833–836. doi: 10.1038/nphys4151.

T. Torres, A. Coutant, S. Dolan, and S. Weinfurtner (2018). "Waves on a vortex: rays, rings and resonances". *Journal of Fluid Mechanics.*, **857** 291–311. doi: 10.1017/jfm.2018.752.

W. G. Unruh (1981). "Experimental black-hole evaporation?". *Physical Review Letters*, **46** 1351–1353. doi: 10.1103/PhysRevLett.46.1351.

G. B. Whitham (1974). *Linear and Nonlinear Waves*. New York, Wiley. ISBN 9780471359425.

J. Z. Wu, H. Y. Ma, and M. D. Zhou (2006). *Vorticity and Vortex Dynamics*. Springer-Verlag. ISBN 10 3-540-29027-3.

L. Zhao and A. C. Cangellaris (1996). "A general approach for the development of unsplit-field time-domain implementations of perfectly matched layers for FDTD grid truncation". *IEEE Microwave and Guided Wave Letters*, **6** 209–211. doi: 10.1109/75.491508.

A. Ziampras, W. Kley, and R. P. Nelson (2023). "Hydrodynamic turbulence in disks with embedded planets". *Astronomy and Astrophysics*, **670**. doi: 10.1051/0004-6361/202245325.

E. Zuccoli, E. J. Brambley, and D. Barkley (2023). "Trapped free surface waves for a Lamb-Oseen vortex flow". *Journal of Fluid Mechanics (under review)*, . doi: 10.48550/arXiv.2209.14011.